Lucas H.J. Eskens

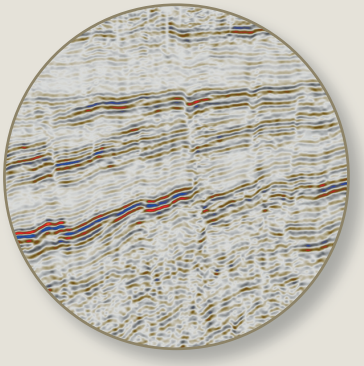

On the mechanisms controlling alongstrike variations in pro-forelandbasin development

A case study of the Alps-Molasse Basin system

KIT Scientific Publishing

Lucas H.J. Eskens

On the mechanisms controlling along-strike variations in pro-foreland basin development

A case study of the Alps-Molasse Basin system

On the mechanisms controlling along-strike variations in pro-foreland basin development

A case study of the Alps-Molasse Basin system

by
Lucas H.J. Eskens

KIT Scientific Publishing

Karlsruher Institut für Technologie
Institut für Angewandte Geowissenschaften – Allgemeine Geologie

On the mechanisms controlling along-strike variations in pro-foreland basin development: a case study of the Alps-Molasse Basin system

Zur Erlangung des akademischen Grades eines Doktors der Naturwissenschaften (Dr. rer. nat.) von der KIT-Fakultät für Bauingenieur-, Geo- und Umweltwissenschaften des Karlsruher Instituts für Technologie (KIT) genehmigte Dissertation

von Lucas H.J. Eskens

Tag der mündlichen Prüfung: 12. Februar 2025
Erster Gutachter: TT. Prof. Dr. Nevena Andrić-Tomašević
Zweiter Gutachter: Prof. Dr. Christoph Hilgers

Impressum

Scientific Publishing

Karlsruher Institut für Technologie (KIT)
KIT Scientific Publishing
Straße am Forum 2
D-76131 Karlsruhe

www.bibliothek.kit.edu/ksp.php | E-Mail: info@ksp.kit.edu | Shop: www.ksp.kit.edu

Print on Demand 2026 – Gedruckt auf FSC-zertifiziertem Papier

ISBN 978-3-7315-1443-5
DOI 10.5445/KSP/1000182696

Acknowledgements

The pursuit of a PhD is, well, a dynamic adventure in many ways, one could say. Sometimes you're in this high because you bump into this amazing result, or a manuscript got accepted for publication. However, then, the next day, this tough revision lands on your desk, and you start asking yourself, "Why do I do this again?". As such, conducting doctoral research is a marathon rather than a sprint. It requires stamina, perseverance, and discipline from the student. But you don't do it alone. Down the road, many people support you in different ways. I want to thank everyone who made this time unforgettable and helped me during various steps of this research project.

First and foremost, I would like to thank my promotor Nevena Andrić-Tomašević for allowing me to embark on this personal and scientific adventure. When I started working at the KIT, I came in as this little fellow unbeknownst to the world of Science, say a mali krompir. During this time, she more than adequately guided me scientifically, professionally, and personally. On top of this, she supported me in conducting part of my research at SLB in the UK, which was a very valuable experience I otherwise would have never had. Furthermore, she allowed me to help shape the Basin Analysis and Modelling course, where I could share my passion for seismic interpreting and basin analysis with the MSc. students at the KIT. I can safely say that Nevena was the best supervisor I could have hoped for, and I feel honoured to have conducted my doctoral research with her. Now, 3.5 years later, I leave the KIT still unbeknownst to many things this world has to offer. Yet, a krompir that is a little wiser in the way of Science, thanks to her.

Apart from Nevena, the General Geology Group comprised my amazing colleagues Giridas Maiti, Paul Baville, and Robert Šamarija. Together, we formed the fundaments for the General Geology Group, which I will never forget we did together. I had many interesting (geological) discussions with all of you that challenged me to think outside the box and taught me much. Apart from the scientific side of life, I will not forget the good times we shared and the

plethora of alcoholic beverages that came with them. I could not have done this without your support and the fun times we had together.

My colleagues from the Structural Geology group at the KIT are also gratefully thanked for making the last few years the good times they were. I want to thank Bruno Mendes, Dorina Juhász, Johanna Berckhan, Chaojie Cheng, Felix Allgaier, and Melike Yildirim for all the fun conversations and laughs we had in the hallway; it made all the difference. Furthermore, I would like to thank Benjamin Busch for teaching me some things about permeability, porosity and their links to reservoir quality, as well as the discussions about European and regional geology. Oh, and the weird moments when passing eachother in the hallways. Furthermore, I would like to thank Jasmin Ölmez for helping me translate the abstract from English to German, as well as both insightful and fun conversations.

I would also like to thank Todd Ehlers for the supervision, his time reviewing manuscripts, positive support during different conferences, and the discussions about how to tackle research in general.

Furthermore, I would like to express my gratitude to Barbara Claussmann for the amazing three months we worked together at SLB in the UK and her help preparing the manuscript regarding our work. Our discussions were a lot of fun and educational, and she was a big contributor to my good time while visiting the UK. I see her as my third supervisor, and she played a crucial role in shaping the outcome of this research.

Peter Süss is gratefully acknowledged for his supervision during the early stage of this project, for discussions regarding the evolution of the Alps-Molasse Basin system, and teaching me different workflows regarding seismic interpretation and structural modelling.

I also want to gratefully thank Andrea Piccolo for all the energy and effort he put into our collaborative effort. He always made time to explain certain model features or answer other questions I had, and he helped with writing the manuscript of the research we worked on together.

During my research, I also had the pleasure of collaborating with Magdalena Scheck-Wenderoth and Ajay Kumar. My communication and discussions with them were very fruitful and interesting, for which I am very thankful.

Robert Ulwig, Igor Kozlov, and Bahaa Elzarei are also thanked for the interesting- and insightful discussions we had during their MSc. theses, the funny interactions while having these discussions and keeping me scientifically on my toes.

Matthias Müller and Rolf Herrmann are sincerely thanked for the discussions regarding the development of the Molasse Basin, teaching me workflows regarding seismic interpretation, and the general progression of the project. Furthermore, I would like to acknowledge ONEO GmbH for providing the data that made this study possible.

The people who support you outside of the academic activities are at least half as important as the people with whom you work. They help to keep you sane by providing distractions from work, or you can come knocking at their door to complain about how difficult things are. For this, I would like to thank Bas Koene and Niels van de Pol for providing mental support on many occasions (or simply by drinking a beer). I also want to thank Gyan van der Jagt, who, during the first 2.5 years, shared the mentality “apes together strong” while working parallel on our doctorates. Lastly, I want to thank my parents, Antoinette Roetgerink and Ferry Eskens, for supporting my throughout the highs and the lows of this adventure.

Abstract

In source-to-sink systems, sedimentary sinks (i.e., basins) preserve the erosional products of the source, transcribing the Earth's surface evolution. geologists can read these records to reconstruct the climatic, eustatic, biologic, and tectonic history. Basins records are essential to help us understand the effects of climate change on weather patterns. Furthermore, basins host crucial resources such as drinkwater reservoirs and targets vital for geological applications involved in the energy transition (e.g., geothermal heat production, storage sites, and critical minerals such as Lithium or Copper). However, overlap of the signals of basin-forming mechanisms obscure which of these is dominant in controlling basin architecture. To optimize resource use and decrease exploration risks, it is paramount to understand the interaction between these mechanism(s) and how they control basin architecture.

In this thesis, I aimed to investigate which mechanism(s) is/are of primary importance in causing along-strike variations in foreland basin architecture and a diachronous underfilled to overfilled transition. Because slab breakoff and lateral tearing are often hypothesised as dominant drivers for these features, defining their signals as recorded by the synorogenic basin fill was of particular interest. To tackle these goals, a multidisciplinary and multiscale approach integrates a tectonostratigraphic analysis with 2D forward stratigraphic modelling of an orogen-foreland basin system influenced by slab breakoff. To this end, we use the Alps-Molasse Basin system as a natural laboratory.

Chapter 2 presents a detailed basin-scale tectonostratigraphic analysis of the Molasse Basin based on reflection seismic, calibrating wells, existing subsurface models, and literature. Comparing the Molasse Basin's evolution to that of the Alps demonstrates that subduction and collision of the irregular European margin resulted in a diachronous collision between the European and Adriatic plates. This, in turn, led to spatiotemporal variable slab breakoff(s), causing orogen-parallel variation in sediment supply. This culminated in the diachronous underfilled to overfilled transition in the Molasse Basin.

Chapter 3 quantitatively examines seismic-scale syn-flexural normal fault growth in a foreland basin, linking this to mechanisms controlling flexure, using the Molasse Basin as a case study. The results lead to a new 4D syn-flexural normal fault growth model in foreland basins. Additionally, basin-orthogonal temporal variations in fault nucleation record forebulge migration. Furthermore, west-to-east increases in cumulative offsets evidence that along-strike variations in topographic loads and crustal strength did not primarily control the distribution of flexure. Instead, along-strike variations in lithospheric strength of the lower plate did contribute to the flexure distribution and, thereby, basin architecture.

Chapter 4 explores mechanisms driving orogenward forebulge migration, using the Aquitanian-Burdigalian narrowing of the Eastern German Molasse as a case study. Integration of seismic interpretations with semi-numerical models demonstrates that increased topographic loading of the stationary Eastern Alps temporarily caused orogenward forebulge migration. However, this change in basin architecture was short-lived, and other mechanisms quickly overshadowed the control of topographic loading on foreland flexure.

Chapter 5 evaluates the tectonostratigraphic signal of slab breakoff in foreland basins using a one-way coupling workflow between 2D geodynamic slab breakoff models and forward stratigraphic models. Results show that slab necking- and breakoff cause isostatic rebound of the basin floor and adjacent mountain range, with the latter forcing increased sediment supply. This forces a change from aggradational to progradational deposition concurrent with a coarsening upward trend, potentially leading to an underfilled to overfilled transition. For this transition, basin floor uplift is of first-order importance. These changes in deposition are more pronounced for steeper slabs in a low-viscosity mantle setting.

Lastly, Chapter 6 summarises the results regarding the hierarchy of mechanism(s) controlling foreland basin architecture, as well as the tectonostratigraphic fingerprint from slab breakoff. Furthermore, an overall tectonostratigraphic model of the evolution of the Alps-Molasse Basin system is presented. Finally, I present remaining open questions and suggest how to tackle them.

Zusammenfassung

In Geologische Quelle-Senke-Systemen bewahren Becken die Erosionsprodukte der Quelle auf und zeichnen die Entwicklung der Erdoberfläche auf., wodurch sich Rückschlüsse auf Klima, Tektonik und andere Prozesse ziehen lassen. Zudem enthalen Becken wichtige Ressourcen wie Trinkwasserreservoire und Ziele, die für geologische Anwendungen im Rahmen der Energiewende von entscheidender Bedeutung sind (z. B. geothermische Wärmeerzeugung, Kohlenwasserstoffe, und Speicherstätten für CO2). Da sich die stratigrafischen Signale verschiedener Beckenbildungsmechanismen überschneiden, ist unklar, welcher dominiert. Ein besseres Verständnis ihrer Weschselwirkungen ist entscheidend, um Ressourcen gezielt zu nutzen und Explorationsrisiken zu minimieren.

In dieser Arbeit habe ich untersucht, welche(r) Mechanismen/Mechanismus vorrangig für einen Diachronen Übergang von Unterfüllung zu Überfüllung in Vorlandbecken verantowrlich ist/sein. Im Fokus standen die tektonischen Signale von Da slab breakoff- and trearing, wie sie in der synorogenen Beckenfüllung erkennbar sind. Um diese Ziele zu erreichen, wurde ein multidisziplinärer und multiskaliger Ansatz gewählt, der eine tektonostratigraphische Analyse mit einer 2D-stratigraphischen Vorwärtsmodellierung eines durch slab breakoff beeinflussten Orogenen-Vorland-Beckensystems verbindet. Zu diesem Zweck nutzen wir das Alpen-Molasse-Becken-System als natürliches Labor.

In Kapitel 2 wird eine detaillierte tektonostratigraphische Analyse des Molassebeckens auf der Grundlage von Reflexionsseismik, Kalibrierungsbohrungen, bestehenden Untergrundmodellen und Literatur vorgestellt. Die Ergebnisse zeigen, dass die Subduktion und Kollision des unregelmäßigen Europäischen Kontinentalrandes zu einer diachronen Kollision zwischen der Europäischen und der Adriatischen Platte führte. Dies wiederum führte zu räumlich und

zeitlich variablen slab breakoffs, die eine orogenparallele Variation des Sedimentangebots zur Folge hatten. Dies gipfelte in dem diachronen Übergang von der Unterfüllung zur Überfüllung des Molassebeckens.

Kapitel 3 untersucht quantitativ das seismische Wachstum von synflexiblen Abschiebungen in einem Vorlandbecken und stellt eine Verbindung zu den Mechanismen her, die die Biegung kontrollieren. Die Ergebnisse führen zu einem neuen 4D-Modell des synflexuralen Wachstum von Abschiebungen in Vorlandbecken. Darüber hinaus zeigen die beckenorthogonalen zeitlichen Schwankungen der Störungsentstehung die Migration der Vorgebirge. Zudem zeigen von Westen nach Osten zunehmende kumulative Offsets, dass Variationen in der lithosphärischen Festigkeit der unteren Platte entlang des Strangs zur Biegeverteilung und damit zur Beckenarchitektur bei.

Kapitel 4 untersucht die Mechanismen, die die orogenwärts gerichtete forebulge migration antreiben. Die Integration seismischer Interpretationen mit seminumerischen Modellen zeigt, dass eine erhöhte topographische Belastung der stationären Ostalpen vorübergehend eine orogenwärts gerichtete forebulge migration verursachte. Diese Veränderung der Beckenarchitektur war jedoch nur von kurzer Dauer, und die Kontrolle der topographischen Belastung wurde relativ schnell durch andere Mechanismen überschattet.

In Kapitel 5 wird das tektonostratigraphische Signal von slab breakoff in Vorlandbecken mithilfe 2D geodynamischer und stratigraphischer Modelle untersucht. Die Ergebnisse zeigen, dass Platteneinschnürung und -abbruch einer isostatischen Hebung von Beckenboden und Gebirge führt, was die Sedimentzufuhr erhöht. Dadurch ändert die Ablagerung von aggradational zu progradational, gleichzeitig mit Körnervergrößerung. Die Hebung des Beckenbodens ist von erster Ordnung für diese Übergänge. Diese Veränderungen in der Ablagerung sind bei breakoff von steilerem slabs in einem Mantel mit niedriger Viskosität stärker ausgeprägt.

Abschließend werden in Kapitel 6 die Ergebnisse hinsichtlich der Hierarchie der Mechanismen, die die Architektur der Vorlandbecken steuern, sowie der

tektonostratigraphische Fingerabdruck von slab breakoff zusammengefasst. Darüber hinaus wird ein umfassendes tektonostratigraphisches Modell der Entwicklung des Alpen-Molasse-Becken-Systems vorgestellt. Abschließend stelle ich die verbleibenden offenen Fragen vor und empfehle, wie sie angegangen werden können.

Samenvatting

In geologische bron-tot-put-systemen bewaren bekkens de erosieproducten van de respectievelijke bron. De geologische informatie opgeslagen in de vorm van sediment in bekkens zijn essentieel om ons te helpen de effecten van klimaatverandering op weerpatronen te begrijpen. Bovendien herbergen bekkens cruciale bronnen voor de energietransitie (bijv. geothermische warmteproductie of opslaglocaties voor CO_2) en drinkwaterreservoirs. Omdat stratigrafische signalen van verschillende bekkenvormende mechanismen met elkaar overlappen, is onduidelijk welke dominant is voor de resulterende bekkenarchitectuur. Een beter begrip van de interacties tussen deze processen is cruciaal om doelgericht gebruik te maken van de bronnen die bekkens bieden.

In dit proefschrift heb ik onderzocht welk(e) mechanisme(n) van primair belang is/zijn voor het veroorzaken van laterale variaties in de architectuur van voorlandbekkens en een diachrone overgang van een onder- naar overvuld bekken. De focus ligt hierbij op de effecten van slab breakoff- en tearing, en hoe deze processen worden weerspiegeld in de synorogene bekkenvulling. Hiervoor heb ik een multidisciplinaire, multischaalbenadering gebruikt, gebruikmakende van de integratie van tektonostratigrafische analyse met 2D voorwaartse stratigrafische modellering van een orogen-voorlandbekken. Hiervoor gebruiken heb ik het Alpen-Molassebekken systeem als een natuurlijk laboratorium.

Hoofdstuk 2 presenteert een gedetailleerde tektonostratigrafische analyse op schaal van het Molassebekken op basis van seismische reflecties, boorgegevens, bestaande ondergrondmodellen en literatuur. De resultaten tonen aan dat de onregelmatige Europese marge de diachrone collisie tussen de Europese en Adriatische platen bevorderde. Dit leidde op zijn beurt tot spatiotemporele variabele afbraak(en) van Europese slabs, vertaald in orogeen-parallelle variatie in opheffing van de Alpen. Op zijn beurt leidt did

tot orogen-parallel variatie in sedimentaanvoer, met als gevolg de diachrone overgang van onder- naar overvulde architectuur van het Molassebekken.

Hoofdstuk 3 onderzoekt de vorming van syn-flexurale afschuivingsbreuken in voorlandbekkens, en koppelt deze aan mechanismen die de buiging van de voorlandplaat controleren. De toename van cumulatieve afschuivingsgrootte van west naar oost toont aan dat laterale verschillen in lithosferische sterkte van de voorlandplaat van primair belang zijn voor de verdeling van buiging van de voorlandplaat, en daarmee de bekkenarchitectuur.

Hoofdstuk 4 onderzoekt de mechanismen die orogene forebulge migratie veroorzaken aan de hand van de Aquitanisch-Bardigalische vernauwing van de Oost-Duitse Molassebekken. De integratie van seismische interpretaties met seminumerieke modellering laat zien dat verhoogde topografische belading uitgeoefend door de stationaire oostelijke Alpen tijdelijk forebulge migratie richting het gebergte veroorzaakte. Deze verandering in de architectuur van het bekken was echter van korte duur, en andere mechanismen overstemden snel de controle van topografische belading op het buigprofiel van de voorlandplaat.

In hoofdstuk 5 wordt het tektonostratigrafische signaal van afbraak van slabs in voorlandbekkens geanalyseerd met behulp van gekoppelde 2D geodynamische- en voorwaartse stratigrafische modellen. De resultaten tonen aan dat het insnoeren en afbreken van een slab leidt tot een isostatische terugvering van de bekkenbodem en het gebergte, waardoor de sedimentaanvoer toeneemt. Als gevolg verandert het afzettingspatroon van aggradationeel naar progradationeel, gelijktijdig met vergroving van het sediment. De opheffing van de bekkenbodem is van eerste orde belang voor deze veranderingen in sedimentatie. De verandering in depositiestijl zijn meer uitgesproken voor afbraak van steilere slabs in een mantel met lage viscositeit.

Hoofdstuk 6 vat de resultaten samen met betrekking tot de hiërarchie van de mechanismen die de architectuur van het voorlandbekken bepalen.

Bovendien wordt de tectonostratigrafische vingerafdruk van het afbreken van een slab in een voorlandbekken bediscusseerd. Verder wordt een algemeen tectonostratigrafisch model van de evolutie van het Alpen-Molassebekkensysteem gepresenteerd. Tot slot presenteer ik resterende open vragen en stel ik voor hoe deze kunnen worden aangepakt.

Contents

Appendix

Declaration of originiality

Chapter 2: As first author, Lucas H.J. Eskens made all the seismic interpretations and combined them with published data to reconstruct the Molasse Basin. The basin-wide geological model using structural modelling was generated with the assistance of Peter M. Süss and Matthias Müller. The presented datasets were acquired during the PhD research by Nevena Andrić-Tomašević. Lucas H.J. Eskens developed the models derived from the results, made the figures, and wrote the article with valuable inputs to all of these from Nevena Andrić-Tomašević, Peter M. Süss, Matthias Müller, Rolf Herrmann, and Todd A. Ehlers.

Chapter 3: As the first author, Lucas H.J. Eskens made all the seismic interpretations, made the figures, developed the models, and wrote the manuscript, which included valuable inputs from Nevena Andrić-Tomašević, Ajay Kumar, and Magdalena Scheck-Wenderoth. Additional data regarding the distribution of the lithospheric- and crustal strength of the European plate and the integration thereof with fault growth was supplied by- and discussed with Ajay Kumar and Magdalena Scheck-Wenderoth. Furthermore, additional input from Nevena Andrić-Tomašević helped develop the implications of the results and added to the quality of the manuscript.

Chapter 4: As first author, Lucas H.J. Eskens conducted the forward stratigraphic modelling, prepared the figures and tables. The geodynamic models were set up and run by Andrea Piccolo. Discussions with- and supervision from Barbara Claussmann, Mostfa Lejri, and Nevena Andrić-Tomašević aided with setting up the forward stratigraphic models and making parameter choices. The article was written with resourceful inputs from Nevena Andrić-Tomašević, Andrea Piccolo, Barbara Claussmann, Mostfa Lejri, Marcel Thielmann, and Todd A. Ehlers.

Chapter 5: As first author, Lucas H.J. Eskens made the seismic interpretations, prepared most of the figures, developed the suggested model, and wrote

most of the manuscript with constructive comments from Giridas Maiti and Nevena Andrić-Tomašević. The semi-numerical flexural modelling, the preparation of the related figure, and the description of the results therefrom were done by Giridas Maiti. Discussions and input from Nevena Andrić-Tomašević to the model and writing added to the quality of the manuscript.

Chapter 1
Introduction & motivation

1.1 Motivation

Analyses of source-to-sink systems (Meade, 1972) in geology attempt to invert information extracted from sedimentary sinks (i.e., basins) to reconstruct the evolution of the respective sediment source(s) (Allen, 2008; Sømme et al., 2009). The sediment catchment and basin are genetically linked, meaning that changes in the amount and type of sediment supplied by the source due to intrinsic and external forcing mechanism(s) (e.g., tectonics, exposure of a different source lithology, climate change) will result in morphological changes in the related basin. Additionally, alterations to the basin geometry may cause changes in depositional styles. Sedimentary basins are 1) targets for a multitude of subsurface applications important for the energy transition (e.g., geothermal exploration or CO2/nuclear storage, Alexander et al., 2015; Bachu, 2003; Cacace et al., 2010; Schrag, 2009), 2) contain drinkwater/hydrogen reservoirs and storage sites, and 3) host critical minerals (e.g. Lithium, Stober et al., 2023). To identify potential prospects and to prevent potential environmental damage from any of these applications, it is crucial to understand the development of a source-to-sink system.

Orogen-foreland basin systems are prime examples of source-to-sink systems (with the orogen being the source and the foreland basin the sink). In such a tectonic setting, oceanic subduction followed by a post-collisional stage leads to increasing elevation of the mountain range (Royden, 1993a; Schmid et al., 1996). As the elevation of a mountain range progressively increases, it is subject to (increased) erosion (Ehlers and Poulsen, 2009; Montgomery and Brandon, 2002; Whipple, 2009). This results in the degradation of the mountain range, leaving only fragments of the would-be orogenic architecture. Palinspastic reconstructions offer insight into the geodynamic and plate kinematic context of orogenesis (McQuarrie, 2002; Woodward et al., 1989). However, because the record is incomplete due to erosion of the mountain range, deciphering the full tectonic story solely based on this method remains elusive. The erosional products from the mountain range are (partially) preserved in the adjacent foreland basin(s) (DeCelles, 2012; Naylor and Sinclair,

2008). Therefore, it also contains clues regarding the regional tectonic, erosional, and climatic evolution of the orogen-foreland basin system. By applying source-to-sink principles (i.e., linking changes in sediment supply from the catchments, due to, e.g., tectonics or climate, to their signal in the respective basin), it is possible to invert the spatiotemporal development of a foreland basin architecture in terms of key processes that determine its architecture. As such, a tectonostratigraphic analysis of a foreland basin yields additional clues regarding the tectonic evolution of the orogen-foreland basin system.

Pro-foreland basins, from here on referred to as foreland basins, are the flexural basins that develop on the continental lithosphere of the lower plate in front of an advancing orogenic wedge (Beaumont, 1981; DeCelles and Giles, 1996; Roure, 2008, Figure 1.1). Overthrusting of the lower plate by the orogenic belt results in migration of the foreland basin, leading to the spatiotemporal cratonward migration of the four depozones (wedge-top, foredeep, forebulge, and backbulge, Figure 1.1, DeCelles, 2012). The architecture of a foreland basin is the combined expression of flexural subsidence of the foreland plate generating accommodation space and sediment supply derived from the adjacent orogenic wedge (DeCelles, 2012; Jordan and Flemings, 1991). The flexural subsidence that generates accommodation space results from the interplay between intrinsic lithospheric- and crustal-scale mechanisms, as well as external processes independent of the orogenic tectonics. The lithospheric-scale mechanisms that control foreland flexure are the strength of the foreland plate (Burov, 2011; Cardozo and Jordan, 2001; Waschbusch and Royden, 1992) and the magnitude of slab loading (Royden, 1993b; Sinclair, 1997b). The crustal-scale mechanisms include thrusting in the developing orogen leading to the development of a topographic load (DeCelles and Giles, 1996; Flemings and Jordan, 1990; Karner and Watts, 1983) and the inherited crustal architecture of both the lower- and upper plates (Cooper et al., 1995; Dewey and Kidd, 1974; Roure, 2008; Sinclair, 1997a). Additionally, eustacy (partly) controls the accommodation space (Posamentier and James, 1993) and the mountain range's tectonic- and climate history influencing the sediment supply (Molnar and England, 1990;

Montgomery and Brandon, 2002; Schaller and Ehlers, 2021; Whipple, 2009) are external forcing mechanisms that control foreland basin architecture.

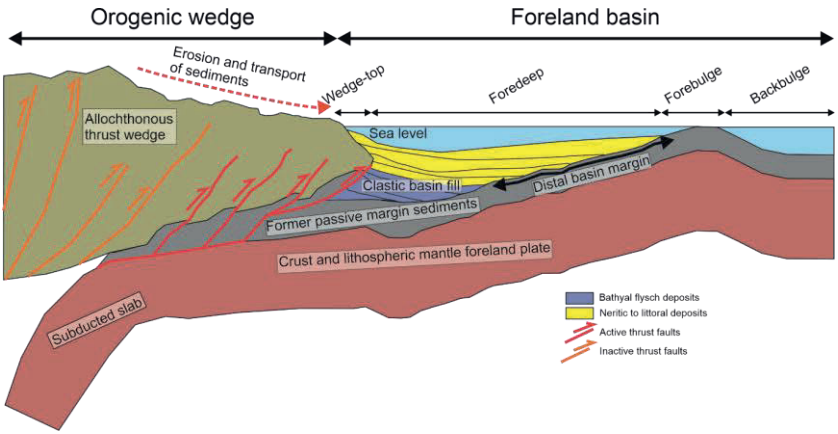

Figure 1.1: Schematic representation of the different elements of an orogen-foreland basin system during frontal propagation. The geological elements are not to scale. Modified from Figure 4.1 (Chapter 4).

The interactions between the abovementioned processes are preserved in the synorogenic fill of a foreland basin (e.g., Beaumont, 1981; DeCelles and Giles, 1996). For a geologist, this sedimentary sequence can be read like a history book in which basin architectural changes in response to the tectonic and environmental forcing processes are transcribed. In many foreland basins (e.g., Northern Alpine, Appalachian, Apenninic, and Tarim foreland basins, Amadori et al., 2019; He et al., 2016; Lash, 1988) the synorogenic fill records along-strike variations in basin development such as a diachronous transition from underfilled to overfilled deposition (i.e., the coeval existence of both continental- and deep water depositional environments, sensu Carroll and Bohacs, 1999), and/or variations in thicknesses. This hints at orogen-parallel variations in the abovementioned processes that control the accommodation

space and sediment supply. Previous authors suggested orogen-parallel variations in 1) topographic loads (DeCelles and Mitra, 1995; Whiting and Thomas, 1994), 2) sediment supply from the adjacent orogen related to climatic conditions (Garefalakis and Schlunegger, 2019; Kuhlemann and Kempf, 2002b; Malkowski et al., 2017; Schlunegger and Castelltort, 2016), 3) crustal architecture of the pre-flexural platform (Cooper et al., 1995; Dewey and Kidd, 1974; Roure, 2008; Sinclair, 1997a), 4) eustacy (Jin et al., 1995; Lemcke, 1988), and 5) lateral slab tearing (Ascione et al., 2012; Meulenkamp et al., 1996; Schlunegger and Kissling, 2022; Van der Meulen et al., 1998) to be the dominant mechanism(s) to induce along-strike variations in foreland basin development.

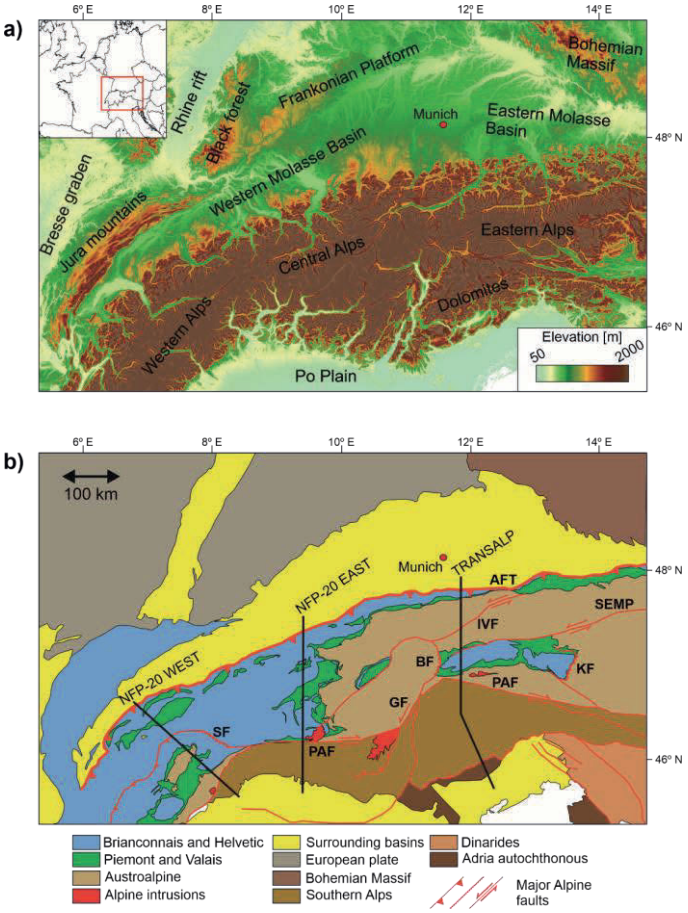

Figure 1.2: a) Digital elevation model of the Molasse Basin and the surrounding areas. **b)** Geological map of the Alps and the surrounding region. **AFT** – Alpine Frontal Thrust, **IVF** – Inntall Valley Fault, **BF** – Brenner Fault, **GF** – Giudicarie Fault, **PAF** – Periadriatic Fault, **SF** – Simplon Fault, **SEMP** – Salzach-Ennstal-Mariazell-Puchberg Fault, **KF** – Katschberg Fault.

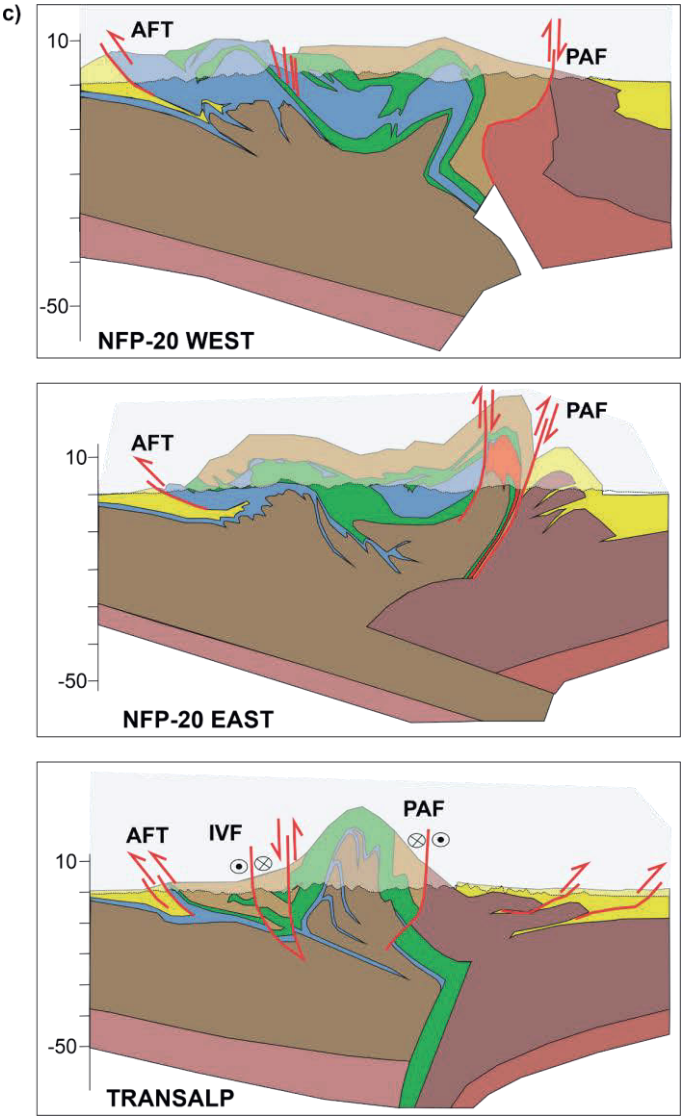

Figure 1.2 (continued): **c)** Three cross sections perpendicular to the strike of the Alps highlighting the orogen-parallel variation in the architecture of the mountain range. Drawn after (Schmid et al., 2004b).

However, these processes often operate simultaneously, leading to overlapping signals of the respective processes. Therefore, it remains unclear which mechanism(s) is/are dominant in causing along-strike variable foreland basin architecture and/or a diachronous underfilled to overfilled transition. To get a better understanding of the hierarchy of the different basin-forming mechanisms causing along-strike variations in foreland basin architecture, I focused my PhD research on the Northern Alpine Foreland Basin (NAFB, from here on referred to as the Molasse Basin, Figure 1.2a).

The Molasse Basin is the foreland basin of the Alps that developed during the continental collision between the lower European- and upper Adriatic plates (Handy et al., 2010; Schmid et al., 1996). The lateral variation in the composition and structure of the Alpine nappe stack, for example the lack of material derived from the Brianconnais terrane and lack of external massifs in the Eastern Alps (Handy et al., 2010; Schmid et al., 2004b; Schmid et al., 1996; Stampfli et al., 1998, Figure 1.2b and 1.2c), hints at orogen-parallel variations in Alpine tectonics. In the Molasse Basin, this is reflected as a diachronous underfilled to overfilled transition (Figure 1.3, Kuhlemann and Kempf, 2002; Lemcke, 1988; Sissingh, 1997; Wagner, 1998).

Previous authors attributed this to European slab breakoff- and tearing having caused orogen-parallel variations in sediment supply to the Molasse Basin (Figure 1.3, Kuhlemann and Kempf, 2002; Schlunegger and Kissling, 2022). Alternatively, a 200 m eustatic sea level fall at the end of the Oligocene was suggested to explain along-strike variations in basin architecture (Figure 1.3, Diem, 1986; Lemcke, 1988). However, the effects of along-strike variations in the crustal architecture of the pre-flexural basement (Lemcke, 1988), lithospheric architecture of the subducted European margin (Faupl and Wagreich, 2000; Handy et al., 2010; Stampfli, 1993), and strength of the European lithosphere (Spooner et al., 2022) remain largely undiscussed. Therefore, this area serves as an ideal natural laboratory to identify which mechanism(s) was/were of primary importance for the along-strike variation in foreland basin evolution and the diachronous underfilled to overfilled transition.

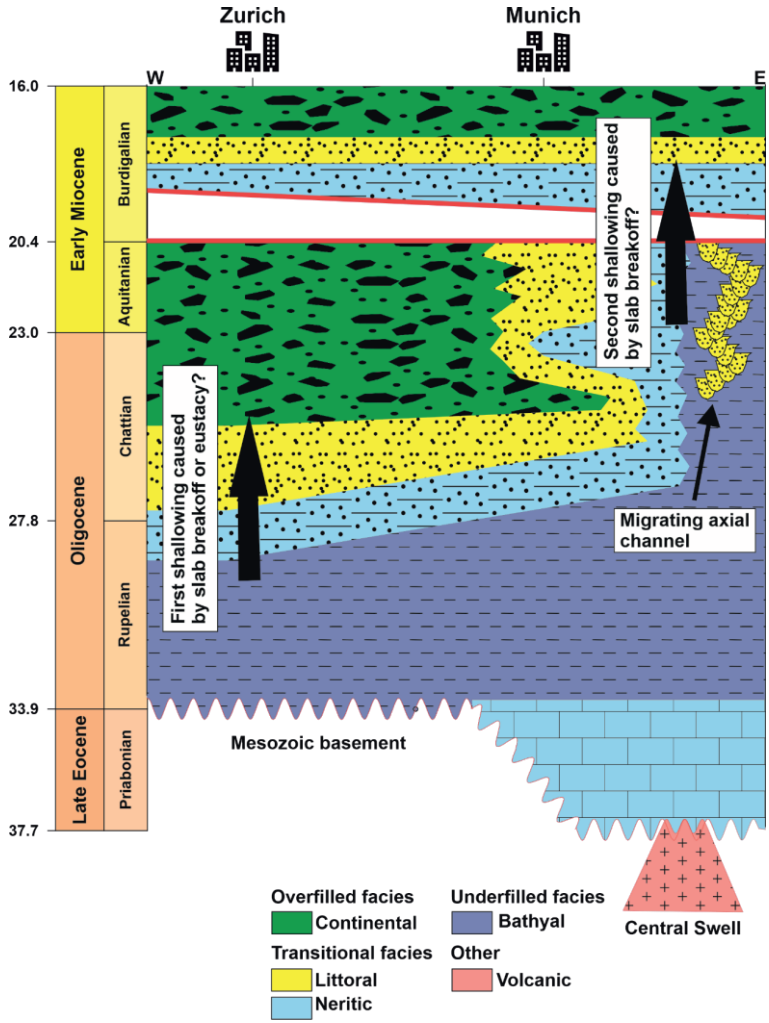

Figure 1.3: Schematic west-east Wheeler diagram of the syn-orogenic fill of the Molasse Basin and the respective depositional environments it represents. Based on Kuhlemann and Kempf (2002), their Figure 2. The migration of the axial channel is based on data from (De Ruig and Hubbard, 2006) and is schematically drawn.

1.2 Aims

The aim of this thesis is to investigate which process(es) is/are dominant in causing along-strike variations in foreland basin architecture and, thereby, a diachronous under- to overfill transition. Of particular interest is the tectonostratigraphic signal from slab breakoff- and tearing in a foreland basin.

To study the influence of different basin-controlling mechanisms on foreland basin architecture, a detailed tectonostratigraphic analysis of the Molasse Basin is made. Additionally, these findings are integrated with results from coupled geodynamic and stratigraphic forward models focussing on quantifying the signal of slab break off in foreland basin fill. My efforts focus on five major aspects:

1. Disentangling the signals from eustacy, lithospheric-, and crustal tectonics in the synorogenic fill of the Molasse Basin.
2. Characterisation of the influence of the irregularities in pre-collisional crustal platform- and lithospheric heterogeneities in foreland plate architecture on foreland basin development.
3. Defining how syn-flexural normal faults in foreland basins grow in 4D can be used to reconstruct forebulge migration, as well as their relation to lithospheric- and crustal mechanism(s) that control flexure of the foreland plate.
4. The effect of post-collisional orogenic thickening on foreland basin architecture.
5. Definition of the sedimentary- and geophysical signal from slab breakoff as recorded in the synorogenic fill of a foreland basin per numerical modelling.

1.3 Overview of the thesis

1.3.1 Lithospheric- and crustal-scale controls on variations in foreland basin development in the Northern Alpine Foreland Basin (Chapter 2)

In Chapter 2, a high-resolution tectonostratigraphic model of the Molasse Basin is constructed by appending interpretations of new reflection seismic data to published data found in literature. Furthermore, a 3D geological model of the Molasse Basin and its Mesozoic basement was constructed to constrain the influence of the inherited platform architecture on the foreland basin development. Comparing this with the Alps' geodynamic evolution and global eustacy allowed us to identify which mechanism(s) controlled the flexural basin architecture.

The results demonstrate that the early Molasse Basin architecture (late Eocene) was primarily controlled by inherited bathymetry of the European Mesozoic platform. However, this effect was quickly overshadowed by progressive slab- and topograhic loading of the European lithosphere. Subsequent along-strike variable development of the Molasse Basin was predominantly controlled by a west-to-east decrease in Alpine topography, resulting in a west-to-east decrease in sediment supply. This orogen-parallel variation in paleotopography is derived from the subduction and collision of the irregular European margin, causing spatiotemporal variations in Alpine exhumation and uplift. These findings underpin the so-far overlooked importance of the inherited rift architecture of the European margin on the subsequent tectonostratigraphic evolution of the Molasse Basin.

1.3.2 Spatiotemporal growth of seismic-scale syn-flexural normal faults in the German Molasse Basin (Chapter 3)

Chapter 3 focuses on a quantitative analysis of seismic-scale syn-flexural normal fault in the German Molasse to constrain their fault growth styles. Furthermore, orogen-parallel trends in syn-flexural throw trends are compared to the distributions of the topographic loads, crustal- and lithospheric strength to assess their contribution to along-strike variations in the Oligocene to early Miocene Molasse Basin architecture. The strength of this approach is that fault activity is solely influenced by tectonic factors controlling foreland architecture, ruling out overprinting by climatic or eustatic effects.

The results demonstrated that extensional strain localised at the surface of the forebulge, promoting shallow nucleation of new faults and reactivating pre-existing faults at shallow depths. The spatiotemporal patterns in the nucleation of the new faults could be used to constrain the propagation of the orogen-foreland system. Furthermore, it was observed that even though deeper-buried normal faults were not reactivated, they still localised extensional deformation in their cover. Lastly, the combination of throw-depth and backstripped throw-length profiles allowed for the development of a 4D fault growth model.

At the basin scale, an eastward increase in cumulative syn-flexural offsets was interpreted to reflect an eastward increase in the magnitude of flexure of the European lithosphere. This was parallel to a decrease in European lithospheric strength, suggesting that this factor contributed to the Oligocene to early Miocene west-to-east deepening of the Molasse Basin. Conversely, the European crustal strength increased from west to east, and the topographic load was low where the magnitude of flexure was high and vice versa. This implies that these factors did not contribute to along-strike variations in the architecture of the Molasse Basin.

1.3.3 Thickening of a stationary orogen and its effect on foreland architecture (Chapter 4)

Chapter 4 focuses on the processes controlling thrustward migration of a forebulge in a foreland basin system. To this end, we used the German Molasse Basin east of Munich as our natural laboratory, where 80 km of southward migration of the forebulge occurred during the Aquitanian-Burdigalian transition. We used 2D analytical models to verify our interpretations.

Seismic interpretations evidenced that thrustward migration of the forebulge was associated with the incision of the former distal margin. The thrustward migration was potentially driven by enhanced topographic loading exerted by the stationary Eastern Alps due to folding- and duplexing of the Tauern window. The 2D analytical models support this interpretation. However, this change in basin architecture was short-lived, and the forebulge migrated back north. This suggests that the effect of topographic loading was quickly overshadowed by other processes controlling flexure, in this case potentially slab breakoff.

1.3.4 The tectonostratigraphic expression of slab breakoff in foreland basins: insights from 2D forward stratigraphic modelling (Chapter 5)

In Chapter 5, the tectonostratigraphic signal from slab breakoff in a foreland basin and potential masking thereof by eustacy is numerically investigated. The numerical experiments were conducted using a one-way coupling approach between 2D geodynamic models constructed in *LaMEM*- and forward stratigraphic models in the Geological Process Modelling software (GPM) embedded in Petrel. The strength of this approach lies in isolating slab breakoff as the sole mechanism to control foreland basin architecture.

Model results illustrate that during necking- and breakoff, the progressively faster decrease in slab pull conducted to the surface results in the uplift of

the foreland basin- and mountain range. The former forces a decrease in accommodation space, while the latter causes an increase in sediment supply from the adjacent mountain range. Together, these processes culminate in a change from aggradational to progradation deposition with a coarsening-upward trend and, ultimately, a transition from underfilled- to overfilled deposition. Because the rate at which accommodation space is reduced due to basin floor uplift is greater than the enhanced sediment supply, the former process is of first-order importance, and the latter of second-order importance is for inducing the underfilled to overfilled transition.

Furthermore, results highlighted that the surface response was more sensitive to the loss of slab pull for a low mantle viscosity and steeper slabs. Within the parameter space, eustacy did not influence the preservation of the tectonostratigraphic signal from slab necking and breakoff. First-order stratigraphic and geophysical signals forced by slab breakoff in the models resemble observations made in the Austrian Molasse, supporting the hypothesis that the basin architecture was influenced by slab breakoff.

1.3.5 General discussion, concluding remarks and future perspectives (Chapter 6)

Chapter 6 summarises the results and provides a synthesis regarding to which degree different basin-forming mechanisms control foreland basin architecture the architecture of the Molasse Basin. It emphasises the feedback between Alpine lithospheric-scale controls and their expression in the synorogenic fill of the Molasse Basin. To conclude, some remaining open questions that could not be answered during this doctoral research are highlighted, along with suggestions for bridging these scientific gaps.

1.4 Parts of this thesis that have been published

Published articles

Eskens, Lucas HJ, et al. "Lithospheric-and crustal-scale controls on variations in foreland basin development in the Northern Alpine Foreland Basin." *Tectonophysics* 878 (2024): 230283.

Submitted manuscripts

Eskens, Lucas HJ, et al. "Spatiotemporal growth of seismic-scale syn-flexural normal faults in the German Molasse Basin." *Basin Research, in review.*

Eskens, Lucas HJ, et al. "The tectonostratigraphic expression of slab breakoff in foreland basins: insights from 2D forward stratigraphic modelling." *Tectonics, in communication.*

Eskens, Lucas HJ, et al. "Thickening of a stationary orogen and its effect on foreland basin architecture." *Terra Nova, in communication.*

Conference contributions

Eskens, Lucas, et al. "Syn-flexural normal faults in pro-foreland basins; what can they tell us about geodynamics?" (2024). *AAPG 2024 Europe Region Conference.*

Eskens, Lucas, et al. "Is Slab Breakoff Recorded in the Stratigraphic Record of a Foreland Basin? Insights from Forward Stratigraphic Modelling." (2023) *AGU Fall Meeting 2023.*

Eskens, Lucas HJ, et al. "Signals of slab breakoff-and tearing in the stratigraphic architecture of a foreland basin." (2023). *7th annual AlpArray Scientific Meeting*.

Eskens, Lucas HJ, et al. "Signals of slab breakoff-and tearing in the stratigraphic architecture of a foreland basin." (2023). *GeoBerlin 2023.*

Eskens, Lucas, et al. "Growth of normal faults in flexural foreland basins: a case study of the Northern Alpine Foreland Basin." (2023). *EGU 2023.*

Eskens, Lucas, et al. "The effects of lithospheric-scale processes on foreland basin development: a case study of the Northern Alpine Foreland Basin." (2022). *6th annual AlpArray Scientific Meeting*.

Eskens, Lucas, et al. "Controls on along-strike variations of basin development: a case study of the Northern Alpine Foreland Basin." (2022). *EGU 2022.*

Chapter 2
Lithospheric- and crustal-scale controls on variations in foreland basin development in the Northern Alpine Foreland Basin

This chapter is based on:

Eskens, Lucas HJ, et al. "Lithospheric-and crustal-scale controls on variations in foreland basin development in the Northern Alpine Foreland Basin." *Tectonophysics* 878 (2024): 230283.

2.1 Introduction

Flexural basins develop next to orogens as a result of topographic and subsurface loading (such as deep-seated loads or subducting slabs) that result in lithospheric flexure of the subducting foreland plate. Their stratigraphic fill and basin architecture record the interplay between the flexural generation of accommodation space and sediment supply from the adjacent mountain range (DeCelles and Giles, 1996; Flemings and Jordan, 1990). Numerous foreland basins (e.g., Appalachian, Apenninic, and Tarim, Amadori et al., 2019; He et al., 2016; Lash, 1988) record along-strike variations in basin architectures (e.g., coeval existence of both underfilled and overfilled deposition, sensu Homewood et al., 1986). Several processes can produce along-strike variable foreland basin architectures. Examples include orogen-parallel variations in crustal thickening of the orogenic wedge (DeCelles and Mitra, 1995; Whiting and Thomas, 1994), lateral slab tearing (Ascione et al., 2012; Meulenkamp et al., 1996; Schlunegger and Kissling, 2022; Van der Meulen et al., 1998), climate change and/or sediment availability (Garefalakis and Schlunegger, 2019; Kuhlemann and Kempf, 2002b; Malkowski et al., 2017; Schlunegger and Castelltort, 2016), and along-strike variations in the inherited pre-foreland crustal architecture (Cooper et al., 1995; Dewey and Kidd, 1974; Roure, 2008; Sinclair, 1997a). A natural example that records along-strike variations in the stratigraphic basin architecture is the Northern Alpine Foreland Basin (e.g., Kuhlemann and Kempf, 2002b, hereafter referred to as the Molasse Basin (MB), Figure 2.1). To better understand the controls of lithospheric- and crustal-scale processes on the along-strike variation in MB architecture, we investigate the tectonostratigraphic evolution of this basin and relate it to the geodynamic evolution of the Alps.

Since the Late Cretaceous, the European and Adriatic plates have been converging (e.g., Handy et al., 2015). By the late Eocene, convergence led to continental collision and the onset of flexural subsidence of the peripheral MB (e.g., Schmid et al., 1996). A key characteristic of the Cenozoic syn-flexural

basin fill is the Oligocene to early Miocene diachronous transition from underfilled- to overfilled deposition (i.e., transition from flysch to molasse deposition; Allen et al., 1991; Bachmann and Müller, 1991; Homewood and Lateltin, 1988; Kuhlemann and Kempf, 2002b; Lemcke, 1988; Sinclair, 1997a).

This transition started at 31.5 to 30 Ma in the Swiss Molasse (Kempf et al., 1999; Kempf and Pross, 2005; Schlunegger et al., 1997b) and reached the Austrian Molasse by 19 to 18 Ma (Hülscher et al., 2019). The mechanisms proposed for this diachronous transition include eustacy (Eastern German Molasse, Bachmann and Müller, 1991; Jin et al., 1995; Zweigel et al., 1998), inherited basement architecture (stratigraphy and structures, Lihou and Allen, 1996, Swiss Molasse), visco-elastic relaxation of the European plate (Borzi et al., 2022, Eastern German and Austrian Molasse; Hülscher et al., 2019; Zweigel et al., 1998), and slab breakoff (Schlunegger and Castelltort, 2016; Schlunegger and Kissling, 2015; Sinclair, 1997a). On the scale of the entire MB, Alpine lithospheric-scale processes may have governed along-strike variations in sediment supply, driving the along-strike diachronous underfill- to overfill transition (Kuhlemann and Kempf, 2002b; Schlunegger and Kissling, 2022). In addition, it has been suggested that lateral tearing of the European slab governed west-to-east depocenter migration along the entire Alpine-Carpathian chain (Meulenkamp et al., 1996). This slab breakoff- and tearing hypothesis explains the mechanisms that induced the diachronous underfill- to overfilled transition in the MB during the Oligocene to early Miocene. Fingerprints of lateral slab tearing include lithospheric-scale STEP faults (sensu Andrić-Tomašević et al., 2023; Govers and Wortel, 2005; Neely and Furlong, 2018), a younging trend of asthenospheric magmatism parallel to the proposed direction of slab tearing (Ferrari, 2004; Ferrari et al., 2012; Menant et al., 2016), and trench-mountain curvature (Andrić-Tomašević et al., 2023; Li et al., 2013). However, such features are less evident in the Alps. Therefore, alternative mechanisms, which may have controlled the Oligocene to early Miocene evolution of the MB, require consideration.

Previous paleogeographic reconstructions suggest an irregular European passive margin (Stampfli, 1993; Faupl and Wagreich, 2000; Stampfli et al., 2002;

Ziegler and Dézes, 2007; Handy et al., 2010; Handy et al., 2015). This irregularity was characterised by the presence of the continental Brianconnais terrane, which tapered out between the future Western/Central- and Eastern Alps (Faupl and Wagreich, 2000; Mohn et al., 2010; Rosenberg et al., 2021). Previous geologic (Zagros mountains, Alipour, 2023; Manatschal et al., 2022; Mohn et al., 2014; Alps, Stockmal et al., 1987) and geodynamic studies (Tetreault and Buiter, 2012; van Hunen and Allen, 2011; Vogt and Gerya, 2012) demonstrated that subduction- and collision of an irregular margin leads to orogen-parallel variations in the foreland basin architecture (Angrand et al., 2018; Gül et al., 2015; Lash, 1988).

However, the influence of a subducting irregular European margin on the MB architecture has received little attention (Lihou and Allen, 1996; Schlunegger and Kissling, 2022; Sinclair, 1997a). The irregularity of the European margin promoted an earlier collision in the western part of the European-Adria suture (also inferred by Schlunegger and Kissling, 2022). If true, this led to an earlier underfill-to-overfill transition in the western part of the MB compared to the eastern part. In this contribution, we evaluate both the hypotheses that the diachronous underfill-to-overfill transition in the MB was controlled by 1) slab breakoff- and tearing or 2) collision- and subduction of the irregular European passive margin.

To test these hypotheses, we construct a 3D geological model of the MB north of the present-day Alpine thrust front using existing subsurface models (GeoMol, 2015; Figure 2.1a). Furthermore, we interpret 2D/3D seismic data in the German Molasse (Figure 2.1a, 2D seismic lines and seismic volumes A and B) for the late Eocene to early Miocene depositional environments and syn-flexural normal fault kinematics. Combining these analyses enables a reconstruction of the tectonostratigraphy of the MB resulting from the geodynamic evolution of the Alps. Our results suggest that the pre-flexural European passive margin architecture controlled the late Eocene architecture of the German Molasse. Furthermore, subduction- and collision of the irregular European margin likely influenced the along-strike variations in the surface uplift of the Alps.

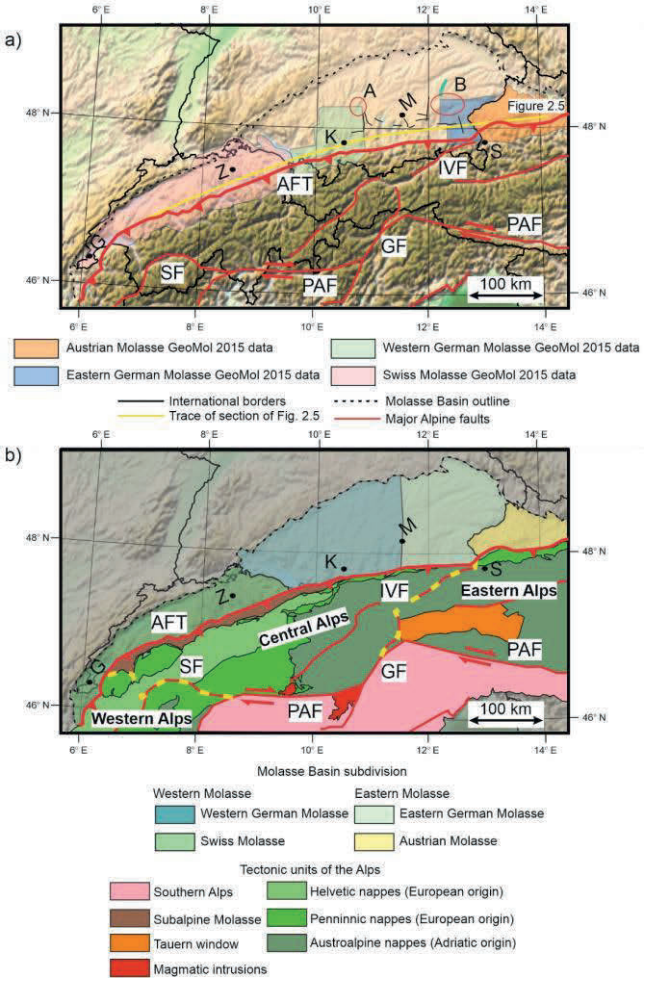
a)
6° E
8° E
10° E
12° E
14° E
48° N
46° N
A
B
M
K
Z
S
AFT
IVF
PAF
GF
SF
Figure 2.5
100 km
Austrian Molasse GeoMol 2015 data
Western German Molasse GeoMol 2015 data
Eastern German Molasse GeoMol 2015 data
Swiss Molasse GeoMol 2015 data
International borders
Molasse Basin outline
Trace of section of Fig. 2.5
Major Alpine faults
b)
Eastern Alps
Central Alps
Western Alps
Molasse Basin subdivision
Western Molasse
Eastern Molasse
Western German Molasse
Eastern German Molasse
Swiss Molasse
Austrian Molasse
Tectonic units of the Alps
Southern Alps
Helvetic nappes (European origin)
Subalpine Molasse
Penninnic nappes (European origin)
Tauern window
Austroalpine nappes (Adriatic origin)
Magmatic intrusions

Figure 2.1 (previous page): **a)** Relief map of the Alps, Molasse Basin, and surrounding areas from the ETOPO1 Global Relief Model (Amante and Eakins, 2009), showing the locations of data and model results presented in this study. The red circles indicate the locations of 3D seismic volumes A and B, and the black lines are 2D seismic lines. The green line north of seismic volume B shows the location of the seismic line shown in Figure A1.14. **b)** Tectonic map of the Alps and Molasse Basin, indicating the subdivision in this study. Tectonic units in the Alps are modified from (Schmid et al., 2004b). The subdivision of the Alps is based on (Kuhlemann and Kempf, 2002), where the yellow dashed lines indicate the borders between different parts of the orogen. The subdivision of the Molasse Basin is based on differences in the tectonostratigraphic development of various parts of the basin (See Subsection 2.2.2 for details). **AFT =** Alpine Frontal Thrust, **GF** = Giudicarie Fault, **SF** = Simplon Fault, **PAF** = Periadriatic Fault, **IVF** = Inntal Valley Fault, **G** = Geneva, **K** = Kaufbeuren, **L** = Linz, **M** = Munich, **S** = Salzburg, **Z** = Zürich.

2.2 Geological setting

The Alps and the adjacent MB extend from south of Lake Geneva to Lower Austria, striking roughly E-W over ca. 700 km (Figure 2.1). From west to east, the MB is bounded north by the Jura Mountains, the Swabian/Franconian Alb, and the Bohemian Massif. The thickness of the syn-flexural Cenozoic fill of the MB increases from north to south, reaching ~5000 m in front of the Alps (e.g. Bachmann and Müller, 1991). A rough division of the MB is typically made between the Oligocene brackish/terrestrial Western Molasse (Swiss and Western German Molasse, Figure 2.1a) and littoral to bathyal Eastern Molasse (Eastern German and Austrian Molasse, Figure 2.1a, Kuhlemann and Kempf, 2002b). Furthermore, we subdivide the Eastern Molasse into the Eastern German Molasse (German Molasse east of Munich) and Austrian Molasse (Figure 2.1a) because of their different histories (Subsection 2.2.2.2).

The adjacent Alps are a nappe stack of European and Adriatic-derived material (e.g., Schmid et al., 1996; Schmid et al., 2004a). While European-derived units dominate the western part of the orogen, Adriatic-derived units are more prominent in the eastern part (Figure 2.1b). This lateral variation in the structure of the nappe stack suggests orogen-parallel variations in Alpine tectonics (e.g., Schmid et al., 1996; Stampfli et al., 1998; Handy et al., 2010).

2.2.1 Geodynamic evolution of the Alpine hinterland

The Penninic domain (Piemont Ocean and Valais Through) separated the Adriatic and European plates from the Late Jurassic until collision in the late Eocene (Le Breton et al., 2021; Mohn et al., 2010; Schmid et al., 1996; Ziegler et al., 1996). Along the future Western and Central Alps, the Piemont Ocean and Valais Trough were separated by the continental Brianconnais terrane (Handy et al., 2010; Mohn et al., 2010; Le Breton et al., 2021; Rosenberg et al., 2021). However, this terrane tapered out towards the future Eastern Alps (e.g. Stampfli et al., 2002; Stampfli, 1993). This led to an irregular European margin. Subduction of the Penninic domain started in the Late Cretaceous (84 Ma, Handy et al., 2010; Handy et al., 2015; Le Breton et al., 2021; Stampfli et al., 1998). By the late Eocene continental collision started (Schmid et al., 1996; Ziegler et al., 1996) leading to the overthrusting of the European margin by the Alpine nappe stack. Alpine nappe stacking and European slab loading caused flexural subsidence of the foreland (Allen et al., 1991; Schmid et al., 1996; Wagner, 1998). At that time, the shelf sediments of the Ultrahelvetic domain were incorporated into the thrust wedge to form the Helvetic nappes (Burkhard, 1988; Pfiffner, 1993; Schmid et al., 1996). Coeval late Eocene to early Oligocene emplacement of intrusives along the Periadriatic Fault (Figure 2.1b, Barth et al., 1989; Dal-Piaz et al., 1988; von Blanckenburg and Davies, 1992) suggests that continental collision was followed by European oceanic slab breakoff (~43-30 Ma, von Blanckenburg and Davies, 1995; Schmid et al., 1996). This led to an increase in exhumation, backthrusting, and low-angle detachment faulting in the Western/Central Alps, which further caused increased erosion rates between 30 and 20 Ma (Hurford, 1986; Schlunegger and Kissling, 2015; Schlunegger and Willett, 1999; Schmid et al., 1996; Von Eynatten et al., 1999). Despite slab breakoff, the Alpine nappes continued to migrate northward, overthrusting the Infrahelvetic domain by the early Oligocene (including the parautochthonous Cenozoic cover of the Aar Massif, consisting out of middle- to late Eocene limestones and early Oligocene flysch, Allen et al., 1991; Heyng, 2012; Pfiffner, 1986; Pfiffner, 1993; Schmid et al., 1996; Zerlauth et al., 2014). Along the Central- and Eastern Alpine front,

the basal Helvetic thrust remained active until at least the late Oligocene (Schmid et al., 1996; Zerlauth et al., 2014). The thrust front of the Eastern Alps continued to migrate northward during the Oligocene and early Miocene (Covault et al., 2009; Hinsch, 2013; Zerlauth et al., 2014).

A second slab breakoff is suggested below the Eastern Alps during the early Miocene (20 Ma, Handy et al., 2015; Schmid et al., 2004a; Ustaszewski et al., 2008). Similar to the late Eocene to early Oligocene breakoff, this break-off event correlates with increased exhumation rates (Fox et al., 2016; Fügenschuh et al., 1997) and increased sediment supply from the Eastern Alps (Kuhlemann, 2000), as well as a switch from in-sequence to out-of-sequence thrusting (Covault et al., 2009; Hinsch, 2013; Hurford et al., 1989; Ortner et al., 2015; Von Hagke et al., 2014). However, continued indentation by the Adriatic plate resulted in the eastward tectonic escape of the Eastern Alps rather than continued northward migration (Favaro et al., 2015; Ratschbacher et al., 1991b; Rosenberg et al., 2007). This tectonic reorganisation was contemporary with the cessation of subsidence in the Eastern Molasse (20 to 18 Ma, Genser et al., 2007; Ortner et al., 2015; Schlunegger and Kissling, 2022). Only southeast of Munich did the subsidence continue after the early Burdigalian (Zweigel et al., 1998). Furthermore, the tectonic reorganisation in the Eastern Alps was coeval with the onset of southward in-sequence thrusting in the Southern Alps (Caputo et al., 2010; Schönborn, 1999).

2.2.2 Stratigraphy of the foreland plate

The following sections give a synoptic overview of the pre-flexural Mesozoic basement stratigraphy (Subsection 2.2.2.1) and syn-flexural basin fill of the Molasse Basin (Subsection 2.2.2.2).

2.2.2.1 Paleozoic and Mesozoic basement

The Variscan crystalline basement of the MB consists of gneisses and granites (Bachmann and Müller, 1991; Herrmann et al., 1985), locally cut by Carboniferous to Triassic grabens (Bachmann and Müller, 1991; Gautschi et al., 2008).

This is overlain by middle Triassic to Late Cretaceous passive margin sediments with a spatially variable thickness distribution (Bachmann and Müller, 1991; Frisch, 1979; Nachtmann and Wagner, 1987; Ziegler, 1990). From west to east, the Mesozoic subcrop of the foreland unconformity changes from Late Jurassic to Late Cretaceous stratigraphy (Bachmann and Müller, 1991; Lemcke, 1988).

2.2.2.2 Cenozoic syn-flexural fill of the Molasse Basin

The oldest Cenozoic deposits of the Western Molasse are found in the parautochthonous cover of the Aar Massif (now part of the fold-and–thrust-belt). Here, Infrahelvetic Lutetian (middle Eocene) littoral sands and limestones overlie the foreland unconformity (Allen et al., 1991; Menkveld-Gfeller, 1995; Menkveld-Gfeller, 1997; Sinclair, 1997b). These deposits are covered by turbiditic bathyal middle to late Eocene sediments (Globigerina marls and Taveyannaz Fm., Allen et al., 1991; Burkhard and Sommaruga, 1998; Sinclair, 1997b; Sissingh, 1997). In contrast, in the autochthonous Western Molasse, similar deposits are either scarce or lacking (up to 10 m thickness, Lemcke, 1988; Müller, 2011). The littoral platform limestones overlying the foreland unconformity represent the lower unit of the underfilled trinity (sensu Sinclair, 1997b, succession of littoral platform limestones overlain by hemipelagic marls and subsequently bathyal siliciclastic turbidites). This unit is interpreted to record a foreland basin's initially slow and sediment-starved subsidence. Early Rupelian bathyal turbiditic conditions are recorded in the entire autochthonous Western Molasse (Elm and Matt Fms. of the parautochtonous cover of the Aar Massif, Deutenhausen Beds, and Rupelian fish Shale for the Western German Molasse, Allen et al., 1991; Maurer, 2006; Pfiffner, 1986; Sissingh, 1997). By the late Rupelian, deposition shallowed to neritic conditions along the southern basin margin (Lower Marine Molasse for the Swiss Molasse and Rupelian Tonmergel/Zupfing Fm. for the Western German Molasse, Allen et al., 1991; Diem, 1986; Mraz et al., 2018; Sissingh, 1997). In the Western Molasse, this shallowing (i.e., the underfill- to overfill transition) occurred between 31.5 and 30 Ma, reaching as far east as the Allgäu (Kempf et al., 1999; Kempf and Pross, 2005; Schlunegger et al., 1997b).

The shallowing was contemporaneous with the development of alluvial megafans along the Swiss Alpine front (Honegg-Napf, Rigi, and Speer fan systems, 31 - 30 Ma, Kempf et al., 1999; Schlunegger et al., 1996). Eastwards along strike the littoral conditions in the Swiss Molasse (Horw Sandstones, Diem, 1986), transitioned into neritic conditions in the Western German Molasse (Rupelian Tonmergel, Mraz et al., 2018; Zaugg and Löpfe, 2011). Littoral depositional conditions reached the Western German Molasse by the earliest Chattian (28 Ma onset of Baustein Beds deposition, Mraz et al., 2018). From the middle Chattian until the end of the Aquitanian, the Western Molasse developed as an eastward draining fluvial environment (26 to 20.5 Ma, Lower Freshwater Molasse and Cyrena Beds, Kuhlemann and Kempf, 2002b; Matter, 1980; Platt, 1992; Platt and Keller, 1992; Reichenbacher et al., 2004; Ziegler and Storch, 2008). Subsequently, this fluvial environment was flooded during the early Burdigalian Transgression, leading to the re-establishment of neritic depositional conditions between 20 to 17 Ma (St. Gallen, Luzern and Baltringer Fm., Garefalakis and Schlunegger, 2019; Keller, 1989; Lemcke, 1988; Matter, 1980; Schlunegger et al., 1997a). However, the depositional environment quickly shallowed back to terrestrial conditions during the middle to late Burdigalian (Kuhlemann and Kempf, 2002b; Matter, 1980). Furthermore, the drainage direction switched from the east to the west (Garefalakis and Schlunegger, 2019; Kuhlemann and Kempf, 2002b).

In the Eastern Molasse, neritic Lutetian (middle Eocene) strata in the Helvetic nappes of the Eastern Alps were deposited in the Helvetic domain, grading southward into bathyal conditions (Adelholzener Schichten, Schwarzerzschichten, and Flöz-Nebengestein, Heyng, 2012). Subsequently, Priabonian (late Eocene) sediments record a deepening of the entire Helvetic domain to bathyal flysch conditions (Stockletten, Heyng, 2012). This was coeval with littoral deposition on top of the foreland unconformity in the autochthonous Eastern Molasse (Basal Sands and Lithothamnium Limestones, Sissingh, 1997; Wagner, 1998; Zweigel et al., 1998). Early Rupelian (34 to 31 Ma) deposition of bathyal marls and turbiditic sands evidence a subsequent rapid deepening to underfilled flysch conditions (Fish shales/Schöneck Fm.

and Heller Mergelkalk/Dynow Fm., Bachmann and Müller, 1991; Jin et al., 1995; Sissingh, 1997; Wagner, 1998; Zweigel et al., 1998). By the late Rupelian (31 to 28 Ma), conditions shallowed from bathyal to neritic following the maximum flooding surface recorded within the Heller Mergelkalk (Bändermergel/Eggerding Fm., Tonmergel/Zupfing Fm., Deutenhausen Fm., Bachmann and Müller, 1991; Hülscher et al., 2019; Jin et al., 1995; Sissingh, 1997; Wagner, 1998; Zweigel et al., 1998). This means the underfilled trinity is prevalent in both the Eastern Alpine nappe stack and the autochthonous Eastern Molasse. Continued shallowing led to the deposition of littoral sands (also considered as underfilled- to overfilled transition) in the Eastern German Molasse by the middle Chattian (26 Ma, Chattian Sands, Jin et al., 1995; Zweigel et al., 1998). However, bathyal conditions remained dominant in the Austrian Molasse throughout the Chattian and Aquitanian (Puchkirchen Fm. recording up to 1000-1500 m water depths, De Ruig and Hubbard, 2006; Hülscher et al., 2019; Rögl et al., 1979; Wagner, 1998). This juxtaposition of under- and overfilled conditions led to the development of the littoral to neritic eastward facing Bavarian Shelf (Jin et al., 1995; Zweigel et al., 1998). To the south, the Austrian Molasse was flanked by fluvio-deltaic wedge-top deposition (Augenstein Fm. on top of the future Northern Calcareous Alps and Inneralpine Molasse in the Lower Inn Valley, Frisch et al., 2001; Hülscher et al., 2019; Ortner and Stingl, 2001; Sharman et al., 2018). Apart from a short period of drowning during the late Chattian (24 Ma), the Bavarian shelf remained at a relatively stationary position during the late Oligocene to early Miocene (Jin et al., 1995; Lemcke, 1988; Zweigel et al., 1998). Like the Western Molasse, the early Burdigalian Transgression led to a re-establishment of neritic conditions in the Eastern German Molasse (Obing Fm., Jin et al., 1995; Lemcke, 1988; Zweigel et al., 1998) while bathyal deposition remained dominant in the Austrian Molasse (basal Hall Fm. overlying Base Hall Unconformity (BHU), De Ruig and Hubbard, 2006; Hülscher et al., 2019). However, by the middle to late Burdigalian (18 to 17 Ma), terrestrial and neritic deposition was dominant in the Eastern German- and Austrian Molasse, respectively (Upper Freshwater Molasse, Neuhofen Beds and Upper Hall Fm., De Ruig and Hubbard, 2006; Hülscher et al., 2019; Jin et al., 1995; Zweigel et al., 1998).

This evidences a rapid transition from underfilled- to overfilled conditions in the Eastern Molasse at 19-18 Ma (Hülscher et al., 2019).

2.3 Data and methods

We constructed a 3D geological model from present-day sea level to 8000 m depth to determine the influence of the European passive margin architecture on MB evolution (Subsection 2.3.1). In addition, 2D/3D reflection seismic data as interpreted using the Petrel software to reconstruct the tectonostratigraphic evolution of the MB. These results are then compared with the tectonic evolution of the adjacent Alps to find spatiotemporal relationships between orogenic processes and basin response (Subsection 2.3.2).

2.3.1 Depth grids and construction of 3D geological model

The 3D geological model of the MB was generated using the 2015 GeoMol subsurface models (GeoMol, 2015) of the Swiss, German, and Austrian Molasse (Figure 2.1a for locations). The subsurface models are based on seismic interpretations, borehole data, and models from previous studies (GeoMol, 2015). The stratigraphic surfaces used in each part of the model are given in Table 2.1. The structural modelling tool in Petrel was used to combine the datasets to generate surfaces spanning the entire MB (Figure A1.1).

Table 2.1: Available surfaces in the various parts of the 2015 Geomol models and seismic profiles from (Ortner et al., 2015). Undefined stands for a lack of definition of whether the top of the Cretaceous consists of Lower, Middle, or Upper Cretaceous sediments. A dash implies a dataset does not contain the respective base or top.

Units/Data source	Swiss Molasse Basin 2015 GeoMol	Western German Molasse Basin 2015 GeoMol	Eastern German Molasse Basin 2015 GeoMol	Austrian Molasse Basin 2015 GeoMol	(Ortner et al., 2015)
Crystalline basement		Top	Top	Top	Top
Permo-carboniferous	Base	-	-	-	-
Lower Triassic	Base	-	-	-	-
Middle Triassic	Top	-	-	-	-
Upper Triassic	Top	-	-	-	-
Lower Jurassic	Top	Top	-	-	-
Middle Jurassic	Top	Top	-	Base	-
Upper Jurassic	Top	Top	Base	Base	Top
Lower Cretaceous	-	-	-	-	-
Middle Cretaceous	-	-	-	-	-
Upper Cretaceous	Top (undefined)	Top (undefined)	Base (undefined)	Base	Top
Late Eocene	Base		Base	Base	
Lower Marine Molasse	Top	Base	Base	Base	Base
Lower Freshwa-ter Molasse	Top	Base	Base	Base	Base
Upper Marine Molasse	Top	Base	Base	Base	-
Upper Fresh-water Molasse	-	Base	Base	Base	-

This tool uses a volume-based implicit approach (for details on implicit stratigraphic modelling, we refer the reader to Caumon and Mallet, 2006;

Mallet, 2004) to create a stratigraphic function based on the type of horizon (conformable, erosional, base, or discontinuous) and input surfaces. In interpolated areas, thickness trends from data-covered regions are preserved. Surfaces were generated for the top crystalline basement, top Lower Jurassic, top Middle Jurassic, top Upper Jurassic, base Lower Marine Molasse (UMM), base Lower Freshwater Molasse (USM), base Upper Marine Molasse (OMM) and base Upper Freshwater Molasse (OSM) (*sensu* Matter, 1980).

Eocene deposits are incorporated in the UMM deposits because of their minor thickness relative to the size of the model. For generated thickness maps, areas with less than 50 m thickness are removed to highlight areas of significant deposition during the respective time windows. The geological model does not extend below the thrust front, as the confidence of the input data is lower there. Subsequently we generated thickness distribution maps for the Middle Jurassic, Upper Jurassic, and Cretaceous using the model results. The thickness distributions provide insights into the paleogeography of the European shelf during the Jurassic and Cretaceous and the basin floor architecture at the onset of flexural subsidence.

2.3.2 Seismic data

Seismic volumes A and B cover parts of the Western- and Eastern German Molasse, respectively (Figure 2.1a for locations). Seismic volume A is an APSDM cube (anisotropic pre-stack depth migrated) in the depth domain and covers an area of 145 km^2, imaging to depths of up to 2000 m. Seismic volume B is a PreSTM (pre-stack time migrated) cube in the time domain located on the Bavarian Shelf, covering an area of 560 km^2. The upper 2500 ms TWT of this volume was of sufficient quality to interpret. Both volumes are displayed in reverse polarity (SEG convention). This means that a downward increase in acoustic impedance is represented by a trough (Figure 2.2; blue reflectors with negative amplitudes) and a decrease in acoustic impedance is reflected by a peak (Figure 2.2; red reflectors with positive amplitudes). The seismic volumes are separated by a 100 km-wide gap covered by sparse 2D seismic data (Figure 2.1a). The structural smoothing attribute was applied to the input

seismic data for conventional horizon tracing to increase the signal/noise ratio. Important stratigraphic surfaces and unconformities are identified for each seismic volume using borehole data. Eight different reflectors are mapped in seismic volume A, which are from top to bottom: Top Baltringer Fm., top USM, top Cyrena Beds, top Baustein Beds, top Malm, base karstified Malm, top Dogger and top Lias (Figure 2.2). Eight seismic horizons were also mapped in seismic volume B, which are from top to bottom: top Hall Fm., Base Hall Unconformity (BHU, sensu De Ruig and Hubbard, 2006; Hülscher et al., 2019), top Chattian Sands, top Rupelian, top Eocene, base Eocene, top Turonian and base Mesozoic (Figure 2.2). Faults cross-cutting the seismic-stratigraphic units were interpreted based on lateral reflector terminations. To enhance the confidence of the fault interpretation, the variance seismic attribute was applied to the input seismics (Koson et al., 2013; Subrahmanyam and Rao, 2008).

Active frontal thrusting drove the migration of the flexural forebulge around which the syn-flexural normal faults were active, thereby governing the spatiotemporal location of the zone of extensional stresses (DeCelles, 2012; DeCelles and Giles, 1996; Langhi et al., 2011; Supak et al., 2006). As the forebulge migrated further cratonward, normal faults cut progressively younger stratigraphy. Therefore, normal faults further from the present-day thrust front cut younger stratigraphy compared to their counterparts closer to the thrust front (Figure 2.3a). The spatiotemporal syn-flexural normal fault activity derived from growth strata (Figure 2.3b) enabled inference of high and low intensities in frontal thrusting activity (Bry et al., 2004). This allowed reconstruction of spatiotemporal variations in hinterland tectonics from syn-flexural normal fault activity in the foreland basin. Furthermore, differences in cumulative Cenozoic offsets along the syn-flexural normal faults implicate a higher magnitude of flexural bending of the European plate. This may have resulted from variations in either 1) combined topographic- and slab loading (Flemings and Jordan, 1990; Sinclair, 1997a) and/or 2) strength variations of the European plate (Flemings and Jordan, 1989; Waschbusch and Royden, 1992).

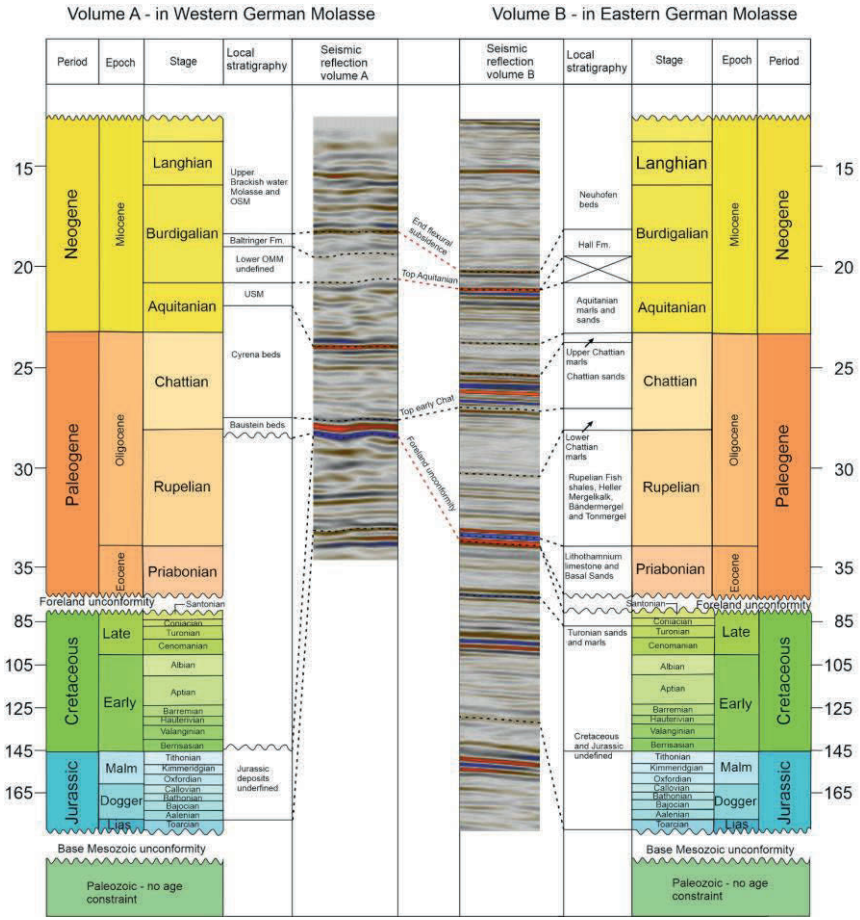

Figure 2.2: Stratigraphic column of the western and eastern German Molasse Basin (study area). Reflectors that indicate the same tectonic event or age are connected with red dashed lines. In seismic volume A, the ages of the surfaces are based on (Heckeberg et al., 2010; Heimann et al., 2009; Kuhlemann and Kempf, 2002b; Shipilin et al., 2020; von Doppler et al., 2005). Ages from the surfaces in seismic volume B are based on (Jin et al., 1995; Zweigel et al., 1998). The ages of the stratigraphy in the parts of Molasse Basin covered by these seismic volumes are derived from biostratigraphy, which yields 1 to 2 Myrs of uncertainty. The stratigraphic gap in the early Burdigalian is based on the time gap presented by the unconformity at the base of the Hall Formation in the Eastern German Molasse (BHU, Hülscher et al., 2019).

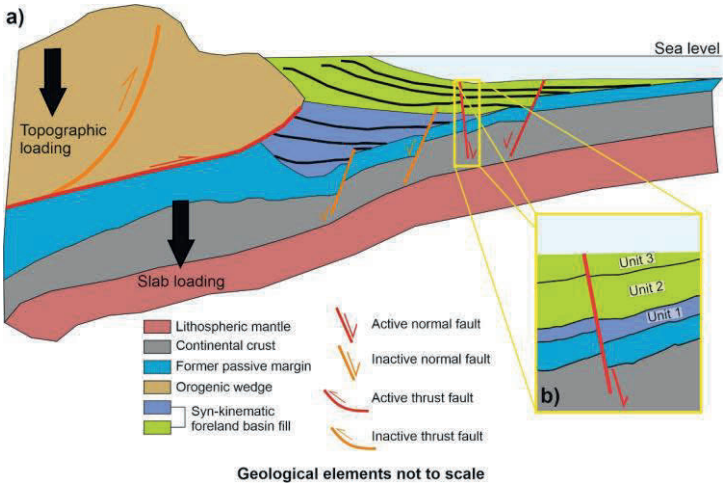

Figure 2.3: a) Schematic illustration of normal faults cutting the crystalline basement, pre-flexural passive margin sediments, and syn-flexural fill of a foreland basin. Generally, normal faults located further away from the present-day thrust front are expected to cut younger syn-flexural fill compared to normal faults closer to the thrust front. This is due to the cratonward migration of the flexural forebulge (i.e. extensional stress field) as the thrust front propagates further onto the foreland plate. **b)** Schematic zoom-in showing how stratigraphic thickness changes caused by syn-flexural normal faulting can be used to infer the spatiotemporal activity of normal faults. Syn-flexural units 1 and 3 record thickness changes across the fault, whereas unit 2 does not record changes across the fault. This alternation in activity and inactivity of the normal faults in foreland basins can be used to infer periods where and when extensional stresses due to flexural subsidence were (not) affecting the foreland plate at the location of the seismic data.

2.4 Results

First, we present the 3D geological model of the thickness distributions of the different Mesozoic basement units and an orogen-parallel profile through the MB (Subsection 2.4.1). This is followed by the seismic data in both volumes to constrain the tectonostratigraphic evolution in different parts of the German Molasse (Subsection 2.4.2). Finally, syn-flexural normal fault kinematics are quantified to assess along-strike variations in the timing and magnitude of flexural subsidence in the German Molasse (Subsection 2.4.3).

2.4.1 3D basin model of the entire Molasse Basin

The Mesozoic units start with the Middle Jurassic deposits, whose thickness decreases from ~450 m in the western Swiss Molasse to less than 100 m in the German Molasse (Figure 2.4a). The overlying Upper Jurassic reaches its highest thicknesses at the western (up to 1100 m, western Swiss Molasse) and eastern (~700 m south of Munich) basin margins, from which it thins to 250 m around Zürich (Figure 2.4b). The Cretaceous stratigraphy is thickest southeast of Munich (~900 m), whereas in the other parts of the basin it is either absent or the thickness is less than 100 m (Figure 2.4c).

In the orogen-parallel direction, the top of the crystalline basement dips 0.3° eastwards from the Swiss- to German Molasse (between 100 and 480 km in Figure 2.5, for the location of the orogen-parallel cross-section, see Figures 2.1a and 2.4). The crystalline basement in the Swiss- and German Molasse is locally cut by Permo-Carboniferous grabens, also imaged in our 3D seismic dataset (see Subsection 2.4.2, Figures 2.5, 2.7, and A1.2). In the Austrian Molasse, the top of the crystalline basement has a westward tilt (around 500 km; Figure 2.5). This likely represents the Central Swell (also observed by Ortner et al., 2023a; their Figure 5.2). Triassic to Middle Jurassic deposits in the eastern Swiss- and Western German Molasse thin from both the west- and east onto the crystalline basement located at a shallow depth around Zürich (between 100 and 300 km, Figure 2.5). Between Zürich and the Bavarian Shelf, Upper Jurassic, and Cretaceous successions thicken to the east from ~700 to ~1600 m (Figure 2.5).

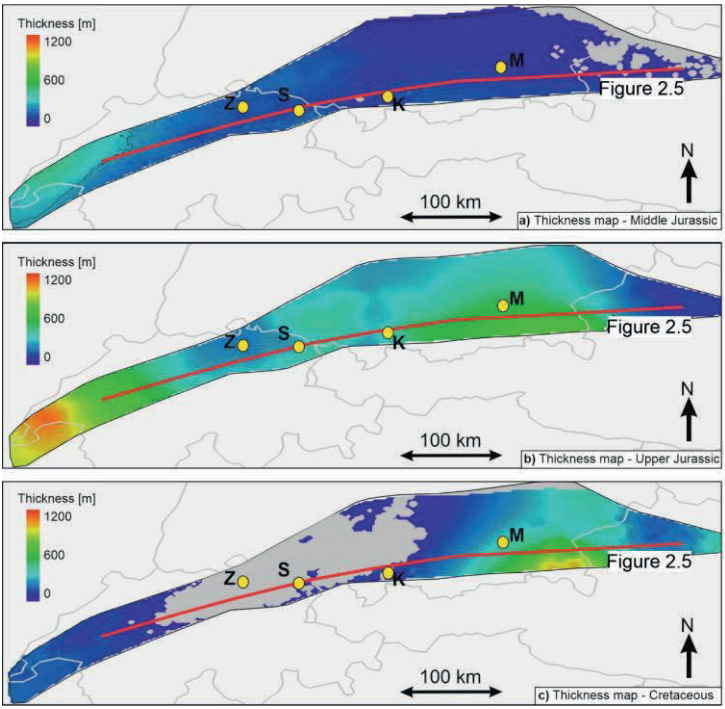

Figure 2.4: Thickness distribution of the **a)** Middle Jurassic, **b)** Upper Jurassic, and **c)** Cretaceous deposits in the Molasse Basin resultant from the 3D model. Grey areas indicate where the thickness of the respective deposit is below 50 m and are not shown because this is below model resolution. **K** = Kaufbeuren, **M** = Munich, **S** = St. Gallen, **Z** = Zürich.

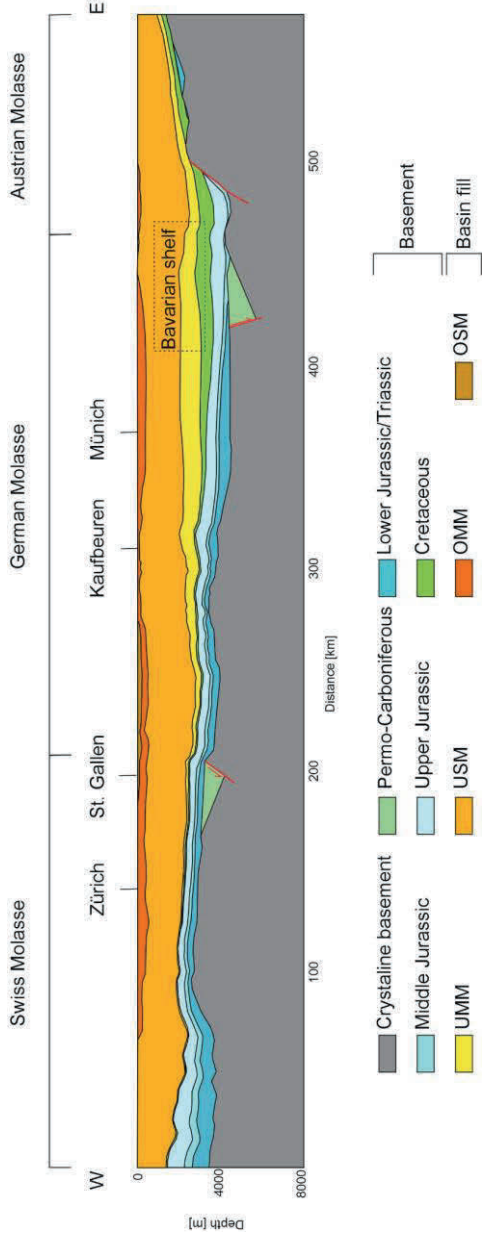

Figure 2.5: Along-strike profile through 3D geological model (for exact location see Fig. 2.1a). The position of the Permo-Carboniferous graben in Swiss Molasse is based on previous studies (Bachmann and Müller, 1991; Heuberger et al., 2016). Black dashed boxes give the locations of the Bavarian Shelf Eastern German Molasse. Apart from faults bounding Paleozoic graben structures in the Swiss Molasse and west of the Central Swell (Ortner et al., 2023a), normal faults are not drawn in this section as they were not explicitly modelled as they have relatively small offsets for our model.

2.4.2 Seismic stratigraphy of seismic volumes A and B

2.4.2.1 Mesozoic basement units

In seismic volume A, the base of the seismically interpretable Mesozoic sequence is defined by the top Lower Jurassic (Lias) reflector (Figure 2.6). The overlying Middle Jurassic unit is characterised by SF-A1 (Table 2.2, Figure 2.6). The Upper Jurassic unit concordantly overlies the Middle Jurassic and is characterised by an internal stratigraphically upward transition from SF-A1 to SF-A2 (Table 2.2, Figure 2.6). This reflects a shift from non-karstified to karstified limestones (also observed in borehole data, Lemcke, 1988; Meyer and Schmidt-Kaler, 1990). The distribution of amplitudes of the variance attribute of the Upper Jurassic unit (Figure A1.3) indicates a high degree of karstification in the WNW, whereas in the ESE there is little- to no karstification. The top of the Jurassic is defined by a strong negative amplitude reflector against which both Upper Jurassic and late Chattian reflectors terminate (Figure 2.6; white and green arrows). This characterises the foreland unconformity in seismic volume A.

The Mesozoic sequence in seismic volume B consists of Jurassic and Cretaceous deposits, locally underlain by the Paleozoic-Triassic Giftthal Through (Figures 2.7 and A1.2, Bachmann and Müller, 1991). The Mesozoic sequence below the top Turonian (Upper Cretaceous) reflector does not show thickness changes across the normal faults that cut the syn-flexural Cenozoic stratigraphy (Figure 2.7). The post-Turnonian Late Cretaceous unit is characterised by SF-B1, which concordantly overlies the undefined portion of the Mesozoic sequence (Figure 2.7). This unit records an eastward-directed thickening from 10 to over 250 m, unrelated to the syn-flexural normal faults (Figure A1.4). Post-Turonian reflectors terminate against the Base Eocene (Figure 2.7; white arrows), marking the foreland unconformity in seismic volume B.

2.4.2.2 Late Eocene - Priabonian

Late Eocene deposits are absent in seismic volume A. In contrast, they are represented in seismic volume B by SF-B2 (Figure 2.7, Table 2.3), and interpreted as Priabonian (Late Eocene) Basal Sands and Lithothamnium Limestones (well data; Sissingh, 1997; Wagner, 1998; Zweigel et al., 1998). These deposits overlie the foreland unconformity and dip to the south (Figure 2.7). At the top, they are conformably overlain by SF-B3 (Figure 2.7, Table 2.3).

2.4.2.3 Early Oligocene – Rupelian

Rupelian deposits are absent in seismic volume A. In seismic volume B, the top of the Eocene is marked by a prominent negative amplitude reflector (Figure 2.7). Based on well data and previous studies (Jin et al., 1995; Zweigel et al., 1998), the overlying SF-B3 is interpreted as Rupelian bathyal to neritic marls and sands. This unit shows a west-to-east thinning from 350 m to 100 m (Figure A1.5). Strikingly, this is the opposite of what was observed for the thickness distribution of the post-Turnonian unit (Subsection 2.4.2.1). Southward thickening towards syn-flexural normal faults (Figure A1.5) reveals the syn-kinematic nature of these sediments. While the lower part of the Rupelian succession is defined by a homogeneous distribution of SF-B3 in the entire volume, it grades stratigraphically upward to SF-B4 to the NW (Figure 2.7, Table 2.3). This means that while the NW bathyal conditions graded into neritic and littoral deposition, bathyal conditions remained dominant in the SE throughout the Rupelian. The top of the Rupelian seismic stratigraphy is characterised by a low negative amplitude reflector, cutting down into both SF-B3 and SF-B4 of the Rupelian unit (yellow arrows in Figure 2.7, Figure A1.6). Early Chattian reflectors onlap onto the top Rupelian towards the NW (Figure 2.7; yellow arrows).

Table 2.2: Seismic facies (SF) examples, descriptions, and interpretations of seismic volume A

Seismic facies	Example	Description	Interpretation
SF-A1	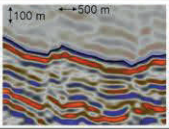	High frequency, high to medium amplitude parallel reflections with good lateral continuity.	Alternation of marine limestones and marls
SF-A2	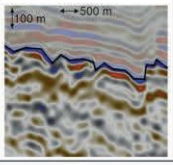	Low frequency, high to low amplitude reflections with poor lateral continuity. Overall chaotic seismic facies.	Heavily karstified platform limestones
SF-A3	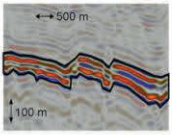	High frequency, high to medium amplitude reflections with good lateral continuity.	Littoral sands containing cross beds.
SF-A4	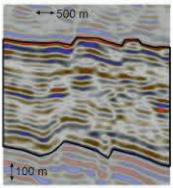	High frequency, low to medium amplitude reflections. Semi-continuous reflectors showing an overall semi-chaotic seismic facies.	Heterolithic brackish deposits, transition between littoral and terrestrial depositional environments.
SF-A5	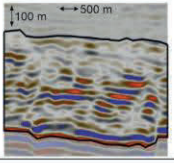	High frequency, low to high amplitude reflections with very poor lateral continuity, having an overall chaotic facies.	Littoral to terrestrial deposits; meandering channels and overbank deposits, lakes.
SF-A6	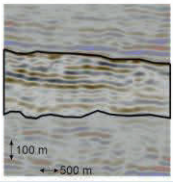	Low frequency, low to medium amplitude reflections with medium to good lateral continuity. Upward amplitude and lateral continuity of reflectors increase.	Neritic deposits consisting out of a mix of sands and shales.

Table 2.3: Seismic facies (SF) examples, descriptions, and interpretations of seismic volume B

Seismic facies	Example	Description	Interpretation
SF-B1	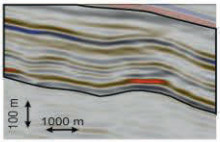	Medium frequency, high to medium amplitude reflections with good lateral continuity. Lower reflectors are parallel with upper set showing contrasting dips.	Mix of marine shales and sands. Lack of sedimentary structures suggests neritic to bathyal environment.
SF-B2	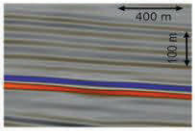	Low frequency, high amplitude pair of parallel reflectors with good continuity.	Littoral sands and limestones.
SF-B3	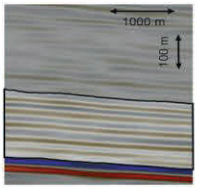	Low frequency, medium to high amplitude reflections with good lateral continuity. Reflectors are parallel.	Homogeneous bathyal flysch deposits mostly consisting out of shales.
SF-B4	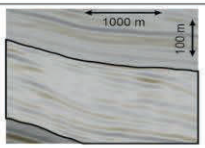	High frequency, low to medium amplitude reflections with sigmoidal shapes. Reflectors show internal onlap, downlap and toplap.	Clinoforms prograding basinward. Bathyal to neritic transition at the base, neritic to littoral transition closer to the top.
SF-B5	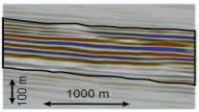	High frequency, high to medium amplitude reflections which have varying lateral continuity. Reflector show internal onlap, downlap and toplap.	Littoral deposits consisting out of a mix of sands and shales. Channel geometries towards the top indicate shallowing towards terrestrial conditions.
SF-B6		Low frequency, low amplitude reflections with good lateral continuity. Reflectors are subparallel.	Neritic deposits consisting mostly out of shales.
SF-B7		High frequency, high amplitude reflections with good lateral continuity. Reflectors are subparallel.	Neritic deposits consisting out of a mix of shales and sands. Lack of sedimentary structures indicates quiet water conditions.

2.4.2.4 Late Oligocene – Chattian

The oldest Cenozoic deposits preserved in seismic volume A are the early Chattian Baustein Beds (based on well data). This unit is characterised by SF-A3 (Table 2.2) with reflectors at the base onlapping to the NNW onto the foreland unconformity (green arrows in Figure 2.7). The observed patches of increased thicknesses of the early Chattian deposits (Figure A1.7) suggest infilling of Upper Jurassic karst pockets. The sweetness attribute map of the early Chattian unit (Figure A1.8) shows N-S striking bands of high values in the west, with the SE characterised by low values. This implies the development of an N-S striking coastline with sand-rich deposits in the west, grading into more shale-rich deposits in the east. Well data shows that the early Chattian stratigraphy contains cross-beds and is cemented at the top by freshwater, fossil-rich carbonates, and coaly silts and marls. This suggests that the early Chattian deposition in seismic volume A are characterised by littoral deposition grading upward into freshwater conditions.

The concordantly overlying seismic-stratigraphic unit represents the middle to late Chattian Cyrena Beds (based on well data). This unit is characterised by a shift to SF-A4 (Figure 2.7, Table 2.2). Thickness changes up to 100 m towards the syn-flexural normal faults (Figure A1.9) reveal the syn-kinematic nature of this unit. A variance slice through this unit (Figure A1.10) reveals the presence of meandering channels, suggesting freshwater conditions at the end of the early Chattian continued to develop into delta plain and fluvial conditions.

The early Chattian reflectors overlying the Rupelian unit in seismic volume B characterise the Lower Chattian Marls (well data, Jin et al., 1995; Zweigel et al., 1998). The seismic facies of this unit (SF-B4, Table 2.3) are similar to that of the underlying Rupelian in the WNW of the data volume, with clinoforms migrating to the ESE across the Bavarian Shelf (Figure 2.7). Clinoforms are absent in the ESE of the volume for this unit, and SF-B3 remains dominant in the lower Chattian (Figure 2.7). Stratigraphically upward this is followed by middle Chattian littoral Chattian Sands (well data; Jin et al., 1995; Zweigel et al.,

1998) characterised by SF-B5 (Table 2.3) in the WNW of seismic volume B (Figure 2.7). In contrast, the middle Chattian reflectors in the ESE of seismic volume B are characterised by SF-B3 (Figure 2.7, Table 2.3). The sweetness attribute map of the middle Chattian unit (Figure A1.11) reveals NE-SW striking bands of high values in the west of the seismic volume and low values in the east. These observations suggest a NE-SW striking coastline grading eastward from littoral neritic or bathyal conditions.

Middle Chattian reflectors terminate against the top Chattian Sands reflector in the WNW (Figure 2.7, green arrows). To the ESE incision into the middle Chattian stratigraphy is observed (Figure 2.7; green arrows). The overlying late Chattian unit is characterised by SF-B6 (Figure 2.7, Table 2.3) and represents the neritic Upper Chattian Marls (well data; Jin et al., 1995; Zweigel et al., 1998). Reflectors of this late Chattian unit onlap towards the NNW onto the top Chattian Sands reflector (Figure 2.7; green arrows).

2.4.2.5 Early Miocene – Aquitanian

Early Aquitanian seismic stratigraphy in volume A has the same seismic facies as the underlying Cyrena Beds (Figure 2.6, Subsection 2.4.2.4). This likely represents an upward continuation of the same depositional environment. The early to late Aquitanian seismic facies grades upward from SF-A4 to SF-A5 (Figure 2.6, Table 2.2). A variance attribute map of the late Aquitanian reflectors (Figure A1.12) reveals the continued development of meandering channels.

In seismic volume B, the Aquitanian unit concordantly overlies the Chattian seismic-stratigraphy (Figure 2.7) and represents the bathyal- to neritic Aquitanian Series (well data; Jin et al., 1995; Zweigel et al., 1998). In the WNW of the seismic volume, a transition from SF-B4 to SF-B5 is observed at the Chattian-Aquitanian interface (Figure 2.7, Table 2.3). In contrast, in the ESE of the seismic volume, this same change in seismic facies is observed within the Aquitanian unit (Figure 2.7). The top of the Aquitanian unit is defined by the BHU against which Aquitanian reflectors toplap (Figure 2.7). An incision of

Aquitanian deposits is observed in the SE of seismic volume B (Figure A1.13, yellow arrows).

2.4.2.6 Early Miocene – early Burdigalian

The early Burdigalian reflectors in seismic volume A represent an undefined part of the neritic OMM and the Baltringer Fm. (based on well data). Reflectors of this unit onlap towards the NW onto the Aquitanian reflectors (Figure 2.6; black arrows). The unit is characterised by SF-A6 (Table 2.2), and the reflectors generally have a shallower southward dip compared to Aquitanian and older reflectors (Figure 2.6).

The Aquitanian-Burdigalian transition in seismic volume B is defined by the BHU throughout the entire seismic volume, marking a change from SF-B5 to SF-B4 (Figure 2.7). Early Burdigalian reflectors onlap onto the BHU towards the NW and have a shallower SE-directed dip compared to underlying reflectors (Figure 2.7, black arrows and Figure A1.13, orange arrows).

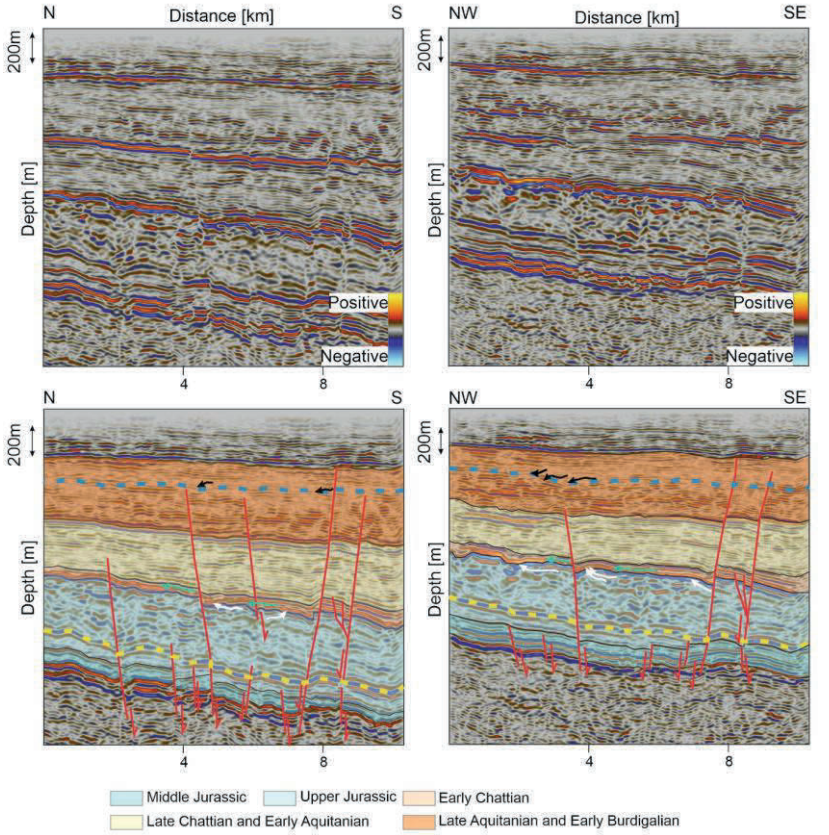

Figure 2.6: The upper panels show uninterpreted examples of N-S and NW-SE seismic lines through seismic volume A. The bottom panels show the same lines with the seismic-stratigraphic bodies interpreted throughout the entire seismic volume. Red lines indicate normal faults and their respective kinematics, the yellow dashed reflectors mark the base of the karstified Upper Jurassic sequence, and the blue dashed line is the top Aquitanian reflector. White arrows mark terminating Upper Jurassic reflectors against the top Upper Jurassic, green arrows terminating early Chattian reflectors against the top Upper Jurassic, and black arrows terminating early Burdigalian reflectors against the top Aquitanian.

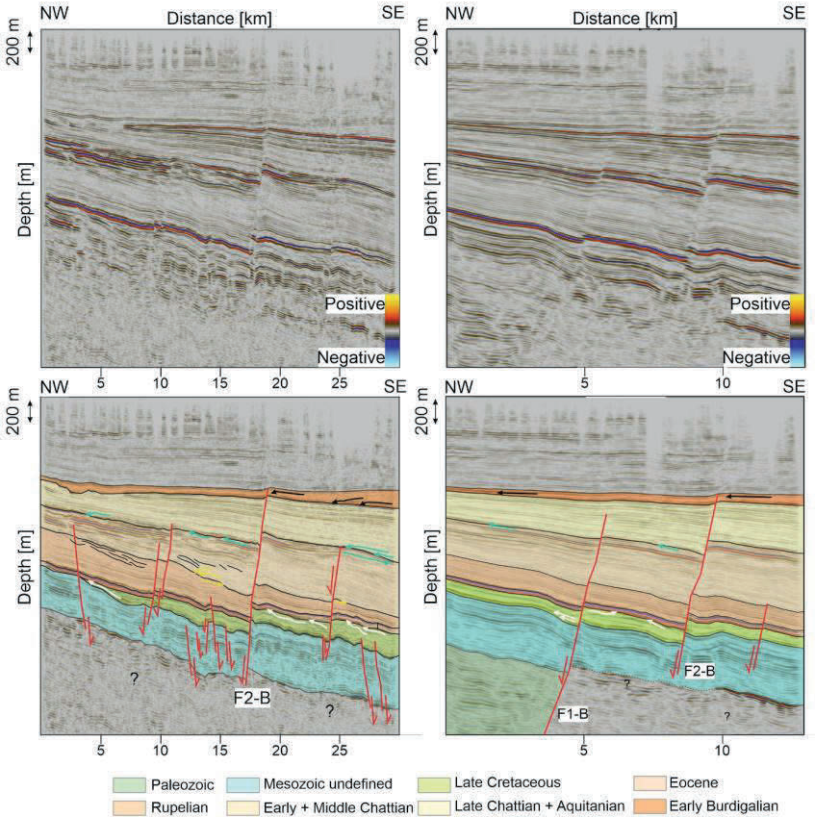

Figure 2.7: The upper panels show uninterpreted examples of N-S and NW-SE seismic lines through seismic volume B. The bottom panels show the same lines with the seismic-stratigraphic bodies interpreted throughout the entire seismic volume. Red lines indicate normal faults and their respective kinematics. White arrows mark terminating late Cretaceous reflectors against the Base Eocene, yellow arrows late Rupelian and early Chattian reflector terminations against the top Rupelian, green arrows terminating Middle and early Chattian reflectors against the top Chattian Sands, and black arrows terminating early Burdigalian reflectors against the Base Hall Unconformity.

2.4.3 Magnitude and timing of syn-sedimentary flexural normal fault activity

Quantifying throw distributions of different reflectors along syn-flexural normal faults constrains the timing and magnitude of flexural subsidence of the European plate (Figure 2.3). In both seismic volumes, syn-flexural normal faults strike E-W (Figure 2.8). The exception is F1-B striking NW-SE (Figure 2.8). F1-B is a reactivated pre-flexural fault associated with the Permo-Triassic Gifthal Trough (Subsection 2.4.2.1) leading to its deviating strike. In volume A, syn-flexural faults dipping both to the north and south resulted in the formation of a graben-like structure (Figures 2.6 and 2.8a). In seismic volume B, most faults dip northward (Figure 2.8b). The syn-flexural normal faults cut the Mesozoic basement units. Structural maps of early Chattian and early Burdigalian reflectors reveal a reduction in the number of active faults for younger stratigraphy in both seismic volumes (Figure 2.8). This implies that as flexure continued, the deformation became localised.

The backstripped T-x profile of F1-A shows that fault activity was initiated during the early Chattian in seismic volume A (Figure 2.9a). In contrast, in seismic volume B, normal fault activity was initiated in the late Eocene to Rupelian (F2-B, Figure 2.9b). During the early to middle Chattian fault activity decreased in seismic volume B (Figure 2.9b). However, north of seismic volume B, early to middle Chattian stratigraphy records thickness changes across syn-flexural normal faults (Figure A1.14). This suggests a northward migration of the extensional stress field in the Eastern German Molasse. The syn-flexural faults remained active in both study areas until the early Burdigalian (Figure 2.9). Comparing the backstripped T-x profiles of faults in seismic volumes A and B shows that fault F1-A records a lower maximum cumulative Cenozoic offset (150 m; Figure 2.9a) compared to F2-B (220 m; Figure 2.9b). Furthermore, whereas the longest fault in seismic volume is 8400 m long (Figure 2.8a; F2-A), the longest fault in seismic volume B is 25000 m long (Figure 2.8b; F2-B). This implies that the magnitude of syn-flexural normal faulting in volume B exceeded that of volume A.

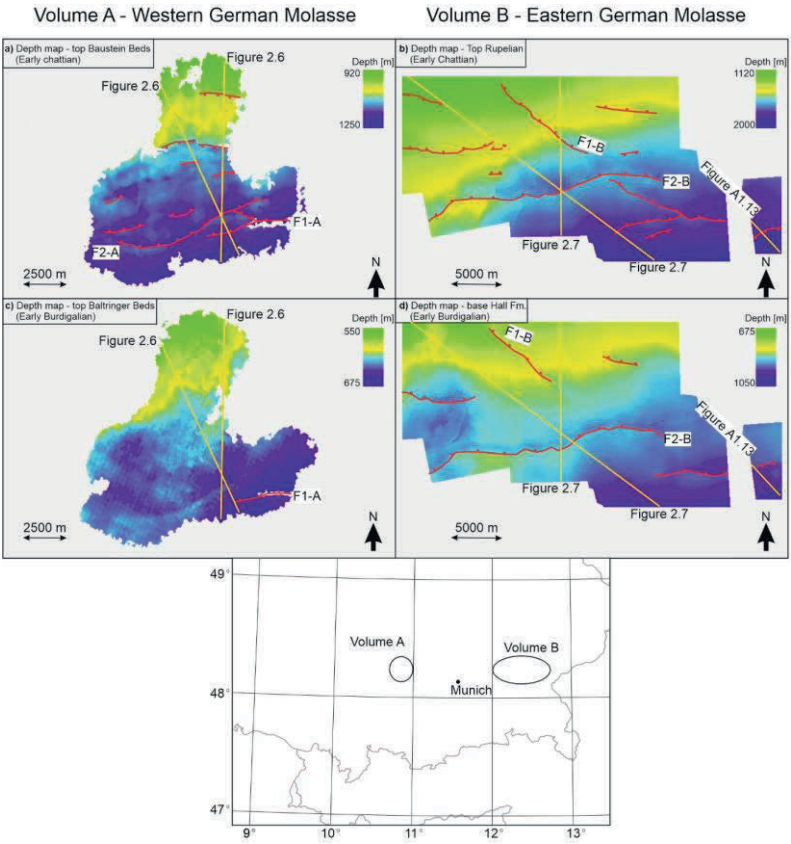

Figure 2.8: Depth-structure maps showing the present-day distribution of the normal faults and their dip direction (red lines with blocks indicating the dip direction) in seismic volumes A and B. Surfaces of reflectors of approximately the same age are placed next to each other. The figure below gives the approximate locations of seismic volumes A and B. **a)** top Baustein Beds (i.e., Early Chattian) **b)** top Rupelian Marls and Sands (i.e., early Chattian) **c)** top Baltringer Fm. (i.e., early Burdigalian) **d)** Base Hall Formation (i.e., early Burdigalian). Yellow lines indicate the locations of cross sections shown in Figures 2.6, 2.7, and A1.14.

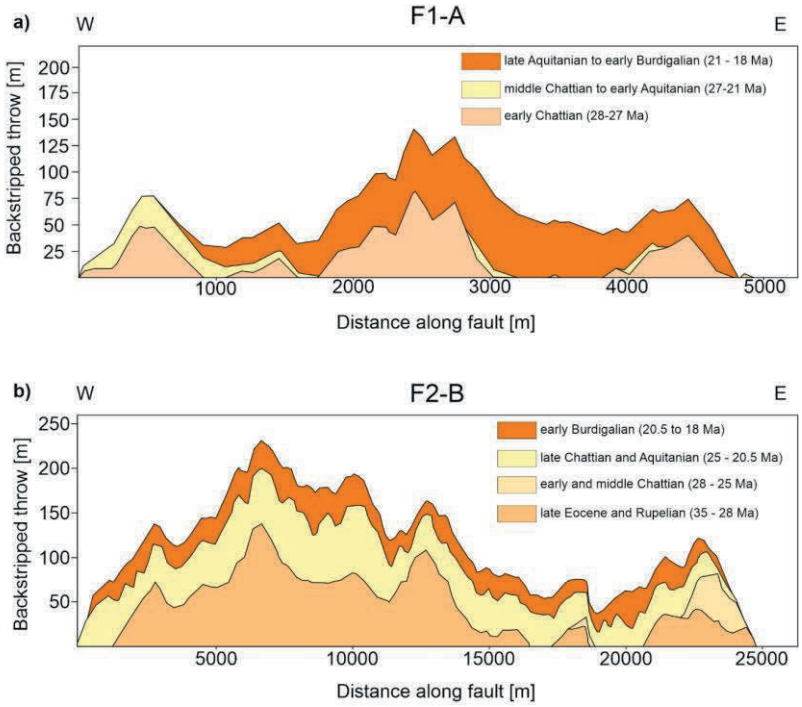

Figure 2.9: Throw-length profiles of faults F1-A and F2-B. Smaller values along the y-axis for F2-B are used because the graph would be too small otherwise. **a)** Backstripped throw-length profile for F1-A (location see Figure 9) showing the kinematic evolution of the fault. **b)** Backstripped Throw-length profile for F2-B (location see Figure 9) showing the kinematic evolution of the fault.

2.5 Discussion

Results from the 3D geological model (Figures 2.4 and 2.5) constrain the pre-flexural architecture of the European margin from the Middle Jurassic until the late Eocene onset of flexure. Furthermore, interpreted 3D seismic data (Figures 2.6 to 2.9) highlight late Eocene to early Miocene spatiotemporal variations in depositional environments and syn-flexural normal faulting in the German Molasse. From this, and previous studies, we constrain the late

Eocene basin architecture and the Oligocene to early Miocene eastward diachronous underfilled- to overfilled transition of the MB. Here, we discuss the implications of our seismic interpretations and 3D geological model for the German Molasse (Subsection 2.5.1). Following this, we discuss the development of the entire MB (Subsection 2.5.2) and possible mechanisms that drove the diachronous underfill to overfill transition in the MB (Subsection 2.5.3).

2.5.1 Tectonostratigraphic evolution of the German Molasse: along-strike variations in syn-flexural normal faulting and depositional environments

Analysis of the 3D geological model combined with seismic data volumes A and B revealed lateral heterogeneities in the basement composition underlying the German Molasse (Figures 2.5, 2.6, and 2.7). The subcrop of the foreland unconformity in the Western German Molasse is characterised by Late Jurassic karstified limestones (Figures 2.5 and 2.6). In contrast, it is characterised by Late Cretaceous deposits in the Eastern German Molasse (Figures 2.5 and 2.7). These results agree with previous studies (Bachmann and Müller, 1991; Lemcke, 1988; Mraz et al., 2018; Shipilin et al., 2020; von Hartmann et al., 2016). Furthermore, the deep-reaching (up to 400 m) karstification of Jurassic deposits in the Western German Molasse (Figure 2.6), also observed in the Swiss Molasse (Herb, 1988), implies long-lasting subaerial exposure of the basement pre-dating flexural subsidence. In contrast, karstification of the Upper Jurassic occurs only in the top 5 m in the Eastern Molasse (Köwing et al., 1968), suggesting significantly shorter subaerial exposure. Furthermore, we observed an eastward thickening of Late Cretaceous deposits in seismic volume B (Figures 2.7 and A1.4). These lateral heterogeneities in the Mesozoic basement architecture could imply either;

1. The European margin of the future Western German Molasse experienced more intense Late Cretaceous to Eocene Alpine uplift and erosion compared to the European margin at the present-day Eastern German Molasse, or,

2. The architecture of the European margin was comprised of a paleo-high and paleo-depocenter, respectively, where the latter was buried below Cretaceous deposits after exposure to subaerial conditions.

As the Triassic to Middle Jurassic deposits are unaffected by the foreland unconformity (Figure 2.5), their distribution can be used to constrain these two interpretations. Thickening of the Triassic to Middle Jurassic sediments away from a crystalline high in the Western German and eastern Swiss Molasse (Figure 2.5, between 100 to 300 km) implies that this structural high existed during the earlier Mesozoic epochs. Furthermore, the Cretaceous depocenter and the paleohigh to the west can be interpreted as the Wasserburger Trog and Rhenish Shield (Figure 2.10a, Lemcke, 1988). The pre-Mesozoic graben identified in our seismic dataset likely represents the Permo-Triassic Giftthal trough (Figure 2.7, Bachmann and Müller, 1991). It is orientated NW-SE to the Alpine front and limited by the Landshut-Neuoetting High to the north. This zone of weakness partly underlies the Wasserburger Trog in the Eastern German Molasse (Figure 2.10a). Therefore, we favour the 2nd hypothesis.

Pre-existing structural fabrics (e.g., horst and grabens) have been shown to lead to variations in crustal rigidity (Angrand et al., 2018). This eastward change from horst to graben-dominated domains in the pre-flexural architecture of the European margin likely caused the eastward decrease in plate strength (Andeweg and Cloetingh, 1998a). Furthermore, the pre-flexural architecture of the European plate seems to have affected the Late Eocene sediment distribution in the German Molasse. This is observed as an eastward thickening of the basal neritic limestones corresponding to the pre-flexural horst and graben locations (Figure 2.10a).

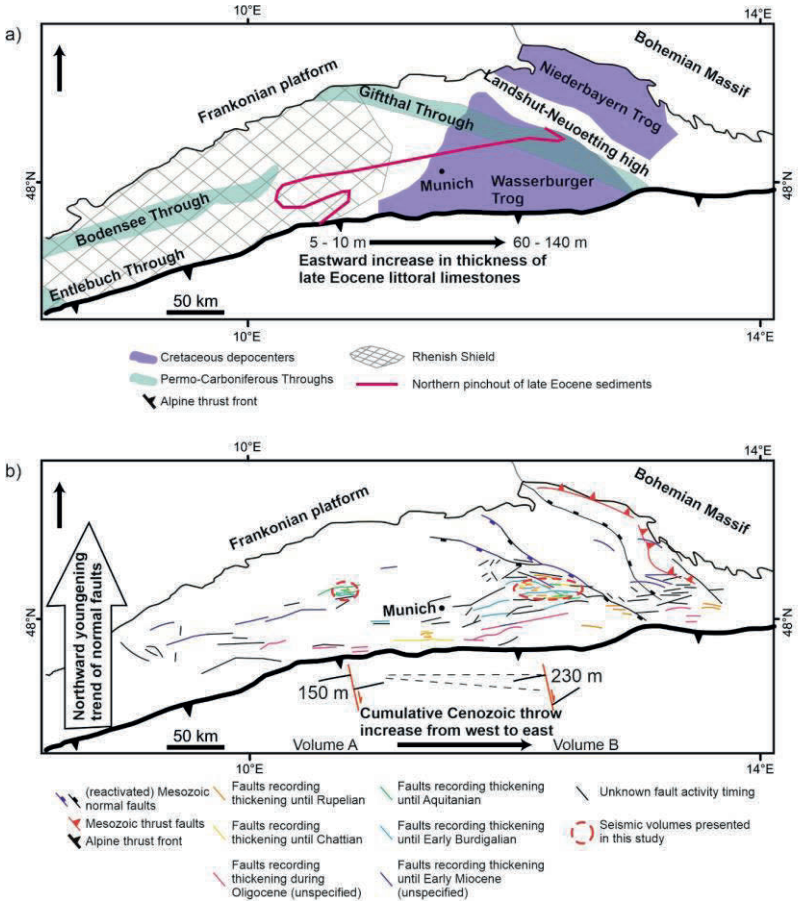

Figure 2.10: a) Location of Permo-Triassic and Cretaceous depocenters underlying the foreland unconformity, the Rhenish Massif, and the northern pinchout of late Eocene sediments characterising the lowest unit of the underfilled trinity in the German Molasse. The thickness of the late Eocene littoral limestones increases from the Western German- to the Eastern German Molasse. Based on data from Bachmann and Müller (1991), Lemcke (1984), Müller (2011), and data presented in this study. **b)** Faults in the Molasse Basin, where for the syn-flexural normal faults the timing of their activity is given. Data outside the seismic volumes presented in this study is taken from (Bachmann and Müller, 1991; Hülscher et al., 2019; Mraz et al., 2018; Shipilin et al., 2020). Faults closer to the present-day orogenic front are active until the Rupelian and Chattian, whereas faults further north are sealed by active until the Aquitanian to early Burdigalian. The cumulative Cenozoic throw value increases from west to east.

The subsequent deposition of the Rupelian Fish shales, Mergelkalk, and Bändermergel along the entire strike of the German Molasse (Figure 2.7, this study, Mraz et al., 2018; Müller, 2011; Shipilin et al., 2020) records the transition towards bathyal turbiditic conditions. This means that the influence of the inherited passive margin architecture on the architecture of the MB had been smoothened out. The intra-Rupelian transition from bathyal to neritic deposition in the German Molasse records a decrease in relative sea level. Truncations of Rupelian reflectors against the top Rupelian (Figure 2.7) suggest an association with an erosive event. This erosion coincides with both tectonic oversteepening of the distal margin observed in the Austrian Molasse (De Ruig and Hubbard, 2006; Hülscher et al., 2019; Masalimova et al., 2015) and a 100-150 m eustatic sea level fall at the end of the Rupelian (Haq et al., 1987). Continued progradational deposition during the early Chattian (ESE-orientated clinoforms, Figures 2.7 and A1.6) argues against deepening due to slope oversteepening. From this, we interpret the observed incision as submarine erosion due to eustatic sea level fall at the end of the Rupelian, as suggested by Diem (1986).

During the early to middle Chattian (28 to 26 Ma), the syn-flexural normal faults in seismic volume B were mostly inactive (Figure 2.9). The continued northward migration of the Alps at this time (Hinsch, 2013; Ortner et al., 2015) may have resulted in a northward migration of the forebulge and the extensional stress field around it (e.g., Langhi et al., 2011; Supak et al., 2006). This interpretation is consistent with early to middle Chattian fault activity north of seismic volume B (Figure A1.14) while faults closer to the thrust front were sealed (Figure 2.10b). This means the area of seismic volume B was incorporated into the axial part of the foredeep, which likely resulted in higher subsidence rates (e.g. Sinclair and Naylor, 2012; Zweigel et al., 1998). However, shallowing from neritic- to littoral conditions at this time (Chattian Sands, Figure 2.7 this study, Jin et al., 1995; Zweigel et al., 1998) suggests a decrease in relative sea level. This likely occurred in response to eustatic sea

level fall at the end of the Rupelian (Haq et al., 1987) combined with an increase in axially transported sediment supply derived from the Western/Central Alps (Kuhlemann, 2000) outpacing the increased flexural subsidence.

Middle Chattian juxtaposition of littoral conditions in the Eastern German Molasse (This study, Jin et al., 1995; Zweigel et al., 1998) and bathyal conditions in the Austrian Molasse (Lower Puchkirchen Fm., De Ruig and Hubbard, 2006; Hülscher et al., 2019; Wagner, 1998) led to development of the eastward facing Bavarian Shelf. Late Chattian (~ 25 Ma) NNW-directed onlap of neritic deposits onto the littoral Chattian Sands (Figure 2.7) evidences a subsequent transgression of the Bavarian Shelf. Jin et al. (1995) and Zweigel et al. (1998) also observed this to the west and south of our study area. These authors attributed this flooding to a 100 m eustatic sea level rise (Haq et al., 1987). However, toplaps against the top Chattian Sands reflector (Figure 2.7) spatiotemporally correlate with renewed late Chattian thrust activity observed in our study area as syn-flexural normal fault activity (Figure 2.9b). Therefore, this relative sea-level rise also had a tectonic component. However, lagoonal and delta plain conditions continued to develop in the Western German Molasse (seen in seismic volume A, Figures A1.10 and A1.12). Therefore, the westward extent of this flooding cannot exceed 100 km (distance between seismic volumes A and B). During the Aquitanian, littoral conditions migrated back to the middle Chattian position (Figure 2.7). This was also observed in the study areas of Jin et al. (1995) and Zweigel et al. (1995). Taken together, this means the Bavarian Shelf remained at a relatively stable position during the late Oligocene to early Miocene (26 to 20 Ma), in accordance with Kuhlemann and Kempf (2002).

Marine conditions were re-established in the German Molasse during an early Burdigalian (~ 20-18 Ma) WNW-directed transgression (Figures 2.6 and 2.7). This finding is consistent with results from previous authors in different parts of the MB (Garefalakis and Schlunegger, 2019; Hülscher et al., 2019; Strunck and Matter, 2002). The combination of a eustatic sea level rise (Haq et al., 1987) and a decrease in sediment supply from the hinterland (Kuhlemann, 2000) facilitated this drowning, as suggested by previous studies (Bieg et al.,

2008; Garefalakis and Schlunegger, 2019; Kuhlemann and Kempf, 2002b). However, early Burdigalian incision of Aquitanian sediments on the Bavarian Shelf (up to 200 m, Figure A1.13), also observed in the Swiss Molasse (Schlunegger et al., 1997a; Schlunegger et al., 1997c), were likely not caused by the aforementioned decrease in sediment supply or increase in eustatic sea level. Instead, this suggests erosion due to the steepening of the distal margin of the Eastern German Molasse. Previous authors interpreted this as the result of hinterland-directed migration of the forebulge due to visco-elastic relaxation of the European plate (Borzi et al., 2022; Hülscher et al., 2019; Zweigel et al., 1998). However, early Burdigalian syn-flexural normal fault activity in the Eastern German Molasse (Figure 2.9b) suggests ongoing flexure of the European plate. This agrees with the early Burdigalian subsidence in the Western German Molasse observed by Ortner et al. (2023). Therefore, results from this study do not support the occurrence of visco-elastic relaxation of the European plate during the early Burdigalian. An alternative explanation is given in Subsection 2.5.3.

The syn-flexural normal faults in the German Molasse were sealed by the middle Burdigalian (Figure 2.9), meaning flexure ceased at that time. Higher cumulative Cenozoic offsets in the Eastern German Molasse compared to the Western German Molasse (Figure 2.9) suggest an eastward increase in the curvature of bending of the European plate.

2.5.2 Spatiotemporal variations in the onset of flexural subsidence and underfilled- to overfilled transition in the Molasse Basin

The obliquity between the northern pinch-out of late Eocene limestones (lower unit of underfilled trinity sensu Sinclair et al., 1991) and the present-day Alpine front was interpreted as resulting from along-strike variations in subsidence, controlled by the architecture of the European margin (Subsection 2.5.1). Considering the entire MB, the lowest unit of the underfilled trin-

ity in the Western Molasse is only preserved in the fold and thrust belt (Helvetic nappes and the parautochtonous cover of the Aar Massif) and sparsely in the autochthonous foreland (Subsection 2.2.2.2 for details). This implies the autochthonous Western Molasse did not subside below sea level by the late Eocene (Figure 2.11a). In contrast, in the Eastern Molasse, this unit is up to 140 m thick in the autochthonous Eastern Molasse (Figure 2.7, Lemcke, 1984; Sissingh, 1997; Wagner, 1998; Zweigel et al., 1998) and is observed in the Helvetic nappes of the Eastern Alps (Heyng, 2012; Hinsch, 2013). This suggests, unlike the autochthonous Western Molasse, the autochthonous Eastern Molasse was already drowned by the late Eocene, in agreement with previous studies (Sissingh, 1997; Ziegler and Dèzes, 2007). These along-strike variations in the flexural subsidence of the European plate correspond to the locations of the pre-flexural horst and graben structures (Rhenish Shield and Giftthal trough/Wasserburger Trog, respectively, Subsection 2.5.1). We suggest the pre-flexural architecture of the European margin had an important influence on the late Eocene architecture of the Molasse Basin. A similar along-strike change in the early architecture of the foreland basin due to margin architecture is also observed in the Western Taiwan Foreland Basin (Chang et al., 2012), Pyrenean foreland basin (Ford et al., 2016), and Andean retroforelands (Horton, 2018). In addition, recent work indicates that variations in passive margin architecture can also affect the underfill-to-overfill transition (Gérard et al., 2023). Certainly, post-Early Miocene along-strike variations in frontal thrusting may have added to the observed obliquity between the late Eocene deposits and the present-day Alpine thrust front, as suggested by Ortner et al. (2015).

The Rupelian stratigraphy records bathyal to neritic deposition along the entire Alpine thrust front (Figures 2.11b and 2.11c). However, depositional environments shallowed towards neritic and littoral conditions in the Western Molasse up to the Allgäu (31.5 to 30 Ma, Figure 2.11c, Kempf et al., 1999; Schlunegger et al., 1996). This was coeval with a 200 m eustatic sea level fall (Haq et al., 1987) and the formation of alluvial megafans along the southern basin margin (Honegg-Napf, Rigi, and Speer fan systems, 31 to 30 Ma,

Figure 2.11c, Kempf et al., 1999; Schlunegger et al., 1996). The development of these alluvial megafans evidences topographic surface uplift in the Western/Central Alps (Kuhlemann et al., 2002a), translated as increased sediment supply from this area (Kuhlemann, 2000). Together, this tectonically driven increase in sediment supply and eustatic sea level fall allowed the Western Molasse to transition from underfilled- to overfilled conditions, as suggested by previous authors (Garefalakis and Schlunegger, 2018; Sinclair, 1997a). This means the underfilled- to overfilled transition was diachronous in the Molasse Basin.

Late Rupelian juxtaposition of littoral and neritic conditions in the Swiss- and Western German Molasse (Horw Sands and Rupelian Tonmergel respectively, Diem, 1986; Mraz et al., 2018) led to the development of an eastward-directed transitional zone in the Allgäu (observed as brackish deposits in Swiss Subalpine Molasse, Zaugg and Löpfe, 2011). However, axial transport of sediment derived from the Western/Central Alps allowed for the eastward migration of littoral conditions to the Bavarian Shelf by the middle Chattian (Subsection 2.5.1). Subsequently, the Bavarian Shelf remained relatively stable from the late Oligocene to the earliest Miocene (Subsection 2.5.1). This suggests that the eastward axial sediment supply was not high enough to outpace the generation of accommodation space in the Eastern Molasse. Moreover, it agrees with previous work suggesting the Bavarian Shelf was an area of sediment storage (Hülscher et al., 2021).

The MB significantly narrowed during the early Burdigalian (20 to 19 Ma, Figure 2.11h). The incision of Aquitanian sediments on the Bavarian Shelf (Figure A1.13) suggests that this narrowing was accompanied by erosion on the distal margin. This narrowing likely reflects hinterland-directed migration of the forebulge, as suggested by previous authors (Kuhlemann and Kempf, 2002b; Zweigel et al., 1998). Furthermore, the shortening of the wavelength of flexure resulted in a deepening of the foreland basin close to the thrust front (Zweigel et al., 1998). Combined with a rise in eustatic sea level (Haq et al., 1987) and a decrease in sediment supply from the Alpine hinterland (Kuhlemann, 2000), these processes led to a WNW-directed transgression

(Figure 2.6, this study, Garefalakis and Schlunegger, 2019; Strunck and Matter, 2002). Whereas neritic conditions were re-established in the Swiss and German Molasse (up to 50 m water depth, Heckeberg et al., 2010; Keller, 1989; Pippèrr, 2011), bathyal conditions remained dominant in the Austrian Molasse (Figure 2.11h, e.g. De Ruig and Hubbard, 2006; Hülscher et al., 2019; Lemcke, 1988).

By the late Burdigalian, the entire MB was dominated by terrestrial deposition (17 Ma, Figure 2.11j). This underfill-to-overfill transition was facilitated by increased sediment supply through the uplift of the Eastern Alps and redeposition of the Augenstein Fm. (Frisch et al., 2001; Hülscher et al., 2019; Kuhlemann, 2007) coeval with the cessation of flexural subsidence (Genser et al., 2007; Ortner et al., 2015; Schlunegger and Kissling, 2022). As such, the underfill- to overfill transition in the Eastern Molasse occurred ~ 12 to 13.5 My later than in the Western Molasse, in rough agreement with Schlunegger and Kissling (2022). This diachronous transition was stepwise rather than continuous. The first step occurred during the late Rupelian to middle Chattian and reached as far as Munich (Figures 2.11c to 2.11g, Kempf and Pross, 2005 and references therein). The second step occurred in the Eastern Molasse during the Burdigalian (Figures 2.11h to 2.11j, Hülscher et al., 2019).

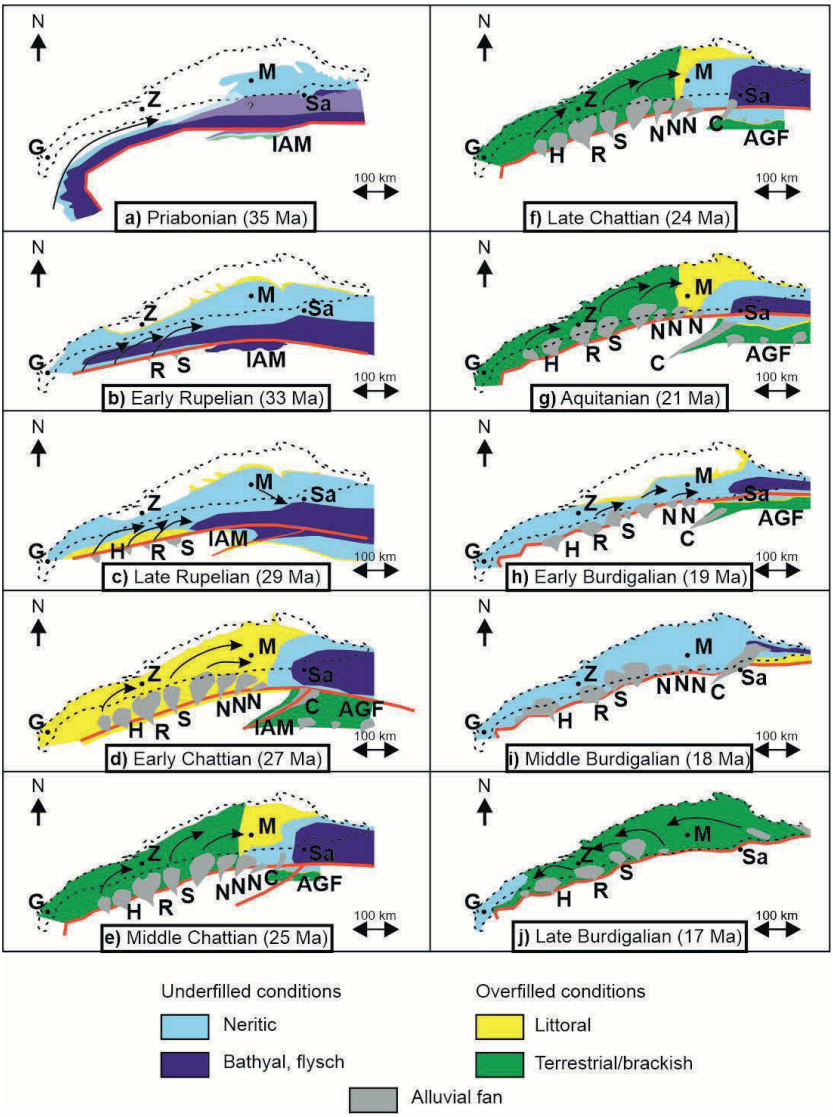
N
M
Z
Sa
G
IAM
100 km
a) Priabonian (35 Ma)
f) Late Chattian (24 Ma)
H
R
S
NNN
C
AGF
b) Early Rupelian (33 Ma)
g) Aquitanian (21 Ma)
c) Late Rupelian (29 Ma)
h) Early Burdigalian (19 Ma)
d) Early Chattian (27 Ma)
i) Middle Burdigalian (18 Ma)
e) Middle Chattian (25 Ma)
j) Late Burdigalian (17 Ma)
Underfilled conditions
Neritic
Bathyal, flysch
Overfilled conditions
Littoral
Terrestrial/brackish
Alluvial fan

Figure 2.11 (previous page): Schematic paleogeographic maps of the Molasse Basin during the late Eocene, Oligocene, and early Miocene, highlighting the diachronous migration of underfill to overfill deposition and transition to homogeneous development. Black arrows indicate the direction of dominant sediment transport, a lack of arrows implies no preferred drainage direction. **a)** Priabonian (~ 35 Ma) where transparent parts are interpolated**.** The location and shape distributions of the Inneralpine Molasse during the Priabonian are poorly constrained and have, therefore, been made transparent. **b)** Early Rupelian (~ 33 Ma). **c)** Late Rupelian (~ 29 Ma). **d)** Early Chattian (~ 27 Ma). **e)** Middle Chattian (~ 25 Ma). **f)** Late Chattian (~ 24 Ma)**. g)** Aquitanian (~ 21 Ma). **h)** Early Burdigalian (~ 19 Ma). **i)** Middle Burdigalian (~ 17 Ma). Our data was complemented with that of previous contributions (Jin et al., 1995; Sissingh, 1997; Zweigel et al., 1998; Ortner and Stingl, 2001; Kuhlemann and Kempf, 2002; Kuhlemann and Pfiffner, 2004; Zaugg and Löpfe, 2011; Garefalakis and Schlunegger, 2019; Hülscher et al., 2019). **H** = Honegg-Napf fan system, **R =** Rigi fan system, **S** = Speer fan system, **N =** Nesselburg fans, **C =** Chiemgau Fan, **AGF =** Augenstein Formation, **IAM** = Inneralpine Molasse, **Z =** Zürich, **M =** Munich, **S =** Salzburg, **G** = Geneva.

2.5.3 Mechanisms behind diachronous underfilled- to overfilled transition

Here we provide a chronology of the Alpine orogen and associated Molasse Basin evolution with attention to driving mechanisms. This is followed by an evaluation of the two hypotheses outlined in Subsection 2.1 in the context of the along-strike diachronous transition from underfilled- to overfilled conditions.

The pre-convergence European margin irregularity was characterised by the continental Brianconnais terrane in front of the future Western/Central Alps tapering out towards the future Eastern Alps (Faupl and Wagreich, 2000; Handy et al., 2010; Stampfli et al., 2002; Trümpy, 1960). Late Cretaceous to early Paleocene Alpine oceanic subduction was likely homogeneous along the entire trench (Figures 2.12a and 2.12b). However, Eocene incorporation of the Brianconnais terrane into the Western/Central Alpine wedge- and slab was coeval with ongoing oceanic subduction in the Eastern Alps (Figure 2.12c). Following previous results from geodynamical models of continental terrane subduction (Duretz et al., 2014; Li et al., 2013; Tetreault and Buiter,

2012; Vogt and Gerya, 2012), it is likely that the Brianconnais terrane impeded subduction along the Western/Central Alps and caused topographic uplift (Figure 2.12d). Furthermore, this may have led to trench-parallel variations in convergence velocities promoting slab breakoff and tearing (Andrić-Tomašević et al., 2023; Duretz et al., 2014; Li et al., 2013; Menant et al., 2016). Therefore, the subduction- and collision of the irregular European margin likely promoted late Eocene to early Rupelian slab breakoff below the Western/Central Alps (35 Ma, Handy et al., 2015; Schlunegger and Kissling, 2022; Schmid et al., 1996; von Blanckenburg and Davies, 1995). This led to uplift of the Western/Central Alps, translated into enhanced sediment supply (Garefalakis and Schlunegger, 2018; Hurford, 1986; Kuhlemann, 2000; Kuhlemann, 2007; Schlunegger and Kissling, 2022; Schlunegger and Willett, 1999; Sinclair, 1997a; Von Eynatten et al., 1999) which forced the transition from underfilled- to overfilled conditions in the adjacent Western Molasse by the late Rupelian (Figure 2.11c, Subsection 2.5.2).

In contrast, sediment supply from the Eastern Alps remained low at the same time due to subdued topography there (Frisch et al., 2001; Kuhlemann, 2000). This promoted protracted underfilled conditions in the Eastern Molasse (Figures 2.11c to 2.11g). The subdued topography may be explained by the Oligocene to early Miocene subduction of transitional/thinned crust (also highlighted in Le Breton et al., 2021) rather than continental collision due to the irregularity of the European margin. It is expected that once the Eastern Alpine thrust wedge encroached onto the European plate with a “normal” thickness (~30-40 km thick), surface uplift and exhumation were enhanced. This is supported by previous analogue and numerical model results (Andrić et al., 2018b; Luth et al., 2013; Vogt et al., 2018).

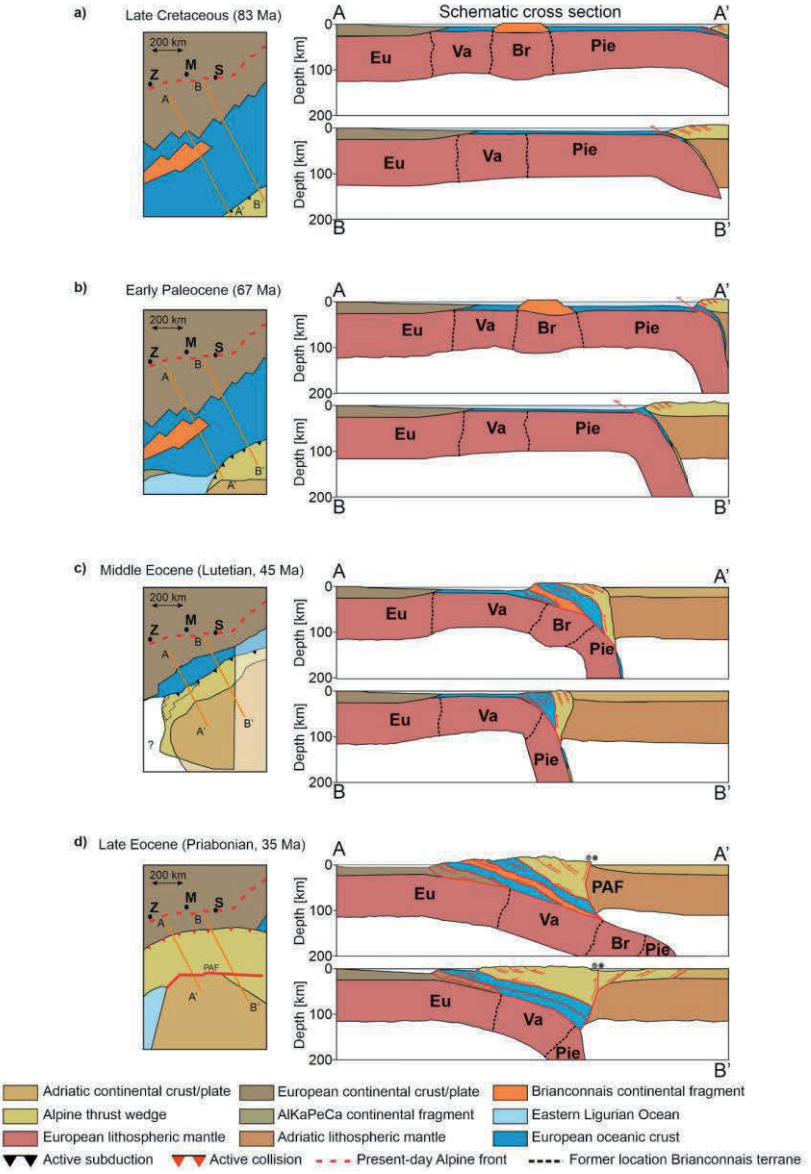
a)
Late Cretaceous (83 Ma)
Schematic cross section
200 km
Z
M
S
A
B
A'
B'
Depth [km]
0
100
200
Eu
Va
Br
Pie
b)
Early Paleocene (67 Ma)
c)
Middle Eocene (Lutetian, 45 Ma)
?
d)
Late Eocene (Priabonian, 35 Ma)
PAF
Adriatic continental crust/plate
European continental crust/plate
Brianconnais continental fragment
Alpine thrust wedge
AlKaPeCa continental fragment
Eastern Ligurian Ocean
European lithospheric mantle
Adriatic lithospheric mantle
European oceanic crust
Active subduction
Active collision
Present-day Alpine front
Former location Brianconnais terrane

Figure 2.12 (previous page): Paleogeographic reconstructions and respective cross sections of the convergent tectonics between the late Cretaceous and late Eocene, based on paleogeographic reconstructions from previous authors (Handy et al., 2010; Handy et al., 2015; Stampfli et al., 2002). **a)** In the late Cretaceous, the subduction of the Piemont Ocean under Austroalpine nappes starts. These nappes were located on the northern margin of the Adriatic plate. **b)** In the early Paleocene, subduction of the Piemont Ocean under the Adriatic plate continues along-strike the entire trench. This resulted in a homogeneous European slab. **c)** By the Middle Eocene, the continental Brianconnais terrane was subducted below and incorporated into the future Western/Central Alpine thrust wedge. To the east, oceanic subduction was uninterrupted. **d)** During the late Eocene, continental collision between the Adriatic and European plates occurred. Like the Middle Eocene, along-strike variations in the architecture of the European slab still existed. The segmentation of the Western/Central Alpine slab into oceanic and continental fragments may have promoted late Eocene to early Oligocene slab breakoff- and tearing.

Late Aquitanian to early Burdigalian (20 Ma) rapid exhumation is recorded in the Eastern Alps (Fox et al., 2016; Fügenschuh et al., 1997) contemporaneous with an increase in sediment supply (Kuhlemann, 2000). Subsequently, enhanced sediment supply triggered the underfilled- to overfilled transition of the Eastern Molasse by 19 to 18 Ma (Hülscher et al., 2019; Schlunegger and Kissling, 2022). Several authors attributed these observations to a second slab breakoff (Handy et al., 2015; Schlunegger and Kissling, 2022; Schmid et al., 2004a). However, if magmatism is a fingerprint of this process (Davis, van Blankenburg, 1995), then the absence of intrusions younger than 20 Ma would imply that the slab breakoff did not occur below the Eastern Alps at this time.

Looking at the mechanisms initiating the process of slab tearing (Andrić-Tomašević et al., 2023; e.g. Rosenbaum et al., 2008; van Hunen and Allen, 2011), the hypotheses tested in this paper (i.e., collision along the irregular margin and slab breakoff and tearing) are linked and represent a cause-and-effect relationship. However, we question whether lateral slab breakoff- and tearing alone could cause the diachronous underfill- to overfilled transition in the Molasse Basin between ~ 30 and ~ 20 Ma. If west-to-east slab tearing occurred between 30 Ma and 20 Ma, it would be followed by a parallel younging trend in magmatism (Ferrari et al., 2012; Rosenbaum et al., 2008). However,

the magmatic products in the Alps cover a time frame between 43 and 28 Ma without any orogen-parallel spatiotemporal trend (Kästle et al., 2020, their Figure 1). The age constraints of magmatic products suggest that if slab tearing occurred, it was probably fast (a few thousand/millions of years, also suggested by Schlunegger and Kissling, 2022, their Figure 11b). Furthermore, lateral slab tearing would lead to eastward younging of surface uplift and a gradual shallowing of the foreland basin along the strike as proposed by Meulenkamp et al. (1996) and Van der Meulen et al. (1998). Instead, the stepwise diachronous underfill-to-overfill transition in the Molasse Basin (Subsection 2.5.2) argues against continuous and slow lateral slab tearing between ~ 30 and 20 Ma.

The Eastern Alpine wedge overthrusting of the Bohemian Spur (acting as a buttress) was coeval with the onset of out-of-sequence thrusting (Covault et al., 2009; Hinsch, 2013; Ortner et al., 2015), surface uplift in the hinterland (Beidinger and Decker, 2014; Heberer et al., 2023a; Heberer et al., 2023b), and cessation of subsidence in the Eastern Molasse after 20 Ma (Genser et al., 2007; Schlunegger and Kissling, 2022). A stepping back of deformation led to uplift- and erosion of the Augenstein Fm. (Frisch et al., 2001; Hülscher et al., 2021). With frontal thrusting "locked", continued indentation of the Adriatic plate led to internal Eastern Alpine thickening (observed as the rapid early Miocene exhumation of the Tauern Window, Favaro et al., 2015; Fox et al., 2016; Fügenschuh et al., 1997; Scharf et al., 2013). This tectonically-driven uplift led to increased sediment supply from the Eastern Alps (Kuhlemann, 2000), which subsequently forced the underfilled- to overfilled transition in the Eastern Molasse by 19-18 Ma (Hülscher et al., 2019). Furthermore, the southward shift of the topographic loading due to internal thickening led to hinterland-directed migration of the forebulge, causing early Burdigalian incision of the northern basin margin (Figure A1.13). Uplift of the Molasse Basin above the Bohemian Spur (Heberer et al., 2023a; Heberer et al., 2023b) coeval with ongoing subsidence of the German- and Swiss Molasse (which we observe as ongoing normal fault activity, Ortner et al., 2023a; Schlunegger and Kissling, 2022) caused a reversal in the drainage direction (Garefalakis

and Schlunegger, 2019; Kuhlemann and Kempf, 2002b). This highlights slab breakoff- and tearing are not necessary to explain the evolution of the Eastern Alps- and Molasse during the early Miocene. However, we admit that with available data, this model cannot explain the Southern Alps changing from retro-wedge to pro-wedge deformation after 20 Ma through a subduction polarity reversal associated with European slab breakoff at ~ 20 Ma (Eizenhöfer et al., 2023; Handy et al., 2015). Further investigations into this topic are needed.

The above discussion highlights how subduction- and collision of the irregular European margin could have induced the diachronous flysch to molasse transition in the Molasse Basin. However, these models have not incorporated the effects of both the global Eocene-Oligocene and Oligocene-Miocene cooling events (Miller et al., 1991; Liu et al., 2009) on the erosion- and sediment supply. The transitions from underfilled- to overfilled conditions in both the Western and Eastern Molasse temporally correspond to these global cooling events. Moreover, such global cooling events have been shown to enhance erosion in mountainous areas (e.g. Herman et al., 2013). Therefore, we suggest that for future research climatic effects on denudation rates should be considered.

2.6 Conclusions

This study analysed along-strike variations in the Mesozoic basement, sedimentary fill, and syn-flexural normal fault kinematics of the MB. Our analysis provides insight into the lithospheric- and crustal-scale processes responsible for the diachronous underfilled- to overfilled transition during the Oligocene to early Miocene. The main conclusions include:

1. The German Molasse was partitioned into a structural high and a depocenter in the west and east, respectively. Both these features existed since the Mesozoic and influenced the late Eocene basin architecture. By

the Rupelian, this effect was smoothened out as recorded by homogeneous depositional environments along-strike the entire Molasse Basin.

2. Increased sediment supply from the Western/Central Alps at the end of the Rupelian (31.5 to 30 Ma) allowed the underfilled- to overfilled transition to occur in the Western Molasse. However, low sediment supply from the Eastern Alps and eastward axial transport of sediments derived from the Western/Central Alps, respectively, was insufficient to force the underfilled- to overfilled transition in the Eastern Molasse.
3. The Bavarian Shelf remained at a relatively stationary position between the Middle Chattian (26 Ma) and the end of the Aquitanian (20.5 Ma).
4. A west-to-east increase in cumulative Cenozoic offsets along syn-flexural normal faults suggests a higher Cenozoic curvature of bending of the European plate in the Eastern German Molasse compared to the Western German Molasse.
5. Subduction- and collision of the irregular European margin promoted late Eocene to early Oligocene slab breakoff, leading to an increase in surface uplift of the Western/Central Alps but not the Eastern Alps. Consequentially, the enhanced sediment supply from this uplift led to an overfilling of the Western Molasse, whereas underfilled conditions remained dominant in the Eastern Molasse. By the early Miocene, deformation may have been forced back into the core of the Eastern Alps because of the architecture of the European margin. This led to an enhanced sediment supply from the Eastern Alps, causing an overfilling of the Eastern Molasse.

Chapter 3
Seismic-scale syn-flexural normal fault development in the Molasse Basin and their relation to geodynamics

This chapter is based on:

Lucas H.J. Eskens, Nevena Andrić-Tomašević, Ajay Kumar, Magdalena Scheck-Wenderoth (in review) "Spatiotemporal growth of seismic-scale syn-flexural normal faults in the German Molasse Basin.*", Basin Research, BRE-031-2024.*

3.1 Introduction

Normal faults in rifts (Bosworth, 1985; Scholz and Contreras, 1998), pro/retro-foreland basins (Bradley and Kidd, 1991), and pull-apart basins (Hempton and Dunne, 1984; Mann et al., 1983) develop in response to crustal extension. Quantifying their activity in time and space is crucial for reconstructing the basin evolution (e.g. Jackson and Rotevatn, 2013; Pan et al., 2022). Furthermore, it allows for assessing the effect of geodynamic processes and tectonic inheritance on basin development (e.g., slab rollback, Giba et al., 2010; Ring et al., 2010). The growth of normal faults in rift basins has been well-established by quantitative studies (e.g. Gawthorpe et al., 2003; Jackson et al., 2017; Walsh et al., 2003). However, their counterparts in pro-foreland basins, hereafter referred to as foreland basins, have received little attention.

The flexural profile of a foreland basin depends on the interplay between gravitational loading (DeCelles and Giles, 1996; Flemings and Jordan, 1990; Sinclair, 1997a), foreland plate strength (Beaumont, 1981; Burov, 2010; Waschbusch and Royden, 1992), the degree of coupling between the converging plates (Willingshofer and Sokoutis, 2009; Ziegler et al., 2002), and inherited architecture of the subsiding crust (structures localising and altering the local stress and strain distribution, Andeweg and Cloetingh, 1998b; Lemcke, 1988). The width of the forebulge (flexural uplift migrating in front of an advancing mountain range, DeCelles and Giles, 1996; Roure, 2008) correlates with the amplitude and wavelength of the flexural profiles. For example, a narrow forebulge corresponds to a high amplitude and short wavelength flexural profile (Beaumont, 1981; Fosdick et al., 2014). This directly affects the width of the extensional deformation field around the hinge line of the forebulge where syn-flexural normal faults accommodate strain (Bradley and Kidd, 1991; Langhi et al., 2011; Supak et al., 2006). Furthermore, the forebulge and associated extensional strain will migrate cratonward as the mountain range encroaches onto the foreland plate. As a result, the zone of active syn-flexural normal faulting migrates in both time and space. The

examples above illustrate how spatiotemporal syn-flexural normal fault evolution can provide insight into the geodynamic processes that controlled the evolution of an orogenic wedge-foreland basin system.

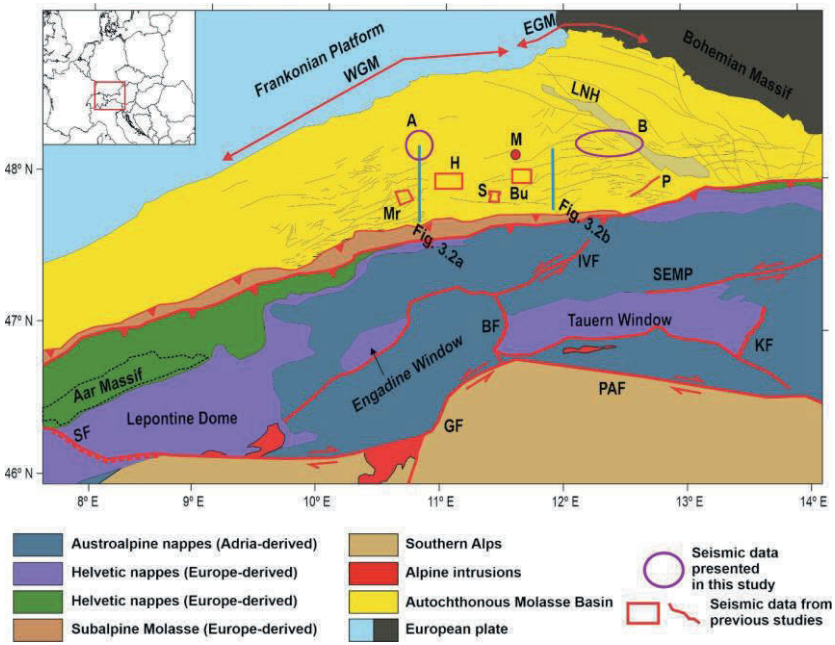

Figure 3.1: Map of the major tectonic units in the Alps, modified from (Schmid et al., 2004a). Thin black lines in the Molasse Basin indicate the locations of syn-flexural normal faults, based on the GeoMol project, (Mraz et al., 2018), and (Freudenberger and Schwerd, 1996). **A**: seismic volume A, **B**: seismic volume B, **LNH**: Landshut-Neuoetting High, **BF**: Brenner Fault, **PAF:** Periadriatic Fault, **KF**: Katschberg Fault, **GF**: Giudicarie Fault, **IVF**: Inntal Valley Fault, **SF**: Simplon Fault. Locations of previous studies: **Bu**: (Budach et al., 2018), **H** = (von Hartmann et al., 2016), **Mr** = (Mraz et al., 2018), **P** = (Cordero Peña, 2007), **S** = (Shipilin et al., 2020).

Previous quantitative assessments of syn-flexural normal fault throw distributions in foreland basins indicate that these structures can nucleate newly at shallow levels in previously unruptured crust and basin fill (Supak et al.,

2006; von Hartmann et al., 2016). Alternatively, pre-flexural basement faults may be reactivated (Bry et al., 2004; Langhi et al., 2011). However, the locus of nucleation is primarily controlled by the distribution of extensional strain in the foreland plate (Bradley and Kidd, 1991; Shipilin et al., 2020; von Hartmann et al., 2016). Furthermore, it has been shown that syn-flexural faults propagate both up- and downward when active, potentially inhibited by ductile interbedded stratigraphy (Langhi et al., 2011; Shipilin et al., 2020; von Hartmann et al., 2016). Finally, it has been demonstrated by previous studies that lateral fault growth of newly nucleated syn-flexural faults follows the isolated fault growth model (Cartwright et al., 1996; La Bruna et al., 2018; Supak et al., 2006).

On the basin scale, previous studies revealed along-strike variations in fault offsets and penetration depth, attributed to the along-strike variations in 1) pre-flexural foreland plate crustal architecture (Bry et al., 2004) or 2) the magnitude of foreland plate deflection (Eskens et al., 2024). Such along-strike variations in growth styles of syn-flexural normal faults in foreland basins hint at orogen-parallel variations in the mechanisms controlling flexure. Therefore, information distilled from syn-flexural normal fault growth can be inverted to better understand the geodynamic evolution of a foreland basin-orogen system.

In this contribution, we study the syn-flexural normal faults in the German Molasse Basin (Figure 3.1). This basin developed due to Late Eocene to early Miocene Alpine (sub)surface loading, causing flexure of the European foreland plate (Handy et al., 2010; Schmid et al., 1996). Flexural bending was accompanied by the development of syn-flexural normal faults on the basinward slope of the forebulge (e.g., Bachmann and Müller, 1991; Lemcke, 1988; Shipilin et al., 2020), hereafter referred to as the distal basin margin. In this contribution, we quantify throw values of syn-flexural seismic horizons along-strike and down-dip syn-flexural normal faults in two 3D seismic volumes on the distal margin of the German Molasse (which is unaffected by Alpine thrusting, Figure 3.1 for locations). This quantitative assessment allows us to 1) evaluate the growth styles and interactions of these faults in 4D and 2)

develop an understanding of the driving parameter(s) for their growth. Orogen-parallel variations in growth styles in different parts of the Molasse Basin are then compared with 1) crustal/lithospheric strength models for the European plate of previous authors (Spooner et al., 2022), 2) the inherited crustal architecture of the European plate and 3) the geodynamic evolution of the Alps. This allows us to assess the link between syn-flexural normal fault growth, tectonics, and foreland plate strength. Our findings imply that a west-to-east increase in cumulative syn-flexural offset along normal faults in the German Molasse may be a fingerprint of basin-parallel variations in the strength of the European lithosphere.

3.2 Geological setting

The German Molasse is part of the Northern Alpine Foreland Basin (Figure 3.1, Kuhlemann and Kempf, 2002; Lemcke, 1988). It is subdivided into the Western- and Eastern German Molasse based on different tectonostratigraphic evolution (Eskens et al., 2024 and references therein, Figure 3.1). The Western German Molasse lies north of the Central Alps (defined as the Alps between the Simplon- and Brenner Faults, Figure 3.1) and the Eastern German Molasse north of the Eastern Alps (defined as the Alps between the Brenner- and Katschberg faults, Figure 3.1). The basin developed from the late Eocene to early Miocene due to the flexural subsidence of the European plate, induced by Alpine slab- and Alpine topographic loading (Eskens et al., 2024 and references therein). This flexural subsidence was accompanied by the development of normal faults striking subparallel to the orogenic front (Bachmann and Müller, 1991; Lemcke, 1988; Ziegler, 1990).

3.2.1 The Alpine hinterland

The flexural subsidence of the German Molasse is inherently related to the Alpine orogeny. Therefore, we provide a synoptic overview of the Alpine tectonics. For a more detailed description, the reader is referred to other contributions (e.g., Handy et al., 2010; Le Breton et al., 2021; Schmid et al., 1996).

The Alps are a stack of Adria-derived Austroalpine- and Europe-derived Penninic and the Helvetic nappes (Figure 3.1), recording the closure of the Penninic domain and subsequent continental collision between the European- and Adriatic plates (Schmid et al., 1996; Trümpy, 1960; Ziegler et al., 1996). The Penninic domain that separated the European- and Adriatic plates consisted of the Piemont-Liguria Ocean, the continental Brianconnais terrane, and the Valais Through (Handy et al., 2010; Mohn et al., 2014; Schmid et al., 1996; Trümpy, 1960). Subduction- and nappe stacking of the Penninic units below the Austroalpine nappes positioned on the northern margin of the Adriatic plate started in the Late Cretaceous (Handy et al., 2010; Stampfli et al., 1998). By the late Eocene, the Penninic domain had been closed, followed by the onset of continental collision (Schmid et al., 1996; Ziegler et al., 1996). Subsequent early Oligocene oceanic slab breakoff led to the exhumation of the previously subducted nappe stack (Davies and von Blanckenburg, 1995; Schmid et al., 1996). Continued convergence resulted in folding, duplexing, and southward backthrusting against the Periadriatic Fault of the exhumed nappe stack in the Western and Central Alps (Hurford, 1986; Rosenberg and Kissling, 2013; Schlunegger and Willett, 1999; Schmid et al., 1996). This was translated into the uplift of the orogenic core and external massifs (e.g., Aar Massif, Lepontine Dome and Engadine Window), resulting in over 2 km of Oligocene topography (Frisch et al., 2001; Kuhlemann, 2007). In contrast, Oligocene topographies in the Eastern Alps remained low. Their growth started only during the early Miocene following the exhumation of the Tauern Window due to Adriatic indentation (Favaro et al., 2015; Kuhlemann, 2007; Scharf et al., 2013; Schmid et al., 2013).

3.2.2 Basement and stratigraphy of the German Molasse

3.2.2.1 The Paleozoic to Mesozoic basement

The Variscan crystalline basement of the German Molasse is made up of gneisses and granites, locally cut by fault-bounded Permo-Carboniferous grabens with a clastic fill (Bachmann and Müller, 1991). The overlying Middle Triassic to Late Cretaceous carbonates and clastics define the passive margin sequence (Bachmann and Müller, 1991; Meyer and Schmidt-Kaler, 1990a). In the Western German Molasse, the Upper Jurassic subcropping the foreland unconformity is locally heavily karstified (Lemcke, 1988; Meyer and Schmidt-Kaler, 1990b; Wolpert et al., 2022). This karstification was likely coeval with the erosion of the uplifted Mesozoic passive margin sediments before the onset of flexure. Erosion due to this uplift led to the development of the foreland unconformity, which now separates the Mesozoic passive margin sequence from the syn-flexural fill (Crampton and Allen, 1995; Ziegler et al., 2002).

The European Mesozoic passive margin was characterised by horst-and-graben domains at the future Western German- and Eastern German Molasse, respectively (Rhenish Shield and Wasserburger Trog, Eskens et al., 2024; Lemcke, 1988). To the north, the Wasserburger Trog in the Eastern German Molasse was delimited by the Lanshut-Neuötting High (Bachmann and Müller, 1991; Brink et al., 1992). This was a NW-SE striking intrabasinal high, presently orientated obliquely to the orogenic front (Figure 3.1). Further east, the Austrian part of the Molasse Basin was delimited to the north by the rigid Bohemian Massif (Figure 3.1).

3.2.2.2 The Cenozoic syn-flexural basin fill

The onset of flexure is recorded by Late Eocene neritic to littoral limestones and sands onlapping to the NNW onto the eroded Mesozoic basement in the Eastern German Molasse (Lithothamnium Limestones, Sissingh, 1997; Zweigel et al., 1998). Subsequent early Oligocene bathyal deposition records

a rapid deepening (Rupelian Sands and Marls, Jin et al., 1995; Sissingh, 1997; Zweigel et al., 1998). However, during the late Oligocene to early Miocene, shallowing led to a transition towards the littoral and terrestrial conditions in the Western German Molasse (Baustein Beds, Cyrena Beds, and Upper Freshwater Molasse, Diem, 1986; Eskens et al., 2024; Kuhlemann and Kempf, 2002). However, littoral to neritic conditions remained dominant in the Eastern German Molasse during the same time (Lower Chattian Marls, Chattian Sands, Upper Chattian Marls, and Aquitanian Series, Eskens et al., 2024; Jin et al., 1995; Zweigel et al., 1998). At the Aquitanian-Burdigalian transition (early Miocene), flooding of the entire German Molasse resulted in the re-establishment of neritic- to bathyal conditions (Upper Marine Molasse, Baltringer Fm., and Hall Fm., Eskens et al., 2024; Heckeberg et al., 2010; Heimann et al., 2009; Hülscher et al., 2019; Jin et al., 1995; Zweigel et al., 1998). However, these renewed neritic- to bathyal conditions were short-lived, with terrestrial conditions dominating the entire German Molasse since the Late Burdigalian (Matter, 1980).

3.2.3 The structural development of the German Molasse

Flexural subsidence of the European foreland plate was accompanied by the development of syn-flexural normal faults generally striking subparallel to the E-W oriented orogenic front (Figure 3.1, Bachmann and Müller, 1991; Lemcke, 1988). These faults developed around the forebulge where extensional stress and strain localised (Langhi et al., 2011; Supak et al., 2006). The synthetic faults dip to the south, and the antithetic faults to the north (Eskens et al., 2024; Shipilin et al., 2020; von Hartmann et al., 2016). During ongoing flexure, the number of active faults decreased over time (Eskens et al., 2024).

Development of syn-flexural normal faults in the autochthonous German Molasse started in the late Eocene and Rupelian (Budach et al., 2018; Mraz et al., 2018; Shipilin et al., 2020). Early fault growth was characterised by either reactivation of Jurassic/Cretaceous normal faults (Budach et al., 2018; Mraz

et al., 2018) or nucleation of new faults within the Mesozoic sequence or crystalline basement (Shipilin et al., 2020). Rupelian fault activity is only recorded in the basin axis of the Western German Molasse (Mraz et al., 2018; von Hartmann et al., 2016). However, syn-flexural faults also developed on the distal margin of the Eastern German Molasse (Budach et al., 2018; Eskens et al., 2024; Shipilin et al., 2020). Intra-Rupelian upward termination in the present-day axial part of the Eastern German Molasse (Figure 3.2b, Budach et al., 2018; Shipilin et al., 2020) suggests a cessation of fault growth. This is not observed in the Western German Molasse (Figure 3.2a, Mraz et al., 2018).

During the Chattian, fault activity continued in the axial Western German Molasse alongside the nucleation of new faults (Mraz et al., 2018; von Hartmann et al., 2016). Contemporaneously, new faults nucleated on the distal margin as well (Eskens et al., 2024). In the axial part of the Eastern German Molasse, new faults also nucleated during the early Chattian within the basin fill (Budach et al., 2018; Shipilin et al., 2020). However, the newly nucleated faults close to the thrust front became inactive quickly after initial growth (Shipilin et al., 2020). As a result, these faults did not propagate into the basement, connect with lower segments, or grow upward into shallower successions (Shipilin et al., 2020). This resulted in vertically unlinked faults (Figure 3.2b). Furthermore, Chattian propagation of the Alpine wedge led to the continued incorporation of internal foreland units into the Alpine wedge, resulting in the formation of the Subalpine Molasse (Ortner et al., 2015; Ortner et al., 2023b).

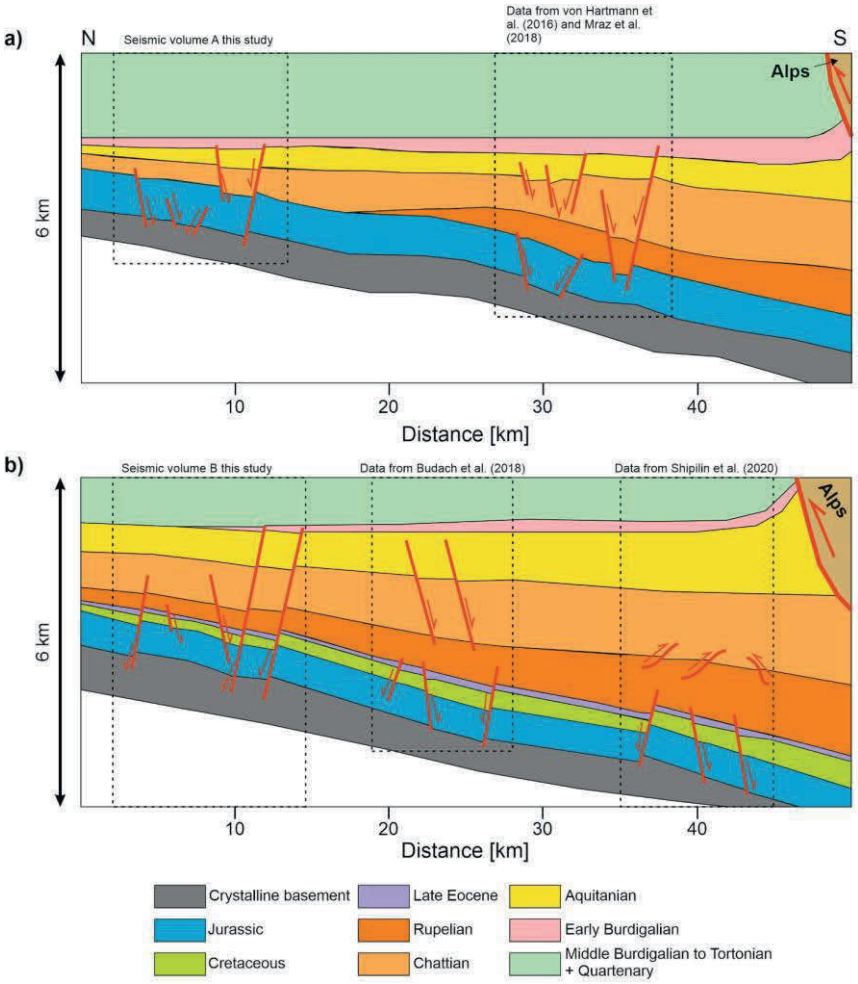
a)
N
Seismic volume A this study
Data from von Hartmann et al. (2016) and Mraz et al. (2018)
S
Alps
6 km
10
20
30
40
Distance [km]
b)
Seismic volume B this study
Data from Budach et al. (2018)
Data from Shipilin et al. (2020)
Alps
6 km
10
20
30
40
Distance [km]
Crystalline basement
Jurassic
Cretaceous
Late Eocene
Rupelian
Chattian
Aquitanian
Early Burdigalian
Middle Burdigalian to Tortonian + Quartenary

Figure 3.2 (previous page): Schematic profile of different styles of syn-flexural normal- and reverse faults observed in the German Molasse Basin. For locations of these transects, see Figure 3.1a. Faults are only drawn where data is available. **a)** In the Western German Molasse syn-flexural normal faults close to the thrust front are observed to cut the entire Cenozoic syn-flexural fill and the underlying basement (e.g., Mauerstetten fault, Mraz et al. 2018). Furthermore, vertically disconnected sets of faults also exist. Whereas the lower set of faults cuts the basement and terminates within the lower Rupelian stratigraphy, the upper set is restricted to Chattian to early Burdigalian stratigraphy. On the northern basin margin syn-flexural normal faults transect the Mesozoic basement, terminating upward within the Cenozoic fill or cutting the entire syn-flexural fill. The cross-section is modified from von Hartmann et al. (2016). The thickness of stratigraphy is only constrained where seismic data is available and interpolated between the volumes. The northern pinch-out of Rupelian stratigraphy is, therefore, not exact. Styles of faulting are based on data from von Hartmann et al. (2016), Mraz et al. (2018), and Eskens et al. (2024). **b)** In the Eastern German Molasse Basin closest to the thrust front, a lower set of normal faults cuts the basement and the succession above up to the lower part of the Rupelian stratigraphy. In contrast, the upper set of faults is characterised by reverse faults restricted to the upper Rupelian and lower Chattian stratigraphy. Further northward, the same set of lower faults restricted to the basement and the lower Rupelian stratigraphy are observed. However, here, the upper set of faults is characterised by normal faults confined to upper Rupelian to Aquitanian stratigraphy. On the northern basin margin, the syn-flexural normal faults cut the basement, terminating upward either within the Cenozoic fill or cutting the entire syn-flexural fill. The cross-section has been modified from Wolpert et al. (2022). Styles of faulting are based on data from Budach et al. (2018), Shipilin et al. (2020) and Eskens et al. (2024).

During the Aquitanian, syn-flexural normal faults in the axial Western German Molasse and the distal margin thereof remained active (Eskens et al., 2024; Mraz et al., 2018; von Hartmann et al., 2016). In the Eastern German Molasse, contemporaneous fault activity is only recorded on the distal margin (Eskens et al., 2024). This pattern remained the same during the early Burdigalian, with all faults in the German Molasse being sealed by middle Burdigalian stratigraphy (Eskens et al., 2024; Mraz et al., 2018; Shipilin et al., 2020; von Hartmann et al., 2016). Subsequently, syn-flexural faults that had nucleated close to the present-day thrust front during the Chattian in the Eastern German Molasse were reactivated as reverse faults during the middle Miocene (Figure 3.2b, Shipilin et al., 2020). Contemporaneously, frontal propagation of thrusting in the Subalpine Molasse ceased and was followed by out-of-

sequence thrusting in the Central- and Eastern Alps (Ortner et al., 2015; Ortner et al., 2023b).

3.3 Data, methods, and limitations

This work builds on the detailed seismic-stratigraphic analysis and fault interpretations made in seismic volumes A and B (for locations, see Figure 3.1) as presented in Eskens et al. (2024). A description of this seismic data can be found in subsection A1.1. Following the seismic interpretations, we quantify throw distributions along-strike and down-dip the syn-flexural normal faults for different reflectors. This allows us to investigate fault growth styles in both time and space (Subsection 3.3.1). An analysis of the effect of mechanical stratigraphy on the fault growth styles is presented in the Supplementary Material.

3.3.1 Quantitative fault kinematic analysis

In this study, we use the fault- and seismic interpretations from Eskens et al. (2024) to make a detailed kinematic analysis of the syn-flexural normal fault growth styles in the German Molasse. We present results for the two faults with the highest length- and syn-flexural throw values. Because these faults accommodated most of the extensional deformation in the respective seismic volumes, we assume that they represent the structural growth style best. Results for smaller syn-flexural normal faults interpreted in these volumes, which indicate similar growth styles as those presented in the main text, can be found in the Appendix (Figures A2.4 and A2.5).

To study the kinematic evolution of the faults, the interpreted seismic horizons and faults are used to generate a structural model in Petrel. Smoothing was applied to the structural model to exclude effects from fault drag. Subsequently, using the “throw profile” operation for the structural model faults, we can extract the individual throw values for the various reflectors along the

fault plane. In this analysis, the throw is defined as the vertical distance between the intersection of a seismic horizon with the fault in the footwall and the hanging wall, respectively. With this approach, the calculated fault throw is a cumulative of dip- and oblique-slip contributions.

First, we apply the “original” backstripping method (Chapman and Meneilly, 1991; Petersen et al., 1992) to the extracted throw profiles for each interpreted stratigraphic horizon. In this method, the throw value of a shallow reflector is subtracted from that of a deeper reflector at the same along-strike position of a fault. The resulting value then represents the syn-kinematic thickening of the stratigraphic unit. Doing this along the fault plane will give a backstripped throw-length (T-x) profile that measures the transient fault activity along its strike (e.g. Jackson et al., 2017; Pan et al., 2022). Therefore, we can use this type of profile to determine whether the interpreted normal faults grew according to the isolated, constant length or hybrid fault growth models (Figure A2.1). We choose this method over the “modified” backstripping method (Rowan et al., 1998), because the latter approach implicitly makes the a priori assumption of faults growing according to the isolated fault growth model. Negative values obtained from backstripping are set to zero, as these values indicate a net inactivity of the normal fault.

Secondly, we constructed ten throw-depth (T-z) profiles along the length of each T-x profile to provide insight into the stratigraphic position of nucleation and subsequent vertical growth of faults (Figure A2.2). In these profiles, the stratigraphic level of nucleation is recorded by the reflector with the highest throw value. The subsequent downward- and/or upward growth is then constrained by decreasing throw values for both deeper and shallower reflectors, respectively. Lastly, we calculated each seismic-stratigraphic unit's expansion index (EI) at the T-z profile locations. The EI index is a measure of across-fault thickening of a seismic-stratigraphic unit at times when the fault is breaking the free surface and is calculated by dividing the thickness of a seismic-stratigraphic unit in the hanging wall over the thickness of that same unit in the footwall (Jackson et al., 2017; Jackson and Rotevatn, 2013; Thorsen, 1963).

An EI value of 1 implies that fault activity did not cause syn-kinematic thickening when the seismic-stratigraphic unit of interest was deposited. In contrast, an EI > 1 suggests across-fault thickening during syn-depositional fault activity. An EI of <1 is unusual, typically implying difficulties in correctly assessing the thickness of a seismic-stratigraphic unit on either side of the fault (Jackson et al., 2017; Thorsen, 1963).

Secondly, we constructed ten throw-depth (T-z) profiles along the length of each T-x profile to provide insight into the stratigraphic position of nucleation and subsequent vertical growth of faults (Figure A2.2). In these profiles, the stratigraphic level of nucleation is recorded by the reflector with the highest throw value. The subsequent downward- and/or upward growth is then constrained by decreasing throw values for both deeper and shallower reflectors, respectively.

Lastly, we calculated each seismic-stratigraphic unit's expansion index (EI) at the T-z profile locations. The EI index is a measure of across-fault thickening of a seismic-stratigraphic unit at times when the fault is breaking the free surface and is calculated by dividing the thickness of a seismic-stratigraphic unit in the hanging wall over the thickness of that same unit in the footwall (Jackson et al., 2017; Jackson and Rotevatn, 2013; Thorsen, 1963). An EI value of 1 implies that fault activity did not cause syn-kinematic thickening when the seismic-stratigraphic unit of interest was deposited. In contrast, an EI > 1 suggests across-fault thickening during syn-depositional fault activity. An EI of <1 is unusual, typically implying difficulties in correctly assessing the thickness of a seismic-stratigraphic unit on either side of the fault (Jackson et al., 2017; Thorsen, 1963).

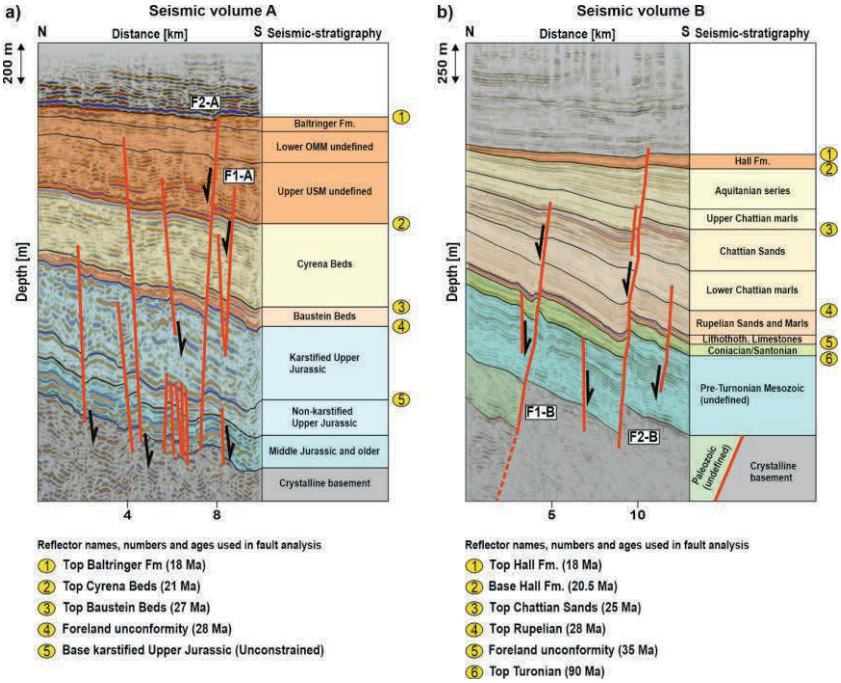

Figure 3.3: a) Seismic stratigraphy in seismic volume A west of Munich, based on Eskens et al. (2024). The ages of reflectors are based on Kuhlemann and Kempf (2002), von Doppler et al. (2005), Heimann et al. (2009), Heckeberg et al. (2010), and Shipilin et al. (2020). **USM** = Upper Freshwater Molasse. **b)** Seismic stratigraphy in seismic volume B east of Munich, based on Eskens et al. (2024). The ages of the different reflectors are based on Jin et al. (1995) and Zweigel et al. (1998). Unconstrained means the age of the reflector is unknown. Reflector numbers are the same as in Figures 3.5 (Volume A), 3.6 and 3.7 (Volume B). Not numbered reflectors are not included in the fault analysis due to poor traceability. Unconstrained means the exact age of the reflector is unknown, and the unlabelled reflectors are not included in the fault analysis due to poor traceability in the entire seismic volume.

3.4 Results

The fault networks in both seismic volumes are dominated by E-W and NW-SE striking faults (Figure 3.4). Most of the faults strike E-W, with NW-SE striking faults characterizing relay faults (e.g., F5-B in Figure 3.4d). The exception to this is F1-B, which is the upward extension of the basin bounding fault of the Paleozoic-Triassic Giftthal Through (Figure 3.4d, Bachmann and Müller, 1991; Eskens et al., 2024). Apart from syn-flexural normal faults, the variance attribute of the foreland unconformity reflector in seismic volume A also reveals elongated, meandering features (Figures 3.4a and 3.4b). These are interpreted as a drainage network of the karstified Upper Jurassic sequence (Eskens et al., 2024, Figures 3.4a and 3.4b). Furthermore, circular shapes with high variance values delineate sinkholes (Figure 3.4a). The syn-flexural fault locations do not show a spatial relation with these karst features (Figures 3.4a and 3.4b). In seismic volume B, karstification features are not as developed as in volume A (Eskens et al., 2024).

3.4.1 Quantitative assessment of throw distributions of the syn-flexural normal faults

3.4.1.1 Syn-flexural normal faults growing according to the isolated model

Early Chattian fault patches along the entire length of faults F1-A and F2-A were initially laterally disconnected (T-x profiles in Figure 3.5). Subsequently, these isolated fault patches were linked laterally during the late Chattian to early Burdigalian without further lengthening of the fault (T-x profiles in Figure 3.5). This evidences lateral fault growth according to the isolated fault growth model (Figure A2.1). Throw minima- and maxima along the fault do not show (major) lateral shifts (T-x profiles in Figure 3.5), implying a dominant dip-slip component during the fault evolution. The T-z profiles along these

faults are dominantly characterised by B- and D-shapes (Figure 3.5). This suggests vertical fault growth follow the isolated- or dip-linkage fault growth styles (Figure A2.2).

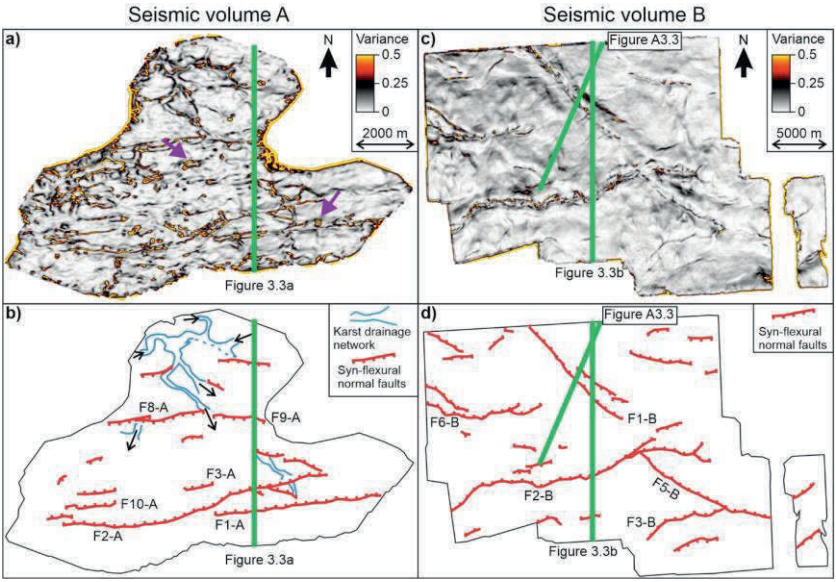

Figure 3.4: a) Variance attribute of the foreland unconformity reflector of seismic volume A (i.e., top karstified Upper Jurassic, Figure 3.3a). Purple arrows highlight some examples of sinkholes recognised as circular features with high variance values. **b)** Present-day distribution of the syn-flexural fault network and the drainage network of the karstified Upper Jurassic, interpreted based on the variance attribute shown in the panel above. Black arrows indicate the assumed drainage direction of the paleokarst network. **c)** Variance attribute of the foreland unconformity reflector of seismic volume B. **d)** Present-day distribution of the syn-flexural normal fault network in seismic volume B, interpreted from the variance attribute of the foreland unconformity shown in the panel above.

Early Chattian fault segments all record throw maxima for the foreland unconformity reflector down-dip the fault (T-z profiles 1 to 3, 5, 6, and 9 in Figure 3.5a, T-z profiles 1, 3 to 7, 9, and 10 in Figure 3.5b). This suggests that

these fault segments nucleated at the top of the Mesozoic basement. This shallow nucleation is also reflected in the EI values for the early Chattian exceeding 1 in these T-z profiles (T-z profiles 1 to 3, 5, 6, and 9 in Figure 3.5a, T-z profiles 1, 3 to 7, 9, and 10 in Figure 3.5b), which suggests that the fault was surface breaking shortly after nucleation. Both the base karstified Upper Jurassic and top Baustein Beds reflectors record lower throw values compared to the foreland unconformity reflector for these T-z profiles (T-z profiles 1 to 3, 5, 6, and 9 in Figure 3.5a, T-z profiles 1, 3 to 7, 9 and 10 in Figure 3.5b). This evidences that nucleation was followed by both up- and downward propagation of the fault.

Fault patches that developed later due to lateral growth have T-z profiles with D-shapes, with throw maxima recorded by the top Baustein Beds or top Cyrena Beds reflectors (T-z profiles 7, 8, and 10 in Figure 3.5a, T-z profiles 7 and 8 in Figure 3.5b). Reflectors directly above- and below these throw maxima record lower throw values (T-z profiles 7, 8, and 10 in Figure 3.5a, T-z profiles 2 and 8 in Figure 3.5b). This suggests that these fault segments nucleated within the basin fill during flexure, followed by up- and downward propagation.

Between 1700 to 2700 m along F1-A, the fault was inactive during the late Chattian to early Aquitanian (T-x profile in Figure 3.5a). Here, the T-z profiles have B shapes with a second, shallow throw maximum recorded by the top Cyrena Beds reflectors (T-z profiles 5, 6, and 9 in Figure 3.5a). This indicates that inactivity was followed by late Aquitanian to early Burdigalian nucleation at the top of the Cyrena Beds. Subsequent downward propagation led to dip-linkage with the formerly inactive lower segment.

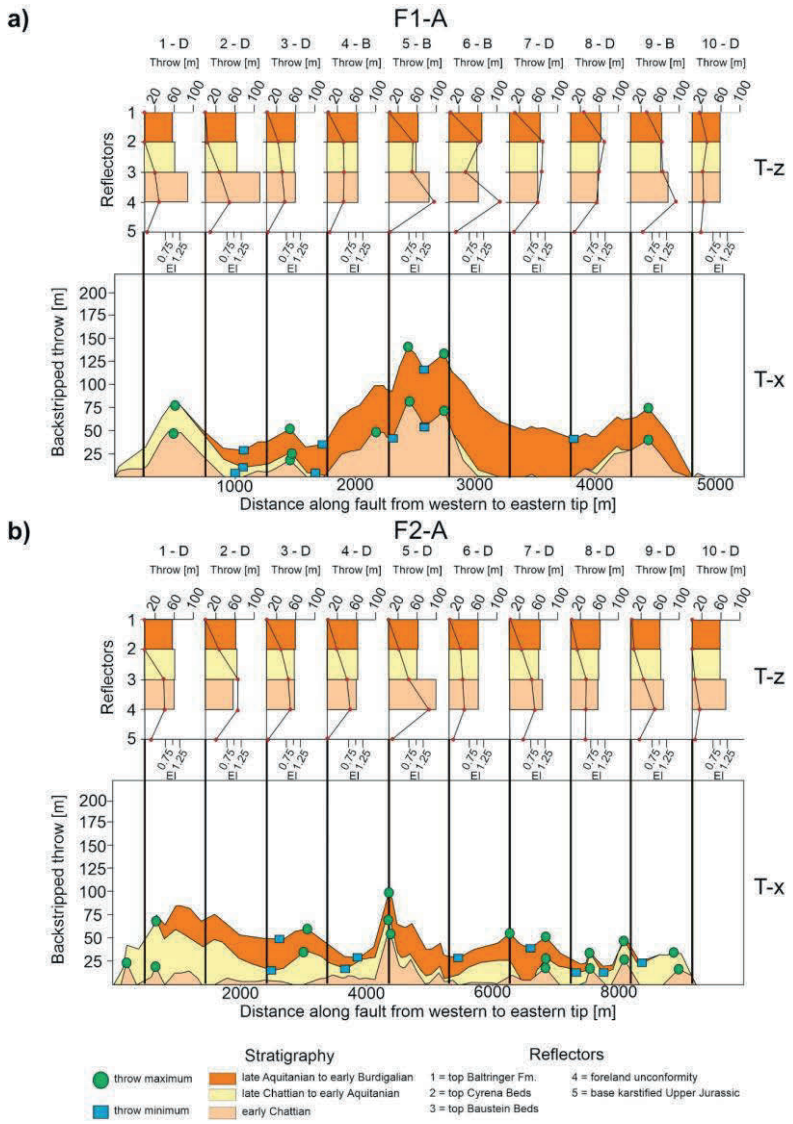

Figure 3.5: Backstripped T-x profiles with 10 T-z profiles along the length of faults **a)** F1-A and **b)** F2-A. EI values of the different seismic-stratigraphic units are given in coloured boxes in the T-z profiles.

3.4.1.2 Syn-flexural normal faults growing according to the constant-length fault growth model

Fault F1-B attains the final fault length during the first phase of fault growth (T-x profile in Figure 3.6). This indicates lateral fault growth following the constant length model (Figure A2.1). Like F1-A and F2-A, throw minima- and maxima along the backstripped T-x profile do not show (major) lateral shifts (T-x profile in Figure 3.6). T-z profiles along the fault are dominantly characterised by either B- or D-shapes (Figure 3.6), which implies a mix of dip-linkage and isolated fault growth (Figure A2.2).

The foreland unconformity reflector records a throw maximum in all T-z profiles along the fault (Figure 3.6). Both the deeper top Turonian and shallower top Rupelian reflectors record lower throw values than the foreland unconformity reflector (Figure 3.6). This implies that this fault nucleated at the top of the Mesozoic basement and subsequently propagated both up and downward. This corroborates with EI values higher than 1 for the late Eocene to Rupelian stratigraphy (Figure 3.6), implying the fault was surface breaking shortly after nucleation. This early fault growth pattern resembles that observed for F1-A and F2-A (Subsection 3.4.1.1). Furthermore, nucleation at the top of the Mesozoic basement implies that the lower segment that bounded the Paleozoic Giftthal Through (Figure 3.3b, Bachmann and Müller, 1991; Eskens et al., 2024), located at 480 m depth at the onset of flexure (Figure A2.3), was not reactivated during flexure.

F1-B is characterised by a phase of inactivity during the early to middle Chattian along its western half (Figure 3.6, from 500 to 5500 m along the backstripped T-x profile). This is reflected in the T-z profiles having B-shapes with a second shallow throw maximum recorded by the top Chattian Sands reflector (T-z profiles 1 to 6 in Figure 3.6). This implies that the phase of inactivity was followed by nucleation of an upper segment at the top of the Chattian Sands during the late Chattian. Subsequently, this upper segment dip-linked with the lower, formerly inactive segment. This reflects fault growth styles as observed for F1-A and F2-A (Subsection 3.4.1.1).

Along the eastern end of the fault, the T-z profiles have D-shapes for which lower throw values are recorded for successively younger syn-flexural reflectors (Figure 3.6, from 5500 to 9500 m along backstripped T-x profile). This evidences that the eastern end of this fault was characterised by growth faulting following late Eocene to Rupelian nucleation at the top of the Mesozoic basement.

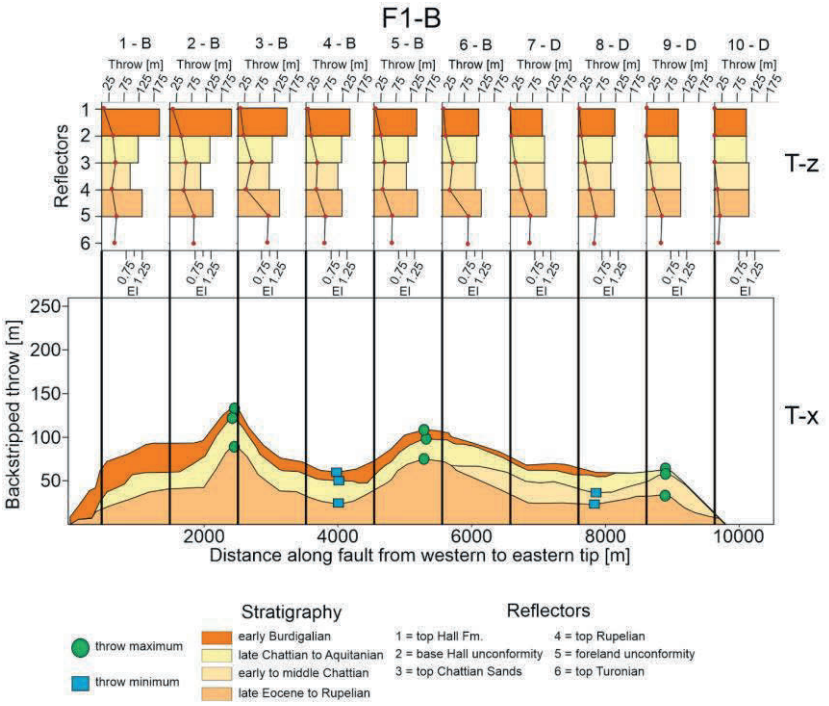

Figure 3.6: Backstripped T-x profile with 10 T-z profiles along the length of fault F1-B. EI values of the different seismic-stratigraphic units are given in coloured boxes in the T-z profiles.

3.4.1.3 Syn-flexural normal faults growing according to the hybrid fault growth model

Late Eocene and Rupelian fault growth was characterised by the development of laterally isolated fault patches along the entire length of F2-B (T-x profile in Figure 3.7). This was followed by early to middle Chattian inactivity along most of the fault (T-x profile in Figure 3.7). Subsequent reactivation during the late Chattian to Aquitanian led to lateral linkage along the eastern fault segment, throw accumulation, and 1.5 km westward tip propagation along the western segment (T-x profile in Figure 3.7). This evidences that this fault grew laterally following the hybrid growth model (Figure A2.1).

T-z profiles are dominated by B- and D-shapes (Figure 3.7). This evidences that vertical growth of F2-B was dominantly characterised by isolated growth or dip-linkage of a lower- and upper fault segment (Figure A2.2). Patches where fault growth initiated during the late Eocene to Rupelian record throw maxima for the foreland unconformity and top Turonian reflectors (T-z profiles 2 to 7, 9, and 10 in Figure 3.7). In case of the foreland unconformity recording a throw maximum, the deeper top Turonian- and shallower top Rupelian reflectors record lower throw values (T-z profiles 2 to 7 in Figure 3.7). This means that initial fault nucleation of these patches occurred at the top of the Mesozoic basement, followed by up- and downward propagation. This corresponds with EI>1 for the late Eocene to Rupelian stratigraphy (Figure 3.7), indicating these segments were surface-breaking shortly after nucleation. Conversely, the upward throw decrease from the top Turonian reflectors towards the foreland unconformity and top Rupelian reflectors along the eastern segment (T-z profiles 9 and 10 in Figure 3.7) suggests a Mesozoic fault was reactivated. However, EI>1 for late Eocene to Rupelian stratigraphy along this segment indicates that this part of the fault also reached the surface shortly after reactivation.

Fault patches that developed later due to lateral growth have T-z profiles with B- and D-shapes for which the top Chattian Sands and top Rupelian reflectors record throw maxima (T-z profiles 1 and 8 in Figure 3.7). This suggests that

these segments started developing after the initial onset of flexure and nucleated within the basin fill. Furthermore, along segments where the fault was inactive during the early to middle Chattian, the T-z profiles are characterised by B- and Z-shapes (T-z profiles 2 to 7 and 9 in Figure 3.7). The Z-shaped T-z profiles indicate that reactivation occurred through upward propagation of the segment that was sealed during inactivity. Alternatively, the B-shaped T-z profiles indicate an upper segment nucleated within the basin fill that subsequently dip-linked with the lower segment that was previously sealed.

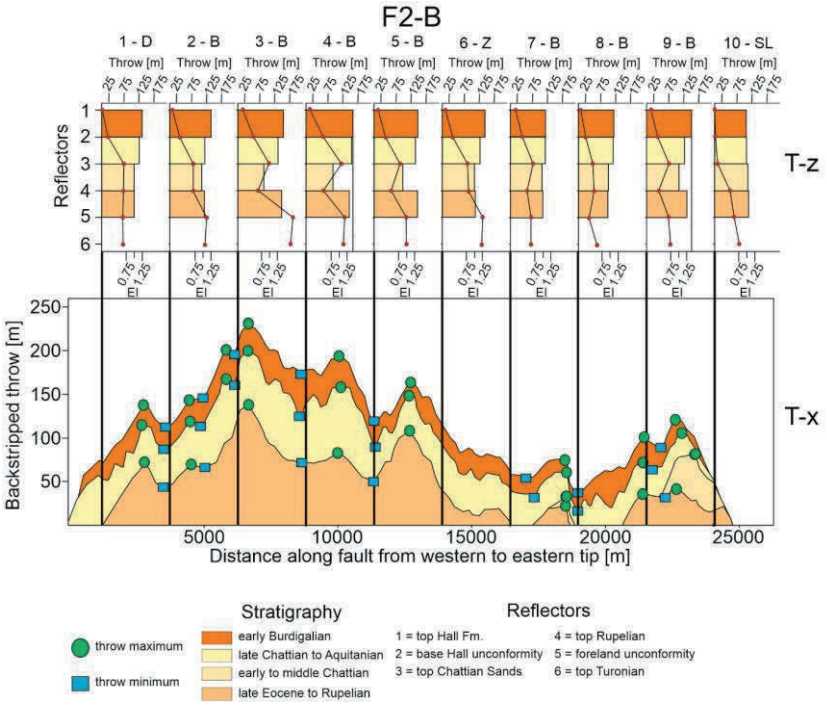

Figure 3.7: Backstripped T-x profile with 10 T-z profiles along the length of fault F2-B. EI values of the different seismic-stratigraphic units are given in coloured boxes in the T-z profiles.

3.5 Discussion

Our data reveals growth styles, kinematics, and the distribution of the offsets of late Eocene to early Miocene syn-flexural normal faults in the German Molasse Basin. First, we discuss the implications of our quantitative analysis in terms of 4D syn-flexural normal fault growth in the German Molasse (Subsection 3.5.1). Subsequently, we identify agreements and discrepancies of syn-flexural fault growth in the entire Molasse Basin and discuss the implications thereof (Subsection 3.5.2). Lastly, we discuss the spatiotemporal variations in syn-flexural normal fault growth styles in the Molasse Basin in terms of mechanism(s) that controlled the flexure of the European plate during the Alpine orogeny (Subsection 3.5.3).

3.5.1 The nucleation and growth styles of seismic-scale normal faults in the German Molasse Basin

In our data volumes, the syn-flexural normal faults have an E-W/SW-NE strike (sub)parallel to the orogenic front (Figure 3.4), in agreement with previous studies in the German Molasse (e.g., Budach et al., 2018; Mraz et al., 2018; Shipilin et al., 2020; von Hartmann et al., 2016). This reaffirms that these faults grew in response to flexure-related extensional stresses around the forebulge migrating in front of the orogen. Additionally, it reflects the results from analogue (Supak et al., 2006) and numerical (von Hartmann et al., 2016) experiments. Faults in our data volumes that strike NW-SE either characterise relay faults (e.g., F5-B, Figures 3.4c and 3.4d) or are related to pre-existing faults (F1-B, Figures 3.4c and 3.4d, basin-bounding fault of the Paleozoic-Triassic Giftthal Through, Bachmann and Müller, 1991; Eskens et al., 2024). The lack of a correlation between karst features and normal fault locations (Figure 3.4b) implies that these pre-existing weaknesses did not localise deformation. Furthermore, throw minima- and maxima barely shifting laterally along the fault planes (Figures 3.5, 3.6, 3.7) suggests little to no strike-slip and, thereby, oblique-slip on the faults.

The onset of flexural subsidence (late Eocene to Rupelian and early Chattian for volumes A and B, respectively) led to the nucleation of new fault patches at the top of the pre-flexural basement (Figures 3.5, 3.6 and 3.7). This suggests that the highest strain related to the extensional stress resulting from bending around the forebulge was localised close to- or at the surface (in agreement with previous studies, Langhi et al., 2011; Supak et al., 2006). However, higher throw values for Mesozoic basement reflectors compared to the foreland unconformity or basin-fill reflectors for some faults (T-z profiles 8 to 10 in Figure 3.7, T-z profiles 1 to 6 in Figure A2.4b and T-z profiles 2 to 10 in Figure A2.5b) imply reactivation of Mesozoic pre-flexural faults. Therefore, flexure was associated with both the reactivation of pre-existing faults and the nucleation of a new fault network. This agrees with previous studies in the German Molasse (Budach et al., 2018; Mraz et al., 2018; Shipilin et al., 2020; von Hartmann et al., 2016).

The onset of flexural subsidence (late Eocene to Rupelian and early Chattian for volumes A and B, respectively) led to the nucleation of new fault patches at the top of the pre-flexural basement (Figures 3.5, 3.6 and 3.7). This suggests that the highest strain related to the extensional stress resulting from bending around the forebulge was localised close to- or at the surface (in agreement with previous studies, Langhi et al., 2011; Supak et al., 2006). However, higher throw values for Mesozoic basement reflectors compared to the foreland unconformity or basin-fill reflectors for some faults (T-z profiles 8 to 10 in Figure 3.7, T-z profiles 1 to 6 in Figure A2.4b and T-z profiles 2 to 10 in Figure A2.5b) imply reactivation of Mesozoic pre-flexural faults. Therefore, flexure was associated with both the reactivation of pre-existing faults and the nucleation of a new fault network. This agrees with previous studies in the German Molasse (Budach et al., 2018; Mraz et al., 2018; Shipilin et al., 2020; von Hartmann et al., 2016).

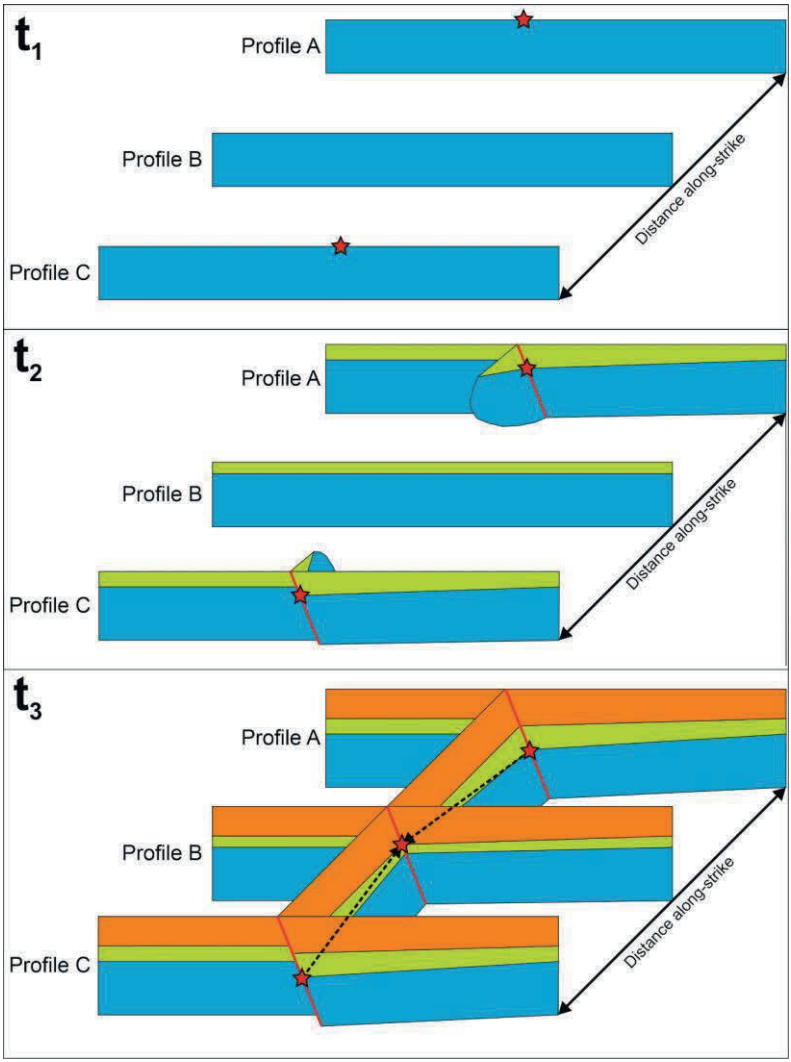
t1
Profile A
Profile B
Profile C
Distance along-strike
t2
Profile A
Profile B
Profile C
Distance along-strike
t3
Profile A
Profile B
Profile C
Distance along-strike

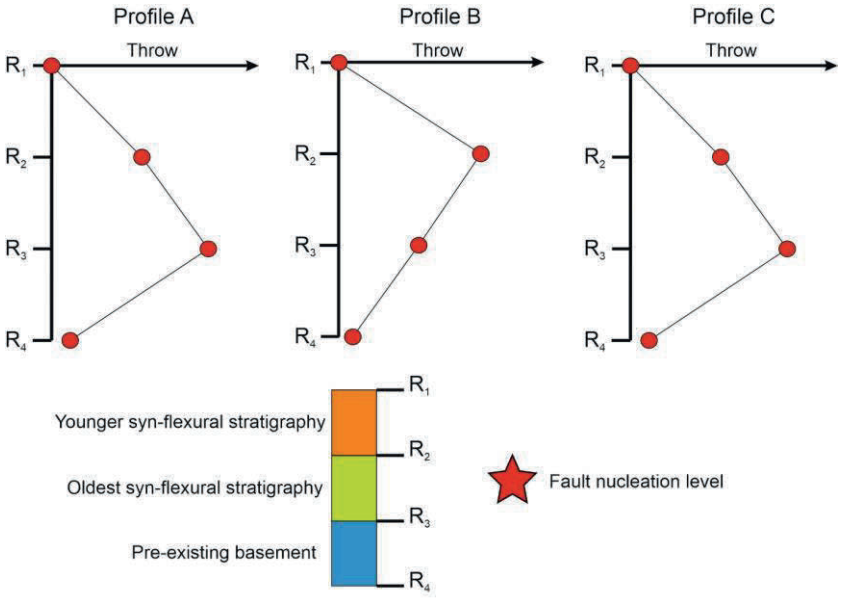

Figure 3.8 (previous- and this page): Schematic illustration of nucleation and subsequent isolated lateral growth of syn-flexural normal faults as observed in the German Molasse basin, where R_1 to R_4 indicate the seismic-stratigraphic reflectors. $\mathbf{t_1}$, The normal fault nucleates along profiles A and C, whereas initiation of fault growth along profile B is delayed. At this time, syn-flexural sediment thickness is negligible. $\mathbf{t_2}$ Sedimentation contemporaneous with fault activity along profiles A and C results in syn-kinematic thickening. However, the fault has not laterally propagated to the position of profile B, so the coevally deposited sediments in profile B are thinner and do not record fault-related thickening. $\mathbf{t_3}$ Continued upward propagation of the fault in profiles A and C results in the thickening of the youngest syn-flexural stratigraphy. Furthermore, due to lateral fault growth, the sediments deposited along profile B will now also record fault-related thickening. This means the fault tip migrated laterally and stratigraphically upward, as the black dashed lines indicates. In T-z profiles along the fault, the throw maximum is therefore observed to be recorded at different stratigraphic levels.

Whereas reactivated faults grew laterally following the constant length model (T-x profiles of F9-A and F5-B, Figures A2.4b and A2.5b), newly nucleated faults follow the isolated or hybrid fault growth models (T-x profiles in Figures 3.5 and 3.7). This implies reactivation promoted rapid lengthening, a process which is also observed in rift basins (Giba et al., 2012; Rotevatn et al., 2018; Walsh et al., 2002; Whipp et al., 2014). Furthermore, linkage segments are characterised by nucleation within the syn-flexural basin fill (e.g., T-z profiles 7 and 8 in Figure 3.5a, T-z profiles 2 and 8 in Figure 3.5b). This implies that the fault tip migrated stratigraphically upward during the lateral growth of newly nucleated faults (Figure 3.8). Fault segments characterised by inactivity
during flexure that were subsequently reactivated were observed to correspond with T-z profiles with either B- or Z-shapes (e.g., T-z profiles 5 and 6 in Figure 3.5a, T-z profiles 1 to 6 in Figure 3.6, and T-z profiles 2 to 7 and 9 in Figure 3.7). The first suggests that new segments could nucleate within the basin fill during ongoing flexure and subsequently dip-link with the sealed lower segments (Figure 3.9). This was also observed by previous authors (Shipilin et al., 2020; von Hartmann et al., 2016). The latter implies that, alternatively, the buried segments were reactivated and propagated upward.

Interestingly, F1-B grew laterally following the constant-length model even though it nucleated newly at the top of the Mesozoic basement at the onset of flexure. This indicates that even though the Paleozoic segment was not reactivated, it may have localised deformation in its cover. As a result, this forced the deviating NW-SE strike and rapid lengthening of F1-B. Nucleation of new faults above pre-existing basement faults rapidly attaining their final length was also found by previous authors in the German Molasse (Faults Gartenberg S and Gelting N, Shipilin et al., 2020) as well as in the Timor Through subduction trench (Langhi et al., 2011). This suggests that pre-flexural basement faults at greater depths were not reactivated during flexure. Instead, basement faults may have lowered the required strain to nucleate a syn-flexural fault in its cover.

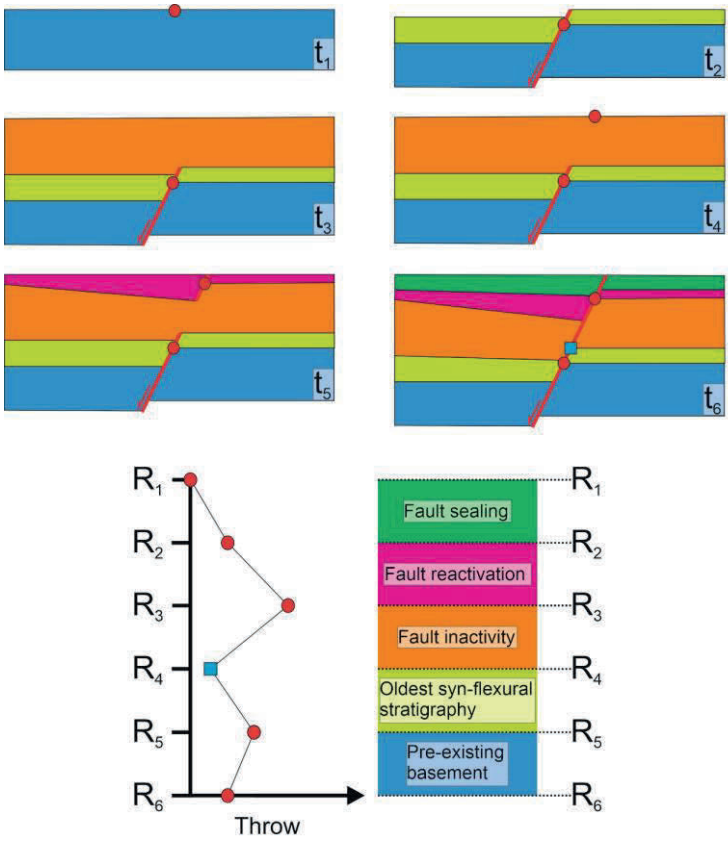

Figure 3.9: Schematic representation of how vertically linked faults developed in the German Molasse, with resultant T-z profile along a vertically linked segment. **t_1** Fault growth nucleates at the top of the pre-existing basement at the onset of flexural subsidence when no syn-flexural sediments have been deposited. **t_2** Ongoing flexural subsidence leads to the development of a normal fault that grows both downward into the pre-existing basement and upward in the syn-flexural basin fill, recorded as syn-kinematic thickening. **t_3** Fault growth ceases, with the remnant topography being filled by sedimentation. **t_4** Renewed tectonic activity leads to the nucleation of an upper segment at the top of the syn-flexural stratigraphic sequence present at this time instead of the deeper segment being reactivated. **t_5** The new fault grows downward into the syn-flexural fill that was initially unaffected by faulting and upward into the newly deposited sediments. **t_6** Downward propagation of the fault leads to vertical linkage at the upper tip of the lower fault segment, and upward growth leads to syn-kinematic thickening of newly deposited sediments. After some time, the fault is sealed.

3.5.2 Syn-flexural normal faults in the Molasse Basin

Previous authors identified syn-flexural normal faults in the Swiss Molasse that nucleated close to the top of the pre-existing basement during flexure, subsequently linking at depth with pre-flexural Mesozoic faults (Roche et al., 2020, their Figures 3.10 and 3.11). Similarly, T-z profiles of faults interpreted by previous authors in the Austrian Molasse (Gross et al., 2015; Masalimova et al., 2015) also indicate nucleation at the top of the Mesozoic basement, within the syn-flexural basin fill, and reactivation of Mesozoic basement faults (Figure A2.6). Therefore, the nucleation- and growth patterns in the Swiss- and Austrian Molasse reflect the findings of this and previous studies in the German Molasse (Subsection 3.5.1). This suggests that the growth styles of the syn-flexural faults were homogeneous in the entire Molasse Basin. However, our data in the German Molasse show that the strike of syn-flexural normal faults may deviate from the general E-W trend in case they are related to pre-existing structures (e.g., F1-B, Figures 3.4c and 3.4d). Moreover, syn-flexural faults that developed close to either pre-existing highs (Landshut-Neuötting High and Bohemian Massif, Figure 3.1) or basins (F1-B of Giftthal Trough, this study; Unterlören Graben, Heuberger et al., 2016) do not necessarily strike (sub)parallel to the orogenic front. This suggests that pre-flexural structures that are either incorporated in the foreland basin or located at its margin, exert an important control on the local strain partitioning, governing the strike of syn-flexural normal faults.

Combining our data with that of previous authors shows that the cumulative syn-flexural offsets increase from north to south (Figure 3.10a). This implies the magnitude of flexure increased towards the south, which corroborates with the southward deepening of the basin during ongoing flexure (e.g., Bachmann and Müller, 1991; Lemcke, 1988). More striking, however, is that the cumulative syn-flexural offsets increase from the Western- to the Eastern German Molasse on both the distal margin and the axial part of the basin (Figure 3.10a). This suggests an increase in the magnitude of strain accommodated by syn-flexural faulting in the Eastern German Molasse compared to

the Western German Molasse. Zhang et al. (2023) showed with a 3D flexural model that a lateral increase in deflection of a subducting oceanic plate leads to an increase in the magnitude of extensional stresses in the same direction as the increasing flexure. Taking this as an analogue, the increase in the extensional strain accommodated in the Eastern German Molasse was likely facilitated by an increase in the deflection of the European plate towards the east. This interpretation corroborates with the late Oligocene to early Miocene along-strike deepening of the depositional environments from the Western German- to the Eastern German Molasse Miocene (e.g., Kuhlemann and Kempf, 2002; Lemcke, 1988; Sissingh, 1997). Furthermore, syn-flexural normal faults further north from the orogenic front are sealed by progressively younger stratigraphy (Eskens et al., 2024). Growth of syn-flexural normal faults in the vicinity of the Alpine front (German Molasse SW of Munich) initiated during the early Rupelian (Figure 3.1, Mraz et al., 2018), whereas their counterparts 35 km to the north started developing later during the early Chattian (ca. 27.5 Ma, Seismic volume A, Figures 3.1 and 3.5). This gives us an average northward migration rate of 7.8 mm/yr of the flexural forebulge during the early Oligocene. This is comparable with northward propagation rates of the Alpine wedge based on 1) the onlap patterns of the basal limestones (8.5 - 12.9 mm/yr, Sinclair, 1997b), 2) restoration of geological cross-sections (at least 5.5 to 4.5 mm/yr, Schmid et al., 1996), and 3) plate tectonic reconstructions (6 to 8.9 mm/yr, Handy et al., 2015; Le Breton et al., 2021; Van Hinsbergen et al., 2020). We interpret this migration to have resulted from the northward advance of the forebulge and associated extensional stress- and strain field as the Alps continued encroaching the European margin. This means that similar to how normal faults are used to trace the migration of the extensional stress field due to slab rollback in a back-arc basin (Giba et al., 2010), syn-flexural normal faults in a pro-foreland basin can be used to reconstruct the spatiotemporal location of the forebulge.

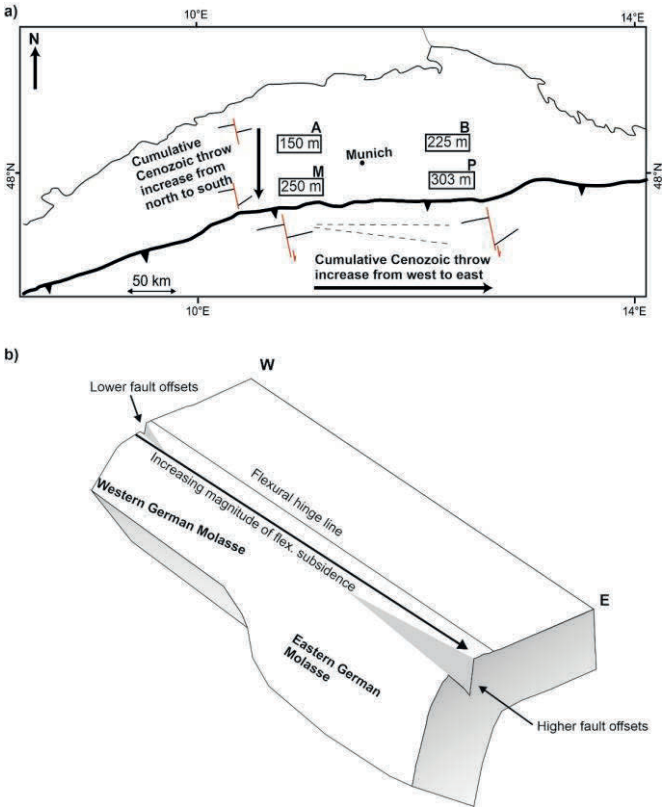

Figure 3.10: a) Magnitude of maximum cumulative syn-flexural offsets down-dip the normal faults in the German Molasse Basin, based on data presented in this work as well as from previous studies (Cordero Peña, 2007; Mraz et al., 2018). **A** = seismic volume A presented in this study, **B** - seismic volume B presented in this study, **M** - data from Mraz et al. (2018), and **P -** data from Peña (2007). For the derivation of the syn-flexural throw values from the time to the depth from time domain data from Peña (2007), see subsection A1.2.3. **b)** Due to an eastward increase in the magnitude of flexural subsidence of the European lithosphere during the Alpine orogeny, the cumulative offsets down-dip the syn-flexural normal faults are higher in the Eastern German Molasse compared to the Western German Molasse. Normal fault offsets are not to scale with the foreland plate. Figure 3.10b inspired by Zhang et al. (2023).

3.5.3 Syn-flexural normal faults as fingerprints of the geodynamic evolution of the Alpine orogeny

Using thermomechanical and elastic modelling, previous authors showed that the thickness of the lithospheric mantle, which contributes 70% to the integrated lithospheric strength, decreases from the Western- to the Eastern German Molasse (Spooner et al., 2022). This is translated into a reduction in the strength of the European lithosphere in the same direction (Figure 3.11a, Andeweg and Cloetingh, 1998b; Spooner et al., 2022).

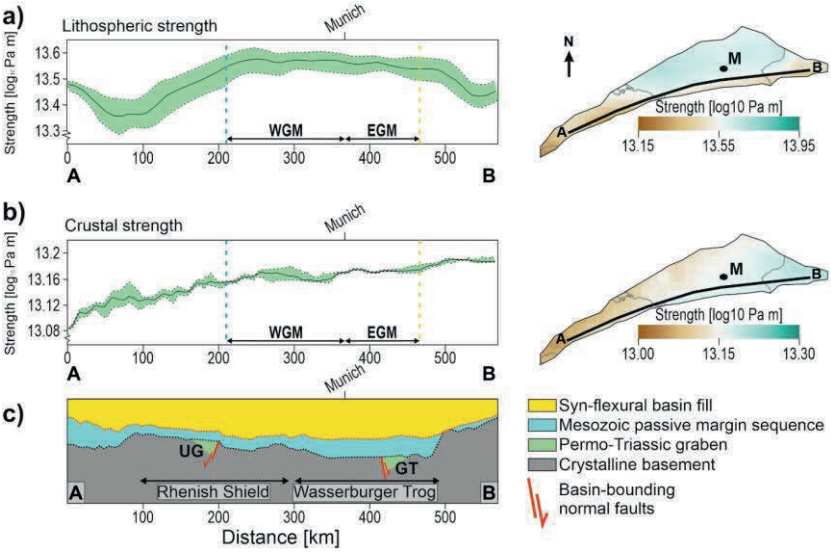

Figure 3.11: A 20 km wide swath profile of the present-day showing **a)** integrated lithospheric strength (crust and lithospheric mantle) and **b)** crustal strength in the Molasse Basin along profile A-B (Spooner et al., 2022). The vertical blue dashed line indicates the border between the Swiss and German Molasse, and the yellow vertical dashed line is the border between the German and the Austrian Molasse. **WGM** - Western German Molasse, **EGM** - Eastern German Molasse. **c)** Crustal profile along profile A-B, indicating the location of the pre-flexural Rhenish Shield and Wasserburger Trog. Adapted from Eskens et al., (2024). **UG** - Unterlören Graben, **GT** - Giftthal Through.

As lithospheric strength "is frozen in" (Watts and Burov, 2003), we can assume that the present-day strength of the European lithosphere shown in Figure 3.11a is representative of the Oligocene to early Miocene time. This assumption is supported by the similarity in estimates of the European lithospheric strength below the Alpine wedge for both the present-day (Willingshofer and Cloetingh, 2003) and Oligocene (Pfiffner et al., 2002). As lithospheric strength is one of the factors dictating the magnitude and wavelength of the flexural profile of a foreland basin (Flemings and Jordan, 1989; Waschbusch and Royden, 1992), we interpret the observed eastward increase in deflection of the European plate (based on mapped syn-flexural normal faults, Subsection 3.5.2) as a fingerprint of this lateral strength variation of the European plate. A similar cause-effect relationship is also observed in the Polish Carpathian foreland basin. There, syn-flexural fault offsets are higher in the eastern foreland basin that developed above the Tornquist-Teisseyre Zone (Paleozoic suture, i.e. a lithospheric weak zone, Narkiewicz et al., 2015; Smit et al., 2016) compared to the western foreland basin that developed on the Western European Platform (Krzywiec, 2001). This suggests that the magnitude of foreland basin deflection was higher where the foreland lithosphere was weaker. In contrast to the lithospheric strength, crustal strength increases from the Western- to the Eastern German Molasse Basin (Figure 3.11b, Spooner et al., 2022). Spooner et al. (2022) interpret this to be caused by a cooler crustal geotherm in the Eastern German Molasse. Furthermore, the local variations in the crustal strength correspond to the variations in the European passive margin architecture, i.e. low strength is estimated for the area of the Rhenish Massif, while higher strength is estimated for the Wasserburger Trog (Figures 3.11b and 3.11c).

This paradox suggests that the distribution of crustal strength is not of primary control on the magnitude of flexure of the foreland plate, and the effect of the lithospheric strength prevails. However, it is noteworthy that the magnitude of flexure increases south of the Bohemian Massif. As Andeweg and Cloetingh (1998) suggested, this may have resulted from the downward squeezing of the European plate between the approaching Eastern Alpine

wedge and the Bohemian Massif acting as a buttress. As a result, subsidence had to be accommodated by a smaller area, which may have contributed to the higher magnitude of flexure of the European plate towards the east (Subsection 3.5.2). Furthermore, the general strike of the syn-flexural normal faults changing around the Landshut-Neuoetting High (Figure 3.1) suggests that this pre-existing high influenced the local deformation. Therefore, in contrast to crustal strength, pre-existing local crustal heterogeneities may alter the distribution of strain and subsidence.

Inherently, the eastward increase in deflection of the European plate likely led to a shortening of the wavelength and an increase in the amplitude of the flexural profile in the Eastern German Molasse, consistent with weaker foreland lithosphere (Figures 3.11a and 3.12a). Consequently, this would lead to an eastward narrowing of the zone experiencing extensional stresses (Figure 3.12b), which should be expressed in the spatiotemporal pattern of syn-flexural fault activity. During the early Chattian to early Burdigalian, fault activity is recorded in both the basin axis (Mraz et al., 2018) and on the distal margin (Eskens et al., 2024) of the Western German Molasse. In contrast, coeval activity in the Eastern German Molasse was restricted to the distal margin (Eskens et al., 2024). This suggests an eastward decrease in the width of the zone accommodating extensional deformation following the eastward plate weakening trend, consistent with our model (Figure 3.12).

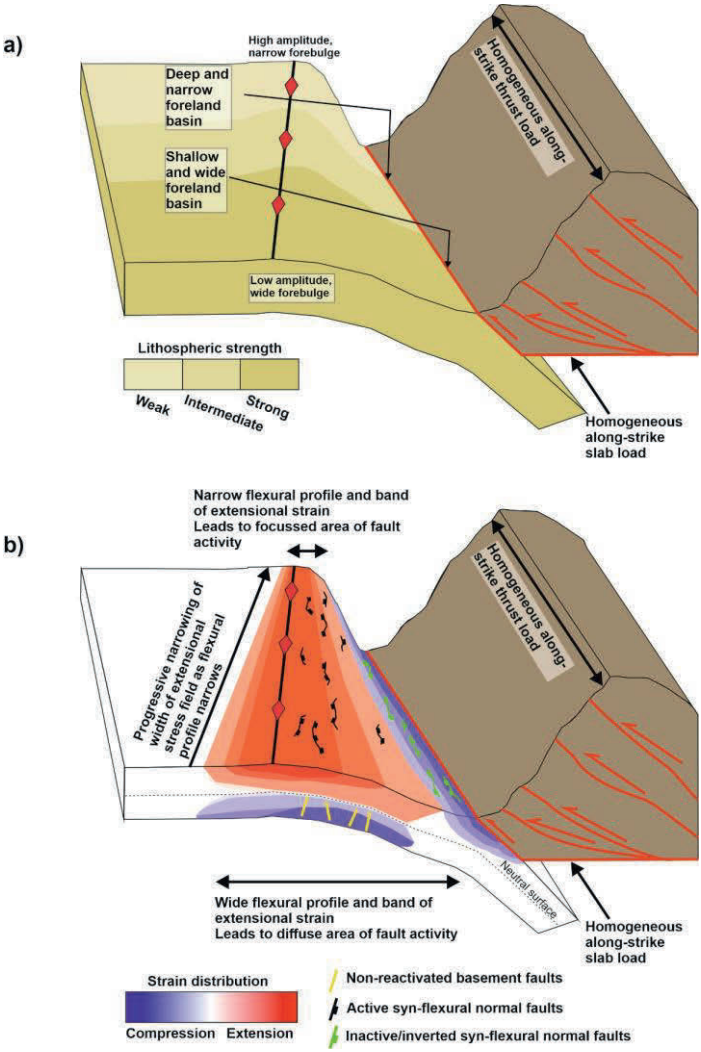

Figure 3.12: a) Schematic model of the flexure of a foreland plate with along-strike variable lithospheric strength. Please note that orogen-parallel variations in (sub)surface loads, plate coupling, or the presence of pre-flexural structures in the foreland are not accounted in this model. **b)** Where the flexural wavelength is narrow, the zone of extensional stresses around the forebulge is more focused. On the contrary, where the flexural profile is wide, the zone of extensional stresses is more diffuse. Close to the orogenic front compressive stresses are dominant.

It is noteworthy that lateral variations in the lithospheric –and/or crustal strength, inducing along-strike variable amounts of the foreland plate flexure, may arise from several factors, such as 1) pre-existing weakness (Calignano et al., 2015; Roure, 2008; e.g. Willingshofer et al., 2005) 2) passive margin irregularity (e.g. promontories and embayments, Lash, 1988; Maiti et al., in revision) and/or 3) margin obliquity (Maiti et al., in revision). In all these cases, continental lithosphere of laterally variable strength would be involved in the collision, leading to along-strike variations in the foreland plate flexure (assuming laterally constant loads). Therefore, it is likely that the along-strike heterogeneity in architecture of the European lithosphere, represented by the continental Brianconnais terrane (in front of the Western- and Central Alps) laterally transitioning to the oceanic Penninic domain (in front of the Eastern Alps, e.g., Faupl and Wagreich, 2000; Mohn et al., 2014; Rosenberg et al., 2021), induced lateral strength variations in the European plate. Subsequently, these may have been expressed as spatiotemporal variations in flexure along strike in the Molasse Basin.

Apart from lateral lithospheric strength variations, orogen-parallel variations in the degree of coupling between the Alps and the European plate (Willingshofer and Sokoutis, 2009; Ziegler et al., 2002)and magnitudes of the topographic- and slab loads (Beaumont, 1981; DeCelles and Giles, 1996; Flemings and Jordan, 1989; Roure, 2008; Sinclair, 1997a) should be considered when discussing lateral variations in foreland plate flexure.

During the Oligocene to early Miocene, only the internal foreland deposits at the thrust front were accreted at the base of the Alpine wedge to form the Subalpine Molasse (Ortner et al., 2015; Ortner et al., 2023b). Further north of the present-day thrust front, Oligocene to early Miocene compressional structures are not observed. This implies that the transmission of compressive stresses was minimal and, therefore, a decoupling between the Alpine wedge and the European foreland along the German Molasse. However, despite still flexurally subsiding (Ortner et al., 2015), normal faults close to the thrust front south of Munich were inverted during the middle Miocene (Shipilin et al., 2020) and syn-flexural normal faults along the entire German

Molasse were sealed (Figures 3.5, 3.6 and 3.7, Mraz et al., 2018; von Hartmann et al., 2016). This suggests enhanced effectivity in transmitting compressional stresses from the Alpine wedge into the German Molasse Basin, preventing continued extensional normal faulting around the forebulge from the middle Miocene onward. As Willingshofer and Sokoutis (2009) suggested, this may have resulted from a temporal change from decoupling to coupling between the orogenic wedge (Central and Eastern Alps) and the European foreland.

Oligocene to early Miocene southward backthrusting against the Periadriatic Fault, folding of the Alpine wedge, and duplexing of European middle to lower crust (exhumation of Lepontine Dome and Engadine Window, Hurford, 1986; Rosenberg and Kissling, 2013; Schmid et al., 1996) led to over 2 km of Oligocene topography in the Central Alps (Frisch et al., 2001; Kuhlemann, 2007). In contrast, topography in the Eastern Alps remained low until early Miocene folding and exhumation due to Adriatic indentation (Tauern Window exhumation, Favaro et al., 2015; Kuhlemann, 2007; Scharf et al., 2013; Schmid et al., 2013). As a result, the Oligocene to early Miocene wedge was thicker and, therefore, likely heavier in the Central Alps compared to the Eastern Alps. As a result, the topographic load exerted by the Central Alps was likely higher than that exerted by the Eastern Alps. Therefore, if the topographic loads were the primary control on the deflection of the European plate, the magnitude of the European plate deflection during the Oligocene to early Miocene of the Western German Molasse should have been higher compared to that beneath the Eastern German Molasse. However, this contradicts the eastward increase in flexure of the European plate as recorded by both the eastward increase in syn-flexural offsets along normal faults (Subsection 5.2) and the stratigraphic architecture of the Molasse Basin (Eskens et al., 2024; Kuhlemann and Kempf, 2002; Lemcke, 1988; Schlunegger and Kissling, 2022; Sissingh, 1997). Therefore, this suggests that the topographic loading is not the primary mechanism controlling the along-strike variation in the Oligocene to early Miocene cumulative offsets of syn-flexural normal faults. This decoupling between topographic loads and foreland flexure has been observed by

previous authors as well (Schlunegger and Kissling, 2015). Furthermore, this has been observed in other foreland basins, e.g., the Maturin Basin–Serrania thrust wedge (Jácome et al., 2003) and Carpathian (Maţenco et al., 1997) orogen-foreland systems.

Estimating the potential role of slab loading on the flexure variations along the Molasse Basin during the Oligocene to early Miocene times is challenging. Current thermochronological, sedimentological, and geological datasets are used to suggest multiple hypotheses regarding the Alpine slab dynamics, including (multiple) slab break-offs at 35, 20, and 2 Ma (Fox et al., 2016; Handy et al., 2010; Handy et al., 2015; Schmid et al., 2004a; Schmid et al., 1996), lateral slab tearing (Meulenkamp et al., 1996; Schlunegger and Kissling, 2022), and a subduction polarity reversal during the early Miocene (Eizenhöfer et al., 2023; Handy et al., 2015). Recent numerical modelling studies that focused on compressional settings show that processes leading to lateral variations in slab pull (such as episodic slab break-off events and/or slab tearing) subsequently lead to orogen-parallel variations in loading and, thereby, along-strike variations in foreland basin subsidence (Andrić-Tomašević et al., 2023; Maiti et al., in revision). In this scenario, the still attached part of the slab may provide a substantial load and thereby induce higher plate flexure than the part of the foreland basin beneath which the slab has been detached. However, evaluating the contribution of each of these aforementioned mechanisms on the European plate deflection and subsequent syn-flexural normal fault evolution in the Molasse Basin requires further investigation.

3.6 Conclusions

Here, we analysed the spatiotemporal growth of seismic scale syn-flexural normal faults by comparing T-x and T-z profiles of various faults in two different seismic volumes along-strike the German Molasse. Furthermore, we also used normal fault activity to calculate the Oligocene continent-ward propagation of the orogen-forebulge system. The main conclusions of our study are as follows;

1. The observed fault network records deformation associated with both reactivation of Mesozoic faults and newly nucleated Cenozoic syn-flexural normal faults. Deformation was dominated by orogen-parallel E-W striking faults, dipping both N and S. Few of these faults are connected with shorter NW-SE striking relay faults.
2. The nucleation of syn-flexural normal faults at the onset of flexure occurs close to or at the surface around the forebulge. This is because the magnitude of extensional deformation is maximum along the hinge line at the surface of the forebulge, promoting the nucleation of new faults.
3. In case pre-existing faults were located at greater depth in the pre-flexural basement, they were not reactivated in the German Molasse. Instead, they may characterise a lower segment of a dip-linked fault.
4. The lateral fault growth of newly nucleated normal faults in the German Molasse followed either the isolated or hybrid fault growth model. In contrast, reactivated faults followed the constant-length growth model.
5. During lateral fault growth, fault tips of syn-flexural faults in the German Molasse migrated stratigraphically upward as fault planes grew laterally.
6. Spatiotemporal variations in the nucleation of normal fault activity in foreland basins can be used to calculate the migration rate of the orogen-forebulge system. Consistent with results from other independent methods, we find that the Alpine orogen-forebulge system migrated northward with an average velocity of 7.8 mm/yr during the Oligocene.
7. The eastward increase in the cumulative offsets of the syn-flexural normal faults correlates with the lateral decrease- and increase in strength of the European lithosphere and crust, respectively. This implies that lithospheric strength exerts a first-order control on foreland flexure. However, the contribution of along-strike variations in slab loads cannot be excluded.
8. The Oligocene to early Miocene orogen-parallel variations in topographic loading were not the primary mechanism controlling the distribution of flexure in the German Molasse.

9. As suggested before by Willingshofer and Sokoutis (2009), we find that coupling between the Alps and the European plate increased during the early to middle Miocene, resulting in enhanced efficiency in compressional stress transfer into the German Molasse and, thereby, cessation of extensional normal faulting.
10. An eastward decrease in the strength of the European lithosphere contributed to the Oligocene to early Miocene increase in magnitude of deflection of the European plate to the east. Additionally, the Landshut-Neuoetting High and the Bohemian Massif (Andeweg and Cloetingh, 1998b) may have acted as buttresses in front of the approaching Alpine orogen, further enhancing the narrowing- and deepening of the flexural profile to the east due to downward squeezing. This is reflected in higher syn-flexural offsets along the normal faults in a narrower band in the Eastern German Molasse compared to the Western German Molasse.

Chapter 4
Thickening of a stationary orogen and its effect on foreland basin architecture

This chapter is based on:

Lucas H.J. Eskens, Giridas Maiti, Nevena Nevena Andrić-Tomašević "Thickening of a stationary orogen and its effect on foreland basin architecture", in review in Terra Nova, TER-2024-0100.

4.1 Introduction

Pro-foreland basins, from hereon referred to as foreland basins, form adjacent to growing mountain ranges due to the flexural bending of the downgoing plate (Beaumont, 1981; DeCelles and Giles, 1996; Roure, 2008). The foreland basin system consists of four discrete depozones: the wedge-top, foredeep, forebulge and back-bulge (Figure 4.1, DeCelles and Giles, 1996). Most of the syn-orogenic deposits are preserved in the foredeep (DeCelles, 2012; DeCelles and Giles, 1996). The forebulge is a flexural upwarp that marks the cratonward limit of the foredeep (Figure 4.1, DeCelles, 2012). The magnitude of the (sub)surface loads (Beaumont, 1981; DeCelles and Giles, 1996; Flemings and Jordan, 1989; Sinclair, 1997a) and flexural strength of the lower plate (Royden, 1993b; Waschbusch and Royden, 1992) primarily determine the flexural profile of a foreland basin.

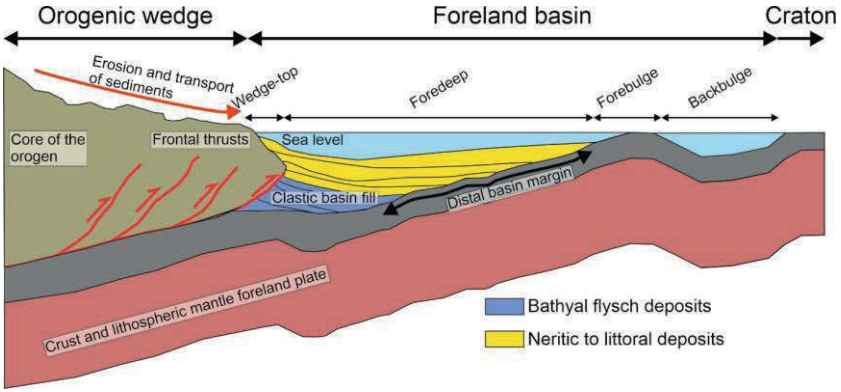

Figure 4.1: Schematic representation of the general architecture of a foreland basin. The different geological elements are not to scale. Modified after (DeCelles and Giles, 1996).

The forebulge migrates cratonward as the mountain range encroaches the lower plate (Figure 4.1, Chang et al., 2012; DeCelles, 2012; Sabbatino et al., 2021), either continuously or episodically (Filer, 2003; Waschbusch and

Royden, 1992). The migration of the forebulge generates a diachronous unconformity (Crampton and Allen, 1995) that traces its spatiotemporal location (Crampton and Allen, 1995). Apart from cratonward migration, orogenward migration of the forebulge (i.e., the forebulge migrating towards the orogen concurrent with basin deepening- and narrowing) has been recognized in various foreland basins (Northern Alpine, Colville, and Appalachian foreland basins, Coakley and Watts, 1991; Kuhlemann and Kempf, 2002; Ver Straeten and Brett, 2000). This process has been attributed to 1) visco-elastic relaxation of the lower plate (Quinlan and Beaumont, 1984; Zweigel et al., 1998), 2) onset of frontal thrusting (in-sequence thrusting) after a period of quiescence (Flemings and Jordan, 1990; Quinlan and Beaumont, 1984), or 3) thickening of the mountain range concurrent with cratonward propagation (Naylor and Sinclair, 2008; Sinclair et al., 1991).

The Northern Alpine Foreland Basin (NAFB, Figure 4.2a) is the foreland basin that developed north of the Alps during the convergence between the European- and Adriatic plates (Lemcke, 1988; Schmid et al., 1996). During the Aquitanian-Burdigalian transition, the eastern NAFB (east of Munich, Figure 4.2a) narrowed by 80 km whilst the proximal foredeep continued to subside (Figure 4.2c, Eskens et al., 2024; Kuhlemann and Kempf, 2002; Lemcke, 1988; Zweigel et al., 1998). Previous authors attributed these observations to visco-elastic relaxation of the European plate (Hülscher et al., 2019; Zweigel et al., 1998). However, lithospheric relaxation is a process that may take tens of millions of years to express itself on a crustal scale and, thereby, the synorogenic basin fill (Beaumont, 1981; Burov, 2011; Coakley and Watts, 1991; Thatcher and Pollitz, 2008). Furthermore, Eastern Alpine thrusting changed from in-sequence to out-of-sequence during the Aquitanian-Burdigalian transition (Covault et al., 2009; Hinsch, 2013; Ortner et al., 2015). Therefore, the other two mechanisms mentioned earlier, i.e. the (reinstalment of) in-sequence thrusting concurrent with thickening of the orogenic wedge, cannot explain the orogenward migration of the forebulge in this case either. Therefore, alternative explanations need to be considered.

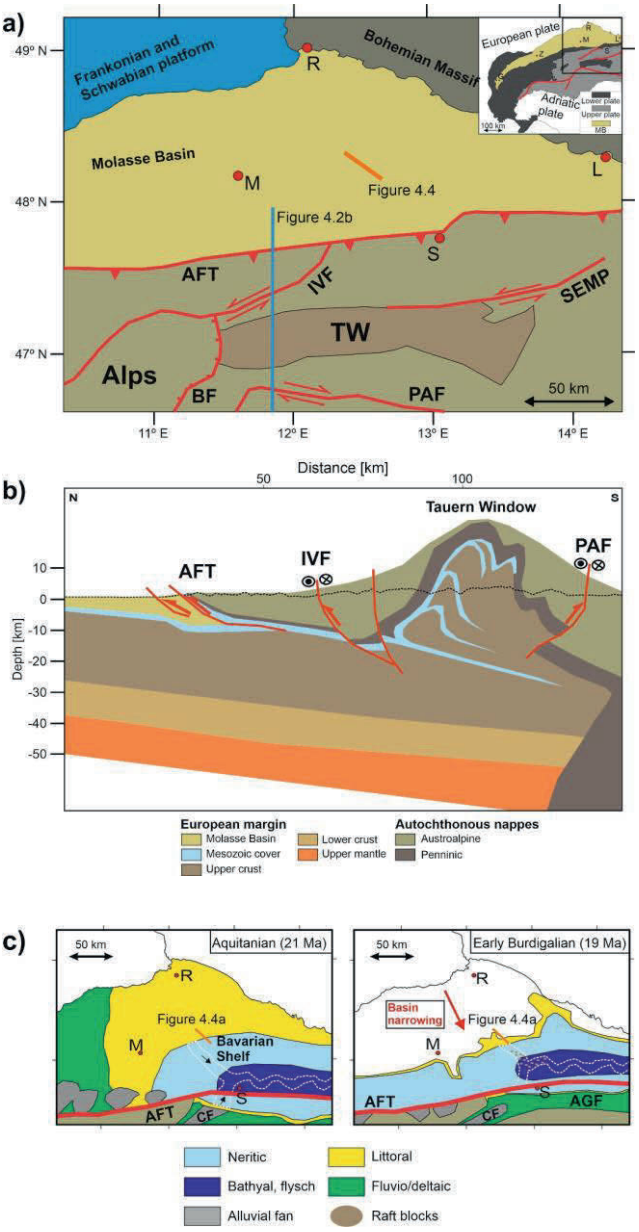
a)
49° N
48° N
47° N
11° E
12° E
13° E
14° E
Frankonian and Schwabian platform
Bohemian Massif
Molasse Basin
R
M
L
S
Figure 4.4
Figure 4.2b
AFT
IVF
SEMP
TW
Alps
BF
PAF
50 km
European plate
Adriatic plate
b)
Distance [km]
50
100
N
S
Tauern Window
AFT
IVF
PAF
Depth [km]
10
0
-10
-20
-30
-40
-50
European margin
Molasse Basin
Mesozoic cover
Upper crust
Lower crust
Upper mantle
Autochthonous nappes
Austroalpine
Penninic
c)
50 km
Aquitanian (21 Ma)
Figure 4.4a
Bavarian Shelf
AFT
CF
Early Burdigalian (19 Ma)
Basin narrowing
AGF
Neritic
Littoral
Bathyal, flysch
Fluvio/deltaic
Alluvial fan
Raft blocks

Figure 4.2 (previous page): **a)** Present-day geological map of the Molasse Basin and Alps. The orange line is the location of the NW-SE striking seismic line shown in Figure 4.4. **G =** Geneva, **M =** Munich, **P =** Passau, **R =** Regensburg **S =** Salzburg **Z =** Zürich, **AFT** = Alpine Frontal Thrust, **BF** = Brenner Fault, **IVF** = Inntal Valley Fault, **IF** = Inntall Fann, **MB** = Molasse Basin, **PAF** = Periadriatic Fault, **SEMP** = Salzach-Ennstal-Mariazell-Puchberg Fault. **b)** North-south cross section through the proximal Molasse Basin and Eastern Alps north of the PAF, highlighting the duplexing and folding of the European basement in the Tauern Window. The black dashed line shows the present-day topography, with the transparent units above having been eroded. Modified from Schmid et al. (2004), their Figure 3d. **c)** Paleogeographic reconstructions of the Aquitanian and early Burdigalian Molasse Basin. White dashed lines delineate the meandering Puchkirchen channel belt in the Austrian Molasse, with the black arrows indicating the flow direction. From the Aquitanian to the early Burdigalian, the forebulge migrated thrustward. **AGF** = Augenstein Formation, **IF** = Inn Fann. Modified from (Eskens et al., 2024).

Onset of out-of-sequence thrusting was coeval with rapid exhumation of Tauern Window (through duplexing and folding, Favaro et al., 2015; Fügenschuh et al., 1997; Scharf et al., 2013; Schmid et al., 2013). This leads us to hypothesise that enhanced topographic loading exerted by the core of the stationary orogen (Figure 4.1) forced the orogenward migration of the forebulge in the eastern NAFB. To test this, we interpret reflection seismic data north of the Tauern Window (Figures 4.2a and 4.2c for location) to constrain changes in basin architecture coeval with the Aquitanian to Burdigalian thickening of the stationary Eastern Alps. Quantitative flexural modelling of a stationary increasing topographic load is used to verify the validity of our hypothesis.

4.2 Geological background

Because we focus on the changes in basin architecture during the Aquitanian-Burdigalian transition, we do not give an in-depth description of the entire evolution of the Alps-NAFB system. For a complete synopsis, the reader is referred to other contributions (Eskens et al., 2024; Handy et al., 2010; Kuhlemann and Kempf, 2002; Lemcke, 1988; Schmid et al., 1996).

4.2.1 Eastern Alpine orogenic wedge

The Eastern Alps are a stack of Adria- and Europe-derived nappes that document the closure of the Alpine Tethys (Penninic and Valais domains) that separated the European and Adriatic plates (e.g., Handy et al., 2010; Schmid et al., 1996; Trümpy, 1960). By the late Eocene, the Alpine Tethys had subducted (Schmid et al., 1996; Ziegler et al., 1996) and the Eastern Alps overthrust the Helvetic margin (Burkhard, 1988; Pfiffner, 1993; Schmid et al., 1996). The Eastern Alpine thrust front propagated northward (i.e., in-sequence thrusting) up until the Aquitanian (Covault et al., 2009; Hinsch, 2013; Ortner et al., 2015; Zerlauth et al., 2014). During this time, wedge-top deposition of the terrestrial Augenstein Formation evidences that topography remained low (Figure 4.2c, Frisch et al., 2001; Kuhlemann and Kempf, 2002).

By the Aquitanian-Burdigalian transition, out-of-sequence thrusting started (Covault et al., 2009; Hinsch, 2013; Hurford et al., 1989; Ortner et al., 2015; Von Hagke et al., 2014). Continued indentation by the Adriatic plate was accommodated by folding and duplexing in the Tauern Window from 20 Ma, leading to rapid exhumation (up to 4 mm/yr, Favaro et al., 2015; Fügenschuh et al., 1997; Scharf et al., 2013; von Blanckenburg et al., 1989). Additionally, convergence was accommodated by orogen-scale strike-slip faulting, resulting in eastward extrusion of the Eastern Alps (Ratschbacher et al., 1991a; Ratschbacher et al., 1991b). This led to the development of intramontane basins from 18 Ma onward (e.g., Wagrain Basin and Ennstal depression, Dunkl et al., 2005; Neubauer, 2016).

4.2.2 Eastern Northern Alpine Foreland Basin

During the early Oligocene, the NAFB developed as an underfilled flysch basin (Sissingh, 1997; Wagner, 1998). From the late Oligocene to early Miocene, the Western NAFB (west of Munich, Figure 4.2c) was characterised by terrestrial deposition (Kuhlemann and Kempf, 2002; Lemcke, 1988), deepening towards

the neritic Bavarian Shelf and bathyal Eastern NAFB (Jin et al., 1995; Sissingh, 1997; Wagner, 1998).

During the Aquitanian, sediments derived from the western NAFB were transported across the Bavarian Shelf (Figure 4.2c, Jin et al., 1995; Zweigel et al., 1998) into the deep marine channel belt to the east (Figure 4.2c, De Ruig and Hubbard, 2006; Masalimova et al., 2015; Wagner, 1998). Additionally, sediments derived from the Central Alps were transported to the Eastern NAFB via the Inn Fan (De Ruig and Hubbard, 2006; Figure 4.2c, Frisch et al., 2001; Kuhlemann et al., 2006).

By the early Burdigalian (ca. 19 Ma), the eastern NAFB narrowed by 80 km and its northern margin was uplifted (Figure 4.2c, Kuhlemann and Kempf, 2002; Lemcke, 1988) while the proximal foredeep continued to subside (Genser et al., 2007; Zweigel et al., 1998). Coevally, up to 500 m wide raft blocks were deposited in the submarine channel belt downslope the Bavarian Shelf (Figure 4.2c, Hubbard et al., 2009). This change in basin architecture was contemporaneous with a 50 m eustatic sea level fall (Haq et al., 1987), the onset of out-of-sequence Eastern Alpine thrusting (Covault et al., 2009; Hinsch, 2013; Ortner et al., 2015), and folding- and duplexing of the Tauern Window (from 20 Ma onward, Favaro et al., 2015; Fügenschuh et al., 1997; Scharf et al., 2013; Schmid et al., 2013). At the same time, sediment supply from the Eastern Alps decreased, followed by an increase at 18 Ma (Kuhlemann, 2000). By the middle Burdigalian, deposition again reached as far north as the Aquitanian northern basin margin (Kuhlemann and Kempf, 2002), roughly coinciding with the present-day location of the forebulge (Andeweg and Cloetingh, 1998a).

4.3 Data and Methods

4.3.1 Seismic data

The seismic data presented in this study is a 2D PreSTM (pre-stack time migrated) line east of Munich (Figures 4.2a and 4.2c) extracted from seismic data volume B presented in Eskens et al. (2024). The structural smoothing seismic attribute was applied to improve the signal-to-noise ratio. Subsequently, a time-to-depth conversion was applied (See Appendix 1.1 for details) to obtain real instead of apparent geometries. On the depth-converted seismic data, six reflectors were picked, which are from top to bottom: the top Hall Fm., the Base Hall Unconformity (BHU, sensu De Ruig and Hubbard, 2006; Hülscher et al., 2019), the top Chattian Sands, the top Mesozoic, the top Turonian and the base Mesozoic (Figure 4.3). The upper 5 horizons are constrained by well data, while the base Mesozoic is interpreted based on a downward change in seismic facies corresponding with a high positive amplitude reflector (Figure 4.3).

4.3.2 Flexural modelling

The lower continental plate is generally treated as a linear elastic solid in flexural modelling on short timescales (<20-30 Myr; Sinclair et al., 1991). For a static load on a linear elastic plate, the geometry of deflection remains unchanged through time. In contrast, on a viscoelastic plate the geometry of deflection narrows and deepens with time (Quinlan and Beaumont, 1984). Previous studies have applied both types of lower plates to flexural modelling of foreland basins (Quinlan and Beaumont, 1984; Sinclair et al., 1991; Naylor and Sinclair, 2008). In this work, we consider a linear elastic plate model because we focus on short timescales during which basin architecture changes occur (2 Myrs, Figure 4.1c).

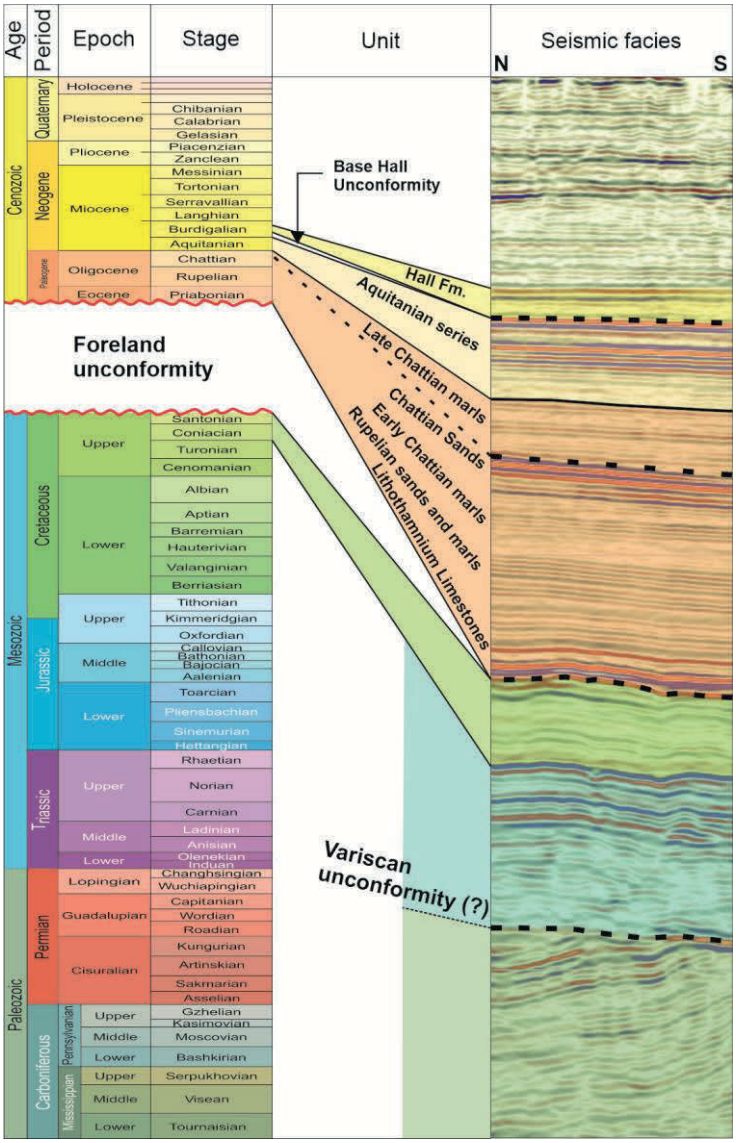

Figure 4.3: Seismic-stratigraphic chart of the interpreted data. Ages of the pre-Turonian Mesozoic and Paleozoic stratigraphy are not constrained. Ages and units overlying the foreland unconformity are as defined by previous studies in the same study area (Jin et al., 1995; Zweigel et al., 1998).

To model the effect of internal thickening of a stationary orogen, we use a a semi-numerical solution to model the foreland flexure for different magnitudes of topographic loading (Allen and Allen, 2013, see Appendix 1.2; Wangen, 2010). In our model-, we only increase the topographic load in the center of the mountain range while keeping the orogenic front stationary. We first model the flexural profile of NAFB with an initial mountain range topography of 500 m (model M500) to represent the Aquitanian "hilly" Eastern Alpine paleo topography (i.e., before basin narrowing, Frisch et al., 1998). In the second stage, we increase the topographic height to 1500 m (model M1500), representing the paleoaltitude in the eastern Eastern Alps at the start of the Burdigalian (estimated to have been 900 to 1800 m, Jiménez-Moreno et al., 2008). Finally, we increase the topographic height to 3000 m (model M3000), which is the suggested Burdigalian peak elevation following the exhumation of Tauren Window (Kuhlemann, 2007). Based on previously estimated data for the Alps-Molasse Basin system, we take a flexural rigidity for the lower plate to reflect that of the European plate 1×10^{23} Nm (Andeweg and Cloetingh, 1998a; Gutscher, 1995). We take standard values for densities of the mantle (3300 kg m^{-3}) crust (2750 kg m^{-3}) used in previous studies (Andeweg and Cloetingh, 1998a; Gutscher, 1995; Maiti et al., 2024).

4.4 Results

4.4.1 Seismic interpretations

This contribution focuses on the changes in basin architecture in the eastern NAFB during the early Miocene Aquitanian to Burdigalian transition (ca. 21 to 19 Ma). Therefore, the pre-Aquitanian stratigraphy is not presented nor discussed in detail. For this, the reader is referred to Eskens et al. (2024).

The Aquitanian seismic-stratigraphy consists of high-amplitude parallel reflectors with good continuity (Figure 4.4a). In the SE of the seismic line, Aquitanian reflectors terminate against the BHU (Figure 4.4b). We interpret this

unconformable relationship to present an erosional truncation resulting from incision. Overlying early Burdigalian seismic-stratigraphy is characterised by medium to low amplitude reflectors with a good continuity (Figure 4.4a). In the SE of the seismic line, early Burdigalian reflectors onlap towards the NW onto the BHU (Figure 4.4b). This implies that during the Aquitanian-Burdigalian transition, deposition was initially restricted to the basin axis, reaching progressively further north.

4.4.2 Flexural modelling results

To model how foreland basin architecture changes with increasing hinterland topography, we first assume an initial topography of 500 m across the entire orogen (model M500, Figure 4.5a), and increasing this to 1500 m (model M1500, Figure 4.5b) and 3000 m (model M3000, Figure 4.5c). For model M500, the resulting flexural profile shows a 180 km wide, 1.25 km deep foredeep bounded by a 80 m high forebulge (Figure 4.5a). Subsequently the hinterland topography is increased to 1500 m whilst the structural front remains stationary in model 1500M (Figure 4.5b). This results in 15 km of orogenward propagation- and 115 m of uplift of the crest of the flexural forebulge (Figure 4.5b). Furthermore, the foredeep depth increases by 1.4 km to 2.65 km (Figure 4.5b). Finally, when hinterland topography is increased from 1500 to 3000 m in model 3000M, another 10 km of orogenward migration of the forebulge concurrent with an additional 98 m uplift of the forebulge crest is observed (Figure 4.5c). Moreover, the foredeep deepens by 0.85 km to a final depth of 3.5 km (Figure 4.5c). Lastly, the models reveal a progressive steepening of the distal basin margin (Figure 4.1) as the topographic load of the stationary mountain range increases (Figure 4.5).

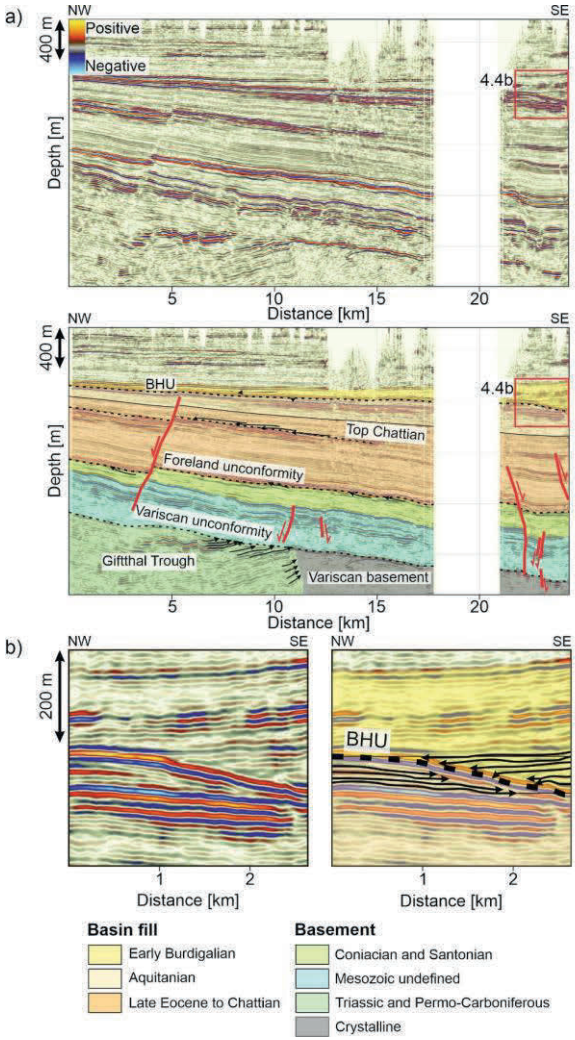

Figure 4.4: a) The Upper panel shows an uninterpreted NW-SE seismic line across the Bavarian Shelf, and the lower panel shows an interpreted version of the same seismic line. Red lines indicate normal faults and their respective kinematics, black dashed lines indicate unconformities. **b)** Uninterpreted and interpreted part of the NW-SE seismic line. Below BHU, the arrows mark Aquitanian reflector terminations due to incision; above BHU, the black arrows mark subsequent early Burdigalian onlapping.

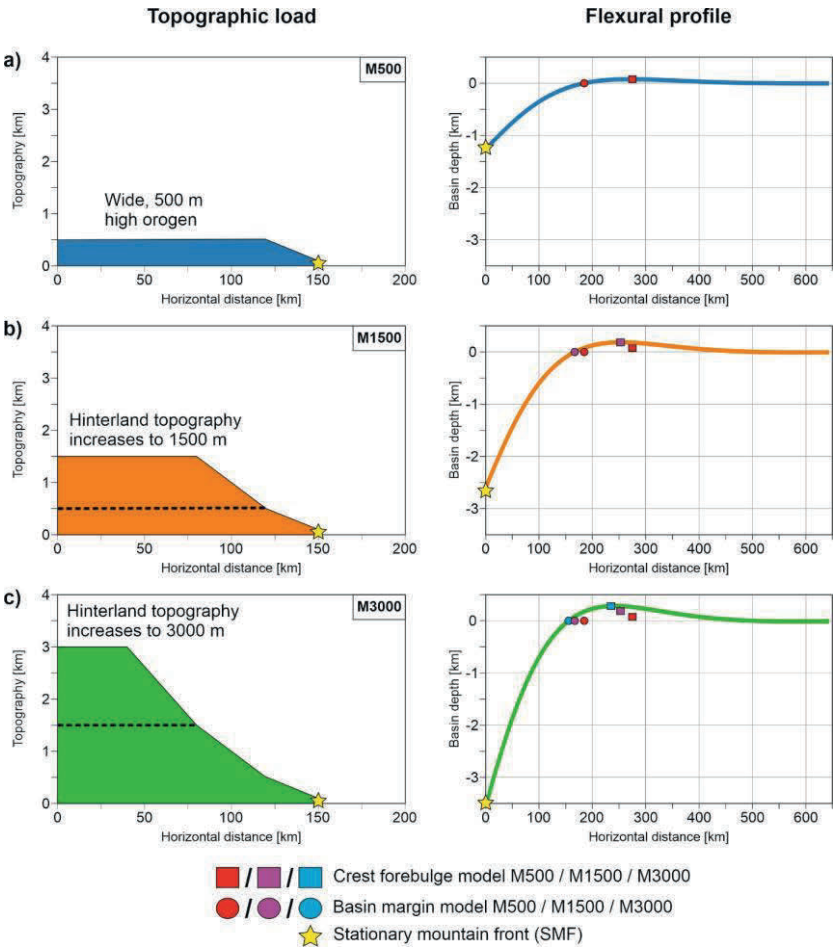

Figure 4.5: Three different scenarios of topographic load distribution in the orogen and respective flexural profile for models **a)** M500, **b)** M1500, and **c)** M3000. For the topographic loads, the coloured area above the dashed line represents the added topographic load from model M500 to model M1500 and from model M1500 to model M3000 in figures b and c, respectively.

4.5 Discussion

Seismic-reflection data north of the Tauern Window (Figures 4.2a and 4.4) evidenced erosion through incision of Aquitanian deposits concurrent basin narrowing. This is in agreement with findings from previous studies (Kuhlemann and Kempf, 2002; Zweigel et al., 1998). We interpret basin narrowing to have resulted from coeval folding- and duplexing of the Tauern Window (Favaro et al., 2015; Fügenschuh et al., 1997; Scharf et al., 2013; Schmid et al., 2013), resulting in enhanced topographic loading exerted by the core of the stationary Eastern Alps. Subsequently, this forced orogenward migration of the forebulge (Figure 4.6b). The resultant narrowing of the flexural profile due to orogenward migration of the forebulge also fits with subsidence of the proximal foredeep (Figure 4.6b, Genser et al., 2007; Zweigel et al., 1998). This interpreted cause-effect relationship was also observed in our 2D flexural models (Figure 4.5).

The orogenward forebulge migration- and subsidence of the foredeep at 20 Ma has been interpreted to have resulted from visco-elastic relaxation of the European plate (Hülscher et al., 2019; Zweigel et al., 1998). The coeval decrease in sediment supply derived from the Eastern Alps (Kuhlemann, 2000) is attributed to visco-elastic relaxation having caused a decrease in Alpine topography (Hülscher et al., 2019; Zweigel et al., 1998). However, visco-elastic relaxation occurs during tectonic quiescence (Flemings and Jordan, 1990; Quinlan and Beaumont, 1984). This does not fit with either post-Aquitanian out-of-sequeuence thrusting (Covault et al., 2009; Hinsch, 2013; Hurford et al., 1989; Ortner et al., 2015; Von Hagke et al., 2014) nor the contemporaneous compression in the Eastern Alps leading to early Miocene folding, duplexing- and exhumation of the Tauern Window (Favaro et al., 2015; Fügenschuh et al., 1997; Scharf et al., 2013; Schmid et al., 2013). Moreover, visco-elastic relaxation may take tens of millions of years to express itself on crustal-scale after cessation of convergence and in foreland basin fill (Beaumont, 1981; Burov, 2011; Coakley and Watts, 1991; Thatcher and Pollitz, 2008). Therefore, we do not favour this interpretation.

Previous authors have emphasised the importance of early Miocene strike-slip faulting for the establishment of a drainage network in the Eastern Alps, as well as further enhancing erosion (Bartosch et al., 2017). However, orogen-scale strike-slip faulting only commenced at 18 Ma, as documented by the formation of intramontane pull-apart basins (Dunkl et al., 2005; Neubauer, 2016). Therefore, we suggest that the time lag between rapid exhumation of the Tauern Window at 20 Ma (Favaro et al., 2015; Fügenschuh et al., 1997; Scharf et al., 2013; Schmid et al., 2013) and increased sediment supply at 18 Ma (Kuhlemann, 2000) was caused by the lack of a well-developed drainage network up until strike-slip faulting commenced. Additionally, and not mutually exclusive, erosion of the sedimentary cover of the Tauern window led to the exposure of the more erosion-resistant European upper crust (Figure 4.2b), which may have contributed to the lag time between tectonics- and the increased sediment supply (Tucker and Slingerland, 1996). Such a delay in the tectonic signal due to variations in erodibility of the source area has also been suggested for the Western NAFB and Swiss Alps (Schlunegger and Castelltort, 2016).

We interpret the incision of Aquitanian deposits (Figure 4.4b) to have resulted from oversteepening of the distal basin margin due to orogenward migration of the forebulge (Figure 4.6b), as observed in our flexural models (Figure 4.5). Additionally, the 50 m eustatic sea level fall during the Aquitanian-Burdigalian transition (Haq et al., 1987) may have contributed to the incision by exposing formerly drowned areas. Deposition of raft blocks in the Puchkirchen channel belt downslope the Bavarian Shelf (Figure 4.2c, Borzi et al., 2022; Hubbard et al., 2009) suggests that these remobilised sediments were transported towards the basin axis (Figure 4.6b). The size of these raft blocks (up to 500 m wide, Borzi et al., 2022) implies that the steepening of the distal margin led to collapse rather than gradual erosion. Subsequent deposition of sedimentary material from the Eastern Alps led to early Burdigalian deposits onlapping onto this collapse unconformity (Figures 4.4b, 4.6c and 4.6d).

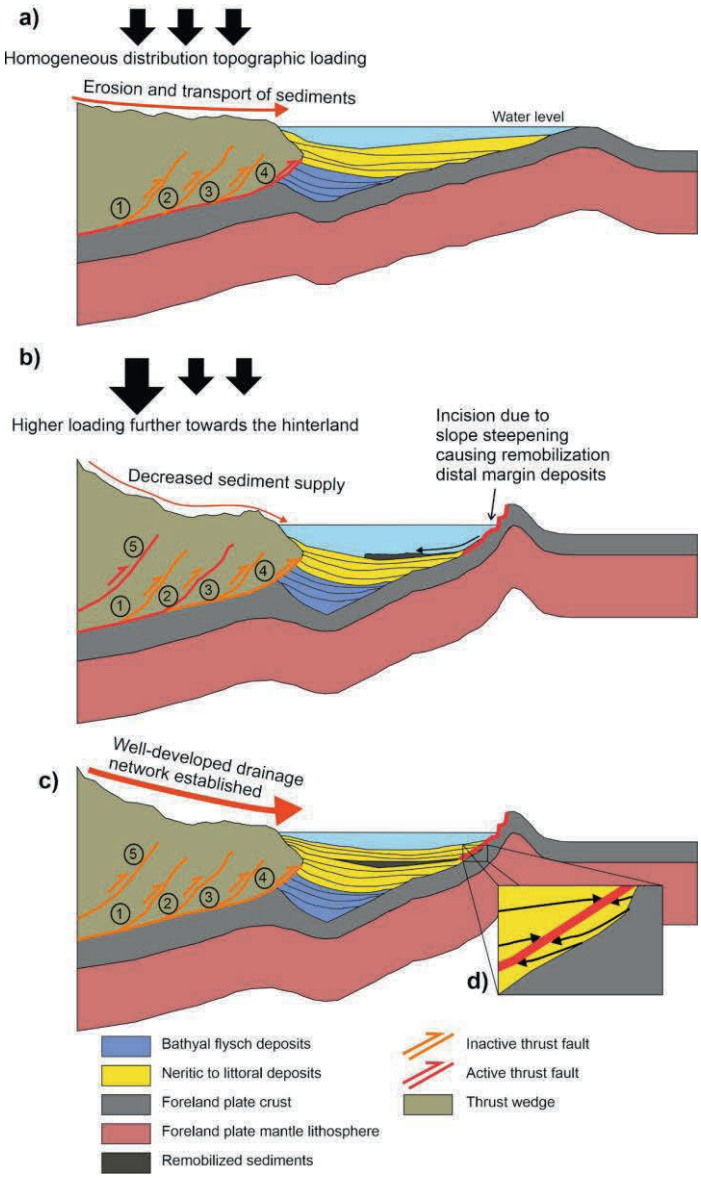
a)
Homogeneous distribution topographic loading
Erosion and transport of sediments
Water level
1
2
3
4
b)
Higher loading further towards the hinterland
Incision due to slope steepening causing remobilization distal margin deposits
Decreased sediment supply
5
c)
Well-developed drainage network established
d)
Bathyal flysch deposits
Neritic to littoral deposits
Foreland plate crust
Foreland plate mantle lithosphere
Remobilized sediments
Inactive thrust fault
Active thrust fault
Thrust wedge

Figure 4.6 (previous page): Schematic model explaining the influence of internal wedge thickening of a stationary orogen on the architecture of a foreland basin. The numbers show the sequence of thrusting in the orogenic wedge. **a)** Ongoing in-sequence has resulted in formation of a foreland basin where basin fill onlaps onto the distal basin margin. **b)** Onset of internal wedge thickening whilst the orogenic front remains stationary leads to uplift of the hinterland topography. This results in the point of maximum loading shifting back into the core of the orogenic wedge, due to which the flexural forebulge migrates thrustward and the amplitude of deflection of the foredeep- and forebulge increase. Due to the increase in amplitude, the basinward slope oversteepens, resulting in incision and remobilisation of the sediments formerly deposited on the distal basin margin. Erosional products of this incision and remobilisation are deposited in the axis of the foredeep. The lack of a drainage network for the new topographic configuration causes an initial decrease in sediment supply. **c)** As a drainage network is established, sediment supply increases. During subsequent deposition, the distal unconformity generated by the orogenward migration of the forebulge is onlapped by younger stratigraphy. **d)** Zoom in showing the angular unconformity generated due to erosion of the shelf (sediments) and the expected reflector terminations. This is similar to what is observed in the seismic line presented in Figure 4.4b.

By the middle Burdigalian, the basin width was again similar to that prior to the orogenward migration of the forebulge (Eskens et al., 2024; Kuhlemann and Kempf, 2002). Furthermore, this northern pinch-out coincides with the present-day location of the forebulge (Andeweg and Cloetingh, 1998a). This implies that the magnitude of the European plate's flexure diminished, which may only have been forced by a decrease in loading in the case of a stationary orogen. It is possible that the combination of eastward crustal extrusion (Ratschbacher et al., 1991a) and erosion led to the decrease in Eastern Alpine elevation during the Burdigalian (Kuhlemann, 2007), and thereby topographic loading. Alternatively, the debated slab breakoff below the Eastern Alps around 20 Ma (Eizenhöfer et al., 2023; Handy et al., 2015; Schlunegger and Kissling, 2022) may have been the perpetrator. However, evaluating the contribution of each of these processes to the architecture of the NAFB is out of the scope of this contribution and requires further investigation.

4.6 Conclusions

During the Aquitanian-Burdigalian transition, the thickening of the stationary Eastern Alpine wedge (i.e., duplexing and folding of the Tauern Window) led to increased topographic loading in the internal hinterland. This forced the orogenward migration and uplift of the forebulge. The seismic data presented in this study show that this process was associated with the collapse of the distal basin margin and redeposition of the eroded material further downslope. Our interpretations are supported by simple flexural models in which we assessed the difference in flexural profiles for various topographic loads of a stationary thrust wedge. To summarize, we propose that a switch from continentward propagation to internal thickening of a thrust wedge while remaining at a fixed position is a possible mechanism to cause a narrowing- and deepening of a foreland basin. However, this will yield short-lived changes in basin architecture and will quickly be overshadowed by other processes controlling foreland flexure.

Chapter 5
The tectonostratigraphic expression of slab breakoff in foreland basins: insights from 2D forward stratigraphic modelling

This chapter is based on:

L.H.J. Eskens, A. Piccolo, M. Thielmann, B. Claussmann, M. Lejri, T.A. Ehlers, N. Andrić-Tomašević, et al. "The tectonostratigraphic expression of slab breakoff in foreland basins: insights from 2D forward stratigraphic modelling", in review in Tectonics, 2024TC008664.

5.1 Introduction

Peripheral pro-foreland basins (from here on referred to as foreland basins) develop adjacent to growing mountain ranges due to topographic- and slab loading causing flexural bending of the downgoing foreland plate (Beaumont, 1981; Catuneanu, 2004a; DeCelles, 2012; DeCelles and Giles, 1996; Flemings and Jordan, 1989; Jordan, 1981; Naylor and Sinclair, 2008). The sedimentary fill records the basin evolution in both time and space resulting from the interplay between tectonic, climate and eustacy forcings (Flemings and Jordan, 1990; Jordan and Flemings, 1991; Sinclair et al., 1991; Van der Meulen et al., 1998).

A major architectural change observed in many foreland basins (e.g., Northern Alpine Foreland Basin, Taiwan, Apenninnic and Alborz foreland basins; Covey, 1986; Kuhlemann and Kempf, 2002b; Meulenkamp et al., 1996; Wilmsen et al., 2009) is the transition from under- to overfilled deposition. Underfilled deposition implies that the rate of accommodation space generation outpaces sediment supply, overfilled deposition the opposite (Carroll and Bohacs, 1999). During this transition, condensed fine-grained deep marine deposition will (rapidly) grade stratigraphically upward into non-condensed, coarse-grained shelf- and littoral sedimentation. Thus, this transition represents a rapid decrease in relative sea level.

As foreland basin development is strongly coupled to that of the adjacent mountain range (e.g., DeCelles, 2012), this shift in basin architecture hints at changes in the orogenic process(es) that control the generation of accommodation space and/or sediment supply. Increases in sediment supply from the adjacent orogenic wedge (Northern Alpine Foreland Basin, Hülscher et al., 2019; Kuhlemann and Kempf, 2002b), slab tearing- and breakoff (Northern Alpine Foreland Basin, Alborz and Appenninic foreland basins, Ascione et al., 2012; Meulenkamp et al., 1996; Schlunegger and Castelltort, 2016; Schlunegger and Kissling, 2022; Sinclair, 1997a; Van der Meulen et al., 1998; Wilmsen et al., 2009), and/or eustacy (Northern Alpine Foreland Basin, Diem,

1986; Flemings and Jordan, 1990 numerical studies, ; Jordan and Flemings, 1991; Lemcke, 1988) can drive this transition in natural examples of foreland basins. In this contribution, we investigate whether slab breakoff can indeed induce the underfill to overfill transition as well as to define its tectonostratigraphic fingerprint preserved in the basin fill.

Slab breakoff (also called slab detachment) is the process during which the lower part of a subducting slab separates from its upper segment and subsequently sinks into the mantle (Isacks and Molnar, 1969; Wortel and Spakman, 2000). Previous geodynamical studies have shown that the predominant deformation mechanism during slab breakoff is viscous thinning of the subducting plate (e.g., Baumann et al., 2010; Burov and Yamato, 2008; Duretz et al., 2012). This process occurs at greater depths and requires more time with increased subducting plate age, convergence rates, or mantle viscosity (e.g., Baumann et al., 2010; Duretz et al., 2011; Gerya et al., 2004; van Hunen and Allen, 2011). The resultant loss of the vertical slab pull force induces an isostatically-driven uplift of the mountain range with rates of up to 19.4 km/Myr (Buiter et al., 2002; Duretz et al., 2011; Gerya et al., 2004) and between 0.1 to 2.65 km/Myr for the adjacent foreland basin (Andrews and Billen, 2009; Duretz et al., 2011).

Slab breakoff leads to the uplift of the foreland basin and adjacent mountain range (Duretz et al., 2011; Gerya et al., 2004; van Hunen and Allen, 2011). If the foreland basin is connected to the global oceans, the uplift of the basin floor will result in a decrease of the relative sea level. Additionally, the uplift of the adjacent mountain range will sustain steeper slopes, enabling channel incision and consequent collapse of hillslopes (Whipple, 2009). Moreover, a high density of earthquakes due to slab breakoff can increase the frequency of hillslope failure (e.g., in the present-day Hindu-Kush or the Vrancea region in Romania, Kufner et al., 2017; Kufner et al., 2021; Sperner et al., 2001). Furthermore, surface uplift associated with breakoff (or other processes) can increase orographic precipitation on windward slopes and will favour higher erosion rates (Ehlers and Poulsen, 2009). The combination of these effects will result in increased erosion rates and sediment transport (Croissant et al.,

2019; Montgomery and Brandon, 2002; Ouchi, 2011), leading to increased sediment supply in the adjacent foreland basin. Taken together, these processes induced by slab breakoff may induce a transition from underfilled- to overfilled conditions in the foreland basin.

This study investigates the tectonostratigraphic signal from slab breakoff in a foreland basin. To this end, we employ a coupling between 2D geodynamical models (GMs) of slab breakoff with 2D stratigraphic forward models (SFMs) for an orogen-foreland system. This allows us to isolate slab breakoff as a forcing mechanism from other external and/or intrinsic forcing processes. We test the effects of different slab breakoff scenarios by varying the 1) initial subduction angle and 2) mantle viscosity in the GMs. The potential impact of third-order eustatic cycles (50 m amplitude, 1 My period) is also tested to understand better whether sea level variations can mask the tectonostratigraphic signal from slab breakoff. Although our models are not aimed at reproducing a particular foreland basin, we compare our results with the Austrian Molasse Basin (eastern part of the Northern Alpine Foreland Basin) to discuss the potential preservation of the tectonostratigraphic signal of slab breakoff for this natural example.

5.2 Material and methods

To quantitatively evaluate the tectonostratigraphic signal induced by slab breakoff in a foreland basin, we use a one-way coupling approach between GMs simulating slab breakoff constructed in *LaMEM* (Kaus et al., 2016; Piccolo et al., 2022) with SFMs using the *GPM* Geological Process Modeling software in Petrel from SLB (Tetzlaff and Harbaugh, 1989). In the following subsections, we introduce *LaMEM* (Subsection 5.2.1.1) and *GPM* (Subsection 5.2.1.2) models. Subsequently, we outline the general modeling workflow employed during this study (Subsection 5.2.2). Lastly, we give a description of the setups used to simulate different slab breakoff scenarios in *LaMEM* (Subsection 5.2.3.1) and the corresponding SFMs in *GPM* software (Subsection 5.2.3.2).

5.2.1 LaMEM

LaMEM is a staggered finite difference code, solving a coupled system of the momentum, mass, and energy conservation equations (Stokes equations) in a Cartesian grid employing the *Boussinesq* approximation (Boussinesq, 1897; Kaus et al., 2016; Piccolo et al., 2022). The material properties for each lithotype are advected using markers that additionally carry historical values such as temperature, total plastic deformation, and stress tensor components. The markers are advected after each timestep, and the stored information is interpolated into the computational grid. For an in-depth description of the equations solved in *LaMEM*, we invite the reader to Subsection A1.4.1.

5.2.2 Geological Process Modeling

GPM Geological Process Modelling software, developed by SLB, is a simulator for stratigraphic and sedimentary processes (Tetzlaff and Harbaugh, 1989) and is integrated with the Petrel E&P software platform. *GPM* allows modelling of the erosion, transport, and deposition of clastic sediments and the in-situ growth of carbonates (independently or concurrently) in different geological settings. This can be done in either 2D or 3D. The erosion, transport, and deposition can be simulated either as solely being diffusional or, additionally, flow-driven. We assume sediment erosion, transport, and deposition on an orogen-foreland basin scale to be driven exclusively by diffusion, in line with similar studies (Flemings and Jordan, 1990; Jordan and Flemings, 1991; Sinclair et al., 1991).

Sediment diffusion is the dispersion of erosional material on the topographic slope driven by gravity, meaning that a steep slope will smoothen over time (Figure 5.1). The resulting redistribution of mass and the resulting change in topography can be described with eq. (1);

$$\frac{\partial h}{\partial t} = D\frac{\partial^2 h}{\partial x^2} \tag{5.1}$$

Here, h the topographic variation in a cell in the model in m, t the time increment between different model increments in years, x the width of a cell in m, and D the diffusivity in m^2/yr.

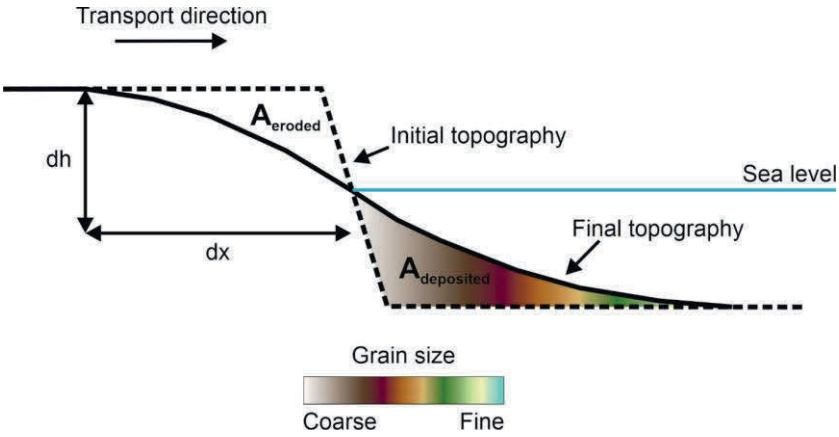

Figure 5.1: Schematic representation of diffusion in GPM of multiple sediment types. A_{eroded} is the area of the initial topography that is eroded after time increment dt, and is equal to the area $A_{deposited}$ downslope.

In *GPM*, the integration of variations in transportability and erodibility of different rock types as well as the dependency of diffusion on topography (i.e., climate and higher average slope steepness at higher elevation) is achieved by multiplying D_c by unitless coefficients representing these dependencies. This leads to a new rate of diffusion (also in m^2/yr) which is calculated using eq. (5.2) in case the basement is being eroded;

$$D = D_c * T_S * C(z) * E_b \quad (5.2)$$

In case formerly deposited sediments are eroded, eq. (5.2) becomes eq. (5.3);

$$D = D_c * T_S * C(z) * E_s \quad (5.3)$$

D_c is a prescribed diffusion coefficient and is a unitless multiplier. T_s is the transportability factor, which depends on sediment type, and is also a unitless multiplier. *C(z)* is curve describing the dependency of the diffusivity on the topography *w.r.t.* sea level at each timestep. E_s and E_b are the erodibility coefficients for the sediment type and basement topography, respectively, and are unitless multipliers. A value for E_s is calculated depending on the volumetric contribution of each sediment type in the mixture.

The Active Layer Thickness (ALT) defines the maximum amount of topography that can be eroded during each time step. Furthermore, the elastic compaction of sediments due to overburden is calculated based on the initial porosity and a compaction coefficient of the respective (mix of) sediment type(s). Conceptually, the compaction coefficient reflects the Youngs's modulus, but applied to long-term compaction due to overburden. Lastly, tectonics in *GPM* can only be modelled for vertical motion. This means that the effects of horizontal tectonics, like overthrusting, cannot be accounted for.

5.2.3 Model Coupling

In this contribution, a one-way coupling between the GMs constructed in *LaMEM* with the SFMs in *GPM* is used to investigate the tectonostratigraphic development of a foreland basin during slab breakoff. We extract uplift- and subsidence profiles of the free surface in response to slab breakoff in different geodynamic settings (Subsection 5.2.3.1). These are used as tectonic input in *GPM*, whereby the changes in surface processes and resulting foreland basin architecture are modelled. The main outputs of the *GPM* models are sediment thickness maps, which allow for calculating the sediment supply rates in the basin through time. Information from Wheeler diagrams for the (average) grain size distribution and depositional water depth was combined (Table 5.1) to generate depositional facies models. Lastly, the porosity and pressure distribution were used to construct synthetic seismic profiles (Subsection A1.4.2).

5.2.4 Experimental setups

5.2.4.1 Geodynamic models for different slab breakoff scenarios

The GM setup represents a simplified post-collisional stage of an orogen evolution in which an oceanic slab is still attached to the lower plate (Figure 5.2). The domain spans from -1000 to 1000 km in the horizontal direction and from -1000 to 50 km in the vertical direction (Figure 5.2). The numerical grid on which the model is resolved is made of 2049 and 1025 nodes in the horizontal- and vertical directions, respectively. There is no post-collisional convergence. Therefore, slab necking- and subsequent breakoff are caused by the negative buoyancy force (i.e., slab pull) of an isothermal (800 °C) slab in an isothermal (1350 °C) mantle (Figure 5.2). The slab has a thickness of $\mathrm{D}_0 = 80\ \mathrm{km}$ and length of $\mathrm{L}_\mathrm{r} = 300\ \mathrm{km}$ (Figure 5.2). We use an isothermal slab because it is easier to control the magnitude of the negative buoyancy force acting on the system, especially when changing the subduction angle. The continental lithosphere on either side of the model consists of 15 km of upper crust, 15 km of lower crust and 70 km of lithospheric mantle (Figure 5.2). It is more buoyant than the oceanic slab and the underlying upper mantle. The geotherm of the continental lithosphere is described by a half-space cooling model with an age of 100 My. A sequence of passive margin sediments overlies the continental lithosphere on the side of the lower plate (Figure 5.2). The orogenic wedge is represented as a triangular shape made of sediments, extending 200 km from the subduction trench at 0 km (Figure 5.2). The rheological properties of the different model domains can be found in Table A4.1. The starting surface elevation is the same for all modelled subduction scenarios (Figure 5.2), serving as the initial basement topography for the SFMs.

Table 5.1: Depositional facies classification in the forward stratigraphic models based on the simulation results. Any combination of depositional water depths and sediment type distributions not covered by the listed conditions is labelled as "marine".

Facies / Conditions	Littoral	Slope/Shelf	Basin axis	Coarse-grained deep water turbidites
D (Depositional water depth) [m]	< 100	100 < D < 500	> 500	> 500
Coarse grain sand content [%]	> 40	> 45	< 5	> 40
Fine sand content [%]	> 20	> 20	< 50	> 20
Silt content [%]	< 20	< 20	> 5	< 20
Clay content [%]	< 20	< 15	> 5	< 20

In the GMs, we change 1) the initial subduction angle (Figure 5.2) and 2) the dislocation creep activation volume of the mantle (now referred to as activation volume). The former will control the magnitude of the downward-directed slab pull on the overlying surface (Capitanio et al., 2007; Forsyth and Uyeda, 1975; Stefanick and Jurdy, 1992), thereby providing direct feedback on the magnitude of isostatic rebound resulting from slab breakoff. The latter describes the dependence of the mantle viscosity on pressure (e.g., Poirier and Liebermann, 1984), based on which the upward buoyancy force and mantle traction counteracting the downward slab pull force may vary. Therefore, changing the activation volume directly influences the duration of slab necking and, thereby, the nature of isostatic rebound resulting from subsequent breakoff (Bercovici et al., 2015).

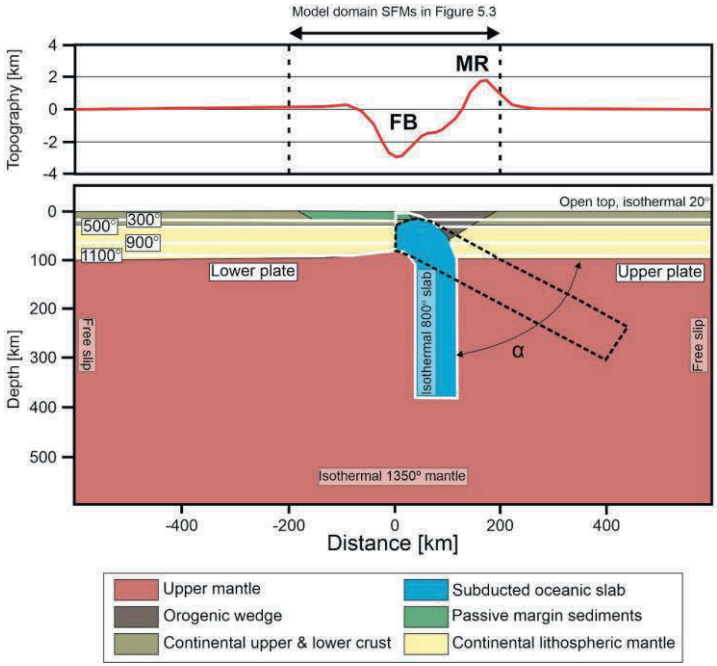

Figure 5.2: Schematic representation of initial conditions in the geodynamic model used for this study. The upper panel shows the surface topography at the start of the model run, which is the same at the start of each model run. The model domain of the SFMs is highlighted. The lower panel shows the lithospheric structure. There is no flux at the lateral model boundaries. Angle **α** is 30°, 45°, 60°, or 90°. **FB** = foreland basin, **MR** = mountain range.

5.2.4.2 Stratigraphic forward models for different slab breakoff scenarios

Figure 5.3 shows the starting model configuration for the SFMs. Because we focus on the foreland basin, we take the central portion of our GMs as the model domain for our SFMs (Figure 5.2). This results in a 400 km wide model domain (Figure 5.3) divided into 200 cells, each 2 km wide. In the SFMs, the sea level remains constant as the basin floor experiences either subsidence or uplift. This means the presented models reflect the evolution of a foreland basin connected to the global seas rather than an isolated basin.

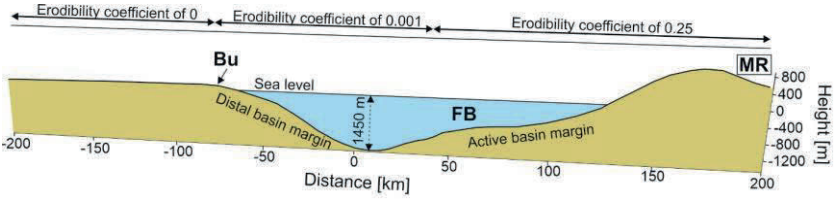

Figure 5.3: Schematic representation of initial conditions in stratigraphic forward models constructed in this study. The basement consists of 25% coarse sand, fine sand, silt, and clay. **FB** = foreland basin, **MR** = mountain range, **Bu** = forebulge.

We refer to the slope of the foreland basin close to the mountain range as the active basin margin and the basinward side of the forebulge as the distal basin margin (Figure 5.3). The foreland basin is drowned up until the crest of the forebulge (Figure 5.3). The basement comprises 25% of 4 different sediment types: coarse sand, fine sand, silt, and clay (Figure 5.3 and Table A4.2). In *GPM*, we turn on the sediment diffusion, compaction, and tectonic processes, using the parameters specified in Table 5.2 and Figure 5.3. The diffusion coefficient used for calculating the diffusion rate (eq. 5.1) is based on a 2D cross-section of the Northern Alpine Foreland Basin (NAFB) from Lemcke (1988). Here, ~400 km^2 of syn-flexural sediments were deposited between 35 and 18 Ma. This results in an average diffusion coefficient of 22 m^2/yr (Table 5.2). The values for the diffusion curve (Figure 5.4a) are adjusted so that the sediment diffusion rates in either continental- or marine environments match with those presented in literature (Nagel et al., 2018, their Table 6).

The ALT used in this study (0.4 m/yr, Table 5.2) is higher than observed erosion rates in nature (as high as 0.1 m/yr, Burbank, 2002; Herman et al., 2013; Montgomery and Brandon, 2002). However, we chose this value to account for the absence of a volumetric sediment source in our 2D models. This allowed us to obtain sedimentation rates in the synthetic foreland within the range observed in natural examples (0.015 to 2.15 mm/yr, Ballato et al., 2008; Burbank et al., 1988; DeCelles and Horton, 2003; Parra et al., 2010).

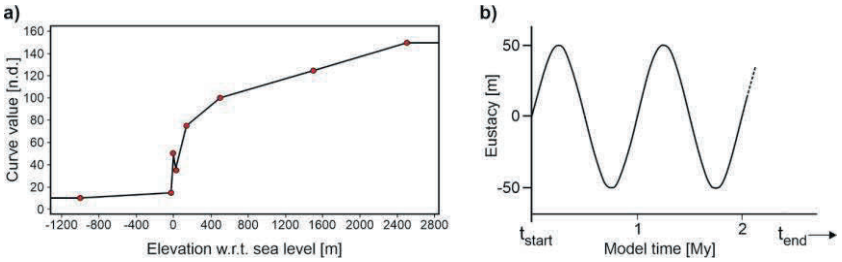

Figure 5.4: a) Diffusion curve used in this study. **b)** Eustacy for models 90DF-E and 90DS-E with an amplitude of 50 m and a period of 1 My.

In models 90DF, 90DS, 60DF, 60DS, 45DF, 45DS, 30DF, and 30DS, all surface parameters (Table 5.2) are kept constant whilst the initial angle of subduction and mantle activation volume are altered (Table 5.3). In models 90DF-E and 90DS-E (Table 5.3), we introduce 50-meter sea level changes with a period of 1 Myr (Figure 5.4b) to models 90DF and 90DS. This allows us to analyse whether third-order eustacy can mask the tectonostratigraphic signal from slab breakoff. Lastly, we conducted a sensitivity test for which the erodibility coefficient is set to 0.25 for all surface domains in the SFM (model 90DF-S, Table 5.3).

Table 5.2: Model parameters used in this study. In all models the sediment type characteristics (Table A4.2) and diffusion curve (Figure 5.4a) are kept constant.

Parameter	Value	Unit
Width of model domain	400	Km
Cell width	2	Km
Method time increment	1	year
Base erodibility backbulge / forebulge / mountain range	0 / 0.001 / 0.25	n.d.
Active Layer Thickness [ALT]	0.4	m
Diffusion coefficient	22	m^2/yr
Contribution basement composition coarse sand / fine sand / silt / clay	25 / 25 / 25 / 25	%

Table 5.3: List of simulations and controlling parameters presented in this study. In model 90DF-S we tested the effect of homogenizing the erodibility coefficient across the entire model domain.

Model name	Initial subduction angle [°]	Mantle dislocation activation volume [µm3 * mol^{-1}]	Eustacy
90DF (reference)	90	8	No
60DF	60	8	No
45DF	45	8	No
30DF	30	8	No
90DS	90	12	No
60DS	60	12	No
45DS	45	12	No
30DS	30	12	No
90DF-E	90	8	Yes
90DS-E	90	12	Yes
90DF-S	90	8	No

5.3 Results

5.3.1 Reference model 90DF

During the reference model evolution (90DF, subduction angle 90° and activation volume 8 $\frac{\mu m^3}{mol}$, Table 5.1) we distinguish between four stages in the simulation; continental collision, slab necking, slab breakoff, and post breakoff (Figure 5.5). During the first stage, *i.e.* the first 0.81 Myr, the subducted oceanic slab hangs below the suture zone and controls the system by conducting a slab pull force to the surface (Figure 5.5a1). This leads to flexural subsidence of the lower plate with a rate of 3.2 km/Myr (Figure 5.5a3), generating accommodation space in the foreland at a rate of $0.25 \cdot 10^{12}$ m^3/Myr (Figure 5.6d). Coevally, the adjacent mountain range is uplifted by 0.41 km/Myr (Figure 5.5a2) during which the sediment supply decreases from $4 \cdot 10^{10}$ to $3.7 \cdot 10^{10}$ m^3/Myr (Figure 5.6d). Sediments derived from the orogen are deposited in an underfilled, deep-water environment with an aggradational depositional trend in the basin while both basin margins were characterized by

sediment bypass (Figures 5.5a3 and 5.6a to 5.6c). In the synthetic seismic profile, these deposits are characterized by low-amplitude parallel reflectors (Figures 5.6f and 5.6g).

During the slab necking stage, thinning of the slab occurs at a depth of 120 km between 0.81 to 2.55 Myr of the model evolution (Figure 5.5b1 and 5.5c1) and is divided into an early and late phase. During early necking (until 2.43 Myr, Figure 5.5b1), foreland subsidence and mountain range uplift slow down (0.46 km/Myr and 0.34 km/Myr, Figure 5.5b2 and 5.5b3). Therefore, the generation of accommodation space and sediment supply also decreases ($0.1 \cdot 10^{12}$ m^3/Myr, $3.46 \cdot 10^{10}$ m^3/Myr, Figures 5.6d and 5.6e). As a result, the sediments do not record a change in basin architecture (Figures 5.6a to 5.6c) and the seismic facies remain unchanged (Figure 5.6d). However, slab thinning accelerates during the late necking phase (2.43 and 2.55 Myr Figure 5.5c1). This results in uplift of both the mountain range and the foreland with rates of 2.75 km/Myr and 3.17 km/Myr respectively (Figures 5.5c2 and 5.5c3), leading to an increase in sediment supply of $2.6 \cdot 10^{10}$ m^3/Myr (Figure 5.6d) and accommodation space reducing at a rate of $1.6 \cdot 10^{12}$ m^3/Myr (Figure 5.6e). The accommodation space reduction rate is two orders of magnitude higher than the increase in sediment supply. Furthermore, active margin uplift results in a retrogradation of coarse-grained deposition to the basin margin, resulting in a switch from sediment bypass to storage (Figure 5.5c3). This retrogradation represents a short phase of sediment starvation and is followed by the coastline migrating basinward (Figure 5.5c3).

During the slab breakoff stage, the oceanic slab detaches at a depth of 140 km after 2.58 Myr of model evolution (Figure 5.5d1). Consequently, short-lived (0.03 Myr, Figure 5.5d1) uplift of the foreland basin and mountain range (25 and 30 km/Myr, Figures 5.5d2 and 5.5d3) occurs. The former forces a reduction in accommodation space at a rate of up to $3.7 \cdot 10^{12}$ m^3/Myr (Figures 5.6a and 5.6e), the latter sediment supply increasing from $5.35 \cdot 10^{10}$ m^3/Myr to a peak of $7.5 \cdot 10^{10}$ m^3/Myr 0.1 Myr after slab breakoff (Figure 5.6d). From this moment onward, coarse-grained shallow water facies prograde over fine-grained facies on the active basin margin (Figures 5.6b and 5.6c). This marks

the basin shallowing and transition from an underfilled to overfilled stage, leading to an overall coarsening upward grading trend (Figure 5.6b), recorded on the active margin 0.7 Myr after breakoff (Figure 5.6c). In the synthetic seismic profile, this transition is recognised as a high amplitude reflector on the active margin defining the top of the syn-necking deposits (Figure 5.6f). The amplitude of this reflector decreases towards the basin axis (Figure 5.6f).

After breakoff, slab sinking (Figure 5.5e1) correlates with mountain range- and foreland basin surface uplift at rates of 0.32 km/Myr and 0.44 km/Myr, respectively (Figures 5.5e2 and 5.5e3). However, despite the mountain range uplift, the sediment supply decreases (Figure 5.6d). Furthermore, this foreland basin uplift causes the accommodation space to decrease at rates which are 2 to 3 orders of magnitude slower compared to previous evolutionary stages (as low as $2.85 \cdot 10^9$ m^3/Myr, Figure 5.6e). Consequently, shallow water facies belts prograde into the basin axis and towards the distal margin at a constant rate of 17.4 km/Myr (Figures 5.3 and 5.6c). In the synthetic seismic profile this is recorded by low amplitude clinoforms (Figures 5.6f and 5.6g).

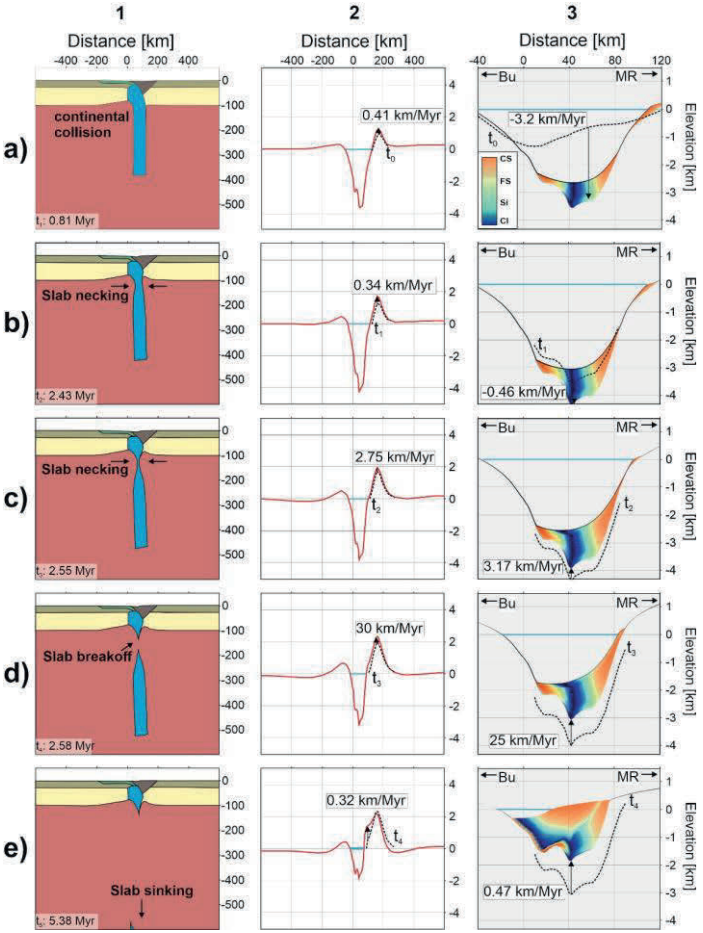

Figure 5.5: Evolution of model 90DF. Column 1 shows the geodynamic evolution, column 2 the free surface topographic profiles of the geodynamic models, and column 3 the corresponding SFM evolution. The solid blue lines in the SFM indicates up until which level the basin is filled with water. The geodynamical models have the same colour bar used in Figure 5.1. **a)** Vertical subduction of the oceanic slab during continental collision (0.81 Myr); **b)** initial phase of slab necking at a depth of 120 km coeval with subsidence of the foreland basin due to slab pull (2.43 Myr); **c)** Last phase of slab necking causing isostatic rebound of foreland basin and mountain range (2.55 Myr); **d)** slab breakoff at 120 km (2.58 Myr); **e)** Slab sinking- and avalanching (5.38 Myr). **CS** = coarse sand, **FS** = fine sand**, Si =** silt, **Cl =** clay; see Table 5.3 for the sediment type characteristics. **MR** = mountain range, **Bu** = forebulge.

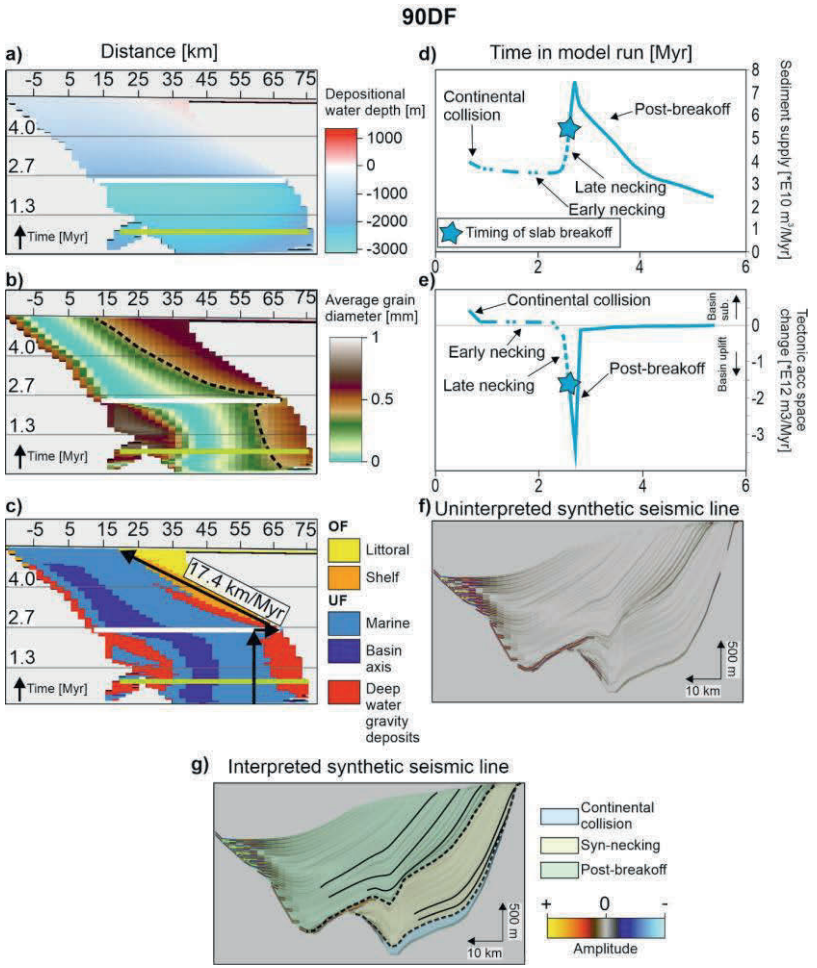

Figure 5.6: Reference model 90DF results. Green horizontal lines in Wheeler diagrams indicate the onset of slab necking, white horizontal lines the timing of slab breakoff. **a)** Wheeler diagram of the depositional water depth. **b)** Wheeler diagram of the average grain size distribution. The black dashed line traces the coarse-grained sediment front. **c)** Wheeler diagram of the depositional environments. **d)** Sediment supply over time. **e)** The magnitude of tectonically created or destroyed accommodation space in the foreland basin. **f)** Uninterpreted synthetic seismic section from model 90DF. **g)** Interpreted synthetic seismic profile from model 90DF. OF = overfilled conditions, UF = underfilled conditions.

5.3.2 Effect of changing the subduction angle

In addition to the reference experiment, three models were created to test the influence of different subduction angles (60°, 45°, and 30°) while keeping mantle viscosity constant (models 60DF, 45DF, and 30DF, Table 5.3, Figures A4.4 to A4.6). In contrast to the vertical slab in the reference model, non-vertical slabs steepen while attached to the lower plate (Figures A4.4a1 to A4.6a1). The slab with the shallowest initial subduction angle experiences the highest magnitude of steepening (28° for model 30DF, Figure A4.6a1), whereas it decreases for greater initial subduction angles to 11° (60DF, Figure A4.4a1). Likewise, lower initial subduction angles correlate with successively lower subsidence rates in the foreland basin in different models (3.2, 1.55, 1.42, and 1.16 km/Myr in the models 90DF, 60DF, 45DF, and 30DF, Figures 5.5a3, A4.4a3, A4.5a3, and A4.6a3). In the case of higher initial subduction angles, the mountain range experiences uplift at a higher rate (0.41 and 0.24 km/Myr for models 90DF and 60DF, Figures 5.5a2 and A4.4a1). In contrast, the mountain ranges subside at higher rates for lower initial subduction angles (0.18 and 1.33 km/Myr for models 45DF and 30DF, Figures A4.5b2 and 4.6b2). In model 30DF, subsidence leads to submergence of the mountain range (Figure A4.6a2). Despite these differences, all models record the deposition of deep-water facies with an aggradational depositional trend in the basin axes (Figures A4.4a3 to A4.6a3). Grain size partitioning is recognised as low amplitude parallel reflectors in models with an initial subduction angle ≥ 45° (Figures 5.5a3, 5.7d and A4.4a3 and A4.5a3). In contrast, in model 30DF, all grain sizes are mixed in a small depocenter (Figure A4.6a3), resulting in high amplitude parallel reflectors (Figure 5.7d).

During early slab necking, thinning of the slab occurs at progressively greater depths for shallower initial subduction angles (Figures A4.4b1 to A4.6b1). Similarly, mountain range uplift rates are lower in the experiments as the initial subduction angle decreases (0.2, 0.17, and 0.07 km/Myr for models 60DF, 45DF, and 30DF, Figures A4.4b2 to A4.6b2). Moreover, sediment supply

generally decreases ($2.6 \cdot 10^{10}$ and $1.44 \cdot 10^{10}$ m^3/Myr for 90DF and 60DF, Figure 5.8a), with model 45DF and 30DF recording an increase instead ($0.37 \cdot 10^{10}$ and $0.1 \cdot 10^{10}$ m^3/Myr, Figure 5.8a).

In model 30DF, sediments are trapped in the depression next to the foreland (resembling a wedge-top basin, Figure A4.6b2). Whereas the endmember models with the highest and lowest initial subduction angles (90DF and 30DF) record foreland basin subsidence (0.46 and 0.22 km/Myr, Figures 5.5b2 and A4.6b2), the intermediate cases record asymmetric uplift with decreasing rates for lower initial subduction angles instead (only the active margin is uplifted with 0.23 and 0.2 km/Myr for models 60DF and 45DF, Figures A4.4b3 and A4.5b3). The latter results in a progradation of coarse-grained facies in a deep-water environment and related coarsening upward for models 60DF and 45DF (Figures 5.7b and 5.7c). This is expressed as a high amplitude reflector at the top of the continental collision deposits in the synthetic seismic profile (Figure 5.7d).

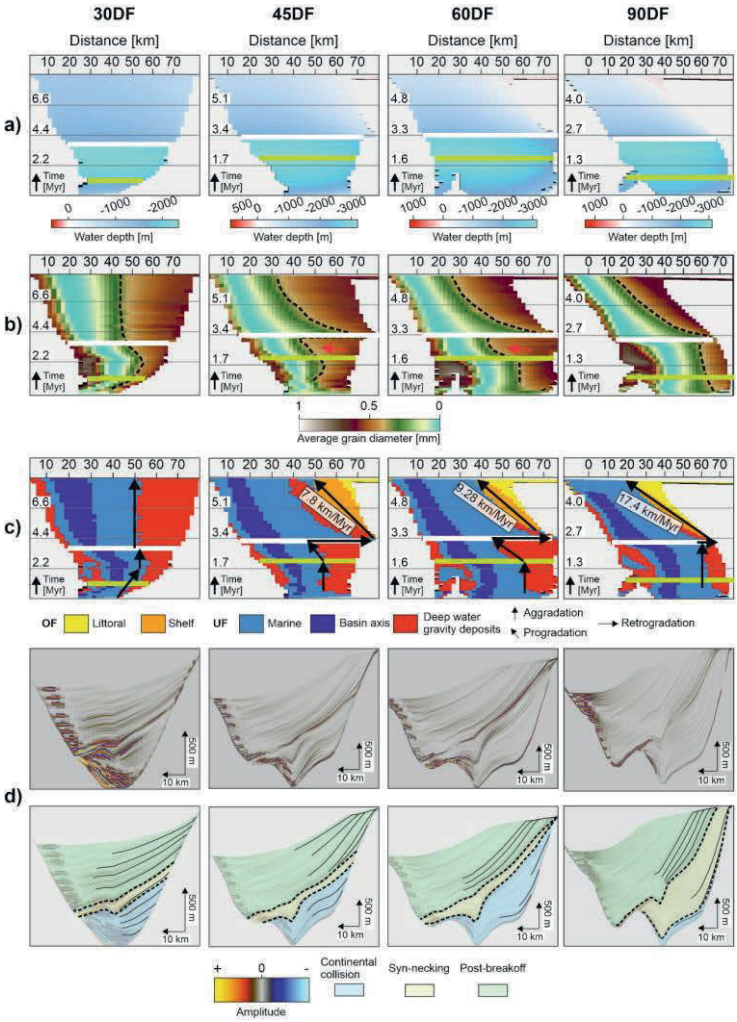
30DF
45DF
60DF
90DF
Distance [km]
a)
b)
c)
d)
Time [Myr]
Water depth [m]
Average grain diameter [mm]
7.8 km/Myr
9.28 km/Myr
17.4 km/Myr
OF Littoral Shelf
UF Marine Basin axis
Deep water gravity deposits
Aggradation
Progradation
Retrogradation
500 m
10 km
Amplitude
Continental collision
Syn-necking
Post-breakoff

Figure 5.7 (previous page): Models results from models 30DF, 45DF, 60DF, and 90DF. Green lines in Wheeler diagrams indicate the onset of slab necking, the white line the timing of accelerated slab necking- and breakoff. **a)** Wheeler diagrams for the depositional water depth. **b)** Wheeler diagrams for the average grain size distribution. The black dashed line the coarse-grained sediment front (i.e., average grain size diameter ≥ 0.4 mm). The red arrows for models 60DF and 45DF highlight progradation of deposition over an intrabasinal bump observed in Figures A4.4a3 and S2a3. A note to the reader is that this should not be mistaken for a tectonostratigraphic signal from slab necking. **c)** Wheeler diagrams for depositional facies. The basinward migration rate of overfilled facies is indicated by the black arrow. **d)** Synthetic seismics for experiments. The black dashed line in the interpreted version traces the reflectors that separates pre- and post-breakoff units.

Like in the reference model, the uplift of the mountain range and foreland occurs during the final stage of necking- and breakoff (Figures A4.4c1 to A4.6c1). Uplift of the mountain range results in enhanced sediment supply (Figure 5.8a). Furthermore, these phases are also characterized by retrogradation (representing a short phase of starvation) and subsequent progradation and related coarsening-upward on the active basin margin in models 90DF, 60DF, and 45DF (Figures 5.7b and 5.7c). On the contrary, in model 30DF, this results in a progradational depositional trend (Figures 5.7b and 5.7c). In either case, this event is marked by a basin-wide high amplitude reflector at the top of the syn-necking deposits (Figure 5.7d). In the endmember models with the highest- and lowest initial subduction angles (90DF and 30DF), the basin records one overall coarsening-upward trend (Figure 5.7b). On the other hand, the intermediate initial subduction angle models (60DF and 45DF) record two coarsening-upward trends following early necking and the slab breakoff stages (Figure 5.7b). The lag time between the transition from the underfilled- to overfilled stage on the active margin and slab breakoff was 0.7, 1.3, and 2 Myr in models 90DF, 60DF, and 45DF (Figure 5.7c). In model 30DF, this transition does not occur (Figure 5.7c).

Slow continued uplift of both the mountain range and foreland basin during slab sinking (Figures 5.5e and A4.4e to A4.6e) do not induce rapid changes in basin architecture (Figure 5.7). Instead, shallow water facies continue to prograde into the basin axis and towards the distal margin at decreasing rates for

initial lower subduction angles (17.4, 9.28, and 7.8 km/Myr for models 90DF, 60DF, and 45DF, Figure 5.7c). This is recognised in the synthetic seismic profiles as clinoforms prograding basinward (Figure 5.7d).

5.3.3 Effect of changing the activation volume

Increasing mantle viscosity, achieved by raising the activation volume from 8 $\frac{\mu m^3}{mol}$ to 12 $\frac{\mu m^3}{mol}$ for each simulation (models 90DS, 60DS, 45DS, and 30 DS, Table 5.3), results in a lower magnitude of slab steepening during continental collision for non-vertical slabs (15 to 3°, Figures A4.7a1 to A4.10a1). Additionally, mountain range uplift/subsidence rates (0.21, 0.07, 0.05, and -0.15 for models 90DS, 60DS, 45DS, and 30DS, Figures A4.7a2 to A4.10a2) and foreland basin subsidence rates (1.06, 0.65, 0.6, and 0.27 km/Myr for models 90DS, 60DS, 45DS, and 30DS, Figures A4.7a3 to A4.10a3) are lower *w.r.t.* the model with the same initial subduction angle but lower mantle viscosity. Like in model 30DF, the subsidence of the mountain range leads to submergence (Figure A4.10a2). Although thicker, deposition occurs in a deep-water environment with an aggradational trend in the basin axes concurrent with margin bypass (Figures 5.9a to 5.9c and A4.7a3 to A4.10a3), similar to the low mantle viscosity models. Furthermore, the seismic facies of these deposits are the same (low amplitude parallel reflectors for models 90DS, 60DS, and 45DS and high amplitude parallel reflectors for model 30DS, Figure 5.9d).

During the necking- and breakoff stages, lower uplift rates for both the mountain range and foreland basins are recorded for models with a higher mantle viscosity (DS models, Table 5.3, Figures A4.7 to A4.10). The highest uplift rates are recorded during the late necking stage in the high mantle viscosity models (Figure A4.7c to A4.10c). This is unlike the low mantle viscosity models, in which the highest uplift rates were recorded for slab breakoff rather than the late- stage necking (Figure 5.5 and A4.4 to A4.6). During this uplift, sediment supply increased in all models except 30DS (Figure 5.8c) in which topography was elevated only 150 m above sea level (Figure A4.10c2). Concurrent rates

with which accommodation space decreased were one order of magnitude higher compared to sediment supply (Figure 5.8c and 5.8d).

The slab necking phase is prolonged, culminating in delayed slab breakoff in the high mantle viscosity models (difference up to 10.77 Myr for 30° initial subduction angle models, Figures A4.7d to A4.10d). Furthermore, instead of instantaneous retrogradation of coarse-grained deposition on the active margin in the low mantle viscosity models, this occurs over a time window of 1-2 Myr in the high mantle viscosity models (Figures 5.9b and 5.9c). Consequently, the accelerated slab necking forcing a redistribution of grain sizes (Figure 5.9b) that are visible as a high-amplitude reflector within the syn-necking deposits (purple dashed lines in Figure 5.9d). This contrasts with the low mantle viscosity models where the final necking- and breakoff stage were condensed in a single reflector.

Although sediment supply decreases during protracted necking (Figure 5.8c), longer-lasting deposition allows for filling of the basins up until a point where water depths are less than 500 m at the active basin margin by the time breakoff occurs (Figures 5.9a and S4d3 to A4.10d3). As a result, there is virtually no lag time between the transition from the underfilled to overfilled stage on the active margin following slab breakoff in models 45DS, 60DS, and 90DS (Figure 5.9c). Like the low mantle viscosity models, necking- and breakoff do not force an underfill to overfill transition in model 30DS (Figure 5.9c).

Slab sinking (Figure A4.7e1 to A4.10e1) also induces uplift of the mountain range (0.04 to 0.13 km/Myr, Figures A4.7e2 to A4.10e2) and foreland basin (0.02 to 0.17 km/Myr, Figures A4.7e3 to A4.10e3). Like the low mantle viscosity models, these processes do not cause rapid changes in basin architecture and overfilled shallow water facies prograde into the basin at a constant rate. However, these progradation rates are lower (16.21, 7.44, and 4.5 km/Myr for models 90DS, 60DS, and 45DS, Figure 5.9c). Compared to their respective countermodels with the same initial subduction angle but lower mantle viscosity. However, this progradation is also expressed as high amplitude clinoforms in the synthetic seismic profiles (Figure 5.9d).

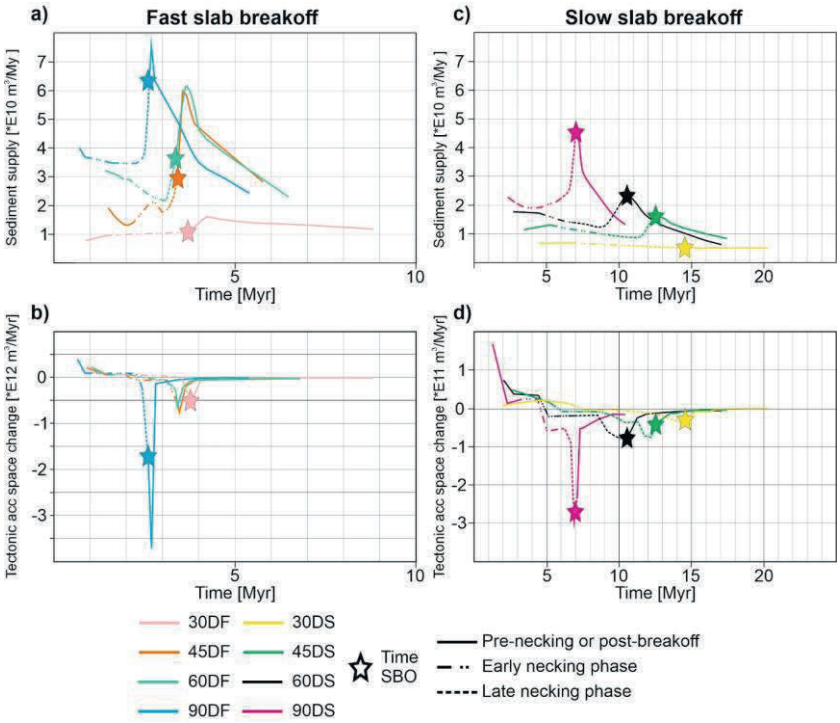

Figure 5.8: a) Sediment supply rate changes for fast breakoff models. The dashed sections of the curves indicate ongoing slab necking. **b)** Volume of accommodation space being generated (positive values) or destroyed (negative values) due to tectonics for the fast slab breakoff models. **c)** Sediment supply rate changes for slow breakoff models. The dashed sections of the curves indicate ongoing slab necking. **d)** Volume of accommodation space being generated (positive values) or destroyed (negative values) due to tectonics for the slow slab breakoff models. **SBO** = slab breakoff.

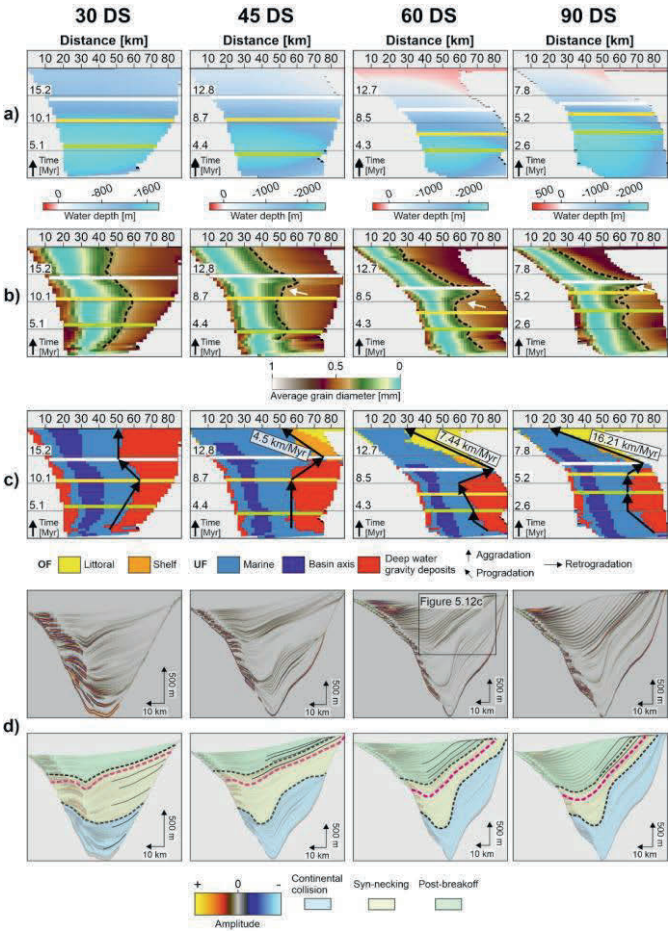

Figure 5.9: Results from models 30DS, 45DS, 60DS, and 90DS. Green lines in Wheeler diagrams indicate the onset of slab necking, the yellow line the onset of accelerated slab necking, and the white line the timing of slab breakoff. **a)** Wheeler diagrams for the depositional water depth. **b)** Wheeler diagrams for the average grain size distribution. The black dashed line the coarse-grained sediment front. White arrows highlight the retrogradation of coarse-grained deposition driven by necking-driven uplift of the active basin margin. **c)** Wheeler diagrams for depositional facies. The time between slab breakoff and first shelf deposition is 0.4 Myr, 1.3 Myr, and 2.6 Myr after slab breakoff for models 90DS, 60DS, and 45DS, respectively. **d)** Synthetic seismics for experiments. Black dashed lines in the interpreted version trace the reflectors that separate pre-necking from the syn-necking and the syn-necking from the post-breakoff units.

5.3.4 Effect of eustacy

In models 90DF-E and 90DS-E, eustatic sea level variations with an amplitude of 50 m and period of 1 Myr (Table 5.3, Figure 5.4b) were superimposed on the system as an external forcing parameter. In the pre-breakoff deposits, 10 km pro- and retrogradations can be observed of the coarse-grained deep-water deposits during the pre- and syn-necking sedimentation (white arrows in Figures 5.10b and 5.10c). However, these features are not distinguishable in the synthetic seismic profiles (Figure 5.10d).

Like in models 90DF and 90DS, necking and breakoff result in retrogradation of coarse-grained underfilled facies back to the margin, followed by progradation of overfilled shallow water facies (Figures 5.10b and 5.10c). Some accelerations and decelerations can be observed for this progradation trend (green arrows in Figure 5.10c), recording the promotion of progradation during a sea-level fall and inhibition thereof during a rise. However, the overall change in basin architecture is similar to the models without eustacy. Moreover, these features cannot be observed in the synthetic seismic profiles (Figure 5.10d).

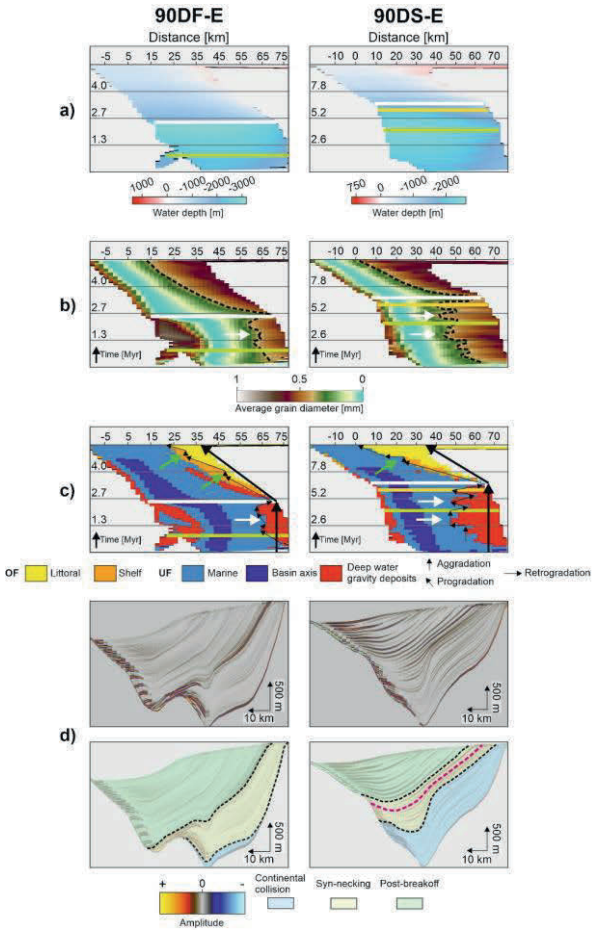

Figure 5.10: Results from models 90DF-E and 90DS-E. Green dashed lines in Wheeler diagrams indicate the onset of slab necking, the white dashed line the timing of slab breakoff. **a)** Wheeler diagrams for the depositional water depth. **b)** Wheeler diagrams for the average grain size distribution. The black dashed line is the coarse-grained sediment front. **c)** Wheeler diagrams for depositional facies. The time between slab breakoff and first shelf deposition is 0.4 Myr, 1.3 Myr, and 2.6 Myr after slab breakoff for models 90DS, 60DS, and 45DS, respectively. Small black arrows indicate short-interval changes in depositional trend induced by eustacy, thick black arrows the overall basin-scale trend dictated by tectonics. **d)** Synthetic seismics for experiments. Black dashed lines in the interpreted version trace the reflectors that separate pre-necking from the syn-necking and the syn-necking from the post-breakoff units.

5.3.5 Symmetric erodibility of the mountain range and forebulge

Increased erodibility of the forebulge leads to more coarse-grained deposition at the base of the distal margin (Figure 5.11b) compared to the reference model 90DF. However, despite this difference, the seismic facies of the sediments deposited during continental collision and slab necking (low amplitude parallel reflectors, Figure 5.11d) is the same as that for the reference model. Progradation of overfilled, coarse-grained shallow water facies induced by slab necking- and breakoff has the same characteristics as in the reference model. However, uplift of the more erodible forebulge leads to a 2.6E10 m^3/Myr greater increase in sediment supply (Figure 5.11e). The extra volume of sediments derived from the forebulge are deposited downslope of the distal margin onto which mountain range-derived sediment onlap. This is expressed in the synthetic seismic profile as an intrabasinal unconformity (Figure 5.11d, yellow dashed line).

5.4 Discussion

In the following subsections, we will discuss the effects of varying parameters on a tectonostratigraphic fingerprint of slab dynamics associated with the slab break-off process and its preservation potential in the foreland basin (Subsection 5.4.1). We then compare our synthetic models to natural examples suggested to have been influenced by slab breakoff to investigate whether first-order features observed in our models align with observations in these basins (Subsection 5.4.2). Lastly, we discuss the shortcomings of our models (Subsection 5.4.3).

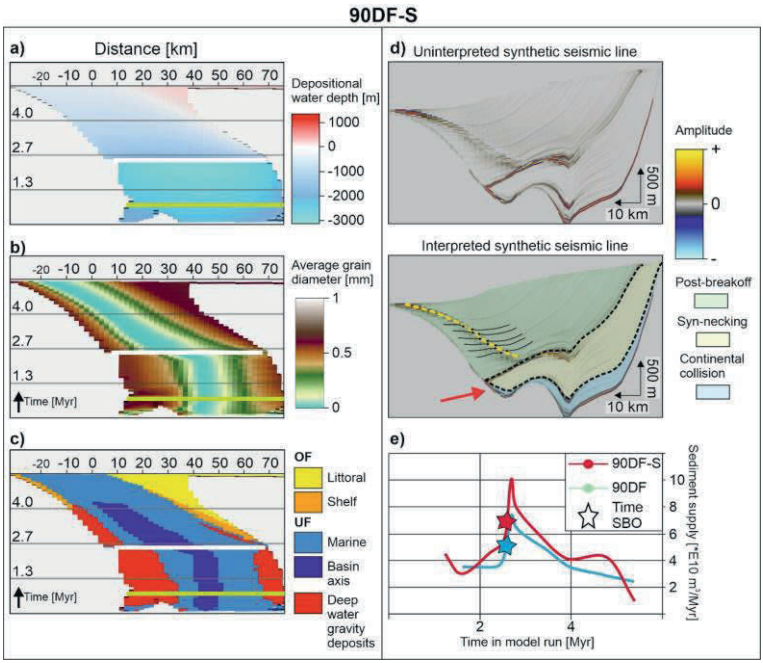

Figure 5.11: Models results from model 90DF-S. Green lines in Wheeler diagrams indicate the onset of slab necking, the white line the timing of slab breakoff. **a)** Wheeler diagrams for the depositional water depth. **b)** Wheeler diagrams for the average grain size distribution. **c)** Wheeler diagrams for depositional facies. **d)** Uninterpreted and interpreted synthetic seismic profiles. dashed lines in the interpreted version traces the reflectors that separate pre-breakoff from the post-breakoff deposits. Yellow dashed line highlights the surface at which post-breakoff sediments derived from the mountain range onlap onto post-breakoff deposits derived from the forebulge.

5.4.1 Summary of the numerical results

5.4.1.1 The tectonostratigraphic fingerprint of slab dynamics in a foreland basin

The continental collision stage is associated with slab steepening, also exemplified in our results (Figures A4.4a1 to A4.6a1 and A4.8a1 to A4.10a1). Our

models show that the magnitude of this steepening decreased for a higher 1) initial subduction angle and 2) mantle viscosity. The former can be explained by a higher initial subduction angle resulting in a lower torque acting on a slab (Lallemand et al., 2008, their eq. 3). The latter is attributed to a more viscous mantle providing greater buoyant support, inhibiting slab steepening. Previous studies demonstrated that slab steepening results in a dissipation of the pull force conducted to the surface (Capitanio et al., 2007; Di Giuseppe et al., 2009), with higher degrees of steepening expected to lead to a greater dissipation. Therefore, the steepening of the slabs with lower initial subduction angles led to a lower pull force being transmitted to the surface, expressed in our models as lower foreland basin subsidence rates (Figures 5.5a3 and A4.4a3 to A4.6a3). Moreover, slabs subducting in a more viscous mantle experienced more buoyant support, leading to subsidence rates being one order of magnitude lower (Figure A4.7a3 to A4.10a3). Likely, the high magnitude of steepening in the models with an initial subduction angle of 30° was responsible for submergence of the mountain range independently of the mantle viscosity (Figures A4.7a3 and A4.10a3).

Subsequent slab necking was dynamic, accelerating in time (Figures 5.5 and A4.4 to A4.10). This was caused by the same pull force acting on an increasingly smaller area as necking of the slab progressed. Consequently, slab necking- and breakoff induced reductions in accommodation space and enhanced sediment supply (Figure 5.8) that lead to a transition from aggradational to progradational depositional trends and the transition from the underfilled to overfilled stage in the foreland basin (except for the 30° slab dip models, Figures 5.7b, 5.7c, 5.9b, and 5.9c). Because the rate of decrease in accommodation space was one to two orders higher compared to the enhanced sediment supply (Figure 5.8), basin uplift due to necking- and breakoff is likely the dominant cause for this transition.

The protracted necking stage in models with a high mantle viscosity resulted in a gradual transition, culminating in a thicker sedimentary sequence recording the change in basin architecture compared to the low mantle viscosity models (Figures 5.5 and A4.4 to A4.10). In the case of a low mantle viscosity,

the system was more sensitive to the loss of slab pull during necking- and breakoff of slabs with different subduction angles. In our models, this is recorded as two coarsening upward cycles recorded within 2-3 Myr in models 60DF and 45DF; the first induced by the onset of slab necking and the second induced by breakoff (Figure 5.7b). In the case of a high mantle viscosity, the higher shear force acting on the slab-mantle interface (Bercovici et al., 2015) moderates the rate at which slab pull decreases, thereby decreasing the related foreland basin- and mountain range uplift rates. As a result, the uplift rates and associated decreases in accommodation space and increases in sediment supply are only high enough during the final necking phase to force a retrogradation-progradation in the high viscosity mantle models (Figures 5.9b and 5.9c). Therefore, only a single coarsening-upward cycle is recorded in these models (Figure 5.9b).

5.4.1.2 Masking of the tectonostratigraphic fingerprint of slab dynamics by environmental conditions

In the models in which eustacy was added (models 90DF-E and 90DS-E, Table 5.3), 10 km pro- and retrogradation could be observed in the pre-breakoff deposits (Figures 5.10b and 5.10c). However, the overall architectural fingerprint of slab necking- and breakoff (i.e., facies belts rapidly migrating basinward) was not altered. Apart from the development of an intrabasinal unconformity (Figure 5.11d), the tectonostratigraphic signal from slab necking- and breakoff in model 90DF-S did not change either. Therefore, although environmental conditions may force km-scale features which are observable at field scale, they are masked by slab dynamics that dictate the basin-scale tectonostratigraphic architecture. In lower resolution data such as reflection seismic data, these features forced by environmental conditions will therefore not be observable when formed concurrent with slab breakoff.

5.4.2 Comparison with a natural example and implications

The most striking feature of our models is the induced transition from the underfilled- to overfilled stage following slab necking- and breakoff. This transition is observed in many natural examples, and is attributed to increasing sediment supply, slab tearing- and breakoff, and/or eustacy (e.g., Ascione et al., 2012; Lemcke, 1988; Meulenkamp et al., 1996; Sinclair, 1997a). In the Austrian Molasse Basin (Figure 5.12a, Eastern Northern Alpine Foreland Basin), this transition is recorded as the stratigraphic upward change from the deep-water Upper Puchkirchen Formation (1000 to 1500 m depositional water depth, Rögl et al., 1979) to the neritic- to littoral Hall Fm. (< 200 m depositional water depth at the top, Grunert et al., 2013; Hülscher et al., 2019) between 19.6 to 18.3 Ma. In the reflection seismic data, this transition is imaged as the basin-wide high amplitude Basal Hall Unconformity (BHU) overlain by prograding clinoforms (Figure 5.12b, Hülscher et al., 2019). This bears a resemblance to the synthetic seismic profile from our model 60DS (Figure 5.12c). Moreover, Le Breton et al. (2023) reported a tectonically-induced foreland basin uplift with a rate of 0.1 to 0.6 km/Myr that spatiotemporally correlates with a proposed slab breakoff below the Eastern Alps at 20 Ma (Handy et al., 2015; Schmid et al., 2004a). This roughly matches with the 0.54 km/Myr observed for the model with a high mantle viscosity and initial subduction angle of 60° (60DS, Figure A4.8d3). Additionally, the increased sediment supply from the Eastern Alps around 20 Ma (Kuhlemann, 2000) might represent increased sediment supply due to necking- and breakoff induced uplift of the mountain range as recorded in model 60DS (Figure 5.8c). This implies that slab breakoff may have been a governing mechanism for the underfill to overfill transition, in agreement with previous authors (Schlunegger and Kissling, 2022).

However, uplift of the Eastern Alps after 20 Ma and the related enhanced sediment supply may alternatively be explained by the Alpine nappe stack overthrusting progressively thicker European lithosphere, inversion of Mesozoic structures on the Bohemian Spur, and indentation of the Eastern Alps by the Adriatic plate (Eskens et al., 2024; Favaro et al., 2015; Heberer et al., 2024; Le Breton et al., 2021). This implies that an increase in sediment supply forced by slab necking- and breakoff in our models is nonunique. Furthermore, following the model from Davies and von Blanckenburg (1995), slab breakoff below the Eastern Alps should have been paired with the intrusion of volcanics in the Eastern Alps around 20 Ma. Therefore, the lack of volcanics of this age in the Eastern Alps would argue against the occurrence of slab breakoff (Eskens et al., 2024). However, recent numerical studies suggest slab breakoff does not always result in intrusive magmatism (Freeburn et al., 2017). Though important, evaluating the link between a potential slab breakoff and (lack of) intrusive magmatism in the Eastern Alps at 20 Ma is not the focus of this contribution, and requires a dedicated study.

In the Betic Cordillera in southern Spain, the Serravallian to Messinian (predating the salinity crisis) evolution of sedimentary basins was coeval with lateral slab tearing of the Gibraltar Arc System (e.g., Chertova et al., 2014; Larrey et al., 2022; Spakman and Wortel, 2004). During this period, most of the basins recorded deepening, often associated with deep-water turbidites, followed by a rapid transition into shallow water ramp carbonate systems (e.g. Sorbas Basin, Andrić et al., 2018a and references therein) implying basin floor uplift rates between 0.3 to 0.6 km/Myr. This is reminiscent of the results for models 60DS (Figure A4.8).

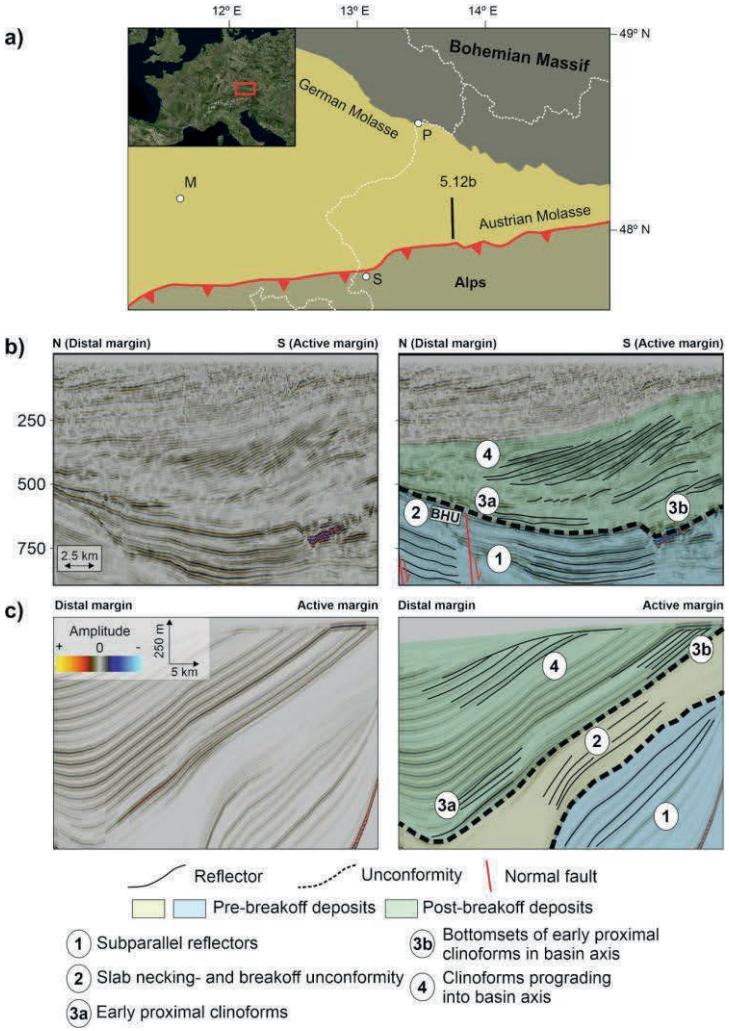

Figure 5.12: a) Eastern Alps and the associated German- and Austrian Molasse Basin. M = Munich, P = Passau, S = Salzburg. **b)** Uninterpreted (left) and interpreted (right) north south reflection seismic line through the Austrian Molasse, modified from Hülscher (2019). BHU = Basal Hall Unconformity. **c)** Uninterpreted (left) and interpreted (right) synthetic reflection seismic line of model 60DS shown in Figure 5.9d.

5.4.3 Model limitations and future directions

The one-way coupled simulations presented in this study allowed characterization of the first-order tectonostratigraphic fingerprint from slab breakoff in a foreland basin. However, previous studies have demonstrated that erosion may induce isostatic uplift in a mountain range (Champagnac et al., 2009; Margirier et al., 2018; Paxman et al., 2016). Furthermore, the large influx of sediments due to slab breakoff may dampen the basin floor uplift from isostatic rebound in the foreland basin by enhancing the sedimentary load (DeCelles and Giles, 1996; Sinclair and Naylor, 2012). However, inherent to the one-way coupling approach used in this study, these dynamic interactions are not accounted for. Ideally, a two-way coupling between GMs and SFMs should be used to account for these interactions. However, this is beyond the scope of this contribution.

In many foreland basins, progressive overthrusting of the foreland plate leads to the basin fill either being overthrusted by- or incorporated into the orogenic wedge (e.g., Northern Alpine, Carpathian, and Guadalquivir foreland basins, Marzec et al., 2018; Marín-Lechado et al., 2017; Ortner et al., 2015). Furthermore, the onset of thrusting may lead to pulses of subsidence in the foreland basin and the basin-orthogonal migration of facies (Flemings and Jordan, 1990). However, previous authors suggested slab breakoff may induce a decrease in plate convergence rates (Ferrari, 2004; Ma et al., 2014; Zhu et al., 2017). Therefore, the tectonostratigraphic signal from slab breakoff will likely not be overprinted by ongoing overthrusting of the foreland. Furthermore, the uplift due to breakoff (Buiter et al., 2002; Fernández-García et al., 2019; van Hunen and Allen, 2011) will likely overshadow other coevally operating processes, as indicated by both our results (Subsection 5.4.1) and the evolution of the Apennines (Lanari et al., 2023).

Lastly, our models only consider the effect of slab breakoff on the tectonostratigraphic development of a foreland basin in 2D. However, many natural examples of foreland basins record along-strike architectural variations (e.g., Northern Alpine, Appalachian, Apenninic, and Tarim foreland basins, Amadori

et al., 2019; He et al., 2016; Lash, 1988; Lemcke, 1988), potentially induced by lateral slab tearing (Meulenkamp et al., 1996; Van der Meulen et al., 1998). Therefore, we suggest expanding the presented research to 3D to quantitatively investigate this hypothesis.

5.5 Conclusions

In this study we combined 2D geodynamic models with stratigraphic forward models, allowing us to quantitatively approximate the first-order tectonostratigraphic signal from slab necking- and breakoff in a foreland basin. Model results exemplify that before slab necking initiates, the lithosphere of the lower plate accommodates the pull force through flexural subsidence. This phase is characterised by deep-water deposition with an aggradational trend. However, during slab necking- and breakoff, the progressively faster decrease in slab pull conducted to the surface results in uplift of the foreland basin- and mountain range. These cause the accommodation space to decrease and the sediment supply to increase, respectively. Together, these processes cause a shift from aggradational to progradational deposition and the basin transitioning from an underfilled- to an overfilled phase. Because the rate at which accommodation space diminishes is greater than sediment supply increases, basin uplift is of first-order importance for the underfill to overfill transition, while sediment supply is of second-order importance. In the case of low mantle viscosity, the system is more sensitive to the loss of slab pull. This led to condensation of the necking- and breakoff stages and their respective tectonostratigraphic signals. In contrast, in a viscous mantle only the uplift rates during final necking are ample to induce changes in grain size distribution and increases in sediment supply to force a change in basin architecture. Lastly, in our parameter space environmental conditions in the form of eustacy and erodibility cannot mask the tectonostratigraphic signal from slab necking- and breakoff.

In our models, the slab necking- and breakoff induced underfill to overfill transition was recorded as a high amplitude reflector overlain by prograding clinoforms. In the Austrian Molasse, a similar sequence records the underfill to overfill transition spatiotemporally correlates with suggested slab breakoff under the Eastern Alps. Therefore, our models support the hypothesis that the underfill to overfill transition of the Austrian Molasse was induced by slab breakoff.

Chapter 6
Summary: the integration of tectonostratigraphic analyses and numerical modelling results

6.1 Concluding remarks

The research presented in this thesis aims at better understanding of process(es) causing along-strike variations in foreland basin architecture and driving a diachronous underfill to overfill transition. Of particular interest is the signal from slab tearing- and breakoff as recorded by the synorogenic basin fill. In this chapter, I summarise the main findings of the conducted tectonostratigraphic analyses and numerical modelling in terms of the main goals of this thesis alongside additional findings (Chapter 6.1). Additionally, I discuss the results within the frame of the evolution of the Alps-Molasse Basin system (Chapter 6.2). Lastly, I present shortcomings and remaining open questions, and suggestions on how to tackle these (Chapter 6.3).

6.2 New constraints on the tectonic evolution of the Alps-Molasse Basin system

The results presented in this thesis demonstrate that orogen-parallel variations in lithospheric-scale Alpine tectonics dominantly controlled the along-strike variable architecture of the Molasse Basin, with local, smaller-scale contributions from crustal tectonics and eustacy. As discussed in Chapter 2, along-strike variations in inherited crustal architecture of the European plate (i.e., bathymetry/topography, Lemcke, 1988) led to lateral variations in foreland basin architecture. In the Swiss Molasse, early variations in basin architecture were also attributed to lateral variations in inherited bathymetry (Lihou and Allen, 1996). Recent numerical modelling of synthetic foreland basins also evidences such control (Gérard et al., 2023). However, this crustal-scale influence on architecture was rapidly suppressed, as evidenced by the lateral homogenisation of basin architecture by the early Rupelian (Figure 2.11a). This likely resulted from slab loading overshadowing the imprint of lateral variations of the inherited crustal architecture.

By the early Oligocene, subduction- and collision of the irregular European margin (Faupl and Wagreich, 2000; Handy et al., 2010; Stampfli et al., 2002) forced early Oligocene slab breakoff (Schmid et al., 1996; von Blanckenburg and Davies, 1995). The subsequent overthrusting of well-developed European continental lithosphere in the Western/Central Alps (Chapter 2) led to folding, duplexing and southward backthrusting against the Periadriatic Fault (Hurford, 1986; Rosenberg and Kissling, 2013; Schlunegger and Willett, 1999; Schmid et al., 1996) and related topographic increase. In contrast, the Eastern Alps continued propagating over transitional continental European lithosphere, promoting frontal thrusting rather than internal wedge thickening and continued slab loading. As a result, the Oligocene paleotopography decreased from the Western/Central Alps to the Eastern Alps, expressed as higher Oligocene sediment supply to the Western Molasse compared to the Eastern Molasse (Frisch et al., 2001; Kuhlemann, 2000; Kuhlemann, 2007). Combined with basin floor uplift, as highlighted by the numerical models presented in this study (Chapter 5), this resulted in Oligocene overfilling of the Western Molasse, whereas underfilled conditions remained dominant in the Eastern Molasse (Figures 6.1 and 2.11c, d, and e). Additionally, the continued loading of the weaker European lithosphere in the Eastern Molasse (Chapter 3) may have contributed to increased subsidence in this area and, thereby, the eastward deepening of the depositional environment. The 200 m eustatic sea level fall at the end of the Rupelian (Figure 6.1, Haq et al., 1987) likely also contributed to shallowing of the basin at this time. However, if this were the dominant process, it would be expected that the northern basin margin would have been exposed, leading to narrowing of the basin. Our paleogeographic reconstructions give no evidence for this (Figure 2.11c and 2.11d). Furthermore, other authors have suggested that this eustatic sea-level drop was 50 m instead of 200 m (Miller et al., 2005), which would have had less of an impact on foreland basin architecture.

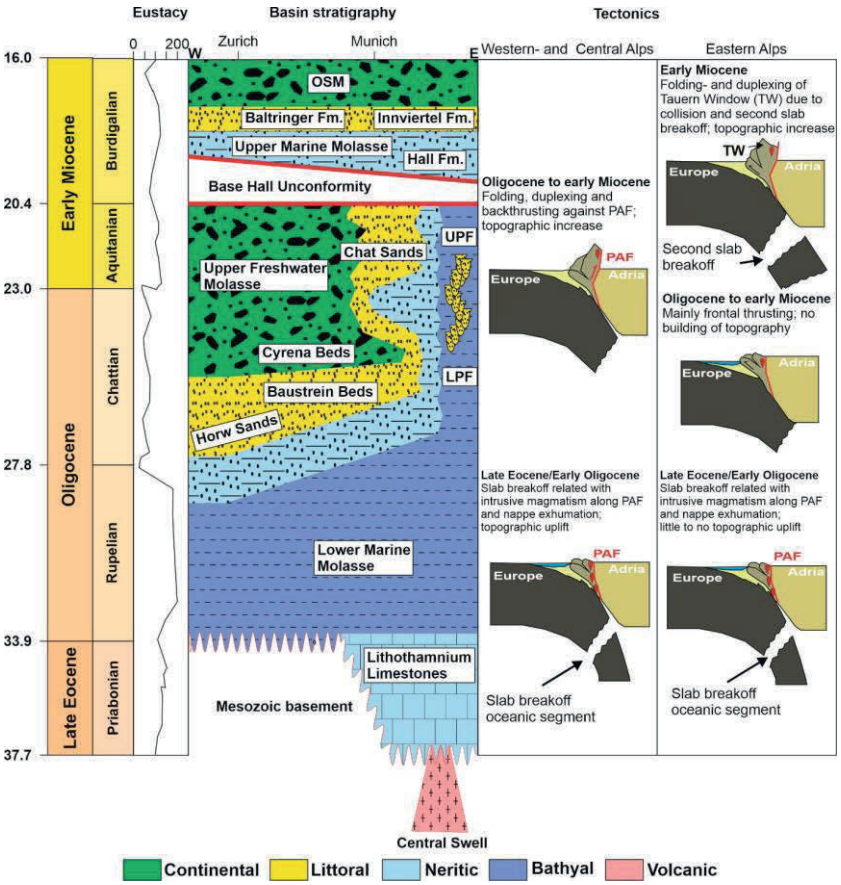

Figure 6.1: Schematic west-east Wheeler diagram of the syn-orogenic fill of the Molasse Basin and the respective depositional environments it represents, as well as coeval eustacy and lithospheric processes. The basin west of Munich defines the Western Molasse, the basin to the east of Munich the Eastern Molasse. Inspired by Kuhlemann and Kempf (2002), their Figure 2. The tectonics pane highlights which processes were fundamental forcing the underfilled to overfilled transition in the Western- and Eastern Molasse, respectively.

Between the middle Chattian to the Aquitanian, this basin configuration remained relatively stable. The juxtaposition of the overfilled Western- and underfilled Eastern Molasse led to the area of Munich developing as an eastward-directed littoral shelf (Bavarian Shelf around Munich, Figures 6.1 and 2.11f and g, Jin et al., 1995; Zweigel et al., 1998). Excess sediment from the Western/Central Alps was transported axially across the Bavarian Shelf into the underfilled Eastern Molasse (De Ruig and Hubbard, 2006; Lemcke, 1988; Wagner, 1998). A 50 m eustatic sea level rise at the end of the Chattian (Haq et al., 1987) led to a ca. 100 km westward transgression of the Bavarian shelf (Figures 6.1 and 2.11f). However, axial sediment transport allowed the shelf to migrate back to its former position by the end of the Aquitanian (Figures 6.1, 2.11g).

By the Aquitanian-Burdigalian transition, the Eastern Alps started to overthrust the Bohemian Spur (acting as a buttress, Heberer et al., 2024) and well-developed European continental lithosphere. This led to the "locking" of the Alpine frontal thrust. As a result, continued Adriatic indentation (Favaro et al., 2015; Ratschbacher et al., 1991b; Rosenberg et al., 2007) was accommodated internally in the wedge, leading to out-of-sequence thrusting close to the structural front (Covault et al., 2009; Hinsch, 2013; Ortner et al., 2015) as well as folding and duplexing in the hinterland (as observed in the Tauern Window, Fügenschuh et al., 1997; Scharf et al., 2013; Schmid et al., 2013, Chapter 2). Increased topographic loading initially led to thrustward migration of the forebulge (Chapter 4), associated with erosion of deposits eroding on the distal margin and deepening of the axial foredeep (Zweigel et al., 1998). A well-established drainage network could develop when continued Adriatic indentation led to eastward tectonic escape and related strike-slip faulting in the Eastern Alps from 18 Ma onward (Chapter 4). In conjunction with the redeposition of the former wedge-top sediments (Augenstein Fm., Frisch et al., 2001; Hülscher et al., 2019), sediment supply increased (Kuhlemann, 2000), allowing the Eastern Molasse to transition towards overfilled deposition. Furthermore, the forebulge migrated back north by the middle Burdigalian to its position prior to the Aquitanian-Burdigalian orogenward migration (Figure

2.11i), suggesting a decrease in applied loads (Chapter 4). This may have been caused by enhanced erosion and lateral extrusion leading to a decrease in Alpine topography (Kuhlemann, 2007) and, thereby, topographic loading. However, as found in Chapter 3, topographic loading is likely not the dominant mechanism controlling foreland flexure. Therefore, the debated slab breakoff below the Eastern Alps around 20 Ma (Figure 6.1, Eizenhöfer et al., 2023; Handy et al., 2015; Schlunegger and Kissling, 2022) is a more likely candidate to explain this subsequent decrease in applied loads.

6.3 Mechanisms controlling along-strike variable foreland basin architecture and the tectonostratigraphic fingerprint of slab breakoff

In this thesis, I assessed the (relative) importance of eustacy, slab breakoff and tearing, lithospheric and crustal strength of the foreland plate, topographic loading, and inherited bathymetry on along-strike variable foreland basin architecture. I used a multidisciplinary and multiscale approach, with the Molasse Basin as a natural laboratory and numerical modelling composing my scientific arsenal. In this chapter, I will discuss the links, feedbacks and fingerprints of the different mechanisms that control foreland basin architecture.

In Chapter 2, it was highlighted that although the inherited bathymetry shaped the early architecture of the Molasse Basin, topographic and slab loading quickly overshadowed this influence (Figure 6.2). Because topographic loads during early orogenesis are likely still relatively small, slab loading likely primarily controls the distribution of foreland flexure and, thereby, foreland basin architecture while sediment supply is still low.

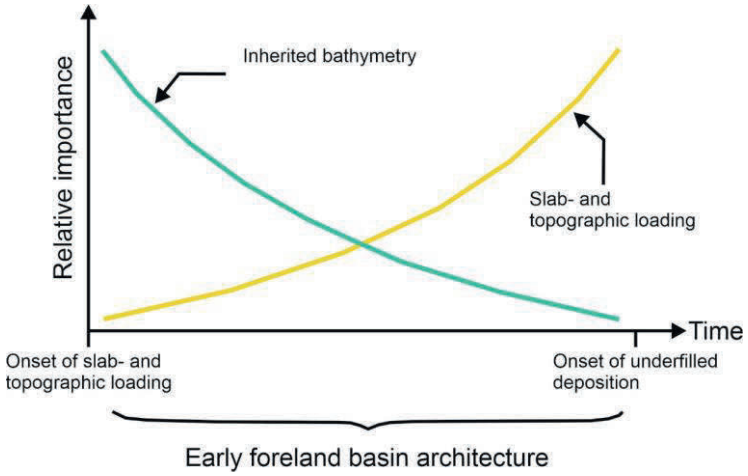

Figure 6.2: First-order trends for the relative importance of inherited bathymetry and slab- and topographic loading on the early foreland basin architecture. Initially, the architecture of the foreland basin is controlled by the inherited bathymetry as the magnitude of the applied loads is still small. However, as the former passive margin is progressively further incorporated into the foreland basin, the importance of slab- and topographic loading for the foreland basin architecture will start to outweigh that of the inherited bathymetry. Modified from (Catuneanu, 2004b), his Figure 21.

During the continued evolution of the Molasse Basin, the diachronous underfilled to overfilled transition occurred parallel to spatiotemporal variable uplift of the Western/Central and Eastern Alps (i.e. proximal source area) at 32 and 20 Ma, respectively. Between these uplift events, the basin architecture remained relatively stable (Figure 2.11). Therefore, our case study suggests long-term along-strike variations in basin architecture are primarily controlled by orogen-parallel variations in source area uplift. Such orogen-parallel variations in paleotopography are driven by oblique collision (Darin and Umhoefer, 2022; Nagel et al., 2013) and subsequent lateral slab tearing (Boonma et al., 2022; Maiti et al., 2024). Subduction- and collision of an irregular lower plate margin will trigger both these processes (Chapter 2). However, both oblique collision and lateral slab tearing lead to orogen-parallel variations in uplift (Maiti et al., 2024) and sediment supply, and therefore

their respective signals are non-unique. However, numerical modelling exemplified that basin floor uplift concurrent with enhanced sediment supply follows slab necking- and breakoff (Chapter 5), allowing these two processes to be distinguished.

Furthermore, the contributions of the distribution of slab loading, lithospheric- and crustal strength, and topographic loading to along-strike variations in foreland basin architecture were assessed. To this end, I compared their distributions to spatiotemporal variations in cumulative syn-flexural normal fault offsets (Chapter 3). The strength of this methodology is that fault growth is unaffected by eustacy and climate, therefore providing independent evidence to investigate the tectonic controls on foreland basin architecture. On the contrary, signals from tectonics derived from the sedimentary fill in a classic tectonostratigraphic analysis may be "muddled" by climate and eustacy. This analysis suggested that along-strike variations in foreland basin architecture were primarily forced by the distribution of lithospheric strength and slab loads controlling the lower plate flexure. In contrast, the distribution of crustal strength of the foreland plate and topographic loads followed trends opposite to those of lithospheric strength and slab loads, contradicting with the observed basin architecture. This suggests that lithospheric-scale factors overshadow the effect of crustal-scale controls on foreland plate flexure. This tenet is reinforced by reorganisations in topographic loads causing short-lived changes in basin architecture, subsequently overruled by the effects of changes in slab loads (Chapter 4).

Apart from the tectonic interactions at play, surface processes also affect the architecture of foreland basins. Eustacy (partly) modulates the available accommodation space (Catuneanu et al., 2009; Posamentier and James, 1993), and climate the sediment supply from the adjacent mountain range (DeCelles, 2012; DiBiase and Whipple, 2011). Although a eustatic sea level rise caused the intrabasinal coastline (Bavarian Shelf) to migrate ca. 100 km westward during the Chattian (Figures 2.11e and 2.11f), it migrated back to its former position within 2 Myrs (Figure 2.11g). The subsequent progradation was most

likely caused by the high sediment supply from the Western/Central Alps, filling the accommodation space generated previously by the sea level rise. This case exemplifies that eustacy may cause short-term changes in foreland basin architecture that affect parts of the basin. However, this change will quickly be overshadowed by the high sediment supply forced by lithospheric-scale tectonics that previously built topography.

It is striking that concurrent with the European climate changing from semi-arid during the late Eocene to more humid in the Oligocene (Kocsis et al., 2014), sediment supply from the uplifting Western/Central Alps increased (Kuhlemann, 2000; Kuhlemann, 2007). However, sediment supply from the low Eastern Alps (Frisch et al., 2001) did not increase simultaneously (Kuhlemann, 2000). Therefore, although increased precipitation may have added to the enhanced sediment supply (Reiners et al., 2003; Zaharia and Ioana-Toroimac, 2009) from the Western/Central Alps, its effect depended on orogen-parallel variations in source area uplift. These, in turn, were controlled by lithospheric-scale tectonics (Chapter 6.1). On the contrary, along-strike variable lithospheric tectonics causing orogen-parallel variations in source area uplift, and thereby slope steepness, would likely still result in lateral variations in sediment supply (Montgomery and Brandon, 2002; Whipple, 2009). This would then translate into along-strike variations in foreland basin architecture. This suggests that although climate (change) may amplify or dampen the signal from along-strike variable lithospheric-scale tectonics, it cannot force along-strike variations in foreland basin architecture independently.

To summarise, the main finding of this thesis is that if the subducting margin is irregular, a chain reaction is triggered where spatiotemporal variable slab breakoff(s) and oblique collision will cause orogen-parallel variations in paleotopography. In turn, this leads to orogen-parallel variations in sediment supply and slab loads, causing along-strike variations in foreland basin architecture and, potentially, a diachronous underfilled to overfilled transition. Although changes in topographic loading and eustacy may cause short-lived changes in basin architecture, they are quickly eclipsed by lithospheric-scale

controls dictating the long-term basin evolution. Furthermore, climate cannot independently cause along-strike variations in foreland basin architecture, as it requires interaction with an along-strike variable source area topography generated by orogen-parallel variations in lithospheric tectonics. In essence, the emerging view is that there is a hierarchy of processes that control foreland basin architecture; the surface processes that lead to along-strike variations in foreland basin architecture are ultimately driven by orogen-parallel variations in lithospheric-scale tectonics.

6.4 Open questions and future perspectives

The results presented in this thesis improved the understanding of different basin-forming processes on the diachronous under- to overfill transition in a foreland basin, taking the Molasse Basin as a natural example. A new model using syn-flexural normal faults was developed to determine the relative importance of orogen-parallel variations in topographic loads, crustal strength, and foreland plate strength for the lower plate flexure. Furthermore, the slab breakoff's sedimentary fingerprint, and its signal as observed from reflection seismic data, was quantitatively defined. However, despite these efforts, some open questions that require further attention. Furthermore, I would like to propose approaches to tackling these questions.

6.4.1 The tectonostratigraphic signal of lateral slab tearing; preliminary results

In this thesis, I presented 2D stratigraphic forward models of a foreland basin-orogen system to define the stratigraphic fingerprint of slab breakoff (Chapter 5). However, slab breakoff may propagate along an orogen, a process known as lateral slab tearing (Menant et al., 2016; Wortel and Spakman, 2000). Lateral slab tearing will lead to a diachronous uplift along the orogen

and foreland (Boonma et al., 2022; Maiti et al., 2024), leading to development of a foreland basin with an along-strike variable architecture (Maiti et al., 2024; Meulenkamp et al., 1996; Van der Meulen et al., 1998). However, although slab tearing likely propagated below the entire Alpine chain during the late Eocene to early Oligocene, along-strike changes in architecture persisted during the Oligocene in Molasse Basin (Chapter 2). This paradox stresses the need to clearly define the tectonostratigraphic response to lateral slab tearing in a foreland basin. To this end, I have combined 3D geodynamic models simulating lateral slab tearing with forward stratigraphic models, following a similar approach presented in Chapter 5 for the 2D models. Here, I will briefly present the models and preliminary findings from them. This may be used as an inspiration in future work to open new scientific avenues regarding the tectonostratigraphic fingerprint from lateral slab tearing as observed in a foreland basin.

3D geodynamic models simulating slab tearing (Figure 6.3, for all parameters see Table 6.1) are constructed using LaMEM (Kaus et al., 2016). The extension of the model domain is 1600 km (- 800 to 800 km) in the x and y-directions, and 750 km (- 700 to 50 km) in the z-direction (Figure 6.3). Erosion and sedimentation processes are turned off in the geodynamic models. The only constraint introduced is that surface topography may not exceed a slope angle of 45°. The initial model setup represents a post-collisional situation where both the lower- and the upper plates are stationary.

The volume of subducted continental lithosphere varies along the strike of the subduction zone (Figure 6.3). This forces lateral slab tearing to initiate where the highest volume of the continental lithosphere is subducted. The activation volume of dislocation creep of dry olivine (now referred to as activation volume) is varied between 8 and 15 $\frac{\mu m^3}{Pa}$ (model 8DC and 15DC respectively, with higher values resulting in a more viscous mantle). This results in variable migration rates of the lateral slab tear. Figure 6.4 shows the initial model configuration for the stratigraphic forward models.

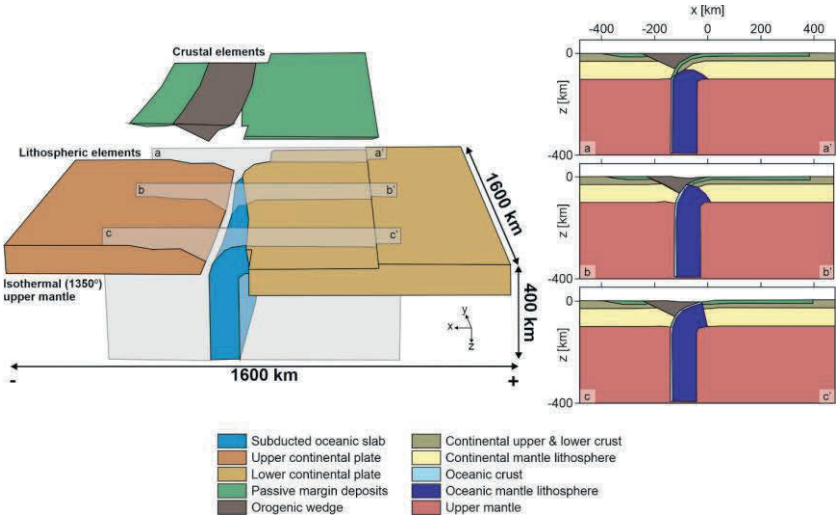

Figure 6.3: Schematic representation of initial conditions of the 3D geodynamic model used in this study to constrain the tectonic response to lateral slab tearing. From cross-section a-a' to c-c' (i.e., along the trench), the volume of subducted continental lithosphere decreases. The surface topography is similar at the start of each model run. The red box highlights which part of the 3D modelling domain is used in the forward stratigraphic models.

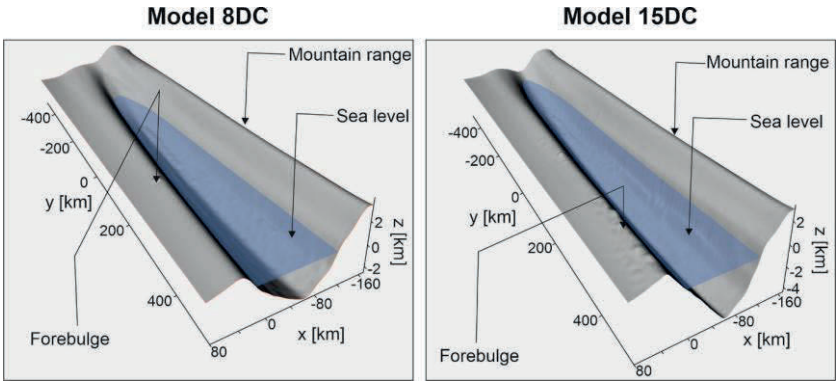

Figure 6.4: Initial conditions at the start of the forward stratigraphic model run for model 8DC and 15DC.

During the evolution of model DC8 (activation volume of the mantle of 8 $\frac{\mu m^3}{Pa}$) we distinguish between four stages: continental collision, slab necking, halfway tearing, and final tearing (Figure 6.5). During the continental collision stage, i.e. the first 0.62 Myr, the mountain range supplies sediment to the foreland basin, and a coastline develops at one end of the model domain (Figure 6.5a). During slab necking (0.62 to 1.62 Myr) the coastline migrates at 0.15 m/yr (Figure 6.5b). During halfway slab tearing, the coastal migration rate is enhanced to 1.28 m/yr (Figure 6.5c). During final tearing, coastline migration slows down to a rate of 0.75 m/yr (Figure 6.5d). Of further note is that the slab tear propagates past the location of the coastline in the foreland basin (Figure 6.5).

Increasing the activation volume of the mantle to 15 $\frac{\mu m^3}{Pa}$ (model DC15) results in prolonged lateral slab tearing (Figure 6.6). Like model 8DC, a coastline develops during the continental collision stage (Figure 6.6a). During slab necking (from 0.19 to 1.46 Myr), the coastline migrates at 0.11 m/yr (Figure 6.5b), closely reflecting the migration rate during continental collision in model 8DC. However, during the subsequent slab tearing, the rate of coastal migration decreases (Figure 6.6c and 6.6d) rather than increases. This is the opposite of what was observed for model 8DC. Interestingly, and also in contrast to model DC8, the location of the slab tear lags behind the location of the coastline during the majority of model evolution (Figure 6.6).

Of these two simulations, model DC8 best represents the evolution of the Molasse Basin, during which a lateral tear propagated along the entire slab, yet overfilled conditions laterally graded into underfilled conditions (Chapter 2). Furthermore, in contrast to the qualitative model tying foreland basin architecture to lateral slab tearing (Meulenkamp et al., 1996; Van der Meulen et al., 1998), the coastline is not a good marker for the location of the slab tear.

Table 6.1: Table of material properties for the geodynamic models. The activation volume of the dislocation creep of the upper mantle and the oceanic slab are target parameters. All materials have the same G (shear modulus) of 50 GPa. α is the same for all material properties at $3e^{-5}$ K^{-1}. C_p is the same for all phases at 1050 $JKg^{-1}K^{-1}$. k is the constant for all phases at 3.0 $Wm^{-2}K^{-1}$. The radiogenic heat production A per unit mass is 0. Lower and upper crust, as well as the continental mantle lithosphere are phases that belong to both the upper and lower plates. The oceanic subducting plate has fixed properties in all experiments except for C/τ_{lim}, while the activation volume of the mantle is changed in the experiments.

Rock unit	Rheological law	B_D [Pa^{-1}]	E_D^a [KJ * mol^{-1}]	V_D^a [µm³ * mol^{-1}]	n	B_{dis} [$Pa^{-n}s^{-1}$]
Upper crust	Wet Plagioclase	4.742^{-11}	159	38	3.0	$1.130e^{-15}$
Lower crust	Wet Plagioclase	4.742^{-11}	159	38	3.0	$1.130e^{-15}$
Continental mantle lithosphere	Dry Olivine	$1.5e^{-9}$	159	5	3.5	$6.22e^{-16}$
Oceanic slab plate & upper mantle & slab	Dry Olivine	$1.5e^{-9}$	159	5	3.5	$6.22e^{-16}$
Orogenic prism & passive margin	Wet Plagioclase	4.742^{-11}	159	38	3.0	$1.130e^{-15}$

Table 6.1 (continued)

Rock unit	E_{dis}^a [KJ * mol^{-1}]	V_{dis}^a [µm³ * mol^{-1}]	ρ_0 [kg * m^{-3}]	Corτ_{lim} (Champagnac et al.)
Upper crust	345	38	2700	10
Lower crust	345	38	2750	10
Continental mantle lithosphere	530	15	3290	10
Oceanic slab & upper mantle	530	8	3300	1
Orogenic prism & passive margin	345	38	2700	1

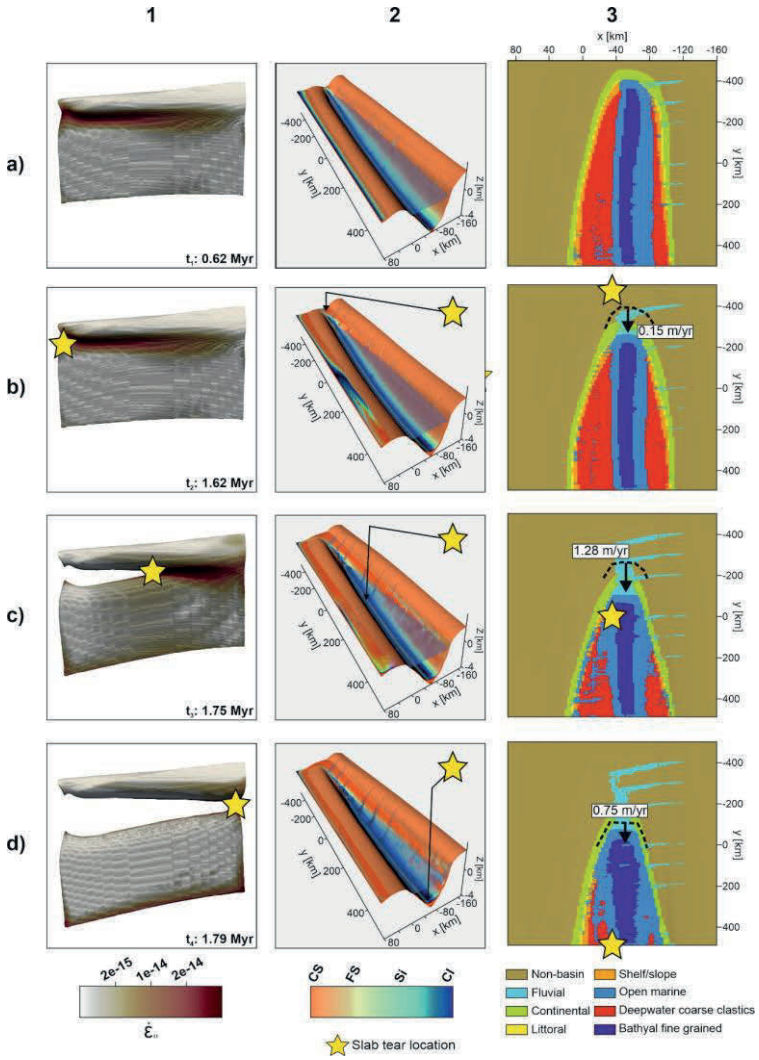
1
2
3
a)
b)
c)
d)
t1: 0.62 Myr
t2: 1.62 Myr
t3: 1.75 Myr
t4: 1.79 Myr
x [km]
y [km]
z [km]
0.15 m/yr
1.28 m/yr
0.75 m/yr
2e-15
1e-14
2e-14
CS
FS
SI
CI
Slab tear location
Non-basin
Fluvial
Continental
Littoral
Shelf/slope
Open marine
Deepwater coarse clastics
Bathyal fine grained

Figure 6.5 (previous page): Evolution of model DC8. Column 1 shows the geodynamic evolution, column 2 the 3D evolution of the orogen-foreland system, and column 3 the distribution of depositional facies in the forward stratigraphic model domain. In the depositional facies maps, the dashed black lines indicate the location of the coastline (transition from fluvial or continental deposition to littoral or open marine) of the previous timestep. The numbers indicate the corresponding migration rates. **a)** The slab remains attached to the lower plate (0.62 Myr) **b)** Onset of slab tearing (1.62 Myr). **c)** The lateral tear has propagated halfway along the slab (1.75 Myr). **d)** The lateral tear has propagated along the slab (1.79 Myr). **CS** = coarse sand, **FS** = fine sand, **Si** = silt, and **Cl** = clay, $\dot{\epsilon}_{II}$ = second invariant of the strain rate tensor.

However, the topography of the mountain range area before slab tearing is over 2 km before slab tearing in both models (Figure 6.4). Furthermore, in model 15DC, the foreland basin is more than 4 km deep, giving a total topographic difference from the top of the mountain range to the basin floor of over 6 km (Figure 6.4). It is likely that before slab breakoff- and tearing occurs, mountain range topographies are lower than presented in these models. The large topographic differences between the mountain range and basin floor in ou model setups might be because the upper- and lower plates are stationary. As a result, slab pull is applied to the same position in the lower plate before slab tearing starts, leading to the formation of anomalously deep basins. Therefore, additional geodynamic models should be run to get more realistic tectonic inputs. Furthermore, depocenter migration and destruction of accommodation space VS sediment supply (as presented in Chapter 5) analyses are required for a more robust definition of the tectonostratigraphic signal of lateral slab tearing. Lastly, the starting basin configuration in the stratigraphic forward models is different (Figure 6.4). This will lead to inherent differences in foreland basin evolution, and therefore the models cannot be compared one-to-one.

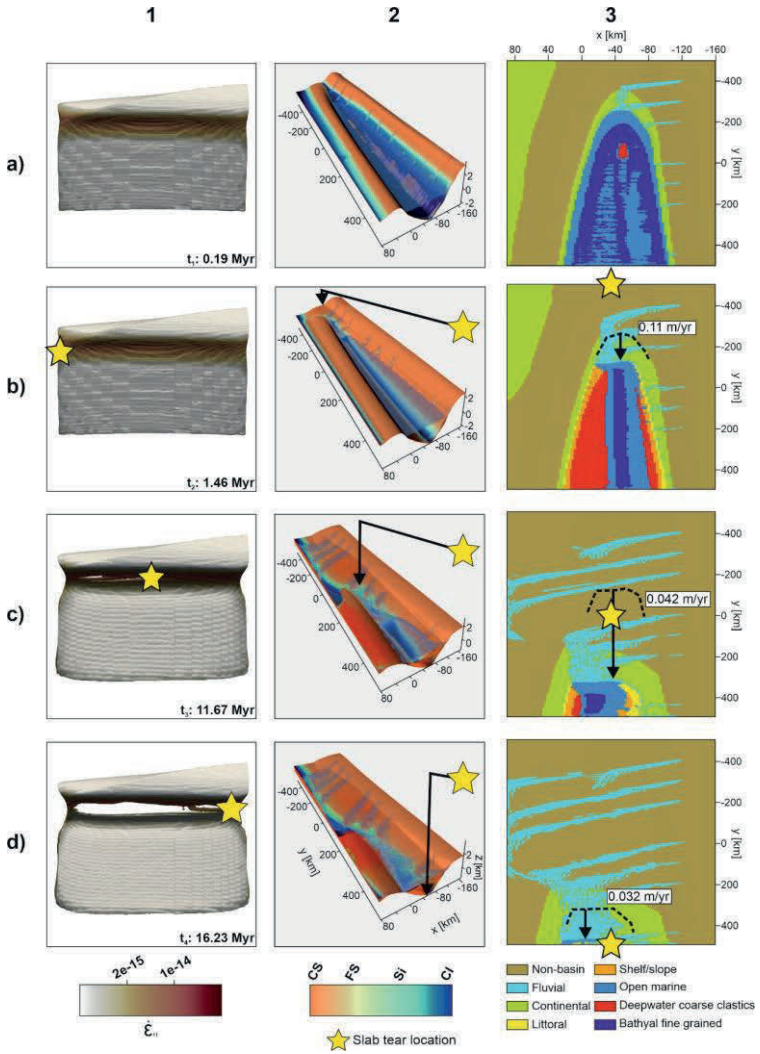
1
2
3
a)
b)
c)
d)
t1: 0.19 Myr
t2: 1.46 Myr
t3: 11.67 Myr
t4: 16.23 Myr
x [km]
y [km]
z [km]
0.11 m/yr
0.042 m/yr
0.032 m/yr
2e-15
1e-14
CS
FS
SI
CI
Slab tear location
Non-basin
Fluvial
Continental
Littoral
Shelf/slope
Open marine
Deepwater coarse clastics
Bathyal fine grained

Figure 6.6 (previous page): Evolution of model DC15. Column 1 shows the geodynamic evolution, column 2 the 3D evolution of the orogen-foreland system, and column 3 the distribution of depositional facies in the forward stratigraphic model domain. In the depositional facies maps, the dashed black lines indicate the location of the coastline (transition from fluvial or continental deposition to littoral or open marine) of the previous timestep. The numbers indicate the corresponding migration rates. **a)** The slab remains attached to the lower plate (0.19 Myr). **b)** Onset of slab tearing (1.46 Myr). **c)** The lateral tear has propagated halfway along the slab (11.67 Myr). **d)** The lateral tear has propagated along the slab (16.23 Myr). **CS** = coarse sand, **FS** = fine sand, **Si** = silt, and **Cl** = clay, $\dot{\varepsilon}_{II}$ = second invariant of the strain rate tensor.

6.4.2 Future directions to further the understanding of the Molasse Basin

The tectonostratigraphic evolution of the German Molasse Basin as presented in this thesis is based on the chronostratigraphic framework presented by Kuhlemann and Kempf (2002). However, biostratigraphic control is poor, especially in the German Molasse Basin, and no radioactive dating is available. To better constrain the cause-effect relationships between forcing mechanism(s) and changes in the architecture of the Molasse Basin, a further refinement of the chronostratigraphic framework is required.

As described in Chapter 2.5.2, an eastward-directed transitional zone may have existed in the Allgäu (northeast of Lake Constance) prior to the underfilled to overfilled transition of the Western Molasse. However, no subsurface data in this area has been published, so the resolution of the presented basin model is low. For a further refinement of the basin model, a tectonostratigraphic analysis of subsurface data in this area would be required.

Additionally, the results suggested that the Oligocene underfilled to overfilled transition of the Western Molasse was primarily forced by European slab tearing- and breakoff leading to enhanced sediment supply from the Central/Western Alps. However, a contemporaneous 200 m eustatic sea level fall at the end of the Rupelian (Haq et al., 1987) likely also contributed to this transition by decreasing the available accommodation space. Depending on the Oligocene paleobathymetry at this time, it is possible this 200 m eustatic

sea level fall may have been ample to expose the basin floor of the Western Molasse above the water level. Therefore, an Oligocene paleobathymetric reconstruction would help in quantifying the relative importance of these coevally operating mechanisms for the underfilled to overfilled transition of the Western Molasse. However, the sea level fall may also have been smaller (50 m), as suggested by Miller et al. (2005).

During the Oligocene to early Miocene, the location of the Bavarian Shelf characterising the transition zone between underfilled and overfilled deposition remained at a relatively stationary position. Here, excess sediment from filling of the Western Molasse was transported into the Eastern Molasse via the Puchkirchen Channel Belt. It is possible that the subsidence rate in the Eastern Molasse and sediment supply were simply balanced in such a way that the Bavarian Shelf remained stationary. Alternatively, similar to the Taiwan foreland basin (Nagel et al., 2018), sediment was transported further east into the Paratethys while a seaway still existed, preventing overfilling. When this connection closed during the Burdigalian (Rögl, 1997), eastward sediment transport was no longer possible. As a result, the remnant depospace was filled, and deposition changed from underfilled to overfilled in the Eastern Molasse. However, a more detailed tectonostratigraphic analysis regarding the connection between the Molasse Basin and basins further to the east (e.g., Vienna Basin or Carpathian foredeep) is required to assess this hypothesis more robustly.

Northward migration of the forebulge during the Burdigalian was likely caused by an unloading event, which we attribute to the proposed slab breakoff around 20 Ma (Figure 6.1, Eizenhöfer et al., 2023; Handy et al., 2015; Schlunegger and Kissling, 2022). However, no concurrent volcanic activity is recorded in the Eastern Alps. This would suggest that slab breakoff will not necessarily leave an igneous signal, as typically assumed following the slkab breakoff model from von Blanckenburg and Davies (1995). This highlights the need to further our understanding of the relation between slab breakoff and volcanic activity.

Furthermore, our numerical models showed that basin floor uplift, not increased sediment supply, due to slab breakoff is of prime importance for the under- to overfill transition of a foreland basin. Therefore, tectonic subsidence curves of Eocene to Rupelian stratigraphic may record a phase of uplift in the Western Molasse. For this reason, I would recommend future studies to construct tectonic subsidence curves for the autochthonous Western Molasse where strata of this age is present, for example in the study area from Mraz et al. (2018). Interestingly, all tectonic subsidence curves constructed for various parts of the Molasse Basin lack an uplift signal during the Eocene to Oligocene in the Swiss (Homewood et al., 1986), German (Zweigel et al., 1998), and Austrian (Genser et al., 2007; Le Breton et al., 2023) parts of the basin. Following our 2D modelling study, such an uplift signal should have been recorded following late Eocene to early Oligocene slab breakoff. Potentially, the uplift signal from slab breakoff may have been masked in these tectonic subsidence curves. Therefore, I would like to suggest future research to assess whether such a late Eocene to early Oligocene uplift signal in the tectonic subsidence curves of the Molasse Basin was suppressed by later processes.

Finally, the influence of climate on foreland basin architecture was not discussed in this thesis. However, as mentioned in Chapter 2.5.3, both the Oligocene and early Miocene underfilled to overfilled transitions of the Western- and Eastern Molasse Basin correspond with global cooling events (Miller et al., 1991; Liu et al., 2009). Such global cooling events have been shown to enhance erosion in mountainous areas (e.g. Herman et al., 2013). Therefore, I suggest future studies to incorporate climatic changes when modelling the tectonostratigraphic response in a foreland basin to slab breakoff- and tearing to shed light on the interaction between these processes.

Appendix

A.1 Appendix Chapter 2

A.1.1 Figures Chapter 2

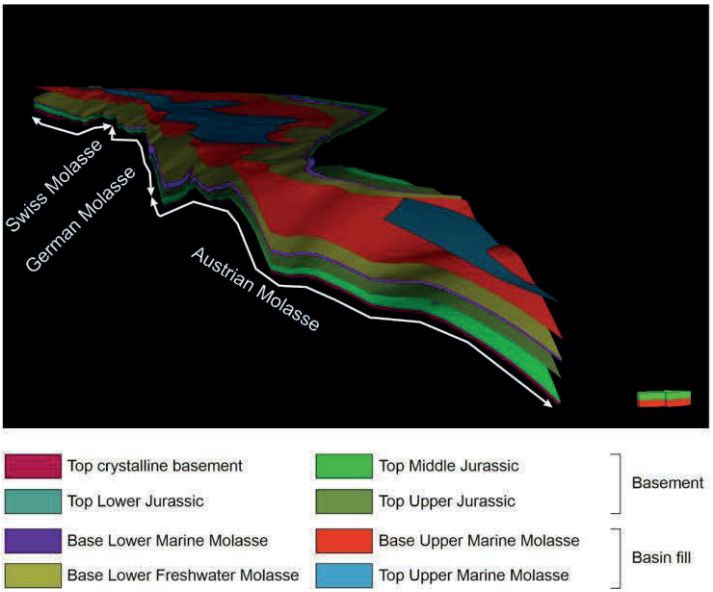

Figure A1.1: 3D view of the low-resolution geological model of the entire Molasse Basin.

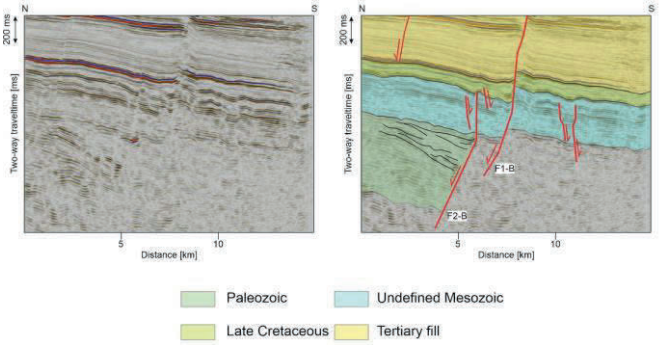

Figure A1.2: Uninterpreted and interpreted N-S seismic lines through seismic volume B. Interpreted line highlights the presence of a fault-bounded Permo-Triassic graben in the study area. This line is given in the time domain, as the depth conversion below the late Cretaceous is inaccurate.

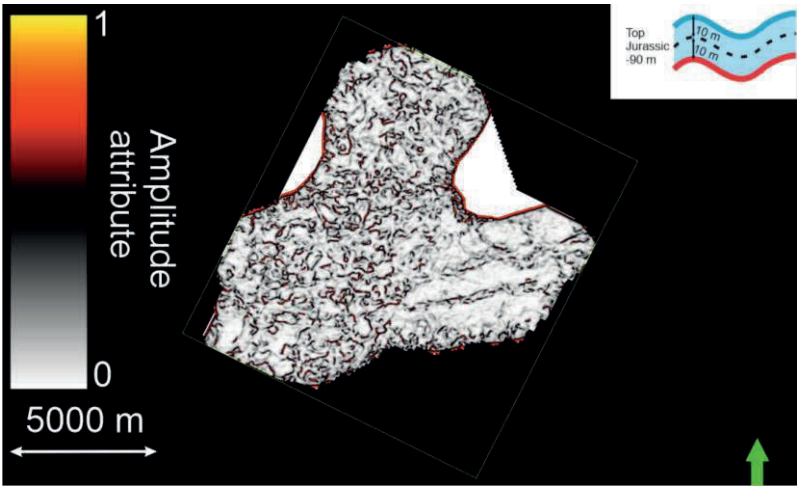

Figure A1.3: Variance attribute map of the Upper Jurassic seismic-stratigraphic body in seismic volume A with a thickness of 20 m. The WNW shows a chaotic distribution of high variance values, which is characteristic of heavily karstified limestones. To the ESE, a patch of dominantly low variance values indicates that the Upper Malm is not (as heavily) karstified here.

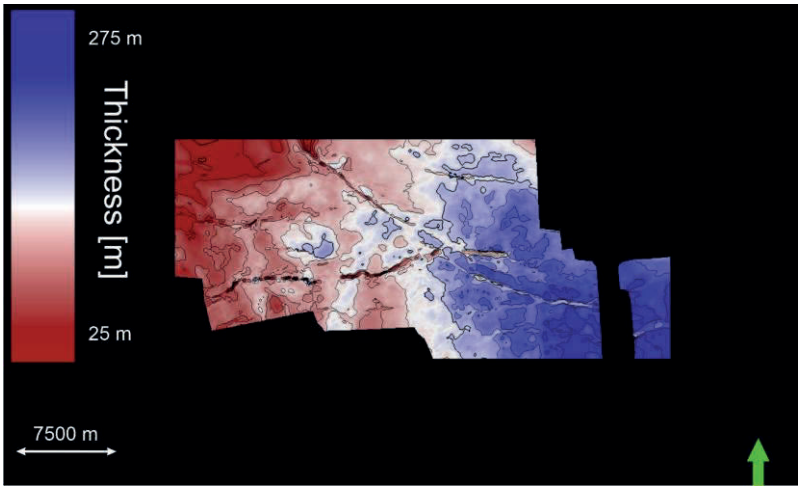

Figure A1.4: Thickness distribution of the post-Turonian late Cretaceous seismic-stratigraphic body in seismic volume B.

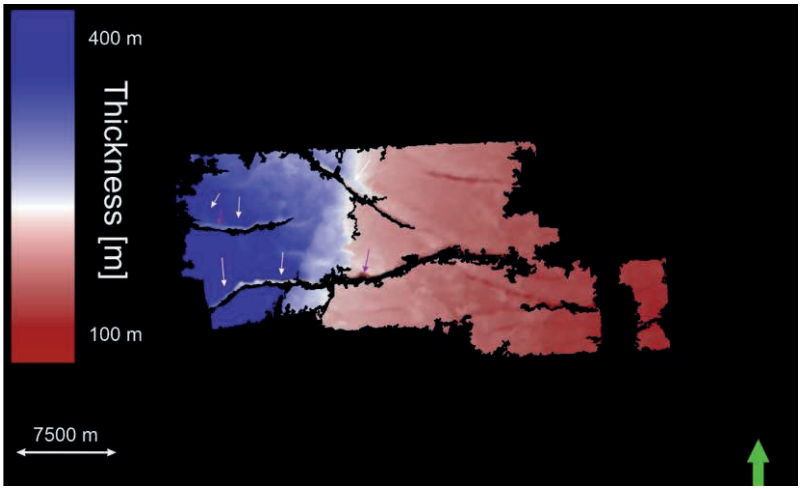

Figure A1.5: Thickness distribution of the Rupelian seismic-stratigraphic body in seismic volume B. White arrows indicate the thickening of the Rupelian towards the faults, and purple arrows indicate locations of thickness artefacts when creating isopachs.

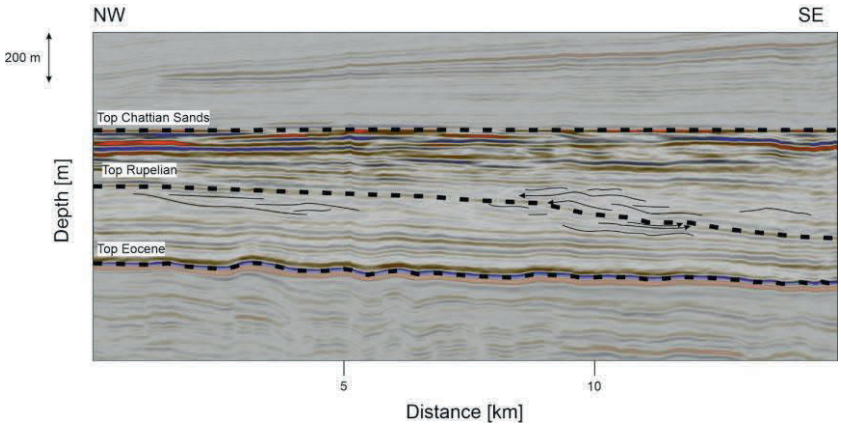

Figure A1.6: SE dipping Clinoforms (black solid lines) in the Upper Rupelian and Lower Chattian seismic stratigraphy. Arrows indicate reflector terminations.

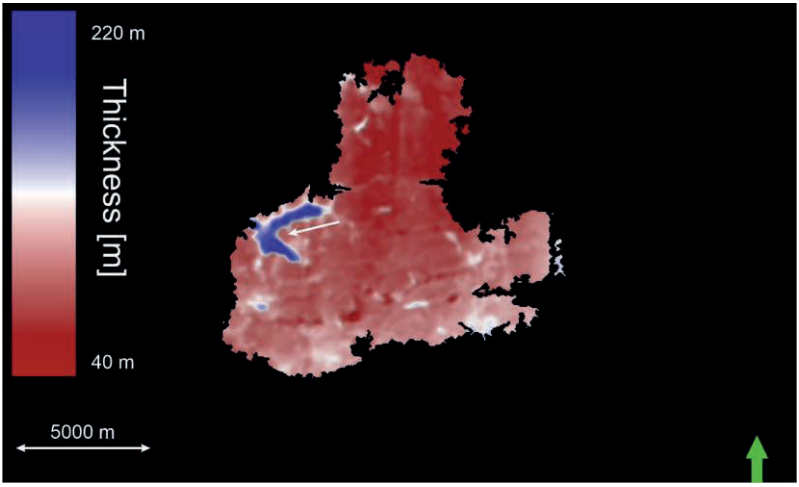

Figure A1.7: Thickness distribution of the Early Chattian seismic-stratigraphic body in seismic volume A. White arrow highlights the local increase in thickness related to karstification of underlying Upper Jurassic limestones.

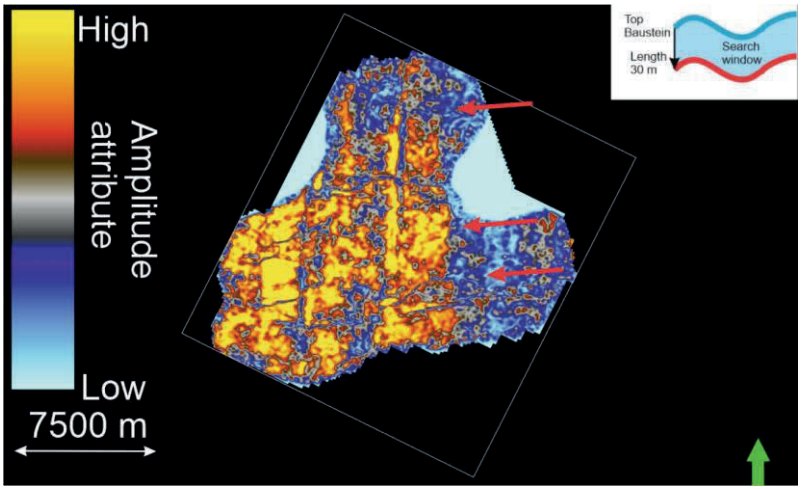

Figure A1.8: Sweetness map of the Early Chattian seismic stratigraphic unit. High amplitudes indicate more sandy areas, and low amplitudes indicate more muddy areas. As such, the N-S bands of high and low sweetness values are interpreted to highlight the orientation of a N-S directed coastline. The western side was a more shallow and sandy area. In contrast, the eastern side is more mud-rich and was likely located in a deeper water depositional environment. Red arrows indicate the direction of onlap.

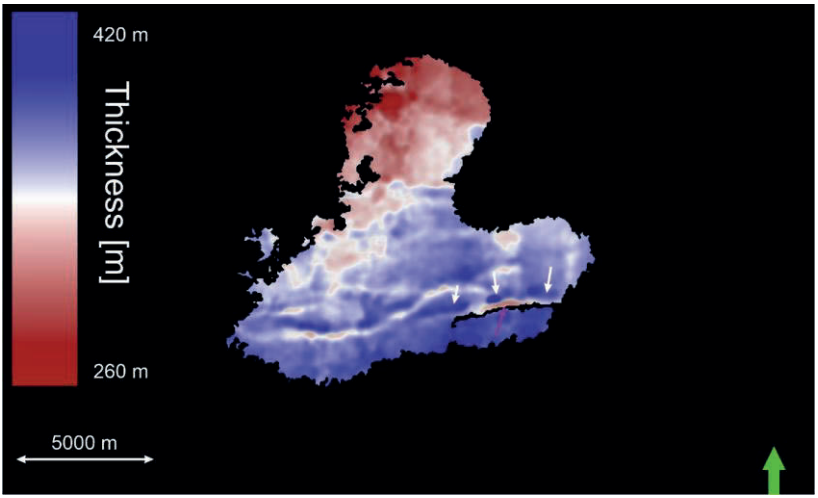

Figure A1.9: Thickness distribution of the Cyrena Beds in seismic volume A. White arrows indicate thickening towards the faults, and purple arrows indicate locations of thickness artefacts when creating isopachs.

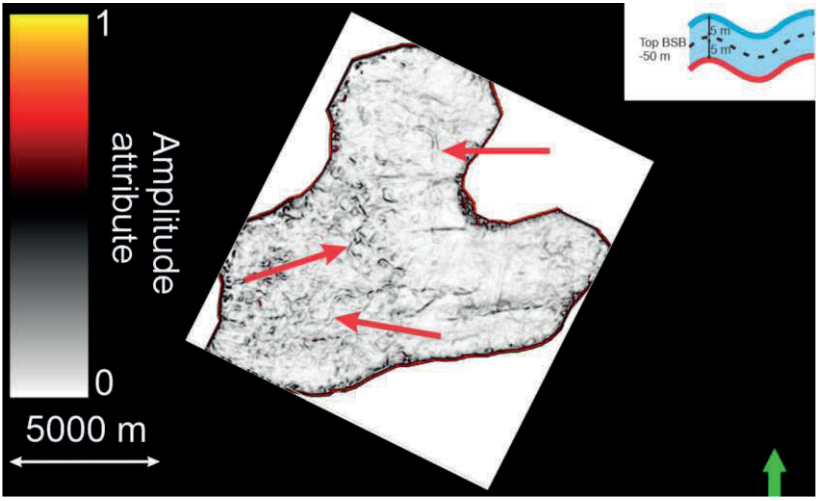

Figure A1.10: Variance attribute map of the Cyrena Beds in seismic volume A with a thickness of 10 m. Red arrows highlight curving bands of high variance values indicate meandering channels.

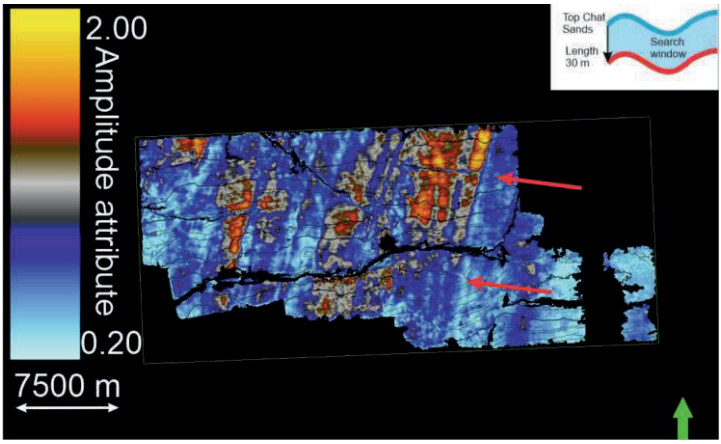

Figure A1.11: Sweetness map of the Middle Chattian seismic stratigraphic unit. High amplitudes indicate more sandy areas, low amplitudes indicate more muddy areas. As such, the NE-SW bands of high and low sweetness values are interpreted to highlight the orientation of an NE-SW directed coastline. The western side was a more shallow and sandy area. In contrast, the eastern side is more mud-rich and was likely located in a deeper water depositional environment. Red arrows indicate the direction of onlap.

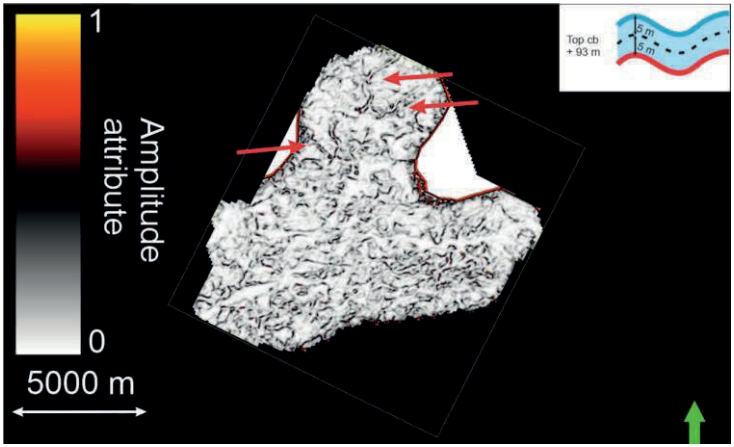

Figure A1.12: Variance attribute map of the late Aquitanian reflectors in seismic volume A with a thickness of 10 m. Red arrows highlight curving bands of high variance values highlighting the positions of meandering channels.

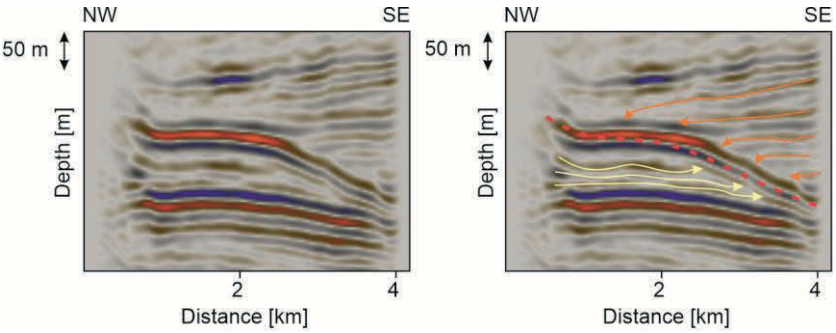

Figure A1.13: Uninterpreted and interpreted parts of an NW-SE trending seismic line in seismic volume B at the western edge of the Austrian Molasse. Yellow arrows mark terminating Aquitanian reflectors, the red dashed line the BHU, and orange arrows onlapping Early Burdigalian reflectors. For location see Figure 2.8.

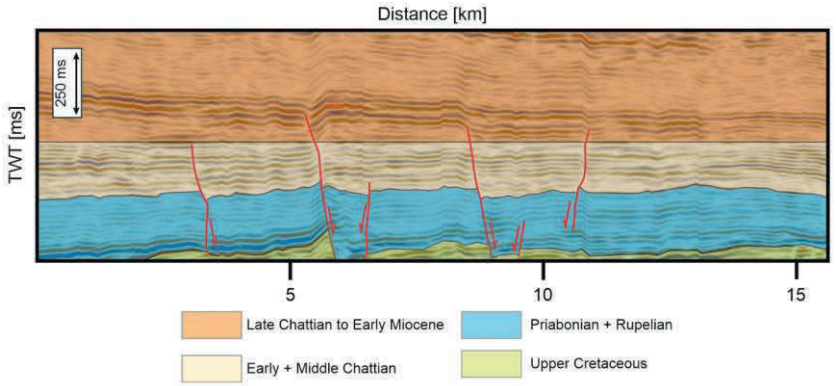

Figure A1.14: Interpreted section flattened on the top Chattian Sands reflector. Red lines indicate syn-flexural normal faults. Thickness changes of the early to Middle Chattian stratigraphy indicate these normal faults were active during the deposition of this unit. For location see Figure 2.1a.

A.1.2 Time Depth conversion of seismic volume B

The seismic data in volume B is in the time domain, which does not give true geometries and, thus, not true fault throws. To produce a time-depth conversion, reflectors were picked in the time domain using welltops where checkshots are available. Based on borehole data, the depth of the stratigraphic surfaces is locally known. Where interpreted time surfaces intersect with wells that drill the corresponding surface, it is possible to calculate average seismic velocities from the surface to the reflector of interest (Table A1). Based on the average velocities of the separate horizons, an overall average velocity of 2678 m/s was calculated from the surface until the top Turonian reflector. This velocity was used to convert the seismic data from the time to the depth domain. Reflectors and faults were then picked on the depth-converted seismics. These interpretations were used to calculate T-x profiles for seismic volume B.

Table A1.1: Average velocities from the surface to interpreted seismic horizon.

Stratigraphic surface	Average velocity (m/s)	Number of wells
Base Hall Unconformity	2709	93
Top Chattian Sands	2516	91
Base Eocene	2729	63
Top Turonian	2739	10

A.2 Appendix Chapter 3

A.2.1 Figures Chapter 3

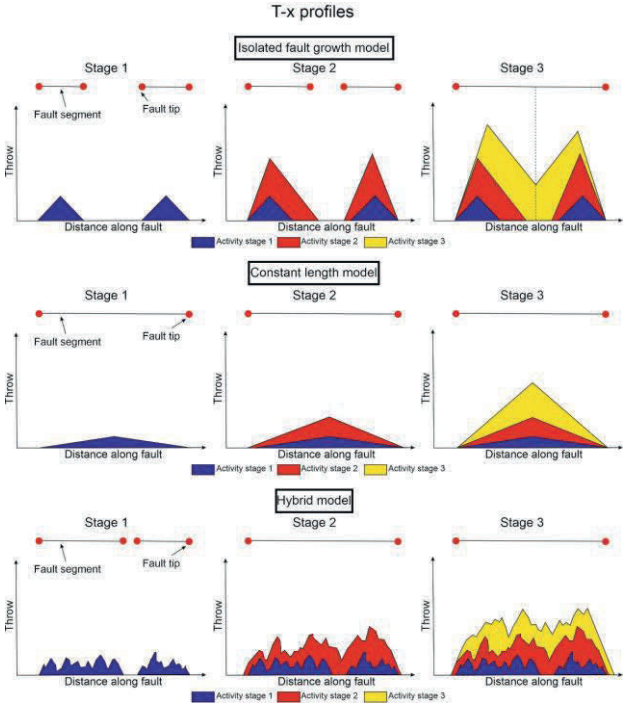

Figure A2.1: Conceptual model for lateral (along-strike) normal fault growth signature in T-x graphs for the isolated, constant length and hybrid fault growth models. For the isolated fault growth model, lateral growth occurs through tip migration and subsequent linkage of previously separated fault segments. Modified from (Hongxing and Anderson, 2007; Peacock and Sanderson, 1991; Ryan et al., 2017; Wang et al., 2022). For the constant length model, the final length of the fault is established during the early stages of fault development, accumulating offset along the entire fault over time (Jackson et al., 2017; Jackson and Rotevatn, 2013; Walsh et al., 2002). The hybrid model combines of the isolated- and constant-length growth models. In this case, the early stage is defined by the lengthening of the fault, laterally linking along (most of) its length. Subsequently, offset accumulates along the fault coeval with minor lengthening (Jackson et al., 2017).

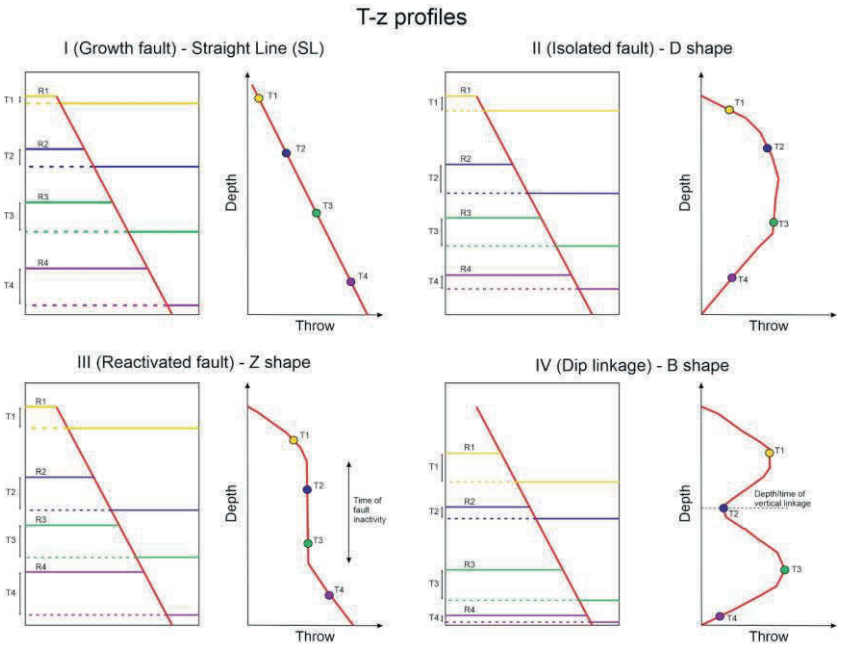

Figure A2.2: Conceptual models for down-dip (vertical) normal fault growth signature in T-z graphs. Assuming the entire fault surface is active during phases of tectonic activity, the stratigraphic surface which records the highest offset indicates the time and point of initial nucleation. (I) A growth fault nucleates at depth, growing continuously upward in the stratigraphy. In a T-z graph, this is recognised as an upward continuous decrease in offsets compared to the lowest stratigraphic surface (Hongxing and Anderson, 2007; Ryan et al., 2017). (II) An isolated fault nucleates in the middle of a stratigraphic sequence, subsequently propagating both down- and upward in the stratigraphy. This is recognised in a T-z graph as the highest offset being recorded midway down the fault, decreasing both down- and upward (Hongxing and Anderson, 2007), giving the T-z profile a D-shape. (III) A reactivated fault nucleates at depth, subsequently becoming inactive before being reactivated during a 2nd phase of activity. In a T-z graph, this is recognised as the maximum throws being observed for the deepest stratigraphic surface, remaining constant for a few surfaces before subsequently decreasing for the youngest stratigraphy cut by the fault (Ryan et al., 2017), giving the T-z profile a Z-shape. (IV) A vertically dip-linked fault initially consisted of two mechanically separated segments which linked as both faults grew down- and upward. In a T-z graph, this is reflected by two throw maxima at different depths with decreasing offsets both down- and upward. Between the throw maxima, a throw minimum indicates the vertical linkage position (Baudon and Cartwright, 2008). Overall, this gives the t-Z profile a B shape. Modified from (Wang et al., 2022).

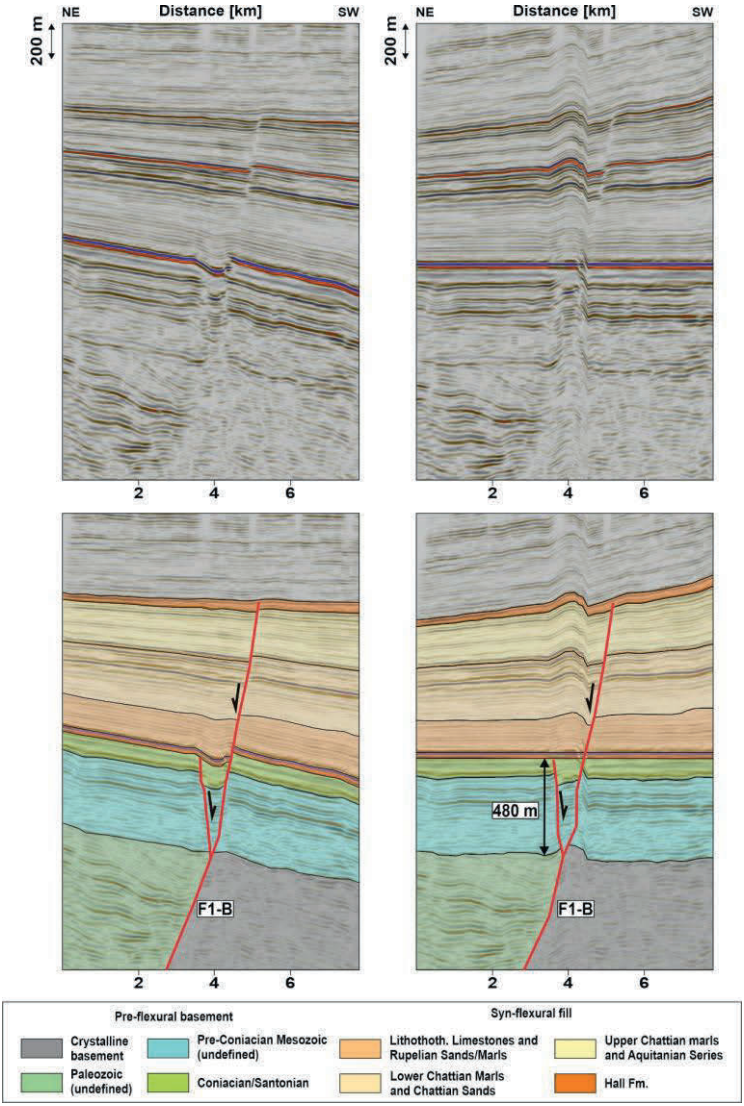

Figure A2.3: Left panels show both an uninterpreted and interpreted unflattened section across F1-B. Right panels show both an uninterpreted and interpreted of the same section, flattened on the foreland unconformity reflector. This section indicates that at the onset of flexure, the lower segment of F1-B which was not reactivated during flexure was buried at a depth of 480 m.

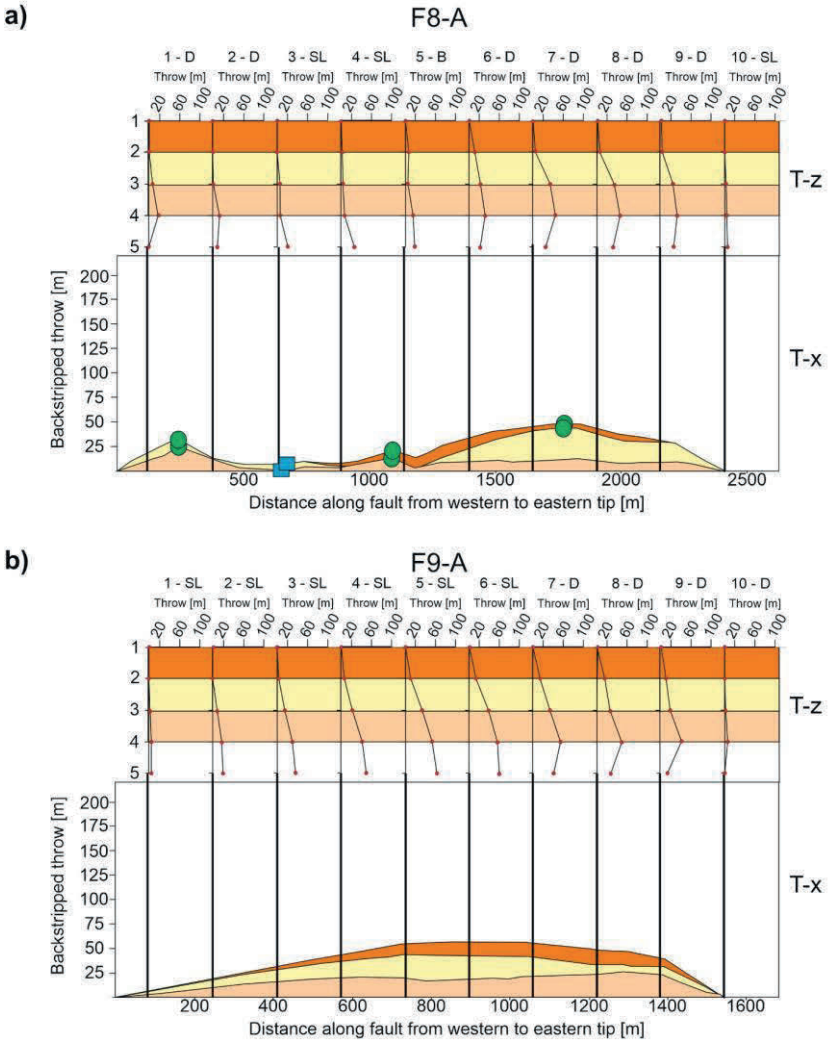

Figure A2.4: T-x profile with 10 T-z profiles along the length of faults **a)** F8-A, **b)** F9-A.

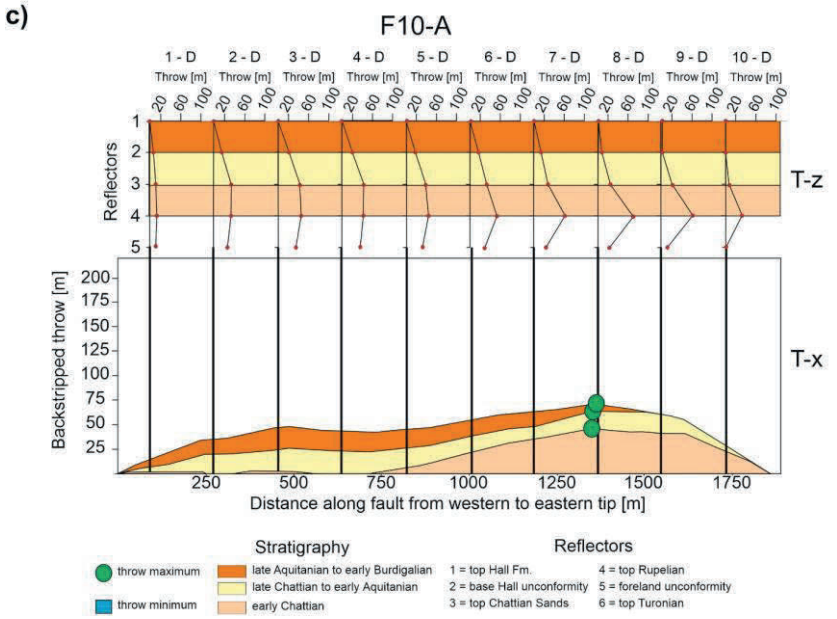

Figure A2.4 (continued): T-x profile with 10 T-z profiles along the length of fault **c)** F10-A.

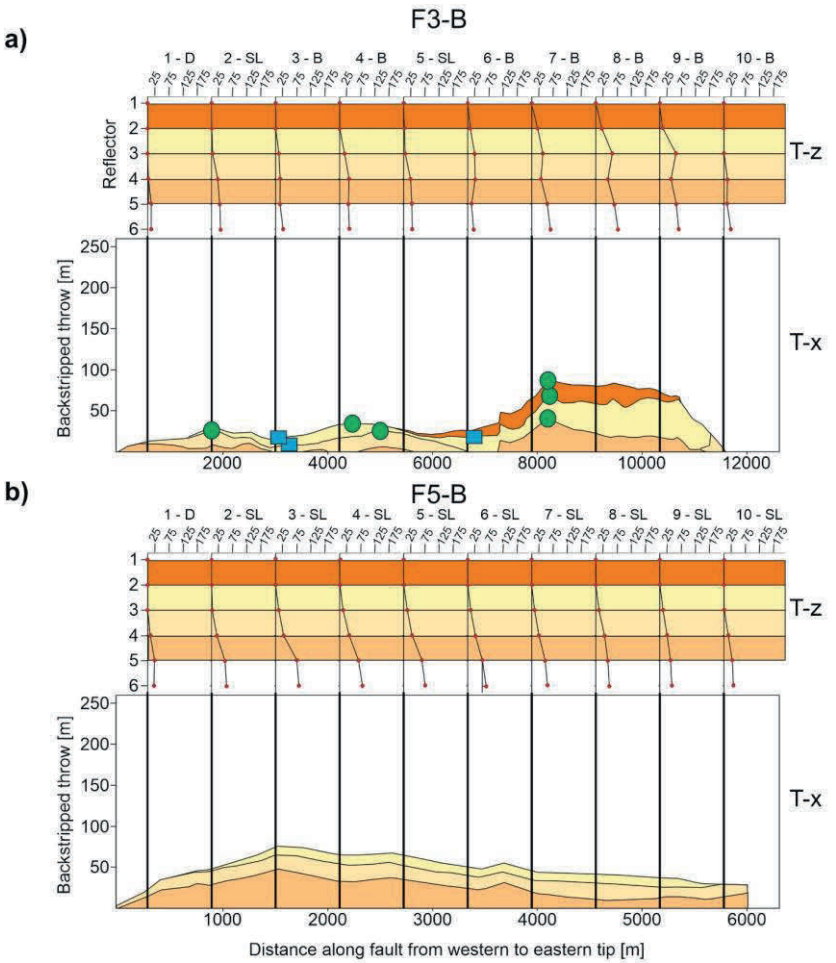

Figure A2.5: *T-x profile with 10 T-z profiles along the length of faults* ***a)*** *F3-B,* ***b)*** *F5-B.*

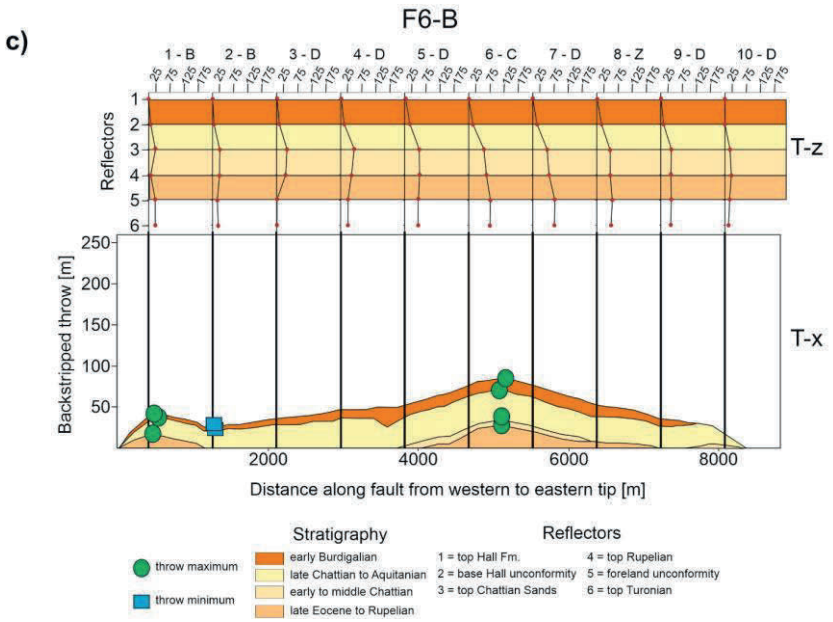

Figure A2.5 (continued): T-x profile with 10 T-z profiles along the length of fault **c)** F6-B.

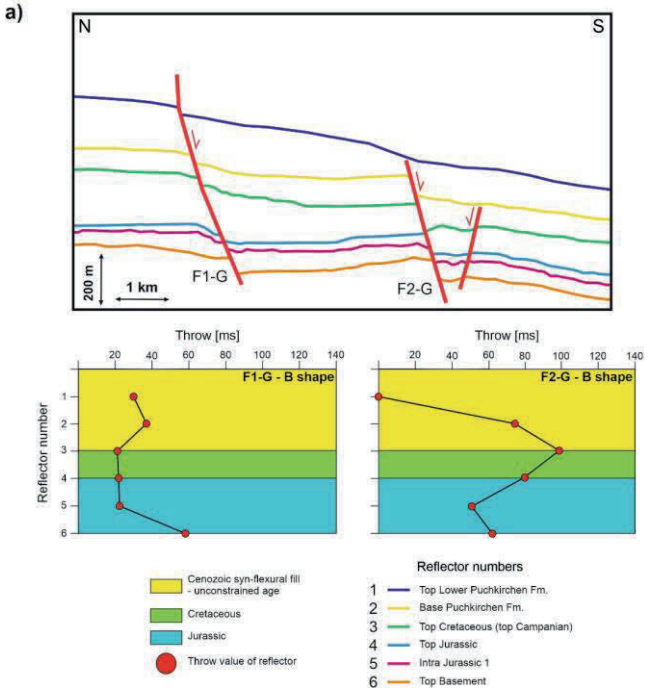

Figure A2.6: a) T-z profiles from 2 normal faults in the Austrian Molasse that cut the Cenozoic syn-flexural stratigraphy, based on seismic data in the Austrian Molasse (Gross et al., 2015, their Figure 8). One extra reflector is interpreted within the Jurassic stratigraphy. T-z profiles indicate dip linkage of a lower segment with a Jurassic origin with upper segments that nucleated within the Cenozoic syn-flexural stratigraphy and at the foreland unconformity at the onset of flexural subsidence (F1-G and F2-G respectively).

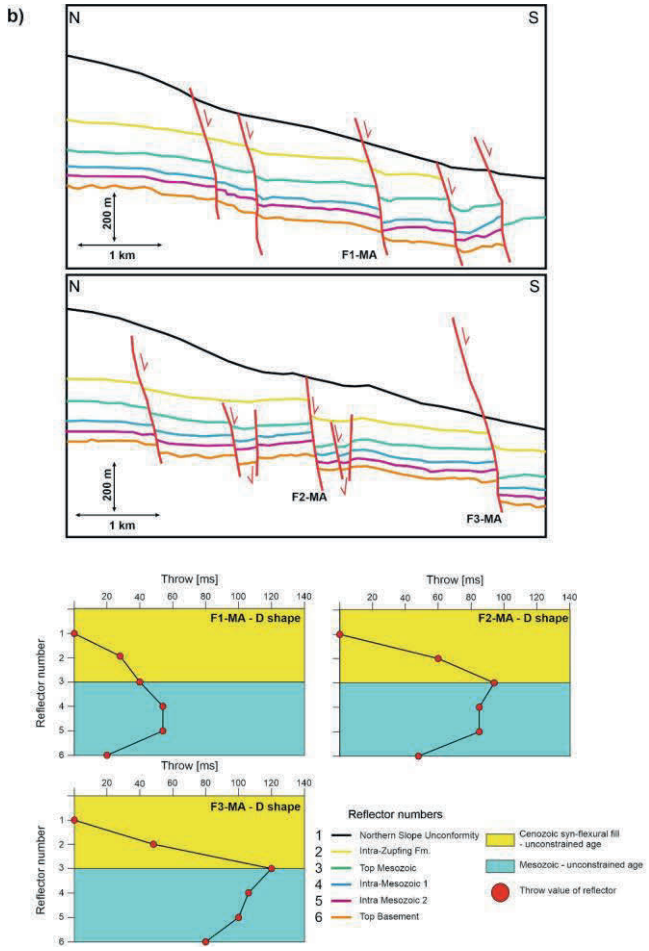

Figure A2.6 (continued): **b)** Interpretation of reflectors and syn-flexural normal faults in the Austrian Molasse (Masalimova et al., 2015, their Figure 14). All T-z profiles have D shapes, indicating isolated nucleation. For F1-MA, this section of the fault represents a Mesozoic fault that was reactivated during Cenozoic flexure. On the other hand, the T-z profiles from faults F2-MA and F3-MA have throw distributions suggestive of isolated nucleation at the foreland unconformity, subsequently propagating up- and downward. Therefore, it is likely these sections of the respective faults nucleated at the top of the Mesozoic basement at the onset of flexure as we observe in the German Molasse.

A.2.2 Seismic data, horizon tracing and fault interpretations

Seismic volumes A and B are located in the Western and Eastern German Molasse respectively (Figure 3.1 for locations). Seismic volume A is an APSDM (anisotropic pre-stack depth migrated) seismic volume in the depth domain, imaging down to 2000 m depth and covering an area of 145 km^2. Seismic volume B is a PSTM (pre-stack time migrated) seismic volume that covers an area of 560km^2. It images down to 5000 ms TWTT depth, with the upper 2500 ms TWTT being of interpretable quality. The line spacing of both seismic volumes is 25 m. For the fault analysis, seismic volume B was converted from the time to the depth domain (See subsection A2 for details). Based on the dominant frequency of 45 Hz in volume B and the average velocity of 2678 $\frac{m}{s}$ in the stratigraphic sequence of interest (Subsection A2) the vertical resolution is up to 15 m (λ/4, Nanda, 2021). Furthermore, both seismic volumes are displayed in reverse polarity (SEG convention). This means that a blue reflector (negative amplitude) indicates a downward increase in acoustic impedance. In contrast, a red reflector (positive amplitude) characterizes a downward decrease in acoustic impedance.

The structural smoothing seismic attribute was applied to the input seismic data to increase the signal/noise ratio for the conventional tracing of prominent seismic horizons. Key stratigraphic horizons were identified based on well data. In seismic volume A, eight different reflectors were mapped, from old to young; top Lias, top Dogger, base karstified Upper Jurassic limestones, top Upper Jurassic limestones (*i.e.* foreland unconformity in this volume), top Baustein Beds, top Cyrena Beds, top Lower Freshwater Molasse (*Untere süßwassermolasse*, USM) and top Baltringer Fm. (Figure 3.3). Because the top USM reflector is very discontinuous in seismic volume A, the USM deposits above the Cyrena Beds and the Early Burdigalian reflectors until the top Baltringer reflector were taken as a single seismic-stratigraphic unit. In seismic volume B, 7 seismic horizons have been mapped: top Turonian, Base Eocene (*i.e.* foreland unconformity), top Eocene, top Rupelian, top Chattian Sands, Base Hall Fm. and top Hall Formation. Fault interpretations were based on

lateral reflector terminations (i.e., juxtaposing different seismic facies or contrasting amplitudes). Furthermore, the variance seismic attribute (Koson et al., 2013; Subrahmanyam and Rao, 2008) was applied to the structurally smoothened seismic data to further enhance the confidence in the fault interpretation as well as to highlight sedimentary structures.

A.2.3 Cumulative Cenozoic offsets along syn-flexural normal faults; from milliseconds to meters

Taking the seismic interpretation of line I from (Cordero Peña, 2007), the foreland unconformity has a throw value of 186 ms TWT. At the location of well "5 Ost" along this seismic line (Cordero Peña, 2007, their Figure 36), the foreland unconformity is located at a depth of 2221 ms TWT. As well "5 Ost" represents the Bromberg-1 well, we also know the foreland unconformity is located at a depth of 3622 m (Müller et al., 1988, their Figure 10). Taken together, this gives an estimate of 3260 m/s for the average seismic velocity of the sediments up until the foreland unconformity. Therefore, the 186 ms offset of the foreland unconformity in the time domain corresponds to an offset of 303 m in the depth domain.

A.2.4 Limitations and pitfalls of structural analyses based on seismic data

Structural information in the time-migrated seismic volume B and time-migrated data presented by previous authors is inherently uncertain(e.g. Fomel and Landa, 2014). Moreover, uncertainties in the applied velocity model to convert this volume to the depth domain are passed along to the constructed T-x and T-z profiles. With a seismic resolution of up to 15 m (Subsection A1), shifting the pick of an interpreted horizon to a single reflector higher or lower in the seismic data may end up drastically changing the geometry of the T-z profiles, backstripped T-x profiles or seismic attributes used to constrain structures (Rankey and Mitchell, 2003). As a result, the structural history as

interpreted from the T-z and backstripped T-x profiles in seismic volume B are more uncertain compared to those from seismic volume A. Lastly, as outlined in the methodology section, seismic data does not allow for the quantitative determination of the dip- and oblique-slip components for the normal faults. However, the lack of throw maxima migrating along the faults in the T-x profiles may indicate oblique slip was negligible.

A.3 Appendix Chapter 4

To model the flexural response of downgoing European plate due to loading by the Alpine thrust sheets, we have used a semi-numerical solution for deflection of an elastic plate under a distributed load provided by Wangen (2010). The distributed load $q(x)$ is treated as a series of blocks of height h_{i}, extending laterally from point x_{i} to $x_{\mathrm{i+1}}$, with a load magnitude V_{i}. The centre of each mountain block is at $x_{\mathrm{i+1}} - x_{\mathrm{i}}$. The load of each individual block (weight) is given by:

$$V_i = \int_{x_i}^{x_{i+1}} q(x)dx = \frac{1}{2}\{q(x_i) + q(x_{i+1})\}(x_{i+1} - x_i) \quad \text{(A.1)}$$

The deflection $w(x)$ of the downgoing plate is then calculated as the sum of all of the individual deflections under $i = N$ load blocks. For a semi-infinite (broken) elastic plate we use the function (Allen and Allen, 2013; Andeweg and Cloetingh, 1998a; Gutscher, 1995):

$$f(u) = \exp(-u)(\cos u) \quad \text{(A.2)}$$

where u is given by

$$u = \left|x - x_{c,i}\right|/\alpha \quad \text{(A.3)}$$

where $x_{c,i}$ is the position of the centre of each load block, and the flexural parameter, $\alpha = \left\{\frac{4D}{\Delta\rho g}\right\}^{1/4}$ (*D* is the flexural rigidity, g is gravity, and Δρ is the density difference between mantle and crust).

The deflection at any position x is then the sum of all the individual deflections;

$$w(x) = \sum_{i=1}^{N} \frac{V_i}{\Delta\rho g\alpha} f(u) \tag{A.4}$$

where the summation before $f(u)$ in is the maximum deflection for each load V_i.

A.4 Appendix Chapter 5

In this supporting material, text A1.4.1 describes how *LaMEM* solves the Navier-Stokes equations under the Boussinesq approach (Boussinesq, 1897). Text A1.4.2 describes how results from a GPM simulation can be used to generate synthetic seismic data. Figures are added to this description to enhance this workflow's reproducibility for future research. Additionally, this file contains Figures A4.1 to A4.7 which show the evolutions of models 60DF, 45DF, 30DF, 90DS, 60DS, 45DS, and 30DS in a similar style as Figure 5.5 in the thesis.

A.4.1 LaMEM

LaMEM is a 3*D* staggered finite difference code, written in *C* that relies on the *PetsC* library to solve the fundamental continuum equation mechanics equations under the *Boussinesq* approximation (Boussinesq, 1897);

$$\nabla\mathbf{v} = 0 \tag{A.5}$$

$$\nabla\underline{\underline{\tau}} - \nabla P - \rho\mathbf{g} = 0 \tag{A.6}$$

$$\rho Cp\frac{\partial T}{\partial t} - \nabla(k(\nabla T) - \rho A - S = 0 \quad \text{(A.7)}$$

eq. (A.5) is the mass conservation, where **v** is the velocity vector. **eq.** (A.6) is the Stokes equation or momentum conservation, where $\underline{\underline{\tau}}$ is the deviatoric stress tensor, P is the pressure, ρ is the density, and **g** is the gravity acceleration vector. **eq.** (A.7) is the conservation of energy equation, where T is the temperature field, C_p the heat capacity, k is the conductivity, A is the radiogenic heat production per unit of mass, and S is the dissipative heat production (which, for the purposes of this work is not active). Density is computed as a function of temperature alone according to the following equation:

$$\rho = \rho_0 (1 - \alpha(T_0 - T)) \quad \text{(A.8)}$$

where ρ_0 is the reference density at the reference temperature T_0. α is the thermal expansivity.

All these equations are solved simultaneously, using P and **v** as prime variable in the case of mass and momentum conservation equation, and T as prime variable for the energy conservation equation. To compute the stress from the velocity, *LaMEM*, in this particular work, is employing a viscoelasto-plastic (*VEP*) constitutive model. After the resolution of the system of equation (**eqs.** (A.5) and (A.6)), LaMEM uses the velocity to compute the strain rate tensor ($\underline{\underline{\dot{\varepsilon}}}$). $\underline{\underline{\dot{\varepsilon}}}$ is then used to compute each component of the $\underline{\underline{\tau}}$ tensor using a combination of *Maxwell* and *Kelvin-Voigt* constitutive model. This model is made of two parallel branches, one containing the main rheological mechanisms, and the other one the lower cut-off viscosity (η_L), a quantity needed to prevent numerical instabilities. We shortly describe the rheology used for the current work, neglecting some passages, for further details on the derivation, we invite the reader to refer to (Spang, 2022). We will use the second invariant of the deviatoric stress and strain rate tensor for facilitating the reading.

τ_{II}^{TOT} is the unknown variable and it is given by the sum of τ_{II}^{U}, the stress of the upper branch, and by τ_{II}^{L}, the stress of the lower branch. The stress in the low branch is given:

$$\tau_{II}^{L} = 2\varepsilon^{L}\dot{\varepsilon}_{II}^{TOT} \tag{A.9}$$

This represents the minimum stress possible for a given strain rate. On the other hand, the stress in the upper branch require a local-iteration approach to find the strain rate partitioning in each of the rheological mechanisms $\dot{\varepsilon}_{II}^{TOT}$. Within the upper branch of the constitutive model each of the rheological mechanism are connected in series. This imply that on each of these mechanism is acting the same τ (*i.e.,* τ_{II}^{U}). From this starting point, we can define the following relation:

$$\dot{\varepsilon}_{II}^{TOT} = \dot{\varepsilon}_{II}^{el} + \dot{\varepsilon}_{II}^{pl} + \dot{\varepsilon}_{II}^{D} + \dot{\varepsilon}_{II}^{N} + \dot{\varepsilon}_{II}^{U} \tag{A.10}$$

where the superscript el, D, N, pl and U indicates respectively the elastic, diffusion, dislocation, plastic and upper cut-off mechanisms. We can relate the strain rate and the stress using the following equation:

$$\dot{\varepsilon}_{II} = \frac{\tau_{II}^{U}}{2\eta} \tag{A.11}$$

where $\dot{\varepsilon_{II}}$ is the strain rate (can be the total or one of the rheological mechanism), and η is the viscosity associated with a particular mechanism:

$$\dot{\varepsilon}_{II}^{TOT} - \frac{1}{2G}\frac{\tau_{II}^{+}}{\Delta t} = \frac{\tau_{II}^{U}}{2\eta_D} + \left(\frac{\tau_{II}^{U}}{2\eta_{N0}}\right)^{n} + \frac{\tau_{II}^{U}}{2\eta_U} + \dot{\varepsilon}^{pl} + \frac{1}{2G}\frac{\tau_{II}^{U}}{\Delta t} \tag{A.12}$$

η_D is the diffusion creep viscosity:

$$\eta_D = 0.5B_D \exp\left(\frac{E_D^{\alpha} + PV_D^{\alpha}}{RT}\right) \tag{A.13}$$

B_D is the pre-exponential factor, E_D^{a} and V_D^{a} are the activation energy and volume, and R is the ideal gas constant. η_{N0} is the strain independent dislocation creep:

$$\eta_{N_0} = 0.5B_N^{\frac{1}{n}} \exp\left(\frac{E_N^{\alpha} + PV_N^{\alpha}}{RT}\right) \tag{A.14}$$

where B_N is the pre-exponential factor, n is the stress exponent, and E_N^{a} and V_N^{a} are the activation energy and volume.

G is the shear modulus, Δt the current timestep. τ^{+} is the stress of the previous timestep. The elastic strain rate is equal to the stress derivative with time:

$$\varepsilon_{ij} = \frac{1}{2G}\frac{\tau_{ij}^{U} - \tau_{ij}^{+}}{\Delta t} \tag{A.15}$$

The stress derivative is computed using the full tensor formulation. And after the computation of each components, it can be converted into the second invariant formulation. The old stress, since it is constant can be transfered into the left side of the equations. $\dot{\varepsilon_{II}}$ is computed using the following strategy. First, we define the yield function:

$$F = \tau_{II} - Ccos(\phi) - Psin(\phi) \tag{A.16}$$

ϕ is the friction angle, C is the cohesion and F is the yield function. Both ϕ and C can evolve as a function of the total accumulated plastic strain. F must be equal or less than 0. If not, τ_{II} must be reduced accordingly, causing plastic deformation. When LaMEM computes the partition between the mechanism, finds an initial guess of τ_{II}^{U} . If τ_{II}^{U} yields a $F \leq 0$ the deformation is accommodated by creep mechanisms and elastic deformation, In the second case, τ_{II}^{U} is adjusted to fulfill $F \leq 0$ critieria, implying that:

$$\dot{\varepsilon}^{pl} = \left(\dot{\varepsilon}_{II}^{TOT} - \frac{1}{2G}\frac{\tau_{ij}^{+}}{\Delta t}\right) - \left(\frac{\tau_{II}^{U}}{2\eta_D} + \left(\frac{\tau_{II}^{U}}{2\eta_{N^0}}\right)^{n} + \frac{\tau_{II}^{U}}{2\eta_U} + \dot{\varepsilon}^{pl} + \frac{1}{2G}\frac{\tau_{II}^{U}}{\Delta t}\right) \tag{A.17}$$

After the τ^{U} is computed, the total stress can be computed by summing the lower and upper branch. After the resolution of the system of equation the material properties are explicitly advected using markers. Markers carry information concerning the phases and historical value such as the stress component, plastic deformation and temperature. LaMEM employs an internal free surface for tracking the topographic evolution. The free surface is initialised at the beginning of the simulation, and as a function of the density distribution within the numerical domain. Each timestep, the velocity is interpolated in the free surface, and it is displaced accordingly.

A.4.2 Generation of synthetic seismic data

Note. Step 1 is only required when (part of) the basin fill in the generated GPM model is positioned above Z=0. If this is not the case, skip to step 2.

Step 1: First, a GPM model must be generated of which the end time is set just before 0. From this GPM model, extract the stratigraphic surfaces of the last timestep. This is done by selecting the "simulation results converter" option by right-clicking on the model result and selecting the "convert to surfaces" option for the last timestep (select none of the properties, Figure A4.1). From these extracted surfaces, calculate the stratigraphic thickness. Additionally, extract the surface of the basin floor. Shift the topography of this surface down by the Z-value of the top of the basin fill. Lastly, calculate the average water depth of the (portion of) the submerged basin.

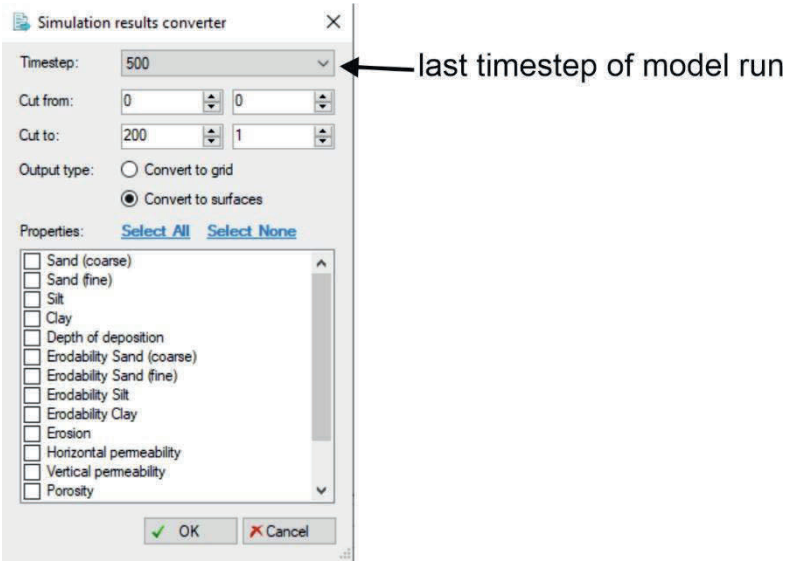

Figure A4.1: Prompt for converting GPM model results to XYZ surfaces.

Second, right-click the model results and select the “trim simulation to right position and age option”. In the prompt, give as input the basin floor that was shifted down in the previous step, the calculated model thickness, select the “cut top” option and give a top age of 0 a. The resulting GPM model will now be shifted downward such that the stratigraphic fill of the basin is completely located below Z=0, which is required to generate synthetic seismic data.

Step 2: Right-click the GPM model and select the “stack models and convert to gird” option. This will create a 3D grid in the model pane that includes all properties of the GPM result. For this grid, the lithostatic pressure is calculated using Eq. (A.18) (Karimi et al., 2014);

$$P = P_0 + g\rho_s \int_0^D dz \tag{A.18}$$

- P is the pressure
- $P_0 = g\rho_w H$ is the pressure at the basin floor due to the overlying water column.
    - g is the gravitational acceleration on Earth (9.81 m/A4.5).
    - ρ_w is the water density (997 kg/m^3).
    - H is the average water depth in the basin.
- ρ_s is the sediment density (2700 kg/m^3)
- D is the thickness of the overlying sediment package.
- z is the depth.

This will generate the subsurface pressure distribution in Pa in the model grid.

Step 3: To calculate a synthetic seismic response, the elastic properties of the subsurface must first be calculated. This is done using the “reservoir elastic modelling” tool in Petrel. Use the porosity and pressure values calculated in the prompt in the grid. The reader is attended to the fact that the pressure

calculated in step 2 is in Pa, whereas for the calculation of the elastic properties the pressure in MPa has to be supplied. Other values were kept default, where we assume most of the porosity is filled with water and a minor contribution of oil.

We selected the Voigt-Reuss bounds in the rocks physics tab (this will give the subsurface elastic parameters' lower- and upper bounds) for the rock matrix. The Krief model (Krief et al., 1990) for the dry rock moduli was used to calculate the subsurface P- and S-wave velocities. For the material composition, we defined the fine- and coarse sand sediment types as quartz, silt as being muscovite-dominated, and clay as a mixture of clay and micas. Default values for the density and elastic properties in Petrel are used. For the fluid substitution model, we use the Gassmann model (expresses the effect of fluid in pore space on elastic properties of rocks, Gassmann, 1951). Together, this will generate P- and S-wavefield in the subsurface based on the elastic parameters supplied.

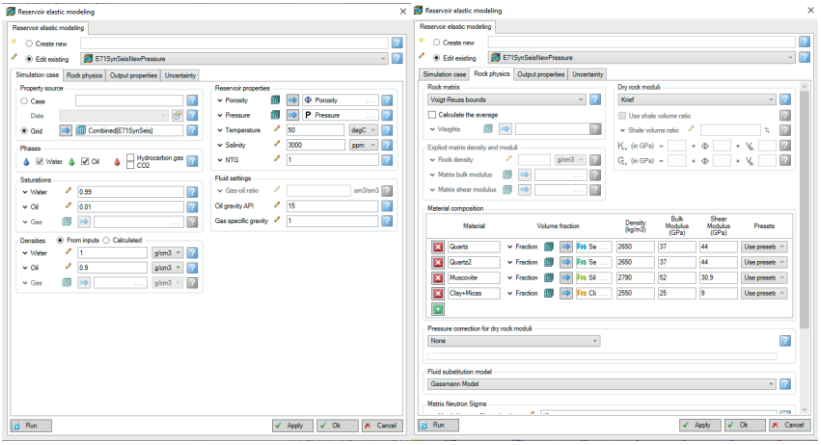

Figure A4.2: Inputs for the reservoir elastic modeling tool to calculate elastic parameters for the GPM grid, based on which the P-wave velocity field is calculated.

Step 4: With the wavelet toolbox, a Ricker wavelet is generated which is commonly used for generating synthetic seismic data (Gholamy and Kreinovich, 2014). We used the default wavelet characteristics (length of 128 ms, sampling rate of 2 ms, and central frequency of 25 Hz). Furthermore, from the calculated P-wave velocity field in the grid, we generated a velocity cube with a vertical increment of 2 ms.

Step 5: Subsequently, reservoir AVO modelling option in the volume attributes tool is used. This tool generates synthetic seismic traces by convolving the supplied wavelet with the reflection coefficients computed from the elastic properties, the P-wave velocity field, bulk density, and source wavelet (Figure A4.3). Other parameters were kept default (Figure A4.3).

A.4.3 Figures Chapter 5

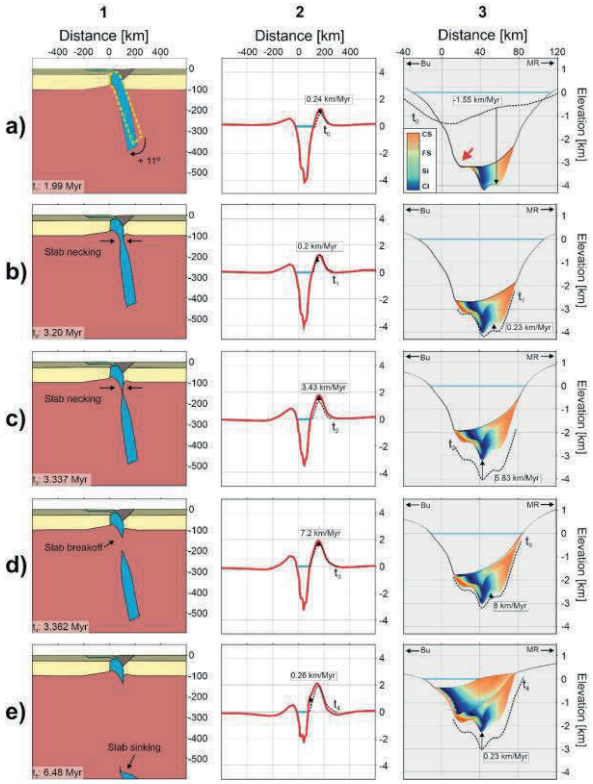

Figure A4.4: Evolution of model 60DF. The left panel shows the geodynamic evolution, the middle panels the corresponding surface topography, and the right panels the corresponding SFM evolution. The solid blue lines in the SFM indicates up until which level the basin is filled with water. The geodynamical models have the same colour bar used in Figure 5.2. When uplift is negligible (< 100 m) with respect to the previous timestep, no magnitude is shown. **a)** 60° subduction of the oceanic slab during continental collision (1.99 Myr) during which the slab steepens by 11° to 71°. Red arrow shows progradation of sediments over intrabasinal bump, unrelated to a lithospheric forcing mechanism; **b)** Initial slab necking at a depth of 120 km coeval with subsidence of the foreland basin due to slab pull (3.20 Myr); **c)** Late phase of slab necking correlating with foreland basin uplift (3.34 Myr); **d)** slab breakoff at 120 km depth (3.40 Myr); **e)** slab avalanching (6.48 Myr). **CS** = coarse sand, **FS** = fine sand, **Si** = silt, **Cl** = clay, see Table A4.2 for the sediment type characteristics. **MR** = mountain range, **Bu** = forebulge.

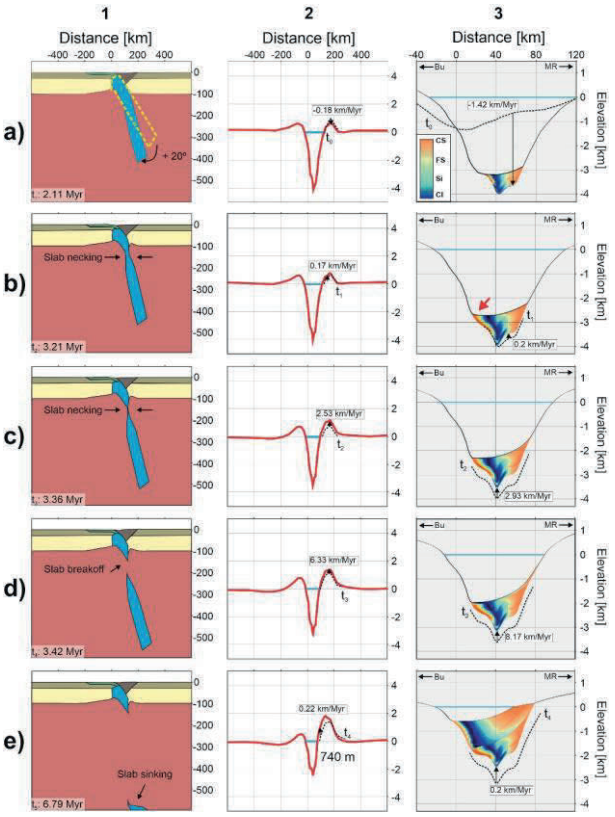

Figure A4.5: Evolution of model 45DF. The left panel shows the geodynamic evolution, the middle panels the corresponding surface topography, and the right panels the corresponding SFM evolution. The solid blue lines in the SFM indicates up until which level the basin is filled with water. The geodynamical models have the same colour bar used in Figure 5.2. When uplift is negligible (< 100 m) with respect to the previous timestep, no magnitude is shown. **a)** 45° subduction of the oceanic slab during continental collision (2.11 Myr) during which the slab steepens with 20° to 65°; **b)** Initial slab necking at 135 km depth coeval with subsidence of the foreland basin due to slab pull (3.21 Myr). The red arrow shows progradation of deposition over an intrabasinal bump, unrelated to lithospheric forcing mechanisms; **c)** Late slab necking correlating with foreland basin uplift (3.36 Myr); **d)** Slab breakoff at 135 km depth (3.42 Myr); **e)** slab avalanching (6.79 Myr); **CS** = coarse sand, **FS** = fine sand, **Si** = silt, **Cl** = clay, see Table A4.2 for the sediment type characteristics. **MR** = mountain range, **Bu** = forebulge.

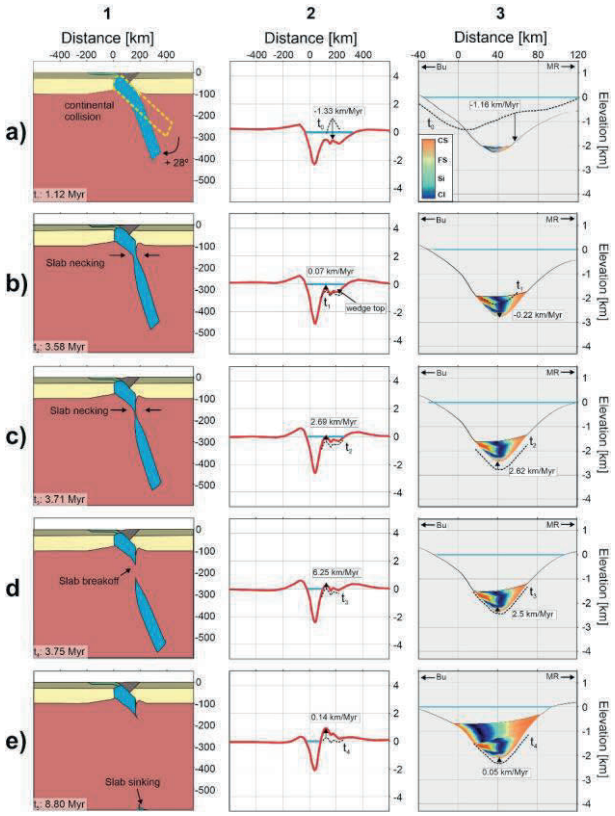

Figure A4.6: Evolution of model 30DF. The left panel shows the geodynamic evolution, the middle panels the corresponding surface topography, and the right panels the corresponding SFM evolution. The solid blue lines in the SFM indicates up until which level the basin is filled with water. The geodynamical models have the same colour bar used in Figure 5.2. When uplift is negligible (< 100 m) with respect to the previous timestep, no magnitude is shown. **a)** 30° subduction of the oceanic slab during continental collision during which the slab steepens and the foreland basin subsides (1.12 Myr) during which the slab steepens with 28° to 58°; **b)** Early slab necking at 150 km depth coeval with subsidence of the foreland basin due to slab pull (3.58 Myr); **c)** Late slab necking already causing isostatic rebound of foreland basin (3.71 Myr); **d)** slab breakoff at 150 km depth (3.75 Myr); **e)** Slab avalanching (4.22 Myr); **CS** = coarse sand, **FS** = fine sand, **Si** = silt, **Cl** = clay, see Table A4.2 for the sediment type characteristics. MR = mountain range, Bu = forebulge.

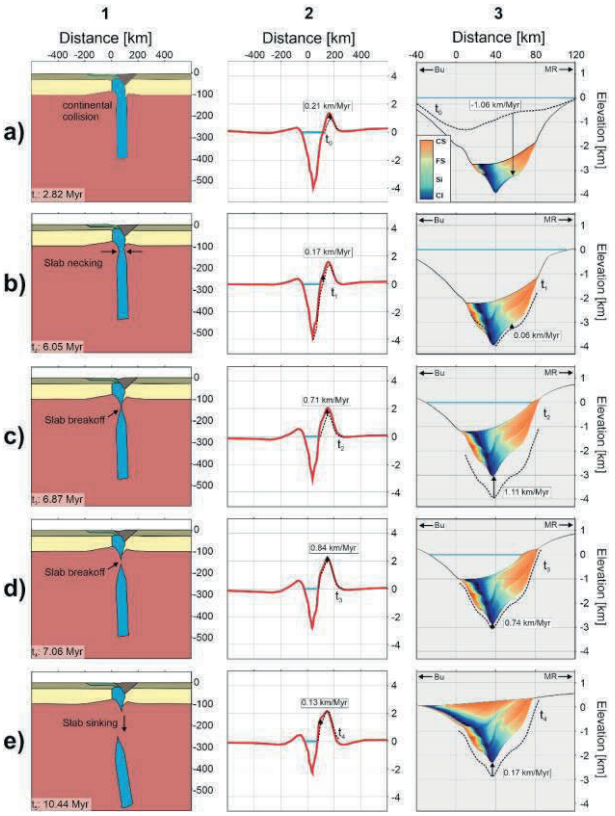

Figure A4.7: Evolution of model 90DS. The left panel shows the geodynamic evolution, the middle panels the corresponding surface topography, and the right panels the corresponding SFM evolution. The solid blue lines in the SFM indicates up until which level the basin is filled with water. The geodynamical models have the same colour bar used in Figure 5.2. When uplift is negligible (< 100 m) with respect to the previous timestep, no magnitude is shown. **a)** 90° subduction of the oceanic slab during continental collision during which slab pull causes subsidence of the foreland basin (4.32 Myr); **b)** Early slab necking at 120 km depth coeval with uplift of the proximal margin of the foreland basin (6.05 Myr); **c)** Late slab necking already causing isostatic rebound of foreland basin and mountain range (6.87 Myr); **d)** slab breakoff at 120 km depth (7.06 Myr); **e)** slab sinking resulting in continued transient uplift of the foreland basin (10.44 Myr); **CS** = coarse sand, **FS** = fine sand, **Si** = silt, **Cl** = clay, see Table A4.2 for the sediment type characteristics. **MR** = mountain range, **Bu** = forebulge.

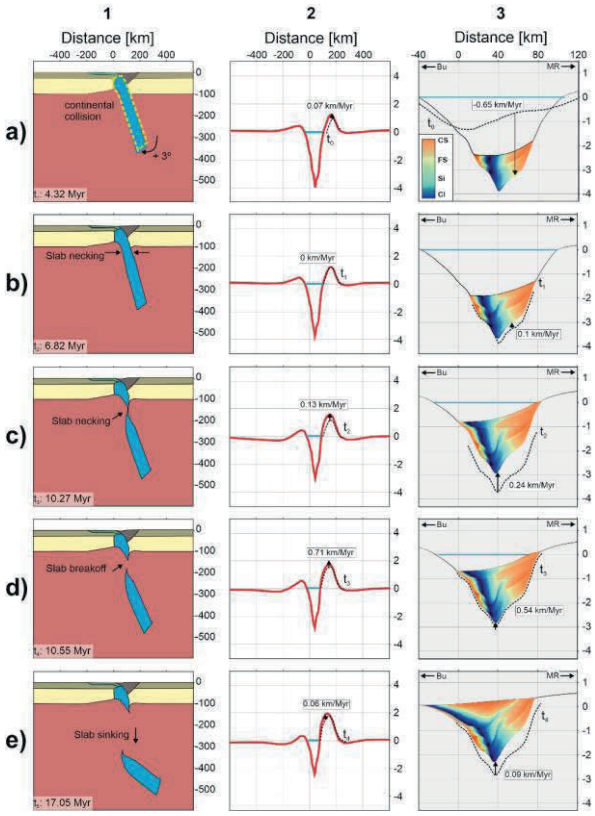

Figure A4.8: Evolution of model 60DS. The left panel shows the geodynamic evolution, the middle panels the corresponding surface topography, and the right panels the corresponding SFM evolution. The solid blue lines in the SFM indicates up until which level the basin is filled with water. The geodynamical models have the same colour bar used in Figure 5.2. When uplift is negligible (< 100 m) with respect to the previous timestep, no magnitude is shown. **a)** 60° subduction of the oceanic slab during continental collision during which slab pull causes subsidence of the foreland basin during which the slab steepens to 63° (4.32 Myr); **b)** Early slab necking at 120 km depth coeval with uplift of the proximal margin of the foreland basin (6.82 Myr); **c)** Late slab necking already causing isostatic rebound of foreland basin and mountain range (10.27 Myr); **d)** slab breakoff at 120 km depth (10.55 Myr); **e)** slab sinking resulting in continued transient uplift of the foreland basin (17.05 Myr); **CS** = coarse sand, **FS** = fine sand, **Si** = silt, **Cl** = clay, see Table A4.2 for the sediment type characteristics. **MR** = mountain range, **Bu** = forebulge.

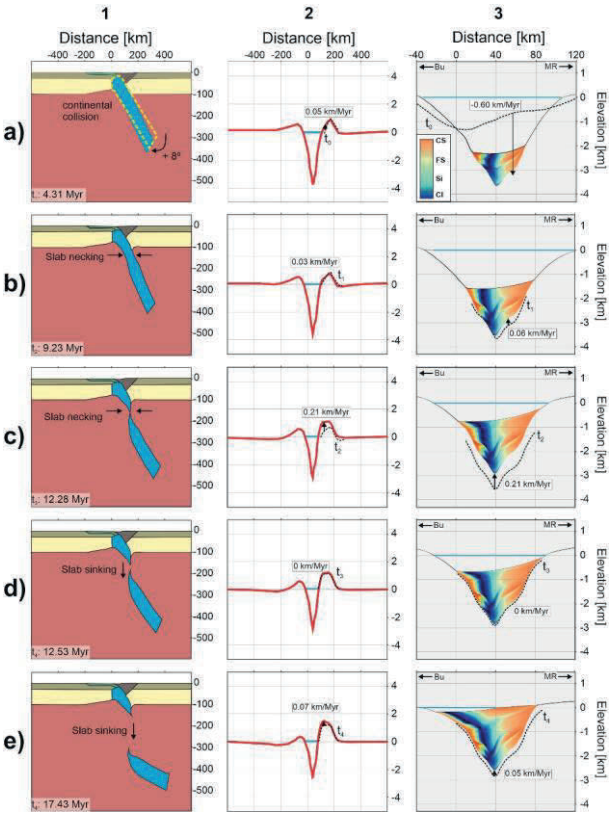

Figure A4.9: Evolution of model 45DS. The left panel shows the geodynamic evolution, the middle panels the corresponding surface topography, and the right panels the corresponding SFM evolution. The solid blue lines in the SFM indicates up until which level the basin is filled with water. The geodynamical models have the same colour bar used in Figure 5.2. When uplift is negligible (< 100 m) with respect to the previous timestep, no magnitude is shown. **a)** 45° subduction of the oceanic slab during continental collision during which slab pull causes subsidence of the foreland basin during which the slab steepens to 51° (4.31 Myr); **b)** Early slab necking at 130 km depth coeval with uplift of the proximal margin of the foreland basin (9.23 Myr); **c)** Late slab necking already causing isostatic rebound of foreland basin and mountain range (12.28 Myr); **d)** slab breakoff at 130 km depth (12.53 Myr); **e)** slab sinking resulting in continued transient uplift of the foreland basin (17.43 Myr); **CS** = coarse sand, **FS** = fine sand, **Si** = silt, **Cl** = clay, see Table A4.2 for the sediment type characteristics. **MR** = mountain range, **Bu** = forebulge.

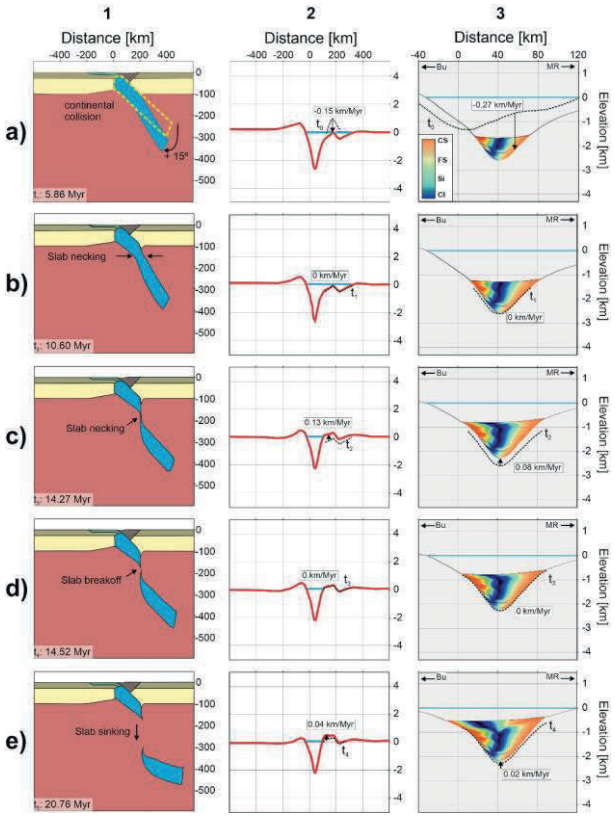

Figure A4.10: Evolution of model 30DS. The left panel shows the geodynamic evolution, the middle panels the corresponding surface topography, and the right panels the corresponding SFM evolution. The solid blue lines in the SFM indicates up until which level the basin is filled with water. The geodynamical models have the same colour bar used in Figure 5.2. When uplift is negligible (< 100 m) with respect to the previous timestep, no magnitude is shown. **a)** 30° subduction of the oceanic slab during continental collision during which slab pull causes subsidence of the foreland basin during which the slab steepens to 45° (5.86 Myr); **b)** Early slab necking at 150 km depth coeval with uplift of the proximal margin of the foreland basin (10.60 Myr); **c)** Late slab necking already causing isostatic rebound of foreland basin and mountain range (14.27 Myr); **d)** slab breakoff at 150 km depth (14.52 Myr); **e)** slab sinking resulting in continued transient uplift of the foreland basin (20.76 Myr); **CS** = coarse sand, **FS** = fine sand, **Si** = silt, **Cl** = clay, see Table A4.2 for the sediment type characteristics. **MR** = mountain range, **Bu** = forebulge.

A.4.4 Chapter 5 additional tables

Table A4.1: Table of material properties for the geodynamic models. The activation volume of the dislocation creep of the upper mantle and the oceanic slab are target parameters. All materials have the same G (shear modulus) of 50 GPa. α is the same for all material properties at $3e^{-5}$ K^{-1}. C_p is the same for all phases at 1050 $JKg^{-1}K^{-1}$. k is the constant for all phases at 3.0 $Wm^{-2}K^{-1}$. The radiogenic heat production A per unit mass is 0.

Rock unit	Rheological law	B_D (Pa^{-1})	E_D^a (KJ * mol^{-1})	V_D^a (µm^3 * mol^{-1})	n	B_n ($Pa^{-n}s^{-1}$)
Upper crust	Wet Plagioclase	4.742^{-11}	159	38	3.0	$1.130e^{-15}$
Lower crust	Wet Plagioclase	$1.5e^{-9}$	159	38	3.0	$1.130e^{-15}$
Continental mantle lithosphere	Dry Olivine	$1.5e^{-9}$	159	5	3.5	$6.22e^{-16}$
Oceanic slab & upper mantle	Dry Olivine	4.742^{-11}	159	5	3.5	$6.22e^{-16}$
Orogenic prism & passive margin	Wet Plagioclase	4.742^{-11}	159	38	3.0	$1.130e^{-15}$

Table A4.1 (continued):

Rock unit	E_N^a (KJ * mol^{-1})	V_N^a (µm^3 * mol^{-1})	ρ_0 (kg * m^{-3})	C	ϕ
Upper crust	345	38	2700	10	30
Lower crust	345	38	2750	10	30
Continental mantle lithosphere	530	5	3290	10	30
Oceanic slab & upper mantle	530	5	3290	1	5.0
Orogenic prism & passive margin	345	38	2700	1	5.0

Table A4.2: Sediment type characteristics used in the stratigraphic forward models.

Sediment type	Density (kg/m³)	Grains size diameter (mm)	Erdobility (n.d.)
Coarse sand	0.8	1	1
Fine sand	1.6	0.1	1
Silt	3.2	0.01	1
Clay	6.4	0.001	1

Sediment type	Transportability (n.d.)	Initial porosity (m³/m³)	Compaction factor (kPa)
Coarse sand	0.8	0.4	60000
Fine sand	1.6	0.4	50000
Silt	3.2	0.55	30000
Clay	6.4	0.55	15000

References

Alexander, W.R., Reijonen, H.M. and McKinley, I.G., 2015. Natural analogues: studies of geological processes relevant to radioactive waste disposal in deep geological repositories. Swiss Journal of Geosciences, 108(1): 75-100.

Alipour, M., 2023. Collision along irregular plate margin controlled the tectono-stratigraphic evolution of the Iranian Zagros fold and thrust belt. Marine and Petroleum Geology, 154: 106311.

Allen, P.A., 2008. From landscapes into geological history. Nature, 451(7176): 274-276.

Allen, P.A. and Allen, J.R., 2013. Basin analysis: Principles and application to petroleum play assessment. John Wiley & Sons.

Allen, P.A., Crampton, S.L. and Sinclair, H.D., 1991. The inception and early evolution of the North Alpine Foreland Basin, Switzerland. Basin Research, 3(3): 143-163.

Amadori, C., Toscani, G., Di Giulio, A., Maesano, F.E., D'Ambrogi, C., Ghielmi, M. and Fantoni, R., 2019. From cylindrical to non-cylindrical foreland basin: Pliocene–Pleistocene evolution of the Po Plain–Northern Adriatic basin (Italy). Basin Research, 31(5): 991-1015.

Andeweg, B. and Cloetingh, S., 1998a. Flexure and 'unflexure'of the North Alpine German-Austrian.

Andeweg, B. and Cloetingh, S., 1998b. Flexure and 'unflexure'of the North Alpine German-Austrian Molasse Basin: constraints from forward tectonic modelling. Geological Society, London, Special Publications, 134(1): 403-422.

Andrews, E.R. and Billen, M.I., 2009. Rheologic controls on the dynamics of slab detachment. Tectonophysics, 464(1-4): 60-69.

Andrić, N., Matenco, L., Hilgen, F. and de Bresser, H., 2018a. Structural controls on sedimentation during asymmetric extension: the case of Sorbas Basin (SE Spain). Global and planetary change, 171: 185-206.

Andrić, N., Vogt, K., Matenco, L., Cvetković, V., Cloetingh, S. and Gerya, T., 2018b. Variability of orogenic magmatism during Mediterranean-style continental collisions: A numerical modelling approach. Gondwana Research, 56: 119-134.

Andrić-Tomašević, N., Koptev, A., Maiti, G., Gerya, T. and Ehlers, T.A., 2023. Slab tearing in non-collisional settings: Insights from thermo-mechanical modelling of oblique subduction. Earth and Planetary Science Letters, 610: 118097.

Angrand, P., Ford, M. and Watts, A.B., 2018. Lateral variations in foreland flexure of a rifted continental margin: The Aquitaine Basin (SW France). Tectonics, 37(2): 430-449.

Ascione, A., Ciarcia, S., Di Donato, V., Mazzoli, S. and Vitale, S., 2012. The Pliocene-Quaternary wedge-top basins of southern Italy: An expression of propagating lateral slab tear beneath the Apennines. Basin Research, 24(4): 456-474.

Bachmann, G.H. and Müller, M., 1991. The Molasse basin, Germany: evolution of a classic petroliferous foreland basin. Generation, accumulation, and production of Europe's hydrocarbons. Special publication of the European association of petroleum geoscientists. Eur Assoc Pet Geosci Spec Publ, 1: 263-276.

Bachu, S., 2003. Screening and ranking of sedimentary basins for sequestration of CO2 in geological media in response to climate change. Environmental Geology, 44(3): 277-289.

Ballato, P., Nowaczyk, N.R., Landgraf, A., Strecker, M.R., Friedrich, A. and Tabatabaei, S.H., 2008. Tectonic control on sedimentary facies pattern and sediment accumulation rates in the Miocene foreland basin of the southern Alborz mountains, northern Iran. Tectonics, 27(6).

Barth, S., Oberli, F. and Meier, M., 1989. U—Th—Pb systematics of morphologically characterized zircon and allanite: a high-resolution isotopic study of the Alpine Rensen pluton (northern Italy). Earth and Planetary Science Letters, 95(3-4): 235-254.

Bartosch, T., Stüwe, K. and Robl, J., 2017. Topographic evolution of the Eastern Alps: The influence of strike-slip faulting activity. Lithosphere, 9(3): 384-398.

Baudon, C. and Cartwright, J., 2008. Early stage evolution of growth faults: 3D seismic insights from the Levant Basin, Eastern Mediterranean. Journal of Structural Geology, 30(7): 888-898.

Baumann, C., Gerya, T.V. and Connolly, J.A., 2010. Numerical modelling of spontaneous slab breakoff dynamics during continental collision. Geological Society, London, Special Publications, 332(1): 99-114.

Beaumont, C., 1981. Foreland basins. Geophysical Journal International, 65(2): 291-329.

Beidinger, A. and Decker, K., 2014. Quantifying Early Miocene in-sequence and out-of-sequence thrusting at the Alpine-Carpathian junction. Tectonics, 33(3): 222-252.

Bercovici, D., Schubert, G. and Ricard, Y., 2015. Abrupt tectonics and rapid slab detachment with grain damage. Proceedings of the National Academy of Sciences, 112(5): 1287-1291.

Bieg, U., Süss, M.P. and Kuhlemann, J., 2008. Simulation of tidal flow and circulation patterns in the Early Miocene (Upper Marine Molasse) of the Alpine foreland basin. Analogue and Numerical Modelling of Sedimentary Systems: From Understanding to Prediction, 40: 145-169.

Boonma, K., García-Castellanos, D., Jiménez-Munt, I. and Gerya, T.V., 2022. Thermomechanical modelling of lithospheric slab tearing and its topographic response. Application to the Gibraltar Arc. Authorea Preprints.

Borzi, A., McPhee, P., Hülscher, J., LeBreton, E., Handy, M.R. and Bernhard, A., 2022. Major Neogene shift in the structural and sedimentary evolution of the North Alpine Foreland Basin, 6th Annual AlpArray scientific meeting, Prague.

Bosworth, W., 1985. Geometry of propagating continental rifts. Nature, 316(6029): 625-627.

Boussinesq, J., 1897. Théorie de l'écoulement tourbillonnant et tumultueux des liquides dans les lits rectilignes à grande section, 1. Gauthier-Villars.

Bradley, D. and Kidd, W., 1991. Flexural extension of the upper continental crust in collisional foredeeps. Geological Society of America Bulletin, 103(11): 1416-1438.

Brink, H.-J., Burri, P., Lunde, A. and Winhard, H., 1992. Hydrocarbon habitat and potential of Swiss and German Molasse Basin: a comparison. Eclogae Geologicae Helvetiae, 85(3): 715-732.

Bry, M., White, N., Singh, S., England, R. and Trowell, C., 2004. Anatomy and formation of oblique continental collision: South Falkland basin. Tectonics, 23(4).

Budach, I., Moeck, I., Lüschen, E. and Wolfgramm, M., 2018. Temporal evolution of fault systems in the Upper Jurassic of the Central

German Molasse Basin: case study Unterhaching. International Journal of Earth Sciences, 107(2): 635-653.

Buiter, S.J., Govers, R. and Wortel, M., 2002. Two-dimensional simulations of surface deformation caused by slab detachment. Tectonophysics, 354(3-4): 195-210.

Burbank, D., 2002. Rates of erosion and their implications for exhumation. Mineralogical Magazine, 66(1): 25-52.

Burbank, D., Beck, R., Raynolds, R., Hobbs, R. and Tahirkheli, R., 1988. Thrusting and gravel progradation in foreland basins: A test of post-thrusting gravel dispersal. Geology, 16(12): 1143-1146.

Burkhard, M., 1988. L'Helvétique de la bordure occidentale du massif de l'Aar (évolution tectonique et métamorphique). Eclogae Geologicae Helvetiae, 81(1): 63-114.

Burkhard, M. and Sommaruga, A., 1998. Evolution of the western Swiss Molasse basin: structural relations with the Alps and the Jura belt. Geological Society, London, Special Publications, 134(1): 279-298.

Burov, E., 2010. The equivalent elastic thickness (Te), seismicity and the long-term rheology of continental lithosphere: time to burn-out “crème brûlée”?: insights from large-scale geodynamic modeling. Tectonophysics, 484(1-4): 4-26.

Burov, E. and Yamato, P., 2008. Continental plate collision, P–T–t–z conditions and unstable vs. stable plate dynamics: insights from thermo-mechanical modelling. Lithos, 103(1-2): 178-204.

Burov, E.B., 2011. Rheology and strength of the lithosphere. Marine and petroleum Geology, 28(8): 1402-1443.

Cacace, M., Kaiser, B.O., Lewerenz, B. and Scheck-Wenderoth, M., 2010. Geothermal energy in sedimentary basins: What we can learn from regional numerical models. Geochemistry, 70: 33-46.

Calignano, E., Sokoutis, D., Willingshofer, E., Gueydan, F. and Cloetingh, S., 2015. Strain localization at the margins of strong lithospheric domains: Insights from analog models. Tectonics, 34(3): 396-412.

Capitanio, F.A., Morra, G. and Goes, S., 2007. Dynamic models of downgoing plate-buoyancy driven subduction: Subduction motions and energy dissipation. Earth and Planetary Science Letters, 262(1-2): 284-297.

Caputo, R., Poli, M.E. and Zanferrari, A., 2010. Neogene–Quaternary tectonic stratigraphy of the eastern Southern Alps, NE Italy. Journal of Structural Geology, 32(7): 1009-1027.

Cardozo, N. and Jordan, T., 2001. Causes of spatially variable tectonic subsidence in the Miocene Bermejo Foreland Basin, Argentina. Basin Research, 13(3): 335-357.

Carroll, A.R. and Bohacs, K.M., 1999. Stratigraphic classification of ancient lakes: Balancing tectonic and climatic controls. Geology, 27(2): 99-102.

Cartwright, J.A., Mansfield, C. and Trudgill, B., 1996. The growth of normal faults by segment linkage. Geological Society, London, Special Publications, 99(1): 163-177.

Catuneanu, O., 2004a. Basement control on flexural profiles and the distribution of foreland facies: the Dwyka Group of the Karoo Basin, South Africa. Geology, 32(6): 517-520.

Catuneanu, O., 2004b. Retroarc foreland systems—evolution through time. Journal of African Earth Sciences, 38(3): 225-242.

Catuneanu, O., Abreu, V., Bhattacharya, J., Blum, M., Dalrymple, R., Eriksson, P., Fielding, C.R., Fisher, W., Galloway, W. and Gibling, M., 2009. Towards the standardization of sequence stratigraphy. Earth-Science Reviews, 92(1-2): 1-33.

Caumon, G. and Mallet, J.-L., 2006. 3D Stratigraphic models: representation and stochastic modelling, Int. Assoc. for Mathematical Geology–XIth International Congres. 4p.

Champagnac, J.-D., Schlunegger, F., Norton, K., von Blanckenburg, F., Abbühl, L.M. and Schwab, M., 2009. Erosion-driven uplift of the modern Central Alps. Tectonophysics, 474(1-2): 236-249.

Chang, J.-H., Yu, H.-S., Hsu, H.-H. and Liu, C.-S., 2012. Forebulge migration in late Cenozoic Western Taiwan foreland basin. Tectonophysics, 578: 117-125.

Chapman, T. and Meneilly, A., 1991. The displacement patterns associated with a reverse-reactivated, normal growth fault. Geological Society, London, Special Publications, 56(1): 183-191.

Chertova, M., Spakman, W., Geenen, T., Van Den Berg, A. and Van Hinsbergen, D., 2014. Underpinning tectonic reconstructions of the western Mediterranean region with dynamic slab evolution from 3-D numerical modeling. Journal of Geophysical Research: Solid Earth, 119(7): 5876-5902.

Coakley, B.J. and Watts, A.B., 1991. Tectonic controls on the development of unconformities: the North Slope, Alaska. Tectonics, 10(1): 101-130.

Cooper, M., Addison, F., Alvarez, R., Coral, M., Graham, R., Hayward, A., Howe, S., Martinez, J., Naar, J. and Peñas, R., 1995. Basin development and tectonic history of the Llanos Basin, Eastern Cordillera, and middle Magdalena Valley, Colombia. AAPG bulletin, 79(10): 1421-1442.

Cordero Peña, F.A., 2007. The early miocene upper marine molasse of the German part of the Molasse Basin: a subsurface study; sequence stratigraphy, depositional environment and architecture, 3D basin modeling, Tübingen, Univ., Diss., 2007.

Covault, J.A., Hubbard, S.M., Graham, S.A., Hinsch, R. and Linzer, H.-G., 2009. Turbidite-reservoir architecture in complex foredeep-margin and wedge-top depocenters, Tertiary Molasse foreland basin system, Austria. Marine and Petroleum Geology, 26(3): 379-396.

Covey, M., 1986. The evolution of foreland basins to steady state: evidence from the western Taiwan foreland basin. Foreland basins: 77-90.

Crampton, S. and Allen, P., 1995. Recognition of forebulge unconformities associated with early stage foreland basin development: example from the North Alpine Foreland Basin. AAPG bulletin, 79(10): 1495-1514.

Croissant, T., Steer, P., Lague, D., Davy, P., Jeandet, L. and Hilton, R.G., 2019. Seismic cycles, earthquakes, landslides and sediment fluxes: Linking tectonics to surface processes using a reduced-complexity model. Geomorphology, 339: 87-103.

Dal-Piaz, G.V., Del-Moro, A., Martin, S. and Venturelli, G., 1988. Post-collisional magmatism in the Ortler-Cevedale massif (Northern Italy). Jahrbuch der Geologischen Bundesanstalt, 131(4): 533-551.

Darin, M.H. and Umhoefer, P.J., 2022. Diachronous initiation of Arabia–Eurasia collision from eastern Anatolia to the southeastern Zagros Mountains since middle Eocene time. International Geology Review, 64(18): 2653-2681.

Davies, J.H. and von Blanckenburg, F., 1995. Slab breakoff: a model of lithosphere detachment and its test in the magmatism and deformation of collisional orogens. Earth and Planetary Science Letters, 129(1-4): 85-102.

De Ruig, M.J. and Hubbard, S.M., 2006. Seismic facies and reservoir characteristics of a deep-marine channel belt in the Molasse foreland basin, Puchkirchen Formation, Austria. AAPG bulletin, 90(5): 735-752.

DeCelles, P.G., 2012. Foreland basin systems revisited: Variations in response to tectonic settings. Tectonics of sedimentary basins: Recent advances: 405-426.

DeCelles, P.G. and Giles, K.A., 1996. Foreland basin systems. Basin Research, 8(2): 105-123.

DeCelles, P.G. and Horton, B.K., 2003. Early to middle Tertiary foreland basin development and the history of Andean crustal shortening in Bolivia. Geological Society of America Bulletin, 115(1): 58-77.

DeCelles, P.G. and Mitra, G., 1995. History of the Sevier orogenic wedge in terms of critical taper models, northeast Utah and southwest Wyoming. Geological Society of America Bulletin, 107(4): 454-462.

Dewey, J. and Kidd, W., 1974. Continental collisions in the Appalachian-Caledonian orogenic belt: Variations related to complete and incomplete suturing. Geology, 2(11): 543-546.

Di Giuseppe, E., Faccenna, C., Funiciello, F., van Hunen, J. and Giardini, D., 2009. On the relation between trench migration, seafloor age, and the strength of the subducting lithosphere. Lithosphere, 1(2): 121-128.

DiBiase, R.A. and Whipple, K.X., 2011. The influence of erosion thresholds and runoff variability on the relationships among topography, climate, and erosion rate. Journal of Geophysical Research: Earth Surface, 116(F4).

Diem, B., 1986. Die Untere Meeresmolasse zwischen der Saane (Westschweiz) und der Ammer (Oberbayern). Eclogae Geologicae Helvetiae, 79(2): 493-559.

Dunkl, I., Kuhlemann, J., Reinecker, J. and Frisch, W., 2005. Cenozoic relief evolution of the Eastern Alps–constraints from apatite fission track age-provenance of Neogene intramontane sediments. Austrian Journal of Earth Sciences, 98: 92-105.

Duretz, T., Gerya, T. and Spakman, W., 2014. Slab detachment in laterally varying subduction zones: 3-D numerical modeling. Geophysical Research Letters, 41(6): 1951-1956.

Duretz, T., Gerya, T.V. and May, D.A., 2011. Numerical modelling of spontaneous slab breakoff and subsequent topographic response. Tectonophysics, 502(1-2): 244-256.

Duretz, T., Schmalholz, S. and Gerya, T., 2012. Dynamics of slab detachment. Geochemistry, Geophysics, Geosystems, 13(3).

Ehlers, T.A. and Poulsen, C.J., 2009. Influence of Andean uplift on climate and paleoaltimetry estimates. Earth and Planetary Science Letters, 281(3-4): 238-248.

Eizenhöfer, P.R., Glotzbach, C., Kley, J. and Ehlers, T.A., 2023. Thermo-kinematic evolution of the Eastern European Alps along the TRANSALP transect. Tectonics: e2022TC007380.

Eskens, L.H., Andrić-Tomašević, N., Süss, P.M., Müller, M., Herrmann, R. and Ehlers, T.A., 2024. Lithospheric-and crustal-scale controls on variations in foreland basin development in the Northern Alpine Foreland Basin. Tectonophysics: 230283.

Faupl, P. and Wagreich, M., 2000. Late Jurassic to Eocene palaeogeography and geodynamic evolution of the Eastern Alps. Mitteilungen der Österreichischen Geologischen Gesellschaft, 92(1999): 79-94.

Favaro, S., Schuster, R., Handy, M.R., Scharf, A. and Pestal, G., 2015. Transition from orogen-perpendicular to orogen-parallel exhumation and cooling during crustal indentation—Key constraints from 147Sm/144Nd and 87Rb/87Sr geochronology (Tauern Window, Alps). Tectonophysics, 665: 1-16.

Fernández-García, C., Guillaume, B. and Brun, J.-P., 2019. 3D slab breakoff in laboratory experiments. Tectonophysics, 773: 228223.

Ferrari, L., 2004. Slab detachment control on mafic volcanic pulse and mantle heterogeneity in central Mexico. Geology, 32(1): 77-80.

Ferrari, L., Orozco-Esquivel, T., Manea, V. and Manea, M., 2012. The dynamic history of the Trans-Mexican Volcanic Belt and the Mexico subduction zone. Tectonophysics, 522: 122-149.

Filer, J.K., 2003. Stratigraphic evidence for a Late Devonian possible back-bulge basin in the Appalachian basin, United States. Basin Research, 15(3): 417-429.

Flemings, P.B. and Jordan, T.E., 1989. A synthetic stratigraphic model of foreland basin development. Journal of Geophysical Research: Solid Earth, 94(B4): 3851-3866.

Flemings, P.B. and Jordan, T.E., 1990. Stratigraphic modeling of foreland basins: interpreting thrust deformation and lithosphere rheology. Geology, 18(5): 430-434.

Fomel, S. and Landa, E., 2014. Structural uncertainty of time-migrated seismic images. Journal of Applied Geophysics, 101: 27-30.

Ford, M., Hemmer, L., Vacherat, A., Gallagher, K. and Christophoul, F., 2016. Retro-wedge foreland basin evolution along the ECORS line, eastern Pyrenees, France. Journal of the Geological Society, 173(3): 419-437.

Forsyth, D. and Uyeda, S., 1975. On the relative importance of the driving forces of plate motion. Geophysical Journal International, 43(1): 163-200.

Fosdick, J.C., Graham, S.A. and Hilley, G.E., 2014. Influence of attenuated lithosphere and sediment loading on flexure of the deep-water Magallanes retroarc foreland basin, Southern Andes. Tectonics, 33(12): 2505-2525.

Fox, M., Herman, F., Willett, S.D. and Schmid, S.M., 2016. The exhumation history of the European Alps inferred from linear inversion of thermochronometric data. American Journal of Science, 316(6): 505-541.

Freeburn, R., Bouilhol, P., Maunder, B., Magni, V. and van Hunen, J., 2017. Numerical models of the magmatic processes induced by slab breakoff. Earth and Planetary Science Letters, 478: 203-213.

Freudenberger, W. and Schwerd, K., 1996. Erläuterungen zur Geologischen Karte von Bayern 1: 500000.-4 Aufl., 329 S., 67 Abb., 21 Tab., 8 Beil. München (GLA).

Frisch, W., 1979. Tectonic progradation and plate tectonic evolution of the Alps. Tectonophysics, 60(3-4): 121-139.

Frisch, W., Kuhlemann, J., Dunkl, I. and Brügel, A., 1998. Palinspastic reconstruction and topographic evolution of the Eastern Alps during late Tertiary tectonic extrusion. Tectonophysics, 297(1-4): 1-15.

Frisch, W., Kuhlemann, J., Dunkl, I. and Székely, B., 2001. The Dachstein paleosurface and the Augenstein Formation in the Northern Calcareous Alps–a mosaic stone in the geomorphological evolution of the Eastern Alps. International Journal of Earth Sciences, 90: 500-518.

Fügenschuh, B., Seward, D. and Mancktelow, N., 1997. Exhumation in a convergent orogen: the western Tauern window. Terra nova, 9(5-6): 213-217.

Garefalakis, P. and Schlunegger, F., 2018. Link between concentrations of sediment flux and deep crustal processes beneath the European Alps. Scientific Reports, 8(1): 183.

Garefalakis, P. and Schlunegger, F., 2019. Tectonic processes, variations in sediment flux, and eustatic sea level recorded by the 20 Myr old

Burdigalian transgression in the Swiss Molasse basin. Solid Earth, 10(6): 2045-2072.

Gassmann, F., 1951. Elastic waves through a packing of spheres. Geophysics, 16(4): 673-685.

Gautschi, A., Schnellmann, M., Albert, W., Blümling, P., Vietor, T., Blaser, P. and Müller, H., 2008. Nagra Technischer Bericht 08-04: Vorschlag geologischer Standortgebiete für das SMA- und das HAA-Lager.

Gawthorpe, R.L., Jackson, C.A.-L., Young, M.J., Sharp, I.R., Moustafa, A.R. and Leppard, C.W., 2003. Normal fault growth, displacement localisation and the evolution of normal fault populations: the Hammam Faraun fault block, Suez rift, Egypt. Journal of Structural Geology, 25(6): 883-895.

Genser, J., Cloetingh, S.A. and Neubauer, F., 2007. Late orogenic rebound and oblique Alpine convergence: new constraints from subsidence analysis of the Austrian Molasse basin. Global and Planetary Change, 58(1-4): 214-223.

GeoMol, 2015. GeoMol – Assessing subsurface potentials of the Alpine Foreland Basins for sustainable planning and use of natural resources. Project Report: 188.

Gerya, T.V., Yuen, D.A. and Maresch, W.V., 2004. Thermomechanical modelling of slab detachment. Earth and Planetary Science Letters, 226(1-2): 101-116.

Gholamy, A. and Kreinovich, V., 2014. Why Ricker wavelets are successful in processing seismic data: Towards a theoretical explanation, 2014 IEEE Symposium on Computational Intelligence for Engineering Solutions (CIES). IEEE, pp. 11-16.

Giba, M., Nicol, A. and Walsh, J., 2010. Evolution of faulting and volcanism in a back-arc basin and its implications for subduction processes. Tectonics, 29(4).

Giba, M., Walsh, J. and Nicol, A., 2012. Segmentation and growth of an obliquely reactivated normal fault. Journal of Structural Geology, 39: 253-267.

Govers, R. and Wortel, M.J.R., 2005. Lithosphere tearing at STEP faults: response to edges of subduction zones. Earth and Planetary Science Letters, 236(1-2): 505-523.

Gross, D., Sachsenhofer, R., Rech, A., Sageder, S., Geissler, M., Schnitzer, S. and Troiss, W., 2015. The trattnach oil field in the north alpine foreland basin (Austria). Austrian J Earth Sci, 108(2): 151-171.

Grunert, P., Hinsch, R., Sachsenhofer, R.F., Bechtel, A., Ćorić, S., Harzhauser, M., Piller, W.E. and Sperl, H., 2013. Early Burdigalian infill of the Puchkirchen trough (North Alpine Foreland Basin, Central Paratethys): facies development and sequence stratigraphy. Marine and Petroleum Geology, 39(1): 164-186.

Gutscher, M.-A., 1995. Crustal structure and dynamics in the Rhine Graben and the Alpine foreland. Geophysical Journal International, 122(2): 617-636.

Gérard, B., Rouby, D., Huismans, R.S., Robin, C., Fillon, C. and Braun, J., 2023. Impact of Inherited Foreland Relief on Retro-Foreland Basin Architecture. Journal of Geophysical Research: Solid Earth, 128(3): e2022JB024967.

Gül, M., Gürbüz, K. and Cronin, B.T., 2015. Irregular plate boundary controls on foreland basin sedimentation (Miocene, Kahramanmaraş Foreland Basin, SE Turkey). Journal of Asian Earth Sciences, 111: 804-818.

Handy, M.R., Schmid, S.M., Bousquet, R., Kissling, E. and Bernoulli, D., 2010. Reconciling plate-tectonic reconstructions of Alpine Tethys with the geological–geophysical record of spreading and subduction in the Alps. Earth-Science Reviews, 102(3-4): 121-158.

Handy, M.R., Ustaszewski, K. and Kissling, E., 2015. Reconstructing the Alps–Carpathians–Dinarides as a key to understanding switches in subduction polarity, slab gaps and surface motion. International Journal of Earth Sciences, 104(1): 1-26.

Haq, B.U., Hardenbol, J. and Vail, P.R., 1987. Chronology of fluctuating sea levels since the Triassic. Science, 235(4793): 1156-1167.

He, B., Jiao, C., Xu, Z., Cai, Z., Zhang, J., Liu, S., Li, H., Chen, W. and Yu, Z., 2016. The paleotectonic and paleogeography reconstructions of the Tarim Basin and its adjacent areas (NW China) during the late Early and Middle Paleozoic. Gondwana Research, 30: 191-206.

Heberer, B., Bernhard, S., István, D., Reinhard, S., Tari, G., Wagreich, M., von Hagke, C. and Wessely, G., 2023a. Rapid Oligocene to Miocene cooling in the easternmost Alps driven by thrusting onto the Bohemian promontory and/or deep mantle processes, Copernicus Meetings.

Heberer, B., Salcher, B.C., Tari, G., Wessely, G., Dunkl, I., Sachsenhofer, R.F., Wagreich, M. and von Hagke, C., 2024. The impact of the Bohemian

Spur on the cooling and exhumation pattern of the Eastern Alpine wedge of the European Alps. Tectonics, 43(3): e2023TC008005.

Heberer, B., Salcher, S., Tari, G., Wessely, G., Dunkl, I., Sachsenhofer, R., Wagreich, M. and von Hsgke, C., 2023b. The impact of the Bohemian Spur on the cooling and exhumation pattern of the Eastern Alpine wedge, 4DMB, Bad Hofgastein.

Heckeberg, N., Pippèrr, M., Läuchli, B., Heimann, F.U. and Reichenbacher, B., 2010. The Upper Marine Molasse (Burdigalian, Ottnangian) in Southwest Germany-facies interpretation and a new lithostratigraphic terminology. Zeitschrift der Deutschen Gesellschaft fur Geowissenschaften, 161(3): 285.

Heimann, F.U., Schmid, D.U., Pipperr, M. and Reichenbacher, B., 2009. Re-interpreting the Baltringer Horizont as a subtidal channel facies: Implications for a new understanding of the Upper Marine Molasse" Cycles"(Early Miocene). Neues Jahrbuch fur Geologie und Palaontologie-Abhandlungen, 254(1): 135.

Hempton, M.R. and Dunne, L.A., 1984. Sedimentation in pull-apart basins: active examples in eastern Turkey. The Journal of Geology, 92(5): 513-530.

Herb, R., 1988. Eocaene Paläogeographie und Paläotektonik des Helvetikums. Eclogae Geologicae Helvetiae, 81(3): 611-657.

Herman, F., Seward, D., Valla, P.G., Carter, A., Kohn, B., Willett, S.D. and Ehlers, T.A., 2013. Worldwide acceleration of mountain erosion under a cooling climate. Nature, 504(7480): 423-426.

Herrmann, P., Draxler, I. and Müller, M., 1985. Erläuterungen zu Blatt 83 Sulzberg, Geologische Bundesanstalt.

Heuberger, S., Roth, P., Zingg, O., Naef, H. and Meier, B.P., 2016. The St. Gallen Fault Zone: a long-lived, multiphase structure in the North Alpine Foreland Basin revealed by 3D seismic data. Swiss Journal of Geosciences, 109(1): 83-102.

Heyng, A., 2012. Lithostratigraphie der Adelholzen-Formation (Eozän, Lutetium) im Raum Siegsdorf (Oberbayern). Verlag Documenta Naturae.

Hinsch, R., 2013. Laterally varying structure and kinematics of the Molasse fold and thrust belt of the Central Eastern Alps: Implications for exploration. AAPG bulletin, 97(10): 1805-1831.

Homewood, P., Allen, P. and Williams, G., 1986. Dynamics of the Molasse Basin of western Switzerland, Foreland basins. Blackwell Scientific Publications Oxford, UK, pp. 199-217.

Homewood, P. and Lateltin, O., 1988. Classic swiss clastics (flysch and molasse) The alpine connection. Geodinamica Acta, 2(1): 1-11.

Hongxing, G. and Anderson, J.K., 2007. Fault throw profile and kinematics of Normal fault: conceptual models and geologic examples. Geological Journal of China Universities, 13(1): 75.

Horton, B.K., 2018. Sedimentary record of Andean mountain building. Earth-Science Reviews, 178: 279-309.

Hubbard, S.M., de Ruig, M.J. and Graham, S.A., 2009. Confined channel-levee complex development in an elongate depo-center: deep-water Tertiary strata of the Austrian Molasse basin. Marine and Petroleum Geology, 26(1): 85-112.

Hurford, A., Flisch, M. and Jäger, E., 1989. Unravelling the thermo-tectonic evolution of the Alps: a contribution from fission track analysis and mica dating. Geological Society, London, Special Publications, 45(1): 369-398.

Hurford, A.J., 1986. Cooling and uplift patterns in the Lepontine Alps South Central Switzerland and an age of vertical movement on the Insubric fault line. Contributions to mineralogy and petrology, 92(4): 413-427.

Hülscher, J., Fischer, G., Grunert, P., Auer, G. and Bernhardt, A., 2019. Selective Recording of Tectonic Forcings in an Oligocene/Miocene Submarine Channel System: Insights From New Age Constraints and Sediment Volumes From the Austrian Northern Alpine Foreland Basin. Frontiers in Earth Science, 7(302).

Hülscher, J., Sobel, E.R., Verwater, V., Groß, P., Chew, D. and Bernhardt, A., 2021. Detrital apatite geochemistry and thermochronology from the Oligocene/Miocene Alpine foreland record the early exhumation of the Tauern Window. Basin Research, 33(6): 3021-3044.

Isacks, B. and Molnar, P., 1969. Mantle earthquake mechanisms and the sinking of the lithosphere. Nature, 223(5211): 1121-1124.

Jackson, C.A.-L., Bell, R.E., Rotevatn, A. and Tvedt, A.B., 2017. Techniques to determine the kinematics of synsedimentary normal faults and implications for fault growth models. Geological Society, London, Special Publications, 439(1): 187-217.

Jackson, C.A.-L. and Rotevatn, A., 2013. 3D seismic analysis of the structure and evolution of a salt-influenced normal fault zone: a test of competing fault growth models. Journal of Structural Geology, 54: 215-234.

Jiménez-Moreno, G., Fauquette, S. and Suc, J.P., 2008. Vegetation, climate and palaeoaltitude reconstructions of the Eastern Alps during the Miocene based on pollen records from Austria, Central Europe. Journal of Biogeography, 35(9): 1638-1649.

Jin, J., Aigner, T., Luterbacher, H., Bachmann, G.H. and Müller, M., 1995. Sequence stratigraphy and depositional history in the south-eastern German Molasse Basin. Marine and Petroleum Geology, 12(8): 929-940.

Jordan, T. and Flemings, P., 1991. Large-scale stratigraphic architecture, eustatic variation, and unsteady tectonism: A theoretical evaluation. Journal of Geophysical Research: Solid Earth, 96(B4): 6681-6699.

Jordan, T.E., 1981. Thrust loads and foreland basin evolution, Cretaceous, western United States. AAPG bulletin, 65(12): 2506-2520.

Jácome, M.I., Kusznir, N., Audemard, F. and Flint, S., 2003. Formation of the Maturin Foreland Basin, eastern Venezuela: Thrust sheet loading or subduction dynamic topography. Tectonics, 22(5).

Karimi, M., Adelzadeh, M. and Mohammadypour, M., 2014. Formula of definite point overburden pressure of reservoir layers. Egyptian Journal of Petroleum, 23(2): 175-182.

Karner, G. and Watts, A., 1983. Gravity anomalies and flexure of the lithosphere at mountain ranges. Journal of Geophysical Research: Solid Earth, 88(B12): 10449-10477.

Kaus, B.J., Popov, A.A., Baumann, T., Pusok, A., Bauville, A., Fernandez, N. and Collignon, M., 2016. Forward and inverse modelling of lithospheric deformation on geological timescales, NIC symposium, pp. 299-307.

Keller, B., 1989. Fazies und stratigraphie der Oberen Meeresmolasse (unteres Miozän) zwischen Napf und Bodensee.

Kempf, O., Matter, A., Burbank, D. and Mange, M., 1999. Depositional and structural evolution of a foreland basin margin in a magnetostratigraphic framework: the eastern Swiss Molasse Basin. International Journal of Earth Sciences, 88(2): 253-275.

Kempf, O. and Pross, J., 2005. The lower marine to lower freshwater Molasse transition in the northern Alpine foreland basin (Oligocene; central

Switzerland–south Germany): age and geodynamic implications. International Journal of Earth Sciences, 94(1): 160-171.

Kocsis, L., Ozsvárt, P., Becker, D., Ziegler, R., Scherler, L. and Codrea, V., 2014. Orogeny forced terrestrial climate variation during the late Eocene–early Oligocene in Europe. Geology, 42(8): 727-730.

Koson, S., Chenrai, P. and Choowong, M., 2013. Seismic attributes and their applications in seismic geomorphology. Bulletin of Earth Sciences of Thailand, 6(1): 1-9.

Krief, M., Garat, J., Stellingwerff, J. and Ventre, J., 1990. A petrophysical interpretation using the velocities of P and S waves (full-waveform sonic). The log analyst, 31(06).

Krzywiec, P., 2001. Contrasting tectonic and sedimentary history of the central and eastern parts of the Polish Carpathian foredeep basin—results of seismic data interpretation. Marine and Petroleum Geology, 18(1): 13-38.

Kufner, S.-K., Schurr, B., Haberland, C., Zhang, Y., Saul, J., Ischuk, A. and Oimahmadov, I., 2017. Zooming into the Hindu Kush slab break-off: A rare glimpse on the terminal stage of subduction. Earth and Planetary Science Letters, 461: 127-140.

Kufner, S.K., Kakar, N., Bezada, M., Bloch, W., Metzger, S., Yuan, X., Mechie, J., Ratschbacher, L., Murodkulov, S., Deng, Z. and Schurr, B., 2021. The Hindu Kush slab break-off as revealed by deep structure and crustal deformation. Nat Commun, 12(1): 1685.

Kuhlemann, J., 2000. Post-collisional sediment budget of circum-Alpine basins (Central Europe). Mem. Sci. Geol. Padova, 52(1): 1-91.

Kuhlemann, J., 2007. Paleogeographic and paleotopographic evolution of the Swiss and Eastern Alps since the Oligocene. Global and Planetary Change, 58(1-4): 224-236.

Kuhlemann, J., Dunkl, I., Brügel, A., Spiegel, C. and Frisch, W., 2006. From source terrains of the Eastern Alps to the Molasse Basin: Detrital record of non-steady-state exhumation. Tectonophysics, 413(3-4): 301-316.

Kuhlemann, J., Frisch, W., Székely, B., Dunkl, I. and Kazmer, M., 2002a. Post-collisional sediment budget history of the Alps: tectonic versus climatic control. International Journal of Earth Sciences, 91: 818-837.

Kuhlemann, J. and Kempf, O., 2002. Post-Eocene evolution of the North Alpine Foreland Basin and its response to Alpine tectonics. Sedimentary Geology, 152(1-2): 45-78.

Kuhlemann, J. and Kempf, O., 2002b. Post-Eocene evolution of the North Alpine Foreland Basin and its response to Alpine tectonics. Sedimentary Geology, 152(1-2): 45-78.

Kästle, E.D., Rosenberg, C., Boschi, L., Bellahsen, N., Meier, T. and El-Sharkawy, A., 2020. Slab break-offs in the Alpine subduction zone. International Journal of Earth Sciences, 109(2): 587-603.

Köwing, K., Kraus, L. and Rückert, G., 1968. Erläuterungen zur Geologischen Karte von Bayern 1:25000.

La Bruna, V., Agosta, F., Lamarche, J., Viseur, S. and Prosser, G., 2018. Fault growth mechanisms and scaling properties in foreland basin system: The case study of Monte Alpi, Southern Apennines, Italy. Journal of Structural Geology, 116: 94-113.

Lallemand, S., Heuret, A., Faccenna, C. and Funiciello, F., 2008. Subduction dynamics as revealed by trench migration. Tectonics, 27(3).

Lanari, R., Reitano, R., Faccenna, C., Agostinetti, N.P. and Ballato, P., 2023. Surface and crustal response to deep subduction dynamics: Insights from the Apennines, Italy. Tectonics, 42(3): e2022TC007461.

Langhi, L., Ciftci, N.B. and Borel, G.D., 2011. Impact of lithospheric flexure on the evolution of shallow faults in the Timor foreland system. Marine Geology, 284(1-4): 40-54.

Larrey, M., Mouthereau, F., Do Couto, D., Masini, E., Jourdon, A., Calassou, S. and Miegebielle, V., 2022. Oblique rifting triggered by slab tearing and back-arc extension: the case of the Alboran rift in the eastern Betics. Solid Earth, 500.

Lash, G.G., 1988. Along-strike variations in foreland basin evolution: possible evidence for continental collision along an irregular margin. Basin Research, 1(2): 71-83.

Le Breton, E., Bernhardt, A., Neumeister, R., Heismann, C., Borzi, A., Hülscher, J., Sanders, R., Grunert, P., Handy, M.R. and McPhee, P.J., 2023. Early Miocene tectono-sedimentary shift in the eastern North Alpine Foreland Basin and its relation to changes in tectonic style in the Eastern Alps.

Le Breton, E., Brune, S., Ustaszewski, K., Zahirovic, S., Seton, M. and Müller, R.D., 2021. Kinematics and extent of the Piemont–Liguria Basin–implications for subduction processes in the Alps. Solid Earth, 12(4): 885-913.

Lemcke, K., 1984. Geologische Vorgänge in den Alpen ab Obereozän im Spiegel vor allem der deutschen Molasse. Geologische Rundschau, 73(1): 371-397.

Lemcke, K., 1988. Das bayerische Alpenvorland vor der Eiszeit.

Li, Z.-H., Xu, Z., Gerya, T. and Burg, J.-P., 2013. Collision of continental corner from 3-D numerical modeling. Earth and Planetary Science Letters, 380: 98-111.

Lihou, J.C. and Allen, P.A., 1996. Importance of inherited rift margin structures in the early North Alpine Foreland Basin, Switzerland. Basin Research, 8(4): 425-442.

Luth, S., Willingshofer, E., Sokoutis, D. and Cloetingh, S., 2013. Does subduction polarity changes below the Alps? Inferences from analogue modelling. Tectonophysics, 582: 140-161.

Ma, L., Wang, B.-D., Jiang, Z.-Q., Wang, Q., Li, Z.-X., Wyman, D.A., Zhao, S.-R., Yang, J.-H., Gou, G.-N. and Guo, H.-F., 2014. Petrogenesis of the Early Eocene adakitic rocks in the Napuri area, southern Lhasa: Partial melting of thickened lower crust during slab break-off and implications for crustal thickening in southern Tibet. Lithos, 196: 321-338.

Maiti, G., Koptev, A., Baville, P., Gerya, T., Crosetto, S. and Andrić-Tomašević, N., in revision. Topography Response to Horizontal Slab Tearing During Retreating Oblique Continental Collision: Insights from 3D Thermomechanical Modelling, 2024BJ029385. Journal of Geophysical Research: Solid Earth.

Maiti, G., Koptev, A., Baville, P., Gerya, T., Crosetto, S. and Andrić-Tomašević, N., 2024. Topography response to horizontal slab tearing and oblique continental collision: Insights from 3D thermomechanical modeling. Journal of Geophysical Research: Solid Earth, 129(10): e2024JB029385.

Malkowski, M.A., Sharman, G.R., Graham, S.A. and Fildani, A., 2017. Characterisation and diachronous initiation of coarse clastic deposition in the Magallanes–Austral foreland basin, Patagonian Andes. Basin Research, 29: 298-326.

Mallet, J.-L., 2004. Space–time mathematical framework for sedimentary geology. Mathematical geology, 36(1): 1-32.

Manatschal, G., Chenin, P., Haupert, I., Masini, E., Frasca, G. and Decarlis, A., 2022. The importance of rift inheritance in understanding the early collisional evolution of the Western Alps. Geosciences, 12(12): 434.

Mann, P., Hempton, M.R., Bradley, D.C. and Burke, K., 1983. Development of pull-apart basins. The Journal of Geology, 91(5): 529-554.

Margirier, A., Braun, J., Robert, X. and Audin, L., 2018. Role of erosion and isostasy in the Cordillera Blanca uplift: Insights from landscape evolution modeling (northern Peru, Andes). Tectonophysics, 728: 119-129.

Marzec, P., Sechman, H., Kasperska, M., Cichostępski, K., Guzy, P., Pietsch, K. and Porębski, S.J., 2018. Interpretation of a gas chimney in the Polish Carpathian Foredeep based on integrated seismic and geochemical data. Basin Research, 30: 210-227.

Marín-Lechado, C., Pedrera, A., Peláez, J.A., Ruiz-Constán, A., González-Ramón, A. and Henares, J., 2017. Deformation style and controlling geodynamic processes at the eastern Guadalquivir foreland basin (Southern Spain). Tectonics, 36(6): 1072-1089.

Masalimova, L.U., Lowe, D.R., Mchargue, T. and Derksen, R., 2015. Interplay between an axial channel belt, slope gullies and overbank deposition in the Puchkirchen Formation in the Molasse Basin, Austria. Sedimentology, 62(6): 1717-1748.

Matter, A., 1980. Flysch and molasse of western and central Switzerland. Wepf & Co.

Maurer, H., 2006. Rekonstruktion der Ablagerungsverhältnisse im nordalpinen Vorlandbecken Südwest-Deutschlands.

Maţenco, L., Zoetemeijer, R., Cloetingh, S. and Dinu, C., 1997. Lateral variations in mechanical properties of the Romanian external Carpathians: inferences of flexure and gravity modelling. Tectonophysics, 282(1-4): 147-166.

McQuarrie, N., 2002. The kinematic history of the central Andean fold-thrust belt, Bolivia: Implications for building a high plateau. Geological Society of America Bulletin, 114(8): 950-963.

Meade, R.H., 1972. Transport and deposition of sediments in estuaries.

Menant, A., Sternai, P., Jolivet, L., Guillou-Frottier, L. and Gerya, T., 2016. 3D numerical modeling of mantle flow, crustal dynamics and magma genesis associated with slab roll-back and tearing: The eastern Mediterranean case. Earth and Planetary Science Letters, 442: 93-107.

Menkveld-Gfeller, U., 1995. Stratigraphie, Fazies und Pelogeographie des Eozaens der helvetischen Decken der Westschweiz (Diablerets- und Wildhorn-Decke). Eclog. geol. Helv, 88: 115-134.

Menkveld-Gfeller, U., 1997. Die Bürgen-Fm: und die Klimsenhorn-Fm.: Formelle Definition zweier lithostratigraphischer Einheiten des Eozäns der helvetischen Decken. Eclogae Geologicae Helvetiae, 90: 245-261.

Meulenkamp, J., Kováč, M. and Cicha, I., 1996. On Late Oligocene to Pliocene depocentre migrations and the evolution of the Carpathian-Pannonian system. Tectonophysics, 266(1-4): 301-317.

Meyer, R.K. and Schmidt-Kaler, H., 1990a. Paläogeographie und Schwammriffentwicklung des süddeutschen Malm—ein Überblick. Facies, 23(1): 175-184.

Meyer, R.K. and Schmidt-Kaler, H., 1990b. Paläogeographischer Atlas des süddeutschen Oberjura (Malm).

Miller, K.G., Kominz, M.A., Browning, J.V., Wright, J.D., Mountain, G.S., Katz, M.E., Sugarman, P.J., Cramer, B.S., Christie-Blick, N. and Pekar, S.F., 2005. The Phanerozoic record of global sea-level change. science, 310(5752): 1293-1298.

Mohn, G., Manatschal, G., Beltrando, M. and Haupert, I., 2014. The role of rift-inherited hyper-extension in Alpine-type orogens. Terra Nova, 26(5): 347-353.

Mohn, G., Manatschal, G., Müntener, O., Beltrando, M. and Masini, E., 2010. Unravelling the interaction between tectonic and sedimentary processes during lithospheric thinning in the Alpine Tethys margins. International Journal of Earth Sciences, 99(1): 75-101.

Molnar, P. and England, P., 1990. Late Cenozoic uplift of mountain ranges and global climate change: chicken or egg? nature, 346(6279): 29-34.

Montgomery, D.R. and Brandon, M.T., 2002. Topographic controls on erosion rates in tectonically active mountain ranges. Earth and Planetary Science Letters, 201(3-4): 481-489.

Mraz, E., Moeck, I., Bissmann, S. and Hild, S., 2018. Multiphase fossil normal faults as geothermal exploration targets in the Western Bavarian Molasse Basin: Case study Mauerstetten. Zeitschrift der Deutschen Gesellschaft für Geowissenschaften, 169(3): 389-411.

Müller, M., 2011. Die Geologie beiderseits des Lechs im Raum Schongau. Geologica Bavarica.

Müller, M., Nieberding, F. and Wanninger, A., 1988. Tectonic style and pressure distribution at the northern margin of the Alps between Lake Constance and the River Inn. Geologische Rundschau, 77: 787-796.

Nachtmann, W. and Wagner, L., 1987. Mesozoic and early Tertiary evolution of the Alpine foreland in Upper Austria and Salzburg, Austria. Tectonophysics, 137(1-4): 61-76.

Nagel, S., Castelltort, S., Wetzel, A., Willett, S.D., Mouthereau, F. and Lin, A.T., 2013. Sedimentology and foreland basin paleogeography during Taiwan arc continent collision. Journal of Asian Earth Sciences, 62: 180-204.

Nagel, S., Granjeon, D., Willett, S., Lin, A.T.-S. and Castelltort, S., 2018. Stratigraphic modeling of the Western Taiwan foreland basin: Sediment flux from a growing mountain range and tectonic implications. Marine and Petroleum Geology, 96: 331-347.

Nanda, N.C., 2021. Seismic data interpretation and evaluation for hydrocarbon exploration and production. Springer.

Narkiewicz, M., Maksym, A., Malinowski, M., Grad, M., Guterch, A., Petecki, Z., Probulski, J., Janik, T., Majdański, M. and Środa, P., 2015. Transcurrent nature of the Teisseyre–Tornquist Zone in Central Europe: results of the POLCRUST-01 deep reflection seismic profile. International Journal of Earth Sciences, 104: 775-796.

Naylor, M. and Sinclair, H., 2008. Pro-vs. retro-foreland basins. Basin Research, 20(3): 285-303.

Neely, J.S. and Furlong, K.P., 2018. Evidence of displacement-driven maturation along the San Cristobal Trough transform plate boundary. Earth and Planetary Science Letters, 485: 88-98.

Neubauer, F., 2016. Formation of an intra-orogenic transtensional basin: the Neogene Wagrain basin in the Eastern Alps. Swiss Journal of Geosciences, 109: 37-56.

Ortner, H., Aichholzer, S., Zerlauth, M., Pilser, R. and Fügenschuh, B., 2015. Geometry, amount, and sequence of thrusting in the Subalpine Molasse of western Austria and southern Germany, European Alps. Tectonics, 34(1): 1-30.

Ortner, H. and Stingl, V., 2001. Facies and basin development of the Oligocene in the Lower Inn Valley, Tyrol/Bavaria.

Ortner, H., von Hagke, C., Sommaruga, A., Mock, S., Mosar, J., Hinsch, R. and Beidinger, A., 2023a. The northern Deformation Front of the European Alps, The Alpine Chain. ISTE-Wiley, London.

Ortner, H., von Hagke, C., Sommaruga, A., Mock, S., Mosar, J., Hinsch, R., Beidinger, A., Bahlhasen, N. and Rosenberg, C., 2023b. The northern

deformation front of the european alps. Geodynamics of the Alps-Collisional Processes, 3: 241-312.

Ouchi, S., 2011. Effects of uplift on the development of experimental erosion landform generated by artificial rainfall. Geomorphology, 127(1-2): 88-98.

Pan, S., Bell, R.E., Jackson, C.A.L. and Naliboff, J., 2022. Evolution of normal fault displacement and length as continental lithosphere stretches. Basin Research, 34(1): 121-140.

Parra, M., Mora, A., Jaramillo, C., Torres, V., Zeilinger, G. and Strecker, M.R., 2010. Tectonic controls on Cenozoic foreland basin development in the north-eastern Andes, Colombia. Basin Research, 22(6): 874-903.

Paxman, G., Watts, A., Ferraccioli, F., Jordan, T., Bell, R., Jamieson, S. and Finn, C., 2016. Erosion-driven uplift in the Gamburtsev Subglacial Mountains of East Antarctica. Earth and Planetary Science Letters, 452: 1-14.

Peacock, D. and Sanderson, D., 1991. Displacements, segment linkage and relay ramps in normal fault zones. Journal of Structural Geology, 13(6): 721-733.

Petersen, K., Clausen, O. and Korstgård, J., 1992. Evolution of a salt-related listric growth fault near the D-1 well, block 5605, Danish North Sea: displacement history and salt kinematics. Journal of Structural Geology, 14(5): 565-577.

Pfiffner, A., 1986. Evolution of the North Alpine Foreland Basin in the Central Alps. The International Association of Sedimentologists, 8: 219-228.

Pfiffner, O.-A., Schlunegger, F. and Buiter, S., 2002. The Swiss Alps and their peripheral foreland basin: Stratigraphic response to deep crustal processes. Tectonics, 21(2): 3-1-3-16.

Pfiffner, O.A., 1993. The structure of the Helvetic nappes and its relation to the mechanical stratigraphy. Journal of structural Geology, 15(3-5): 511-521.

Piccolo, A., Kaus, B.J., White, R.W., Palin, R.M. and Reuber, G.S., 2022. Plume—Lid interactions during the Archean and implications for the generation of early continental terranes. Gondwana Research, 88: 150-168.

Pippèrr, M., 2011. Characterisation of Ottnangian (middle Burdigalian) palaeoenvironments in the North Alpine Foreland Basin using benthic foraminifera—a review of the Upper Marine Molasse of southern Germany. Marine Micropaleontology, 79(3-4): 80-99.

Platt, N.H., 1992. Fresh-water carbonates from the Lower Freshwater Molasse (Oligocene, western Switzerland): sedimentology and stable isotopes. Sedimentary Geology, 78(1-2): 81-99.

Platt, N.H. and Keller, B., 1992. Distal alluvial deposits in a foreland basin setting—the Lower Freshwater Miocene), Switzerland: sedimentology, architecture and palaeosols. Sedimentology, 39(4): 545-565.

Poirier, J.-P. and Liebermann, R., 1984. On the activation volume for creep and its variation with depth in the Earth's lower mantle. Physics of the earth and planetary interiors, 35(4): 283-293.

Posamentier, H. and James, D., 1993. An overview of sequence-stratigraphic concepts: uses and abuses. Sequence stratigraphy and facies associations: 1-18.

Quinlan, G.M. and Beaumont, C., 1984. Appalachian thrusting, lithospheric flexure, and the Paleozoic stratigraphy of the eastern interior of North America. Canadian Journal of Earth Sciences, 21(9): 973-996.

Rankey, E. and Mitchell, J., 2003. That's why it's called interpretation: Impact of horizon uncertainty on seismic attribute analysis. The Leading Edge, 22(9): 820-828.

Ratschbacher, L., Frisch, W., Linzer, H.G. and Merle, O., 1991a. Lateral extrusion in the Eastern Alps, part 2: structural analysis. Tectonics, 10(2): 257-271.

Ratschbacher, L., Merle, O., Davy, P. and Cobbold, P., 1991b. Lateral extrusion in the Eastern Alps, part 1: boundary conditions and experiments scaled for gravity. Tectonics, 10(2): 245-256.

Reichenbacher, B., Uhlig, U., Kowalke, T., Bassler, B., Matzke-Karasz, R. and Schenk, B., 2004. Biota, palaeoenvironments and biostratigraphy of continental Oligocene deposits of the south German Molasse Basin (Penzberg syncline). Palaeontology, 47(3): 639-677.

Reiners, P.W., Ehlers, T.A., Mitchell, S.G. and Montgomery, D.R., 2003. Coupled spatial variations in precipitation and long-term erosion rates across the Washington Cascades. Nature, 426(6967): 645-647.

Ring, U., Glodny, J., Will, T. and Thomson, S., 2010. The Hellenic subduction system: high-pressure metamorphism, exhumation, normal faulting, and large-scale extension. Annual Review of Earth and Planetary Sciences, 38: 45-76.

Roche, V., Childs, C., Madritsch, H. and Camanni, G., 2020. Layering and structural inheritance controls on fault zone structure in three

dimensions: A case study from the northern Molasse Basin, Switzerland. Journal of the Geological Society, 177(3): 493-508.

Rosenbaum, G., Gasparon, M., Lucente, F.P., Peccerillo, A. and Miller, M.S., 2008. Kinematics of slab tear faults during subduction segmentation and implications for Italian magmatism. Tectonics, 27(2): n/a-n/a.

Rosenberg, C., Brun, J.P., Cagnard, F. and Gapais, D., 2007. Oblique indentation in the Eastern Alps: Insights from laboratory experiments. Tectonics, 26(2).

Rosenberg, C.L., Bellahsen, N., Rabaute, A. and Girault, J.B., 2021. Distribution, style, amount of collisional shortening, and their link to Barrovian metamorphism in the European Alps. Earth-Science Reviews, 222.

Rosenberg, C.L. and Kissling, E., 2013. Three-dimensional insight into Central-Alpine collision: Lower-plate or upper-plate indentation? Geology, 41(12): 1219-1222.

Rotevatn, A., Kristensen, T.B., Ksienzyk, A.K., Wemmer, K., Henstra, G.A., Midtkandal, I., Grundvåg, S.A. and Andresen, A., 2018. Structural inheritance and rapid rift-length establishment in a multiphase rift: The East Greenland rift system and its Caledonian orogenic ancestry. Tectonics, 37(6): 1858-1875.

Roure, F., 2008. Foreland and hinterland basins: what controls their evolution? Swiss Journal of Geosciences, 101(1): 5-29.

Rowan, M.G., Hart, B.S., Nelson, S., Flemings, P.B. and Trudgill, B.D., 1998. Three-dimensional geometry and evolution of a salt-related growth-fault array: Eugene Island 330 field, offshore Louisiana, Gulf of Mexico. Marine and petroleum geology, 15(4): 309-328.

Royden, L.H., 1993a. Evolution of retreating subduction boundaries formed during continental collision. Tectonics, 12(3): 629-638.

Royden, L.H., 1993b. The tectonic expression slab pull at continental convergent boundaries. Tectonics, 12(2): 303-325.

Ryan, L., Magee, C. and Jackson, C.A.-L., 2017. The kinematics of normal faults in the Ceduna Subbasin, offshore southern Australia: Implications for hydrocarbon trapping in a frontier basin. AAPG Bulletin, 101(3): 321-341.

Rögl, F., 1997. Palaeogeographic considerations for Mediterranean and Paratethys seaways (Oligocene to Miocene). Annalen des Naturhistorischen Museums in Wien. Serie A für Mineralogie und

Petrographie, Geologie und Paläontologie, Anthropologie und Prähistorie: 279-310.

Rögl, F., Hochuli, P. and Muller, C., 1979. Oligocene–early Miocene stratigraphic correlations in the Molasse Basin of Austria. Annales Geologiques des Pays Helleniques. Tome Hors Series, 30: 1045-1050.

Sabbatino, M., Tavani, S., Vitale, S., Ogata, K., Corradetti, A., Consorti, L., Arienzo, I., Cipriani, A. and Parente, M., 2021. Forebulge migration in the foreland basin system of the central-southern Apennine fold-thrust belt (Italy): New high-resolution Sr-isotope dating constraints. Basin Research, 33(5): 2817-2836.

Schaller, M. and Ehlers, T.A., 2021. Vegetation and climate effects on soil production, chemical weathering, and physical erosion rates. Earth Surf. Dyn. Preprint.

Scharf, A., Handy, M., Favaro, S., Schmid, S.M. and Bertrand, A., 2013. Modes of orogen-parallel stretching and extensional exhumation in response to microplate indentation and roll-back subduction (Tauern Window, Eastern Alps). International Journal of Earth Sciences, 102(6): 1627-1654.

Schlunegger, F., Burbank, D., Matter, A., Engesser, B. and Mödden, C., 1996. Magnetostratigraphic calibration of the Oligocene to Middle Miocene (30-15 Ma) mammal biozones and depositional sequences of the Swiss Molasse Basin. Eclogae Geologicae Helvetiae, 89(2): 753-788.

Schlunegger, F. and Castelltort, S., 2016. Immediate and delayed signal of slab breakoff in Oligo/Miocene Molasse deposits from the European Alps. Scientific reports, 6(1): 1-11.

Schlunegger, F. and Kissling, E., 2015. Slab rollback orogeny in the Alps and evolution of the Swiss Molasse basin. Nature communications, 6(1): 1-10.

Schlunegger, F. and Kissling, E., 2022. Slab load controls beneath the Alps on the source-to-sink sedimentary pathways in the Molasse basin. Geosciences, 12(6): 226.

Schlunegger, F., Leu, W. and Matter, A., 1997a. Sedimentary sequences, seismic facies, subsidence analysis, and evolution of the Burdigalian Upper Marine Molasse Group, central Switzerland. AAPG bulletin, 81(7): 1185-1207.

Schlunegger, F., Matter, A., Burbank, D. and Klaper, E., 1997b. Magnetostratigraphic constraints on relationships between

evolution of the central Swiss Molasse basin and Alpine orogenic events. Geological Society of America Bulletin, 109(2): 225-241.

Schlunegger, F., Matter, A., Burbank, D., Leu, W., Mange, M. and Matyas, J., 1997c. Sedimentary sequences, seismofacies and evolution of depositional systems of the Oligo/Miocene Lower Freshwater Molasse Group, Switzerland. Basin Research, 9(1): 1-26.

Schlunegger, F. and Willett, S., 1999. Spatial and temporal variations in exhumation of the central Swiss Alps and implications for exhumation mechanisms. Geological Society, London, Special Publications, 154(1): 157-179.

Schmid, S., Fügenschuh, B., Kissling, E. and Schuster, R., 2004a. TRANSMED Transects IV, V and VI: Three lithospheric transects across the Alps and their forelands. The TRANSMED Atlas: The Mediterranean Region from Crust to Mantle. Springer Verlag.

Schmid, S.M., Fügenschuh, B., Kissling, E. and Schuster, R., 2004b. Tectonic map and overall architecture of the Alpine orogen. Eclogae Geologicae Helvetiae, 97(1): 93-117.

Schmid, S.M., Pfiffner, O.-A., Froitzheim, N., Schönborn, G. and Kissling, E., 1996. Geophysical-geological transect and tectonic evolution of the Swiss-Italian Alps. Tectonics, 15(5): 1036-1064.

Schmid, S.M., Scharf, A., Handy, M.R. and Rosenberg, C.L., 2013. The Tauern Window (Eastern Alps, Austria): a new tectonic map, with cross-sections and a tectonometamorphic synthesis. Swiss Journal of Geosciences, 106(1): 1-32.

Scholz, C.H. and Contreras, J.C., 1998. Mechanics of continental rift architecture. Geology, 26(11): 967-970.

Schrag, D.P., 2009. Storage of carbon dioxide in offshore sediments. Science, 325(5948): 1658-1659.

Schönborn, G., 1999. Balancing cross sections with kinematic constraints: The Dolomites (northern Italy). Tectonics, 18(3): 527-545.

Sharman, G.R., Hubbard, S.M., Covault, J.A., Hinsch, R., Linzer, H.G. and Graham, S.A., 2018. Sediment routing evolution in the North Alpine Foreland Basin, Austria: interplay of transverse and longitudinal sediment dispersal. Basin Research, 30(3): 426-447.

Shipilin, V., Tanner, D.C., von Hartmann, H. and Moeck, I., 2020. Multiphase, decoupled faulting in the southern German Molasse Basin–evidence from 3-D seismic data. Solid Earth, 11(6): 2097-2117.

Sinclair, H., 1997a. Flysch to molasse transition in peripheral foreland basins: The role of the passive margin versus slab breakoff. Geology, 25(12): 1123-1126.

Sinclair, H., 1997b. Tectonostratigraphic model for underfilled peripheral foreland basins: An Alpine perspective. Geological Society of America Bulletin, 109(3): 324-346.

Sinclair, H., Coakley, B., Allen, P. and Watts, A., 1991. Simulation of foreland basin stratigraphy using a diffusion model of mountain belt uplift and erosion: an example from the central Alps, Switzerland. Tectonics, 10(3): 599-620.

Sinclair, H. and Naylor, M., 2012. Foreland basin subsidence driven by topographic growth versus plate subduction. Bulletin, 124(3-4): 368-379.

Sissingh, W., 1997. Tectonostratigraphy of the North Alpine Foreland Basin: correlation of Tertiary depositional cycles and orogenic phases. Tectonophysics, 282(1-4): 223-256.

Smit, J., Wees, J.-D.v. and Cloetingh, S., 2016. The Thor suture zone: From subduction to intraplate basin setting. Geology, 44(9): 707-710.

Spakman, W. and Wortel, R., 2004. A tomographic view on western Mediterranean geodynamics, The TRANSMED Atlas. The Mediterranean region from crust to mantle: Geological and geophysical framework of the Mediterranean and the surrounding areas. Springer, pp. 31-52.

Spang, A., 2022. Thermomechanical modeling of magmatic systems, Johannes Gutenberg-Universität Mainz.

Sperner, B., Lorenz, F., Bonjer, K., Hettel, S., Müller, B. and Wenzel, F., 2001. Slab break-off–abrupt cut or gradual detachment? New insights from the Vrancea Region (SE Carpathians, Romania). Terra Nova, 13(3): 172-179.

Spooner, C., Scheck-Wenderoth, M., Cacace, M. and Anikiev, D., 2022. How Alpine seismicity relates to lithospheric strength. Solid Earth Discussions, 2020: 1-24.

Stampfli, G., Borel, G.D., Marchant, R. and Mosar, J., 2002. Western Alps geological constraints on western Tethyan reconstructions. Journal of the Virtual Explorer, 8: 77-106.

Stampfli, G., Mosar, J., Marquer, D., Marchant, R., Baudin, T. and Borel, G., 1998. Subduction and obduction processes in the Swiss Alps. Tectonophysics, 296(1-2): 159-204.

Stampfli, G.m., 1993. Le Brianc¸onnais, terrain exotique dans les Alpes? Eclogae Geologicae Helvetiae, 86(1): 1-45.

Stefanick, M. and Jurdy, D.M., 1992. Stress observations and driving force models for the South American plate. Journal of Geophysical Research: Solid Earth, 97(B8): 11905-11913.

Stober, I., Grimmer, J. and Kraml, M., 2023. The Muschelkalk aquifer of the Molasse basin in SW-Germany: implications on the origin and development of highly saline lithium-rich brines in calcareous hydrothermal reservoirs. Geothermal Energy, 11(1): 27.

Stockmal, G., Colman-Sadd, S., Keen, C., O'Brien, S. and Quinlan, G., 1987. Collision along an irregular margin: a regional plate tectonic interpretation of the Canadian Appalachians. Canadian Journal of Earth Sciences, 24(6): 1098-1107.

Strunck, P. and Matter, A., 2002. Depositional evolution of the western Swiss Molasse. Eclogae Geologicae Helvetiae, 95: 197-222.

Subrahmanyam, D. and Rao, P., 2008. Seismic attributes-A review, 7th international conference & exposition on petroleum geophysics, Hyderabad, pp. 398-404.

Supak, S., Bohnenstiehl, D. and Buck, W., 2006. Flexing is not stretching: An analogue study of flexure-induced fault populations. Earth and Planetary Science Letters, 246(1-2): 125-137.

Sømme, T.O., Helland-Hansen, W., Martinsen, O.J. and Thurmond, J.B., 2009. Relationships between morphological and sedimentological parameters in source-to-sink systems: A basis for predicting semi-quantitative characteristics in subsurface systems. Basin Research, 21(4): 361-387.

Tetreault, J.á. and Buiter, S., 2012. Geodynamic models of terrane accretion: Testing the fate of island arcs, oceanic plateaus, and continental fragments in subduction zones. Journal of Geophysical Research: Solid Earth, 117(B8).

Tetzlaff, D.M. and Harbaugh, J.W., 1989. Simulating clastic sedimentation, 1110. Springer.

Thatcher, W. and Pollitz, F.F., 2008. Temporal evolution of continental lithospheric strength in actively deforming regions. GSA TODAY, 18(4/5): 4.

Thorsen, C.E., 1963. Age of growth faulting in southeast Louisiana.

Trümpy, R., 1960. Paleotectonic evolution of the Central and Western Alps. Geological Society of America Bulletin, 71(6): 843-907.

Tucker, G.E. and Slingerland, R., 1996. Predicting sediment flux from fold and thrust belts. Basin research, 8(3): 329-349.

Ustaszewski, K., Schmid, S.M., FüGENSCHUH, B., Tischler, M., Kissling, E. and Spakman, W., 2008. A map-view restoration of the Alpine-Carpathian-Dinaridic system for the Early Miocene. Swiss journal of Geosciences, 101: 273-294.

Van der Meulen, M., Meulenkamp, J. and Wortel, M., 1998. Lateral shifts of Apenninic foredeep depocentres reflecting detachment of subducted lithosphere. Earth and Planetary Science Letters, 154(1-4): 203-219.

Van Hinsbergen, D.J., Torsvik, T.H., Schmid, S.M., Maţenco, L.C., Maffione, M., Vissers, R.L., Gürer, D. and Spakman, W., 2020. Orogenic architecture of the Mediterranean region and kinematic reconstruction of its tectonic evolution since the Triassic. Gondwana Research, 81: 79-229.

van Hunen, J. and Allen, M.B., 2011. Continental collision and slab break-off: A comparison of 3-D numerical models with observations. Earth and Planetary Science Letters, 302(1-2): 27-37.

Ver Straeten, C.A. and Brett, C.E., 2000. Bulge migration and pinnacle reef development, Devonian Appalachian foreland basin. The Journal of Geology, 108(3): 339-352.

Vogt, K. and Gerya, T.V., 2012. From oceanic plateaus to allochthonous terranes: Numerical modelling. Gondwana Research, 25(2): 494-508.

Vogt, K., Willingshofer, E., Matenco, L., Sokoutis, D., Gerya, T. and Cloetingh, S., 2018. The role of lateral strength contrasts in orogenesis: A 2D numerical study. Tectonophysics, 746: 549-561.

von Blanckenburg, F. and Davies, J., 1992. Slab break-off. Explanation of mantle magmatism in the Alps? Transactions of the American Geophysical Union, Eos, 73: 546.

von Blanckenburg, F. and Davies, J.H., 1995. Slab breakoff: a model for syncollisional magmatism and tectonics in the Alps. Tectonics, 14(1): 120-131.

von Blanckenburg, F., Villa, I., Baur, H., Morteani, G. and Steiger, R., 1989. Time calibration of a PT-path from the Western Tauern Window, Eastern Alps: the problem of closure temperatures. Contributions to mineralogy and Petrology, 101(1): 1-11.

von Doppler, G., Heissig, K. and Reichenbacher, B., 2005. Die Gliederung des Tertiärs im süddeutschen Molassebecken.

Von Eynatten, H., Schlunegger, F., Gaupp, R. and Wijbrans, J.R., 1999. Exhumation of the Central Alps: evidence from 40Ar/39Ar laserprobe dating of detrital white micas from the Swiss Molasse Basin. Terra Nova, 11(6): 284-289.

Von Hagke, C., Oncken, O., Ortner, H., Cederbom, C. and Aichholzer, S., 2014. Late Miocene to present deformation and erosion of the Central Alps—Evidence for steady state mountain building from thermokinematic data. Tectonophysics, 632: 250-260.

von Hartmann, H., Tanner, D.C. and Schumacher, S., 2016. Initiation and development of normal faults within the German alpine foreland basin: The inconspicuous role of basement structures. Tectonics, 35(6): 1560-1574.

Wagner, L.R., 1998. Tectono-stratigraphy and hydrocarbons in the Molasse Foredeep of Salzburg, Upper and Lower Austria. Geological Society, London, Special Publications, 134(1): 339-369.

Walsh, J., Bailey, W., Childs, C., Nicol, A. and Bonson, C., 2003. Formation of segmented normal faults: a 3-D perspective. Journal of Structural Geology, 25(8): 1251-1262.

Walsh, J., Nicol, A. and Childs, C., 2002. An alternative model for the growth of faults. Journal of Structural Geology, 24(11): 1669-1675.

Wang, S., Liu, K., Wang, H. and Chen, M., 2022. Growth and linkage of normal faults experiencing multiple non-coaxial extension: A case from the Qikou Sag, Bohai Bay Basin, East China. Basin Research, 34(2): 748-770.

Wangen, M., 2010. Physical principles of sedimentary basin analysis. Cambridge University Press.

Waschbusch, P.J. and Royden, L.H., 1992. Spatial and temporal evolution of foredeep basins: lateral strength variations and inelastic yielding in continental lithosphere. Basin Research, 4(3-4): 179-196.

Watts, A. and Burov, E., 2003. Lithospheric strength and its relationship to the elastic and seismogenic layer thickness. Earth and Planetary Science Letters, 213(1-2): 113-131.

Whipp, P., Jackson, C.L., Gawthorpe, R., Dreyer, T. and Quinn, D., 2014. Normal fault array evolution above a reactivated rift fabric; a subsurface example from the northern Horda Platform, Norwegian North Sea. Basin Research, 26(4): 523-549.

Whipple, K.X., 2009. The influence of climate on the tectonic evolution of mountain belts. Nature geoscience, 2(2): 97-104.

Whiting, B.M. and Thomas, W.A., 1994. Three-dimensional controls on subsidence of a foreland basin associated with a thrust-belt recess: Black Warrior basin, Alabama and Mississippi. Geology, 22(8): 727-730.

Willingshofer, E. and Cloetingh, S., 2003. Present-day lithospheric strength of the Eastern Alps and its relationship to neotectonics. Tectonics, 22(6).

Willingshofer, E. and Sokoutis, D., 2009. Decoupling along plate boundaries: Key variable controlling the mode of deformation and the geometry of collisional mountain belts. Geology, 37(1): 39-42.

Willingshofer, E., Sokoutis, D. and Burg, J.-P., 2005. Lithospheric-scale analogue modelling of collision zones with a pre-existing weak zone. Geological Society, London, Special Publications, 243(1): 277-294.

Wilmsen, M., Fürsich, F.T., Seyed-Emami, K., Majidifard, M.R. and Taheri, J., 2009. The Cimmerian Orogeny in northern Iran: Tectono-stratigraphic evidence from the foreland. Terra Nova, 21(3): 211-218.

Wolpert, P., Aigner, T., Bendias, D., Beichel, K. and Zosseder, K., 2022. A novel workflow for geothermal exploration: 3D seismic interpretation of biohermal buildups (Upper Jurassic, Molasse Basin, Germany). Geothermal Energy, 10(1): 1-20.

Woodward, N., Boyer, S. and Suppe, J., 1989. Balanced Geological Cross-Sections: An Essential Technique in Geological Research and Exploration, Short Course Geol., vol. 6, 132 pp. AGU, Washington, DC.

Wortel, M. and Spakman, W., 2000. Subduction and slab detachment in the Mediterranean-Carpathian region. Science, 290(5498): 1910-1917.

Zaharia, L. and Ioana-Toroimac, G., 2009. Erosion dynamics–precipitation relationship in the Carpathians' curvature region (Romania). Geografia fisica e dinamica quaternaria, 32(1): 95-102.

Zaugg, A. and Löpfe, R., 2011. 1114 Nesslau. Schweizerische Eidgenossenschaft Bundesamt für Landestopografie Swisstopo.

Zerlauth, M., Ortner, H., Pomella, H., Adrian Pfiffner, O. and Fügenschuh, B., 2014. Inherited tectonic structures controlling the deformation style: an example from the Helvetic nappes of the Eastern Alps. Swiss Journal of Geosciences, 107: 157-175.

Zhu, D., Wang, Q. and Zhao, Z., 2017. Constraining quantitatively the timing and process of continent-continent collision using magmatic record: Method and examples. Science China Earth Sciences, 60: 1040-1056.

Ziegler, P., Bertotti, G. and Cloetingh, S., 2002. Dynamic processes controlling foreland development–the role of mechanical (de) coupling of orogenic wedges and forelands. EGU Stephan Mueller Special Publication Series, 1: 17-56.

Ziegler, P. and Dèzes, P., 2007. Cenozoic uplift of Variscan Massifs in the Alpine foreland: Timing and controlling mechanisms. Global and Planetary change, 58(1-4): 237-269.

Ziegler, P.A., 1990. Geological atlas of western and central Europe, 1. Geological Society Publishing House.

Ziegler, P.A., Schmid, S., Pfiffner, A. and Schönborn, G., 1996. Structure and evolution of the Central Alps and their northern and southern foreland basins. Mémoires du Muséum national d'histoire naturelle (1993), 170: 211-233.

Ziegler, R. and Storch, G., 2008. Mammals from the Cyrena Beds of Offenbach (Hesse)-Biostratigraphic correlation. Neues Jahrbuch fur Geologie und Palaontologie-Abhandlungen, 248(3): 267-278.

Zweigel, J., Aigner, T. and Luterbacher, H., 1998. Eustatic versus tectonic controls on Alpine foreland basin fill: sequence stratigraphy and subsidence analysis in the SE German Molasse. Geological Society, London, Special Publications, 134(1): 299-323.

Pro-foreland basins often record along-strike variable architectures in their sedimentary fill, and a diachronous under-to-overfilled transition. However, it remains unclear which process(es) are driving these variations. In this book, analysis of reflection seismic data and a combination of geodynamic–stratigraphic forward modeling is used to reveal the mechanisms controlling along-strike variations in pro-foreland basin architecture. To this end, the Alps-Molasse Basin system is used as a natural laboratory. The results of this work indicate that subduction of a passive margin with an along-strike variable architecture is fundamental in causing diachronous slab breakoff- and tearing. This culminates in a chain reaction forcing orogen-parallel variable sediment supply, translated as along-strike variations in foreland basin architecture and a diachronous under-to-overfill transition.

ISBN 978-3-7315-1443-5
9 783731 514435

Gedruckt auf FSC-zertifiziertem Papier